Sensors, Sampling, and Simulation for Process Control

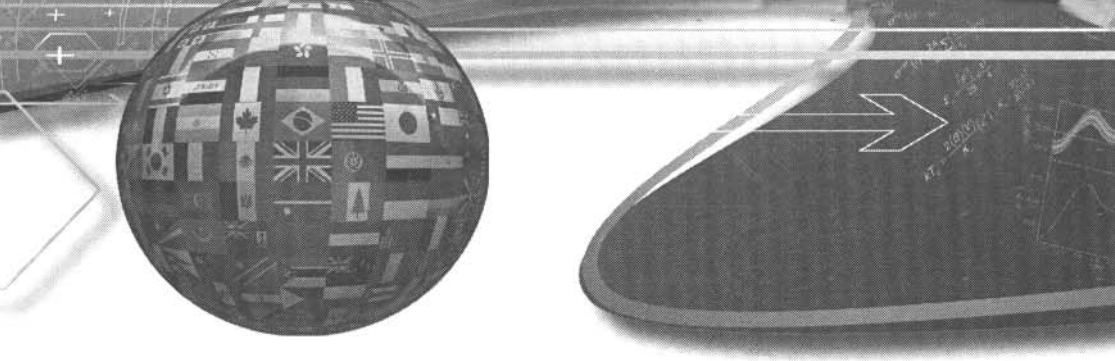

TMS2011

140th Annual Meeting & Exhibition

Check out these new proceeding volumes from the TMS 2011 Annual Meeting, available from publisher John Wiley & Sons:

2nd International Symposium on High-Temperature Metallurgical Processing

Energy Technology 2011:
Carbon Dioxide and Other Greenhouse Gas Reduction Metallurgy and Waste Heat Recovery

EPD Congress 2011

Friction Stir Welding and Processing VI

Light Metals 2011

Magnesium Technology 2011

Recycling of Electronic Waste II, Proceedings of the Second Symposium

Sensors, Sampling and Simulation for Process Control

Shape Casting: Fourth International Symposium 2011

Supplemental Proceedings: Volume 1:
Materials Processing and Energy Materials

Supplemental Proceedings: Volume 2:
Materials Fabrication, Properties, Characterization, and Modeling

Supplemental Proceedings: Volume 3:
General Paper Selections

To purchase any of these books, please visit www.wiley.com.

**TMS members should visit www.tms.org
to learn how to get discounts on these or other books through Wiley.**

Sensors, Sampling, and Simulation for Process Control

Proceedings of a symposium sponsored by
the Process Technology and Modeling Committee
and the Solidification Committee of
the Extraction and Processing Division of
TMS (The Minerals, Metals & Materials Society)
and
Association for Iron and Steel Technology (AIST)

Held during the TMS 2011 Annual Meeting & Exhibition
San Diego, California, USA
February 27-March 3, 2011

Edited by

Brian G. Thomas
James A. Yurko
Lifeng Zhang

WILEY
A John Wiley & Sons, Inc., Publication

TMS

Published by John Wiley & Sons, Inc., Hoboken, New Jersey.
Published simultaneously in Canada.

Library of Congress Cataloging-in-Publication Data is available.

ISBN 978-1-11803-618-1

Printed in the United States of America.

10 9 8 7 6 5 4 3 2 1

WILEY

A John Wiley & Sons, Inc., Publication

TMS

TABLE OF CONTENTS
Sensors, Sampling, and Simulation for Process Control

Sensors, Sampling, and Simulation for Process Control

Liquid Metal Sensing and Online Measurement

Temperature-Related Process Monitoring Systems

Steel Processing; Online Sensors

Foreword

This symposium was created to explore the current state of the art in control of industrial processes in the field of extraction and processing of metals and other materials. New sensor technologies, better sampling methods, and more advanced real-time computational models are enabling better control systems for these processes.

The 18 papers in this proceedings sample the wide range of topics and applications covered in this theme. Many focus on temperature and velocity sensors, especially for online monitoring of molten metals and steel processing. Many aim to improve monitoring capability with the aid of online model simulation.

Molten metal presents a hostile environment for online sensing, which is addressed in several papers. The first two keynote papers review the state-of-the-art in online sampling and sensing of liquid metal quality. The LiMCA inclusion detection sensor is an important commercial tool for molten aluminum, and is still being improved and tested for steel. Other sensors include electro-chemical measurement of dissolved gas composition for porosity monitoring.

Several papers showcase different sensors for measuring and monitoring of velocity in liquid metal. Most of these focus on the surface velocity, which is most important to surface quality in the final product. New non-intrusive electromagnetic-based probes to measure internal velocity are also presented. Challenges remain to find stable materials for reliable sensors in aggressive environments.

Feedback control systems are benefiting from improved process models, which run in real time to serve as "software sensors" when real sensors are not available or are too inaccurate. Recent examples in commercial operation are described for the control of spray cooling in continuous casting of steel slabs, and runout table cooling of steel strip. As computing increase in power, real-time models can increase in accuracy, and control systems such as these should become more widespread.

Simulation can enhance the capability of online sensors. This is explored in several papers, where temperature sensors are augmented using models to "measure" the transient position of the solidification front in continuous metallurgical reactors, the internal temperature in skelp cooling, and the meniscus position in continuous casting of steel. More simulation-aided sensors like these need to be developed and then implemented into control systems.

Specialized online sensors are being applied to processes involving solidification. Examples include imaging pyrometers to measure temperature in laser deposition, measuring coating weight in continuous hot-dipped galvanization, and measuring temperature and strain in the copper mold of steel continuous casting.

Quality problems can also be inferred from simultaneous online detection and analysis of many different process variables. Ultimately, online monitoring of all aspects of the process is crucial, and a high-level management system is needed to integrate the various individual systems together. An example is included here for a steelmaking melt shop.

The work presented here represents just a small fraction of what is now possible. There is great potential for combining better sensors, sampling, and simulation tools together to achieve better control systems for commercial materials processes in the future.

Brian G. Thomas
University of Illinois at Urbana-Champaign
Dec. 6, 2010

About the cover:

Sensors are exemplified in the upper left photo, which shows surface temperature of an experimental vessel of molten zinc being measured by an infrared camera and Flir software. This sensor is part of a system being developed to indirectly sense the location of the solidification front in aluminum reduction cells and other metallurgical reactors, as explained by Clément Bertrand and coauthors in their paper, "Measurement of the Solidification Front Inside a Metallurgical Reactor". See Fig. 8.

Sampling is exemplified in the upper right photo, which shows R. Stone of Heraeus Electro-Nite testing a new ESZpas probe to sample the inclusion content in molten steel. A continuous version of this probe is already used commercially to quantify inclusion content of molten aluminum. These LIquid Metal Cleanliness Analyzer (LiMCA) systems are explained by Rod Guthrie and coauthors in their paper "In-Situ Sensors for Liquid Metal Quality". See Fig. 9.

Simulation is exemplified in the lower left figure, which shows the vertical magnetic field in a scale molten-metal model of a continuous caster. This particular simulation was used to validate the measurements of a new non-invasive sensor, as explained by Klaus Timmel and coworkers in their paper "New Sensors for the Velocity Measurement in Liquid Metal Processes". See Fig. 5.

Process control depends on the information supplied by these three tools. The example process control diagram, shown lower right, schematically describes a new feed-forward feedback control system being developed at ArcelorMittal Global R&D for runout table cooling of steel strip. It is explained by Nicolas Pethe and coauthors in their paper "Dynamic Run-Out Table Cooling Simulator and Temperature Controllers". See Fig. 6.

Organizing Committee

Brian G. Thomas
University of Illinois at Urbana-Champaign, Urbana, IL, USA
bgthomas@uiuc.edu

James A. Yurko
22Ti LLC, USA
jyurko@22tillc.com

Thomas Battle
Midrex Technologies, Pineville, NC, USA
tbattle@midrex.com

Lifeng Zhang
Missouri University of Science and Technology
Rolla, MO, USA
zhanglife@mst.edu

Andrew P. Campbell
WorleyParsons, Melbourne, Australia
andrew.campbell@worleyparsons.com

Srinath Viswanathan
University of Alabama, Tuscaloosa, Alabama, USA
sviswanathan@eng.ua.edu

Editors

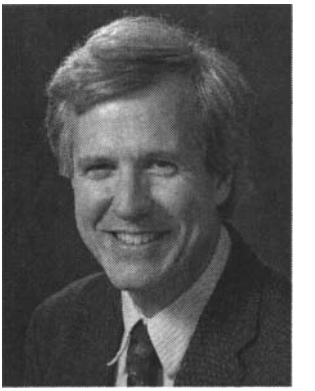

Dr. Brian G. Thomas is the Gauthier Professor of Mechanical Engineering at the University of Illinois and Director of the Continuous Casting Consortium. His research efforts focus on computational models of continuous casting of steel and related processes. He received his Bachelors of Metallurgical Engineering from McGill University, (Montreal, Canada) in 1979 and Ph.D. in Metallurgical Engineering in 1985 from the University of British Columbia, Canada. He has worked in the Research Departments of Algoma Steel, Sault Ste. Marie, Canada and BHP in Melbourne, Australia. Dr. Thomas has coauthored over 270 papers, and has been recognized with a Presidential Young Investigator Award from NSF, Outstanding Young Manufacturing Engineer Award from SME, Xerox Award from UIUC, Distinguished Scientist / Engineer Award from TMS, Fellow of ASM International, and 13 best paper awards. He has given over 175 presentations worldwide and co-instructed many short courses to transfer technology to industry, including the annual Brimacombe Continuous Casting Course.

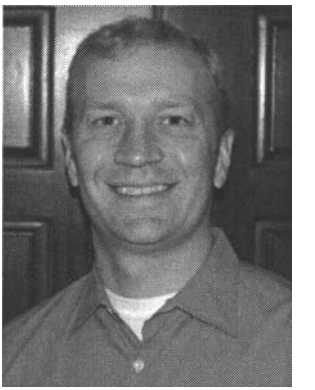

Dr. James A. Yurko is currently the Process Development Manager of 22Ti LLC, an Elkem Metals subsidiary formed in 2007 to commercialize titanium extraction using molten oxide electrolysis (MOE). He received a B.S.E. in materials science and engineering from the University of Michigan and a Ph.D. in metallurgy from the Massachusetts Institute of Technology, where he co-invented the Semi-Solid Rheocasting (SSR) process. He was the R&D team leader and staff metallurgist of BuhlerPrince, Inc., responsible for commercializing the SSR process and various metal die casting development projects. He then co-founded Electrolytic Research Corporation LLC to pursue commercial applications of MOE. Dr. Yurko is a Research Affiliate in MIT's Department of Materials Science and Engineering. He is also a member of TMS and ASM, and serves on the University of Michigan Materials Science and Engineering External Advisory Board. Dr. Yurko is a 2010 winner of the TMS EPD Young Leader Professional Development Award.

Dr. Lifeng Zhang currently is an assistant professor at the Department of Materials Science and Engineering at Missouri University of Science and Technology. Lifeng received his Ph.D. degree from University of Science and Technology Beijing in 1998 and had 13 years teaching and research work at different universities - Norwegian University of Science and Technology, University of Illinois, Technical University of Clausthal and Tohoku University. Lifeng has compound backgrounds in primary production, refining, casting, and recycling of metals, recycling of electronic wastes, and modeling for metallurgical processes. Lifeng has published over 200 papers and made over 150 presentations at meetings and conferences. He is a Key reader (Member of Board of Review) for three journals and a reviewer for over twenty-five journals.

Sensors, Sampling, and Simulation for Process Control
Edited by: Brian G. Thomas, James A. Yurko, and Lifeng Zhang
TMS (The Minerals, Metals & Materials Society), 2011

Sensors, Sampling, and Simulation for Process Control

Liquid Metal Sensing and Online Measurement

Sensors, Sampling, and Simulation for Process Control
Edited by: Brian G. Thomas, James A. Yurko, and Lifeng Zhang
TMS (The Minerals, Metals & Materials Society), 2011

IN-SITU SENSORS FOR LIQUID METAL QUALITY

Roderick Guthrie and Mihaiela Isac

McGill Metals Processing Centre, 3610 University Street, Montreal, Qc, H3A 2B2, Canada

Keywords: LiMCA, metal quality, Electric Sensing Zone (ESZ), ESZpas, ultrasonics

Abstract

The development of effective methods for directly measuring liquid metal quality, prior to casting and final solidification, has long been a goal for Process Metallurgists. Most techniques now in use, either freeze a sample of the metal for later examination, or first concentrate the inclusions through filtering the metal through a porous frit, before then freezing the metal, and again subjecting it to microscopic examination (e.g. PoDFA). An alternative method is to take a sample of metal, freeze it, and then dissolve the metal to release the particles (inclusions) through elutriation (the Slime Technique). The only true on-line, in-situ, methods are the Ultrasonic Liquid Metal Sensors (such as the Mansfield Molten Metal Sensor), and the Electric Sensing Zone Methods (such as LiMCA and ESZ-pas). A brief history of the developments in these approaches will be presented, and their long term prospects will be assessed versus other techniques.

Introduction

In view of the importance of the level of inclusions on metal quality, it is not surprising that a variety of approaches for evaluating metal cleanliness have been developed over the years. These can be divided into four main categories: 1) Chemical Methods, 2) Optical Methods, 3) Operational Methods, and 4) Physical Methods. This review emphasizes some of the important techniques that have been used, or attempted, for the evaluation of cleanliness in melts of aluminum and steel.

Chemical Methods

Gross chemical analysis is of little use in measuring the inclusion content in aluminum, but is well recognized in characterizing inclusion levels in steel. For aluminum, it has been established that measuring the bulk concentration of an element or compound tells nothing about how it is distributed within the metal. For instance, it has been established that there is no correlation between the oxygen concentration and the inclusion level in aluminum. Typical oxygen levels in commercial aluminum range from five to fifty parts per million (ppm), with most of the oxygen present, being in the form of very thin (<2μm) oxide films. Similarly, total carbide levels can be measured by reacting them with water to form methane, which can be detected at very low levels by gas chromatography. However, once again, this approach provides no indication of particle (inclusion) size [1].

In the case of liquid steel, the measurement of total oxygen contents can provide a global indication of a steel's cleanliness. However, it says nothing about the sizes of inclusions responsible [2]. Nonetheless, given its convenience, and quickness, it is common to use total oxygen contents as measured by a LECO oxygen sensor, or equivalent, less dissolved oxygen if appropriate, as a comparative measure of steel quality, as a steel melt goes through the sequence of processing in the furnace, ladle, tundish, and mould, prior to solidification.

An alternative approach, chemically, is to dissolve the metal matrix [3, 4], so as to release the inclusions for analysis through other means; optical microscopy, Coulter Counter analysis, etc.

While this approach has been shown to work for steel (the slime dissolution technique), it is less suitable for aluminum, owing to uncertainties concerning the loss of water soluble inclusions, or the production of artifacts during extraction, and the generally much lower level of inclusions within molten aluminum versus liquid steel to start with. The main drawback to this technique for both metals is the laborious and slow nature of this approach, which clearly renders it unsuitable as a candidate for a rapid method of quality control.

Optical Methods

Perhaps the most common method of assessing the inclusion content in steels and aluminum alloys is in the direct examination of polished sections under the optical microscope, or scanning electron microscope. This is well established in steelmaking practices, where the steel samples can be directly used, given the abundant numbers of small inclusions typically present. For instance, Kaushik, Pielet and Yin [5], recently reported on the use of an Automated SEM system, which are now in common use within the steel industry for assessing steel cleanliness. The data acquired from the analysis are presented as distribution charts, and in the form of ternary phase diagrams, by a data management system. Sometimes, a simulation is conducted on the inclusion data, to show the differences between two-dimensional, and three dimensional, characterization, to estimate the standard deviation of an index, such as inclusion density, and to improve the accuracy of the analysis by minimizing the required sample area. In aluminum, by contrast, at the concentrations typically encountered in reasonably clean aluminum (approximately 5 to 20 particles per ml, 20 μm dia.particles, or larger), one must first pre-concentrate the inclusions, so as to observe a significant number of particles within a reasonable area.

One of the early methods of pre-concentration was the INFA (In-Mould Filtration Apparatus). This test involved passing a fifty pound sample of liquid metal through a glass filter cloth, allowing the metal to solidify while some metal still remained on the upstream side of the filter, cutting out the filter and metal, and finally sectioning and polishing the filter cake. Since the filter cloth was relatively coarse, the method essentially depended on the formation of a cake of alumina films, which in turn, acted as the true filter medium, in retaining other forms of inclusions. Given the erratic data, and the large sample size, resulting from this test, the method was refined to the PoDFA (Porous Disc Filtration Analysis) test, which now calls for a 5 lb sample of melt, forced under pressure through a fine porous aluminum carbide filter disc. The pressure is released before all the metal has passed through, and the remaining sample is allowed to freeze. It is then cut, sectioned, and analyzed optically for inclusion types and sizes. This method is in common use, and inclusion concentrations are quantified in terms of mm^2 of inclusions/kg of melt. However, it is time consuming (~5 days), and "operator" dependent. Despite some forty years of development, the original PoDFA technique remains "semi-quantitative" [1]. Many other similar techniques based on this pre-concentration approach, have since been developed by other producers and sensor companies.

Operational Methods

In view of the lack of an entirely adequate method to evaluate liquid metal quality, reliance has been placed upon the measured performance of production or product materials as a guide for the development of plant practices and melt treatment devices. This includes, for example, the rate of tool wear in machining, extrusion die longevity, the quantity of wire drawn per break, pin holes per unit area of aluminum foil, surface defects per unit area of sheet, failure rates in beverage cans ($1/10^6$), etc. Although these types of "tests" are undeniably relevant, in that they measure actual production or product performance, this approach inevitably leads to costly

rejects, and does not measure true cleanliness. While this approach does serve to develop empirical production procedures that are satisfactory for specific individual applications, it does not permit any possibility for on-line process control.

In the steel industry, one such method of analyzing steel quality is the Mannesmann skate-, or ski-board technique, in which a sample of steel is rolled down to a sample sheet, and the numbers of defects appearing on the surface, as blemishes or scabs, are recorded as a measure of steel quality. Mention should also be made of the ultra-sonic in-line inclusion detector for the characterization of steel sheet products. This is a development by JFE, Japan, in which the inclusions in the rolled product sheet material are subjected to ultra-sonic detection [20]. The method is capable of detecting inclusions down to a volume size ~ 5 x 10^{-5}mm^3, or ~450 μm diam., within the thickness of the sheet. Again, while it is an operational method, any upstream liquid metal quality issues of a constant nature are soon apparent, and can be addressed. Perhaps this is the most satisfactory of all the operational methods developed for sheet material so far. Naturally, the "size" of the inclusions detected using these techniques, are different from the sizes of the exogeneous inclusions caught up within the melt, prior to casting. Their "sizes" are associated with the rolling procedures, which will tend to elongate the inclusions in the rolling direction, and thin them in the transverse section

Physical Methods

In contrast to the techniques discussed in the previous three sections, physical methods have the advantage that they can be carried out relatively rapidly, at least in principle, and therefore allow some hope of implementation as process control techniques for liquid metal quality characterization.

Filtration Rate Tests

The rate of liquid metal filtration at a constant differential pressure has been investigated by ALCAN [1]. However, this approach was abandoned when it became evident that the rate was influenced by all particulates suspended in the metal, including any small oxide films and grain refiner nuclei. This, together with the relatively low concentrations of larger, detrimental inclusions, resulted in the latter exerting little, or no, detectable effect on the filtration rate. The early Union Carbide particulate tester, mentioned by Levy [6], has also been used for filtration rate testing. In this case, the sampler was fitted with a load cell, and the measured weight-time curves were fitted to an equation of the form:

$$W=at^b. \quad (1)$$

An alternative device was considered by Levy et al [7], who investigated the rate of the rise in the differential pressure developed across a porous frit of the ALCOA telegas probe. The fact that inclusions can act as nucleation sites for hydrogen gas bubble formation in the Straupe-Pfeiffer (vacuum-gas) solidification test, lead to the development of that test as a qualitative tool for estimating metal cleanliness quickly. Despite obvious limitations in providing independent data concerning either the hydrogen level or the inclusion content, this approach has proved useful as a quick "pass/fail" test of the overall quality for aluminum.

Ultrasonics

Ultrasonic technology for the non-destructive testing of solid materials is very well established. Indeed, the method is used routinely to inspect welds, extrusion ingots, etc. for macroscopic defects. In general, the sizes of the defects detected by routine ultrasonic inspection are relatively large, typically several millimeters, though resolutions down to the order of 0.1mm are reportedly possible. An attempt to correlate the ultrasonic attenuation of solid samples with their

inclusion concentration was reported by Levy et al [7], who concluded that the former was more a measure of porosity of the sample than of its inclusion content.
In 1968, Pitcher [8] demonstrated that ultrasonic techniques could be applied to liquid metals. This sparked considerable interest in the application of the ultrasonic techniques to measure the cleanliness of aluminum and steel melts, and by 1979, Alcan, Alcoa, and Reynolds Aluminum, all had ultrasonic development programs well underway. T.M.Mansfield of the Reynolds Aluminum Company presented a paper at the 1982 AIME Conference, describing their developments in the field of Ultrasonics [9] and shown in Figure 1. It was capable of making four types of measurements directly in molten aluminum: attenuation, discontinuity detection, velocity, and spectral analysis. Attenuation measurements were reportedly capable of indicating the overall level of suspended particles within the melt, with particles as small as one tenth the wavelength of the imposed ultrasonic oscillation contributing to the attenuation. Since the oscillator described was operated at 10 MHz, and the velocity of sound in molten aluminum is approximately 4700 m/sec [1], the detection limit for attenuation measurements ($c = f\lambda$) would be $(4700/10^7)*0.1 = 47$ microns. Thus, for the direct detection of individual discontinuities (i.e. inclusions) in a molten metal, these can be measured provided, in theory, their size (diameter) is not smaller than half the wavelength of the incoming detection signal. For the probe described by Mansfield, this would be $(4700/10^7)*0.5 = 235$ microns. The velocity measurements refer to the determination of the velocity of sound in the melt and not to any measurement of metal cleanliness. Finally, the spectrum analysis measurements refer to a potential use of the technique to measure attenuation as a function of frequency, which would apparently be subject to the same size of detection limitation as are discontinuity measurements (i.e. $\lambda/2$ or 235 μm for the case at hand).

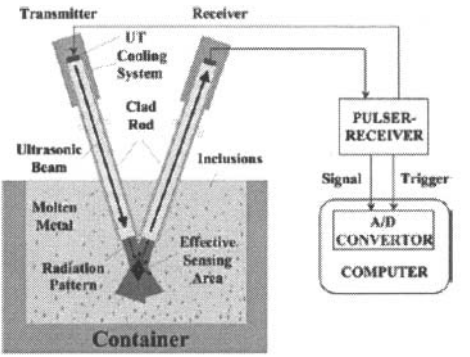

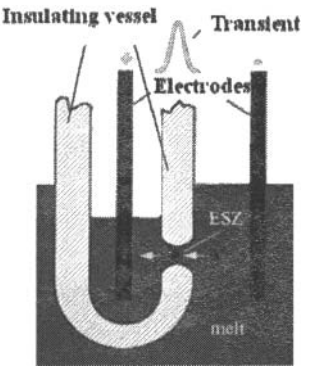

Figure1 – Schematic of an Ultrasonic Inclusion Detector. **Figure 2.** A resistive pulse is generated by the passage of a non-conducting particle through an electric sensing zone, ESZ.

Given that the velocity of sound in liquid steel is very similar to aluminum (~ 4.4 km/s), but the temperatures are much higher ~1600 °C, the detection of inclusions less than ~220 μm is even more difficult, given that the ultrasonic devices have to operate in a very hostile environment at 10^7 Hz. However, the great interest in the potential application of ultrasonics to detect melt quality, demonstrated that there was a great need for an on-line, in-situ, sensor for liquid metals. This was attributable to the development of the aluminum can industry, representing some 30% of ALCAN's metal output, for which no sensor was available to guarantee the extreme metal

cleanliness required by the beverage can makers. In terms of the detection limit of ultrasonic technology, since the particle detection limit is inversely proportional to the excitation frequency, it is evident that the detection limit could, in principle, be made as small as desirable, by using a higher frequency source. Unfortunately, this approach is apparently not feasible due to the necessity of using wave-guides (generally titanium) to conduct the vibrations from the source (generally an oscillating crystal) to the liquid metal. The ultrasonic attenuation of the wave guides rises rapidly with increasing frequency, and thus there is a practical upper limit to the inspection frequency.
Nonetheless, despite the relatively coarse limit of detection, Mansfield was able to qualitatively demonstrate the detrimental effect on metal cleanliness of disturbing a filter and the beneficial effect of allowing a settling period prior to casting metal from a furnace. In contrast to most alternatives, ultrasonic measurements of liquid samples have the distinct advantage of providing a rapid indication of melt cleanliness. Nevertheless, it would seem that considerably more development work still remains to be done before the technique can provide quantitative measurements of liquid metal cleanliness.

The Resistive Pulse or Electronic Sensing Zone, (ESZ), Technique.

In 1979, following a summer of technical work with ALCAN's Kingston Research Laboratories, Dr Guthrie arranged to continue this research back at McGill, having negotiated a top-up ALCAN scholarship to attract a good doctoral student to work with him on the role of salt particles, in affecting the cleanliness of aluminum. Mr Don Doutre, then working at the Noranda Research Centre, was keen to return to McGill University for his Doctorate in Process Metallurgy, and the stage was then set to resolve the problem of detecting inclusions in liquid metals quantitatively. It was given the acronym **LiMCA**, for **Li**quid **M**etal **C**leanliness **A**nalyser. It came about as a possible solution to the problem Doutre and Guthrie were contemplating: the prospect of acquiring many samples of frozen aluminum containing soluble salt particles, and then having to analyze them, in order to quantify the levels of inclusions generated during Cast House, in-line, melt refining processes. This was truly a daunting task. The two researchers decided to see whether the Coulter Counter Technology for aqueous solutions could be applied directly to liquid metals. Prior to that, the only use of the Coulter Counter to monitoring the levels of inclusions (in steel) was reported by Flinchbaugh [3] who used the slime dissolution technique to first dissolve the steel sample in acid, and to pass the resulting "sludge" of inclusions through an off-line, ESZ instrument, termed the Coulter Counter.
Our early exploratory tests at McGill made use of liquid gallium, at room temperature, laced with inclusions of flour. We decided that a much larger DC current (e.g. 60 amps vs 20 mA for aqueous solutions) would be needed to help compensate for the million, or so, times higher electronic conductivity. Using a car battery, we were then able to detect voltage signals from the inclusions. These preliminary tests also revealed that the "Faraday cage" effect of the liquid metal allowed clean microvolt signals to be generated inside the liquid metal, and to be recorded by an oscilloscope, provided ambient electrical noise was minimised.
This preliminary research work lead to the purchase of the necessary logarithmic amplifiers and data loggers needed for the development of a prototype LiMCA machine for liquid aluminum. The prototype inclusion sensor (termed the "Monster"), was demonstrated to ALCAN's top officials. Following their support, arrangements were made to test it out in the Saguenay plant, in collaboration with key researchers at ALCAN. Work progressed well, and patents were filed with the financial support and help of ALCANINT [10]. Within five short years, we had proved the feasibility and use of this new technique. LiMCA II was built by BOMEM, and later made available for the whole aluminum industry, by the late 1990's.

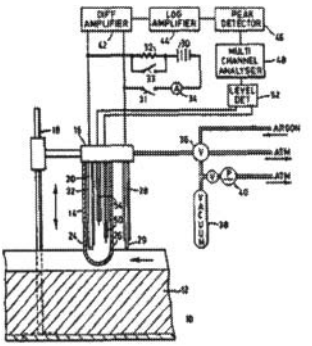

Figure 3 Diagram of LiMCA for aluminum, U.S. patent 4,555,662, Nov 26th, 1985. [10].

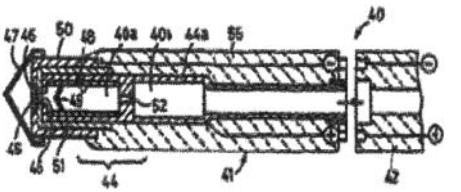

Figure 4. Single use disposable inclusion sensor patented in 1993 by Nakajima and Guthrie [11].

Principle of the ESZ Technique for Liquid Metals

J.C.Maxwell was the first scientist to consider the electrical resistance generated by the presence of a non-conducting particle, in a current carrying fluid, within an infinitely long cylindrical tube. He showed that under these ideal conditions, the effective electrical resistance was increased by a factor of 1.5 times the fractional volume of a relatively small non-conducting particle ($d \leq 0.1D$);

$$\rho_{eff} = \rho\,(1 + 3/2f + \ldots.) \tag{2}$$

For a cylindrical sensing zone of length L and diameter D, filled with a fluid of resistivity, ρ, the resistance is:

$$R_1 = \rho\, L / A = 4\rho L/\pi D^2 \tag{3}$$

When a sphere of diameter d is introduced, the value of f becomes:

$$f = V_{sphere}/V_{cylinder} = 2d^3/3D^2L. \tag{4}$$

Substituting "f" from Equation 4 into equation 2, and Equation 2 into Equation 3, gives the resistance of a cylinder with a small non-conducting sphere contained within it:

$$R_2 = (4\rho L/\pi D^2)\,(1 + d^3/D^2L + \ldots\ldots) \tag{5}$$

Subtracting Equation 5 from 3, we have the desired expression for ΔR

$$\Delta R = 4\rho d^3/\pi D^4 \tag{6}$$

leading to; $$\Delta V = 4\rho I d^3/\pi D^4 \tag{7}$$

Here ρ is the electrical resistivity, I is the applied D.C. current, d is the diameter of the particle, and D is the diameter of the electric sensing zone (at its narrowest location). For spheres larger

than ~30% the diameter of the ESZ, Smythe's correction factor for the ESZ technique can be used. This factor takes into account the increased distortion of the electric flow field around the particle, as it becomes relatively large. For this, f(d/D), is given by:

$$f(d/D) = [\ 1 - 0.8\ (\ d/D)^3\ ]^{-1} \tag{8}$$

so the final equation becomes:

$$\Delta V = 4\rho I d^3/\pi D^4 * [1 - 0.8\ (\ d/D)^3\ ]^{-1} \tag{9}$$

Equation 9 provides the basis for characterizing the size of the inclusion as a function of the various parameters of the ESZ, and of the relative size of the inclusion.
There are some basic differences between the detection of inclusions in aqueous systems, and in liquid metals. Apart from the question of a million fold decrease in electrical resistivity versus aqueous media, and compensation using high DC currents to produce recognizable ESZ signals from inclusions, a strong magnetic "pinch" effect results. This induces a strong self-inductive magnetic field within the ESZ, which tends to deflect non-conducting, or insulating, inclusions towards the sidewalls of the ESZ, as illustrated in Figure 6.

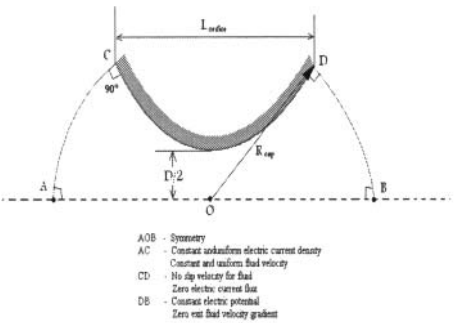

Figure 5 – Computational domain used by Mei Li for mathematical simulations [12].

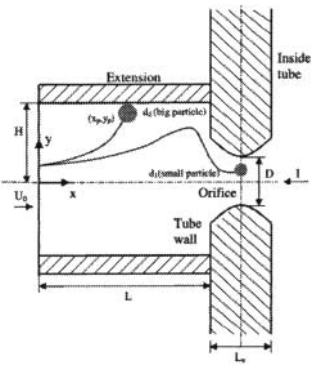

Figure 6. Proposed "smart" probe for separating microbubbles from inclusions

Theory of Inclusion Motion through ESZ.

Figure 5 shows half of a parabolic shaped ESZ (Electric Sensing Zone) that was used to represent conditions in the LiMCA equipment for molten aluminum, for the mathematical modeling work tackled by Mei Li, in ~2000 AD [12], and more recently, by Xiaodong Wang[16]. As seen, the exit and inlet boundaries were defined by spherical caps centered at point O which is the centroid of the orifice. Mei Li used our **Metflo** code to compute the flow field, taking into account electromagnetic effects. Xiadong Wang adapted commercial software, Comsol Multiphysics 3.4 to make similar numerical simulations. The results of both researchers were in close agreement when we compare the shape of the contours of the electric field. Our group has published a large number of theoretical papers exploring particle behavior and dynamics, as inclusions pass through variously shaped electric sensing zones. Advanced numerical simulations have been made, tracking the passage of a particle, or inclusion, through an orifice of arbitrary shape. To predict the trajectories of particles through a typical parabolic ESZ used for

melts of aluminum, we need to solve Newton's Second Law of motion, applied to an inclusion passing through the accelerating flow entering the ESZ:

$$\rho_p V_p \frac{du_p}{dt} = \frac{1}{2} C_{Dstd} \pi a^2 \rho_f |u - u_p|(u - u_p) + \frac{1}{2} \rho_f V_p \left(\frac{Du}{Dt} - \frac{du_p}{dt} \right) + \rho_f V_p \frac{Du}{Dt}$$
$$+ 6a^2 \sqrt{\pi \mu_f \rho_f} \int_0^t \frac{d(u - u_p)/d\tau}{\sqrt{t - \tau}} d\tau + V_p(\rho_p - \rho_f) g - \frac{3(1-\chi)}{4} V_p F_e \qquad (10)$$

This equation states that the mass of an inclusion, multiplied by its acceleration, is equal to the sum of: 1) the standard drag force exerted on the particle owing to relative motion between the local liquid velocity within the ESZ and the particle, together with 2) the "added mass" force which must be included if a particle is accelerating, or decelerating, relative to the fluid, 3) the fluid acceleration term, a history term (4), a buoyancy term (5), and an electromagnetic force term (6). The dominant force terms applying to particles travelling through the ESZ's are the standard drag force, the added mass force, and the electromagnetic force. Gravity (buoyancy) and History force terms are numerically much less. Our simulations have demonstrated a number of important aspects which opens the way for ESZ-type sensors to not merely record the size of a passing inclusion, but also to resolve it into inclusion types.

For instance, we were able to verify theory through the work of Mr Chris Carozza [13] that micro-bubbles could be differentiated from solid particles of the same size, on the basis of arrival times (or times of passage) to the throat of the ESZ; a bubble arrives ahead of the liquid, and a solid, whose density is greater than that of liquid aluminum, arrives later. Similarly, Dr Xiaodong Wang [16] was able to show that bubbles and droplets, even very small ones in our range of interest (15-300 microns approx.), are deformable in a strongly accelerating flowfield, thereby generating lower, longer, signals that are more "spread out" for gas bubbles. Prior to that, Mei Li was able to demonstrate that the short length of the wall thickness, through which the inclusion flows, is responsible for the high "pass through" fractions of inclusions, in all size ranges, and all inclusion types [12]. In short, the theoretical science is helping to lead the way. For instance, we have also developed a theoretically correct "smart probe" for molten aluminum that should float out large gas bubble "inclusions" and only allow small, discrete particles to flow into the ESZ. This is shown in Figure 6 above, as an alternative and better design to those in current use for monitoring metal quality downstream of an in-line hydrogen degassing unit [14].

Experimental Developments

The first LiMCA machines were developed for the aluminum industry. The first commercial unit was the LiMCA II, manufactured by BOMEM, Quebec City, and shown in Figure 7. This was developed from the original "monster" equipment developed at McGill and sent to Arvida, which used an aluminosilicate tube (silica is attacked by aluminum). The tube was drilled, flame shrunk, and annealed, so as to produce a parabolic shaped ESZ. The key to the success of this equipment was this shape of orifice, which, in the presence of a heavy current, reverses the flow field, expelling liquid aluminum outwards from the ESZ. This proved to be essential to the many sucking and blowing events which take a sample of liquid into the sensing zone, and then expels it back into the melt, at the end of each set of data. During the course of a pour, it was found that inclusions would tend to form a raft or cluster upstream of the ESZ throat, thereby filtering the melt, and leading to falsely lower readings, and "cleaner metal" with time. This was an artifact that was resolved by applying a short, intense, current, prior to each uptake cycle. This heavy current prevented, and/or removed, any blockages building up.

Another novelty of LiMCA II was the use of four external electrodes, in order to decrease the effects of environmental electrical noise, especially that associated with the Hall-Heroult cells in the pot line room. These can be seen in Figure 7 where the LiMCA II machine is operating in a launder, through which molten aluminum is flowing down into the moulds of a group of DC casters (DC = Direct Chill).

Once the LiMCA machine for aluminum was proven, we then turned our attention to detecting inclusions in liquid steel. This proved to be a far more challenging task, owing to the materials problems associated with operating in liquids at 1650°C. In our early work at McGill, Dr Hidemasa Nakajima [11] attempted to build an inclusion sensor for liquid steel, using the same principles as developed for molten aluminum. Figure 8 shows such a machine, which we tested at DOFASCO in their 70 tonne tundish, back in the late 1980's. The work was successful, in that inclusions could be detected, but the probe's lifetime was relatively limited, as the silica was subject to softening and erosion. This caused the silica to expand like a balloon, on occasion, or to contract. Guthrie and Lee [15] next reported on correlating the inclusion counts derived from our steel LiMCA equipment, against simultaneous slime samples, again taken simultaneously at Dofasco. It was found that an excellent correlation existed between the two measures of larger (>20 μm) inclusions.

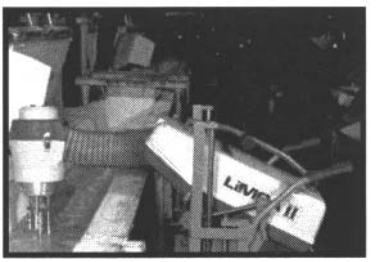

Figure 7. LiMCA II (**L**iquid **M**etal **C**leanliness **A**nalyzer), for the ***in-situ***, on-line, detection of inclusions (size & frequency distributions) in Al melts.

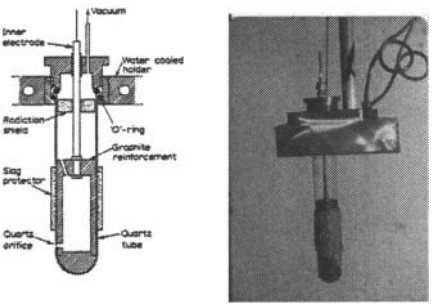

Figure 8 Early Design of an Inclusion Sensor Probe for Steel Melts, and its construction and use by H.Nakajima. (ca.1985).

Given the operational problems of developing continuous probes for steel, it was decided by Heraeus Electro-Nite, and Sumitomo Metals Industries, of Japan, to build a "one-shot" sampler probe. After a very large 10kg sampling probe trial had failed, owing to aspiration problems, they settled on a small, one-shot, silica tube probe, suitable for Heraeus' standard sensor probes for dissolved oxygen, and temperature measurements. The final version developed by Heraus Electro-Nite is shown in Figure 9, where it is being plunged into a ladle full of steel at Sorel Forge in 2007. This work is part of a CRD (Co-operative Research and Development) grant from NSERC (Natural Sciences and Engineering Council).

For the "one-shot" probes, clogging of the probe orifice, upstream of the throat, is not an issue. As such, the holes are laser drilled, and are essentially rectangular cylindrical holes in a silica tube with a slight open taper at their entrance. There is a slight erosion of the orifice during passage of steel through the ESZ, depending on grade. The important thing is the flow through the ESZ is not restricted, and no clogging occurs, hence the acronym, ESZpas.

Figure 9. Mr R. Stone, of Heraeus Electro-Nite, making steel quality measurements using ESZpas at Sorel Forge, Nov. 2007.

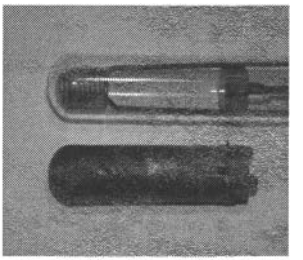

Figure 10. View of the quartz (silica) tube with an inner copper anode, and the solidified steel sample following immersion of the "one-shot" probe.

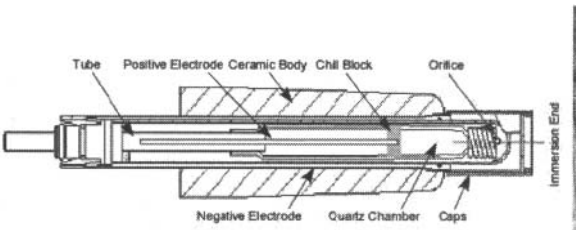

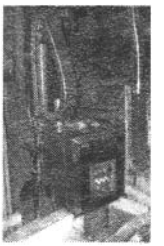

Figure 11. *Schematic of the ESZpas measuring system.* ***Figure 12.*** *LiMCA CM produced by* Bomem ABB for molten aluminum.

Operational Results.

LiMCA, and more recently, ESZpas machines, have proved their worth in industry. Some 200 LiMCA II machines were sold since 1995. They have been used to monitor liquid metal quality, and to improve liquid metal handling and treatment procedures. This includes monitoring the effectiveness of ceramic foam filters (CFF), of deep bed filters (e.g. ABF), of monitoring oxide contamination during the drop of liquid metal from the launder into the DC moulds, and finally, for optimizing liquid metal hold times in the "Holding Furnaces" within the aluminum cast house. This allows for maximum yields and productivities.

For the ESZpas LiMCA machines, many tests have been carried out on a client by client basis, such as Tempkin Steel [18,19], and many others. The equipment has been shown to function very well with medium and higher carbon heats, where filling of the sample chamber occurs 100% of the time. With the ULC grades, successful filling rates are lower, since the superheats are often below about 15°C, for which heat input and thermal equilibrium seem to be the determining factors. As such, ESZpas remains a work in progress. By contrast, the LiMCA II machine has now been replaced by the LiMCA CM (Continuous Monitoring) by ABB Bomem. This machine, shown in Figure 12, replaces the analogue equipment contained in the LiMCA II

machines with digital equipment. Note the sensor is totally encased in a metal shell, for electrical noise suppression.

Future Prospects

The development of LiMCA machines is now at the end of its 3rd decade. While much has been done, much more could be accomplished with the right mix of talents and research personnel. The review presented here aimed to put into perspective the discovery and development of Liquid Metal Cleanliness Analyzers (LiMCA), and their direct competition, the Ultrasonic Probe Technology.

Both are systems which rely on physics, metallurgy, signal processing and electronics, and multi-disciplinary knowledge has always been necessary to make the systems work. This is possibly one of the reasons it has taken such a long span of time for them to reach their current states of development. As noted, commercial variants of the original LiMCA "monster" were operating successfully, within five years of concept, in the form of LiMCA II machines, displacing the UST probes, but this was a result of market pull, rather than of technology push. Once fully commercialized in the early 1990's, LiMCA II was later marketed by ALCANINT and Bomem to other aluminum companies. More recently, Heraeus Electro-Nite now markets a commercial variant of LiMCA, the LiMCA ESZpas, built for monitoring inclusions in liquid steel [18,19]. However, the ESZpas still represents a work in progress, since it has not yet been successfully applied to ultra-low carbon heats on a regular basis. Whilst LiMCA machines have indeed come a long way, there remains a lot of further improvement that is called for, especially in liquid steel applications, where it needs to be marketed to its full potential.

Academic researchers have long predicted that the LiMCA principle can be used to differentiate between solid inclusions, small liquid droplets and air micro-bubbles [17]. This contention is now supported by recent industrial claims that the software developed for registering the metal quality index was independent of whether the sampler was placed within a rising plume, or outside the bubble-driven flow [18, 19].

Similarly, although robust algorithms and codes were developed for the APS II water LiMCA equipment, for discriminating between ambient noise (false) and good ESZ signals, these programs are no longer current, and were not extended to liquid metal sensors. As such, they have yet to be developed for the high temperature systems, and this is clearly another one of the areas where future research and development activities should be channeled.

With respect to the other, on-line, physical method, relying on ultrasonics, the ferrous process metallurgy group headed by Professor Alex McLean at University of Toronto has continued trying to develop an ultrasonic sensor for detecting inclusions in liquid steel. While Dr M. Mountford has been active for many years on this research target, being funded by the American Foundry Society, nothing practical has apparently emerged from their efforts. On the other hand, the application of UST to monitoring inclusions in solidified steel sheet by JFE has been perfected as an on-line technique for monitoring steel sheet quality [20], but the smaller sized inclusions of interest to us, remain below its detection limit of ~450 microns. It proves that steel contains many inclusions that are much larger than those typically considered by steelmakers.

References

1. D. Doutre: "The Development and Application of a Rapid Method of Evaluating Molten Metal Cleanliness" Ph.D.Thesis, McGill University, Montreal, 1984

2. R. Kiessling "Clean Steel – A Debatable Concept", Clean Steel, Proc. of the Second International Conference on Clean Steel, 1-3 June, 1981, Belatonfured, Hungary, The Metals Society, London, pp. 1-9, 1983.

3. D.A. Flinchbaugh., "Use of a Modified Coulter Counter for Determining Size Distribution of Macro-inclusions Extracted from Plain Carbon Steels" Analytical Chemistry, 1971, vol.43, pp.178 -182
4. C.J.Siemensen and G.Strand, "Analysis of Inclusions in Aluminum by Dissolution of the samples in Hydrochloric/Nitric Acid" Fresnius Z.Anal.Chem., 1981, vol308, pp.11-16
5. P. Kaushik, H.Pielet, and H.Yin "Inclusion characterization – tool for measurement of steel cleanliness and process control: Parts 1 and II", Ironmaking and Steelmaking, volume 36, No.8., 2009, pp.561-571 and 572-582.
6. S.A.Levy, 'Applications of the Union Carbide Particulate Tester", Light Metals, TMS of AIME, 1981, pp 723-733.
7. S.A.Levy, J.C.Miller, P.McNamara and D.A. Feitig, "Molten Metal Quality – Particulate Tests", Light Metals, TMS of AIME, 1977, pp.149-170.
8. D.E.Pitcher, "Methods of an Apparatus for Testing Molten Metal", U.S.Patent 3,444,726, May 20, 1969.
9. T. L. Mansfield, "Ultrasonic Technology for Measuring Molten Aluminum Quality", Light Metals, TMS of AIME, 1982, pp.969-980.
10. D.Doutre, R.I.L.Guthrie, "A Method and Apparatus for the Detection and Measurement of Particulates in Liquid Metals", U.S.Patent 4,555,662, November 26th, 1985.
11. H.Nakajima, R.I.L.Guthrie, "A Single–Use Probe for Detecting Inclusions in Liquid Steel", U.S.Patent, 5,198,749, March 30th, 1993.
12. Mei Li and R.I.L. Guthrie, (2001), "In situ Detection of Inclusions in Liquid Metals: Part I. Mathematical Modelling of the Behavior of Particles Traversing the Electric Sensing Zone", Part II . "Metallurgical Applications of LiMCA Systems"*Metallurgical and Materials Transactions B*, Vol. 32B, December 2001, pp. 1067-1079 and 1081-1093.
13. Chris Carozza. M. Eng. Thesis, 1999, McGill University, "Water Modelling of Particle Discrimination using LiMCA Technology"
14. Mei Li and R.I.L.Guthrie; "Molten Metal Inclusion Sensor Probes" U.S.Patent 6,556,853 B2, May 20th, 2003, plus counterpart patents for Japan, Korea, and Canada.
15 R.I.L. Guthrie and H.C.Lee; "On-Line Measurements of Inclusions in Steelmaking Operations", Proc.75th Steelmaking Conference, I.S.S. of A.I.M.E., Toronto, April 1992, pp. 799-805
16. Xiaodong Wang, Mihaiela Isac, R.I.L. Guthrie, "Numerical studies on the *in-situ* measurement of inclusions in liquid steel using the ESZ, or LiMCA technique" ISIJ International, Vol.49, 2009, No.7, pp.975-984.
17. T. Draganovici, X. Shi, G. Carayannis, F. Dallaire, R.I.L. Guthrie, "Towards Inclusion Type Discrimination in Liquid Metals Based on the Electric Field Theory", *Proc. Second Intl Symp. on Metallurgical Processes for the Year 2000 and Beyond*, TMS, San Diego, September 1994, pp. 251-266
18. R.P.Stone, C.C.Liu, and P.C.Glaws: "Experience with an innovative on-line inclusion determination system for liquid steel", Proc. 7th Conference on Clean Steel, Belatonfured, Hungary, June 2007, MVAE Association of the Hungarian Steel Industry, on CD Rom.
19. R.P.Stone, C.C.Liu and P.C.Glaws; "Experience with an innovative on-line inclusion determination system for liquid steel" Iron and Steel Technology,AIST, July 2009, pp.42-48
20. A.Nagawana, H.Takeda, T.Yamasaki, Y.Tomura, T.Sasaki, M.Aratani; "An on-line detection system for internal flaws in as-hot rolled steel strip using an ultrasonic probe array". Second International Symposium on Sensors for Iron and Steelmaking, Conference Chairman; Professor M. Iwase, Kyoto University, November 7-8, 2005.

Sensors, Sampling, and Simulation for Process Control
Edited by: Brian G. Thomas, James A. Yurko, and Lifeng Zhang
TMS (The Minerals, Metals & Materials Society), 2011

SENSORS FOR ON-LINE MONITORING OF MOLTEN METAL QUALITY

Jeffrey W. Fergus

Auburn University; Materials Research and Education Center; 275 Wilmore Laboratories; Auburn, AL, 36849, USA

Keywords: Molten metal, sensors, porosity, inclusions

Abstract

The dissolution of gases in molten metals can lead to porosity and/or formation of inclusions in the resulting product. Real-time control of the process to minimize these defects requires information on the quality of the melt during processing. Electrochemical-based techniques can provide information on the chemical properties of the melt, while electromagnetic- or acoustic-based techniques are used for physical properties, such as the presence of inclusions. The aggressive environments in molten metals create challenges in the development of reliable sensors. In particular, materials that are stable and provide the needed transduction properties at these high-temperature reactive conditions must be identified or developed. In this paper, techniques for measuring dissolved gas and inclusion contents in molten metals are reviewed.

Introduction

The properties of production alloys depend critically on defects, which can be due to the absence of material (*e.g.* porosity) or an undesired material (*e.g.* inclusion). Such defects strongly affect the initiation and growth of cracks, and thus are especially important for the fatigue strength of the material [1,2]. One important cause of porosity and inclusions is the dissolution of gases in the molten metal during processing. Defects can form if the gas either reacts with a component of the alloy or is trapped in the solidified metal.

In the case of steel, some of the compounds formed from the addition of deoxidizers, such as aluminum or ferro-silicon, may remain in the molten metal rather than become incorporated into the slag [3]. As a result, the concentration of inclusions increases with increasing amount of dissolved oxygen, because additional oxygen is available for oxide formation [4]. In the case of aluminum alloys, the most critical gas is hydrogen, the entrapment of which during solidification can lead to porosity in the resulting casting [5]. Thus, the production of high-quality aluminum castings requires degassing to reduce the hydrogen content and the associated porosity [6-10]. Similarly, inclusions can be removed by processes such as filtration [11-15]. Operating these processes cost effectively, while maintaining alloy product quality, requires information on the amounts of dissolved gases and particulates in the molten metal. A review of some of the techniques for obtaining this information is the subject of this paper.

Dissolved Gas

Hydrogen

One approach to measuring the amount of hydrogen in an alloy is through sampling techniques such as vacuum extraction [16] or nitrogen fusion [17]. A commonly used sampling technique is the reduced pressure test (RPT), which is shown schematically in Figure 1 and provides a

measurement of the hydrogen content based on the porosity formed during solidification of a sample under vacuum [18].

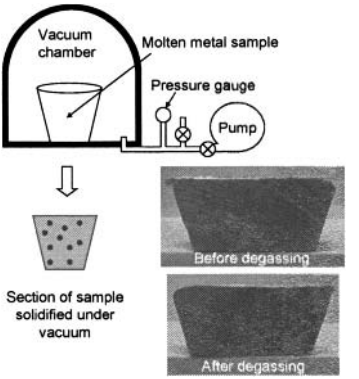

Figure 1. Reduced pressure test (RPT) for measuring hydrogen content in aluminum [18].

Improved process control can be attained by directly measuring the hydrogen content in the melt rather than taking a sample. One example is the AℓScan™ hydrogen sensor, which is shown schematically in Figure 2 and operates by passing nitrogen gas through a porous ceramic inserted into the melt [6]. This gas equilibrates with the hydrogen dissolved in the melt and is then transported to an analyzer for determination of the hydrogen content.

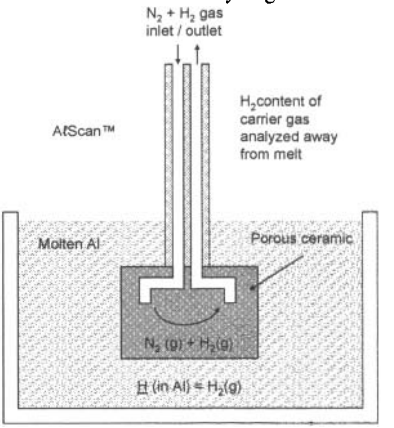

Figure 2. Schematic of AℓScan hydrogen sensor [6].

Another approach is based on a galvanic cell with a solid electrolyte, in which the cell voltage is given by the Nernst equation, where the hydrogen partial pressure at the sensing electrode is established by the equilibrium of the hydrogen dissolved in the molten aluminum with hydrogen gas and at the reference electrode with a gas of known H_2 composition or a two-phase solid mixture. The approach was first demonstrated with a CaH_2 electrolyte and a calcium reference

electrode where the Ca/CaH_2 equilibrium established the reference potential [19]. Subsequently, proton conducting oxides, such as strontium cerate [20] and calcium zirconate [21-24] were used in hydrogen sensors. The cerates typically have higher conductivities than the zirconates, but the zirconates typically have better chemical stability. Because of the aggressive environment and relatively high temperature in molten metals, zirconates are generally preferred for use in sensors for molten metals. Other oxides, such as alumina [25] have also been used in hydrogen sensors.

Schematics of solid electrolyte based hydrogen sensors are shown in Figure 3 [21,22,26]. The sensor on the left uses a gas-phase as the reference electrolyte, while the sensor on the right uses a two-phase solid mixture as the reference electrode. The two-phase mixture can be a mixture of a metal and metal hydride, such as $Ca + CaH_2$, which establishes the same potential as in the use of a calcium electrode with a CaH_2 electrolyte mentioned above [26,27]. However, a mixture of two metal phases with two different hydrogen contents, specifically α-titanium and β-titanium [28], has also been used as the reference electrode.

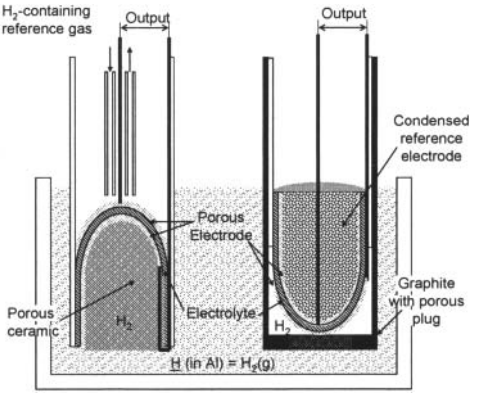

Figure 3. Solid electrolyte based hydrogen sensors [21,22,26].

Sensors are most often operated in an open-circuit potentiometric mode, but improved performance can be obtained using the current reversal technique [29]. In this technique a voltage is applied in the forward and reverse directions and the ratio of the resulting currents in the forward and reverse directions is related to the hydrogen partial pressures established at the two electrodes.

One issue with proton conducting oxides is the possibility of conduction of species other than protons. The predominate defects for conduction in calcium zirconate as a function of oxygen partial pressure and hydrogen partial pressure at 750°C are shown in Figure 4 [6,30,31]. At the low oxygen partial pressures in molten aluminum, as indicated by the Al/Al_2O_3 equilibrium, oxygen vacancies are the predominant defects. In fact, calcium zirconate has been used as an oxygen ion conducting electrolyte [32]. Even though oxygen vacancies may be the predominant defect, the cell voltage, possibly through equilibration between the oxygen vacancies and hydrogen, responds to hydrogen content in the melt.

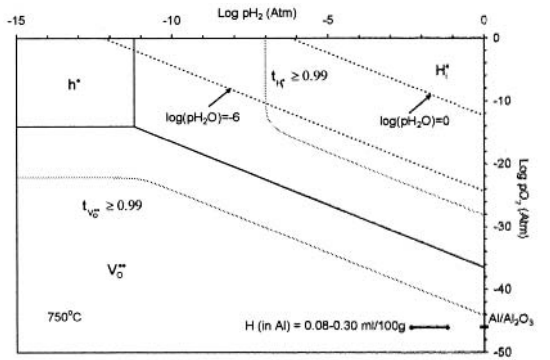

Figure 4. Defect equilibria for $CaZrO_3$ at 750°C [6,30,31].

The ALSPEK-H sensor is a commercially available solid electrolyte based hydrogen sensor. In Figure 5, the hydrogen content measured by the ALSPEK-H is compared with that measured by the AℓScan™ hydrogen sensor and shows that the measurements from the ALSPEK-H sensor correlate better with the measured density [33]. In addition, the ALSPEK-H can be used during degassing to provide immediate response for process control.

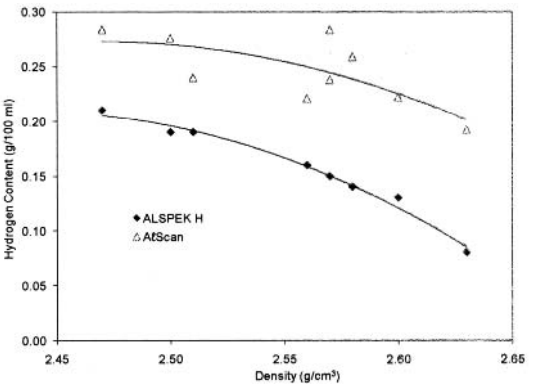

Figure 5. Comparison of AℓScan™ and AL SPEK-H hydrogen sensors [33].

Oxygen

In the case of iron and steel, oxygen is the dissolved gas of primary concern and solid electrolyte based oxygen sensors are widely used [34,35]. The electrochemical oxygen sensors are based on an oxygen ion conductor, usually yttria-stabilized zirconia, and the cell voltage is given by the Nernst equation. Oxygen sensors are produced in different geometries, some examples of which are shown in Figure 6 [36,37]. All of these sensors use a metal + metal-oxide mixture, commonly Cr + Cr_2O_3, as the reference electrode. The plug type sensor uses only a small electrolyte pellet, but requires a good seal between the electrolyte and the support tube. The seal requirements can be relaxed using an electrolyte tube, in which case the seal is further away from

the reference electrode, so a small amount of leakage can be tolerated. Another approach is to coat the reference electrode mixture with the electrolyte, which is shown as the needle-type sensor to the right in Figure 6.

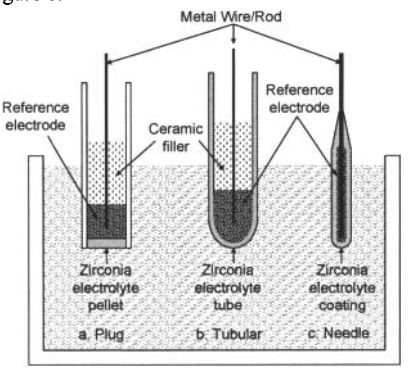

Figure 6. Oxygen sensor geometries [36,37].

As discussed above for the hydrogen sensors, the transport properties of the electrolyte are important for proper sensor operation. In particular, at the low oxygen partial pressures in the molten metal environment, electronic conduction can occur in the electrolyte [38,39]. Conduction of electrons through the electrolyte leads to a decrease in the cell voltage. For small amounts of electronic conduction, a theoretical correction can be applied to the measured voltage, but if the amount of electronic conduction becomes too large, the voltage becomes independent of oxygen partial pressure. Another approach to improved performance at low oxygen partial pressures is to use alternative electrolyte materials that maintain ionic conductivity to lower oxygen partial pressures. For example, other oxides that form the cubic fluorite structure, including thoria [42,43] and hafnia [44,45] perform better at lower oxygen partial pressures. Other materials with good low oxygen partial pressure performance are perovskites, including zirconates [45] and aluminates [46], and β-alumina based materials [47-50].

Another important property for oxygen sensors is thermal shock resistance, since the sensors are heated rapidly during insertion into the molten metal. Thermal shock resistance can be improved by, for example, doping with magnesium in small amounts to produce partially stabilized zirconia [51]. However, the improvement in mechanical properties comes at the expense of electrochemical properties. One approach to obtaining the appropriate combination of properties is to use a double layer design as shown in Figure 7a [52-54]. In this case the Mg partially stabilized zirconia (MgPSZ) provides thermal shock, while the yttria-stabilized zirconia (YSZ) provides the good ionic conductivity and low electronic conductivity.

Another approach is to press the zirconia powder around the reference electrode mixture (see compact sensor in Figure 7b), which has been shown to have good thermal shock resistance and long lifetimes [55,56]. The operational life can also be extended through the use of a non-isothermal probe, in which the reference electrode is at a lower temperature than the working electrode, as shown in Figure 7c [57-59].

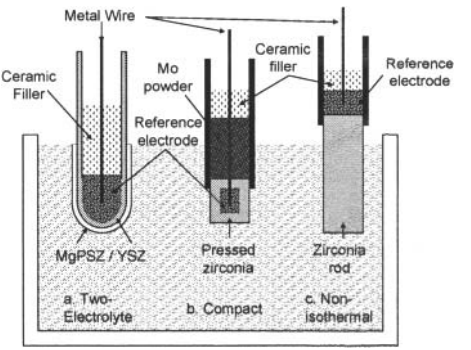

Figure 7. Two-electrolyte [52-54], compact [55,56] and non-isothermal oxygen sensors [57-59].

Oxygen sensors can also be used for measuring the amount of oxygen dissolved in copper [60,61]. Measurement of hydrogen is also important in the processing of molten copper, so hydrogen sensors using zirconate [62-64] or alumina [65] electrolytes have been used. Copper is much less active than aluminum, so, as shown in Figure 8, in conditions typical of copper melts, the predominate defects in calcium zirconate are protons [30,31,63].

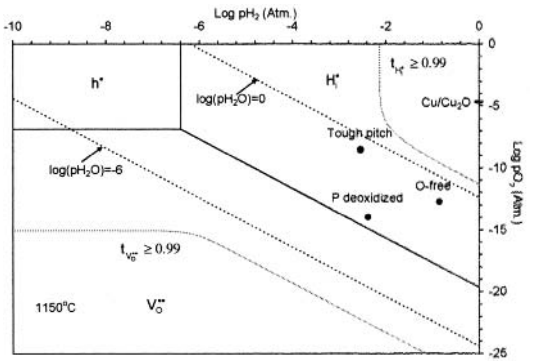

Figure 8. Defect equilibria for $CaZrO_3$ at 1150°C [30,31,63].

The response of potentiometric electrochemical sensors is related to oxygen activity and thus will reach a maximum when the solubility limit of oxygen is reached. Above the solubility limit the response will become constant even if the amount of the oxide phase increases. The total amount of oxygen includes the dissolved oxygen and the oxygen in the oxide phases, so measurement of the total oxygen content requires techniques other than the electrochemical oxygen sensor [66].

Inclusions

Measurement of the second phase inclusions captures the total oxygen content and provides important information on the result of the dissolved gas reacting with alloy components. As

with dissolved gas measurement, there are methods for measuring inclusion content based on analysis of a sample removed from the melt. The Porous Disk Filtration Apparatus (PoDFA) and Prefil Footprinter are two examples of techniques that are based on filtration of a molten metal sample. In the PoDFA technique, shown schematically in Figure 9, a molten metal sample is pulled through a filter and the rate at which the metal flows through the filter provides a measure of the amount of inclusions. In addition, the resulting filtrate can be examined to provide detailed characterization of the inclusions [70]. Measurement of the mechanical properties, such as in the K-mold test, can also be used to evaluate the inclusion content [70-72]. In addition to the information from the measured mechanical property, especially fracture toughness and elongation, examination of the fracture surface can provide details on the types of inclusions. Although these techniques provide information on inclusion content, real-time measurement of the inclusion content would provide faster feedback for improved process control.

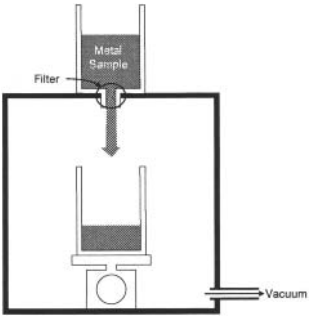

Figure 9. Schematic of porous disk filtration apparatus (PoDFA) [69].

One approach to on-line measurement of the inclusion content is using the electric sensing zone (ESZ) principle. A schematic of one sensor based on this principle, the Liquid Metal Cleanliness Analyzer (LiMCA), is shown in Figure 10 [73-76]. The sensor is based on measurement of the resistance across an orifice in the side of a tube, which will change significantly if an insulating particle passes through the orifice. Metal is forced through the office by alternatively evacuating and pressurizing the inside of the tube. The magnitude of the change is related to the particle size, and the number of particles can be determined by counting the number of measured pulses. The orifice should be dimensioned properly, since too large of an orifice may allow multiple particles to pass simultaneously through the orifice, while too small of an orifice may become blocked.

Other inclusion measurement techniques use an ultrasonic signal to detect and characterize solid inclusions in the molten metal [77,78]. One approach is to measure the signal between two plates, in which case only the molten metal that passes between the plates is evaluated [79]. This limited sample volume facilitates interpretation of the sensor output, but also requires that a sufficient amount and representative sample of the metal flows between the plates. An alternative approach is to use the reflection of the ultrasonic wave from the particles as shown schematically in Figure 11 [80,81]. This approach does not place restrictions on the flow of molten metal and samples a larger volume of metal. Interpretation of the signal is more complicated than with the parallel plate configuration because of the larger number of particles. The reflected signal is dependent on the size and shape of the particles, so there is potential for gathering information on the nature of the particles. The configuration in Figure 11 can be also

used to determine the location of particles. The horizontal position can be determined by directing the signal with waveguides, while the vertical position can determined from the time delay of a pulsed signal. The ultrasonic signal, thus, provides opportunities for obtaining information on the size, position and number of particles.

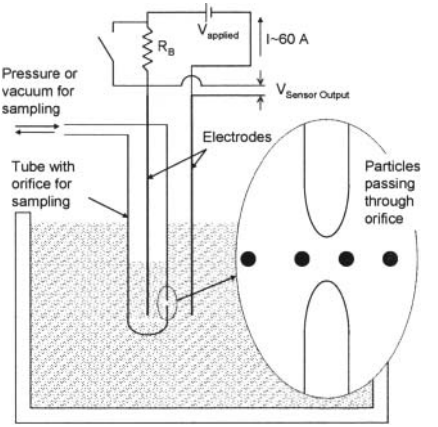

Figure 10. Schematic of Liquid Metal Cleanliness Analyzer (LiMCA) using electric sensing zone (EZS) principle [73-76].

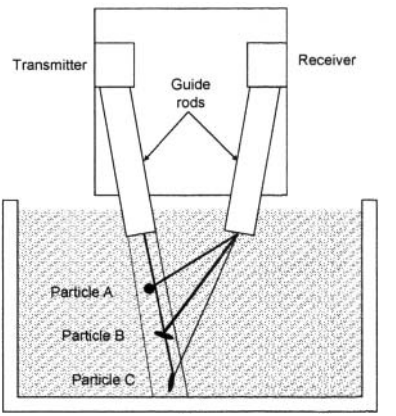

Figure 11. Schematic of ultrasonic probe [80,81].

Conclusions

Effective and efficient control of processing parameters requires real-time feedback to appropriately adjust the operating conditions for production of high-quality materials. This

includes monitoring the formation of solid particles in the liquid melt as well as the dissolved gas content that can lead to the formation of these solid particles or to the formation of porosity.

References

1. H.V. Atkinson and G. Shi, "Characterization of Inclusions in Clean Steels: A Review Including the Statistics of Extremes Methods," *Prog. Mater. Sci.*, **48** (2003) 457–520.
2. L. Zhang and B.G. Thomas, "State of the Art in the Control of Inclusions during Steel Ingot Casting," *Metall. Mater. Trans. B*, **37B** (2006) 733-761.
3. Y. Payendah and M. Soltanieh, "Oxide Inclusions at Different Steps of Steel Production," *J. Iron Steel Res. Int.*, **14**[5] (2007) 39-46.
4. L.E.K. Holappa and A.S. Helle, "Inclusion Control in High Performance Steel," *J. Mater. Proc. Tech.*, **53** (1995) 177-186.
5. S. Shivkumar, L. Wang and D. Apelian, "Molten Metal Processing of Advanced Cast Aluminum Alloys," *JOM*, **43**[1] (1991) 26-32.
6. M.M. Makhlouf, L. Wang and D. Apelian, *Measurement and Removal of Hydrogen in Aluminum Alloys*, (American Foundrymen's Society, Des Plaines, IL, 1998) 29-38.
7. G.K. Sigworth and T.A. Engh, "Refining of Liquid Aluminum – A Review of Important Chemical Factors," *Scand. J. Metall.*, **11** (1982) 143-149.
8. G.K. Sigworth and T.A. Engh,, "Chemical and Kinetic Factors Related to Hydrogen Removal from Aluminum," *Metall. Trans. B*, **13B** (1982) 447-460.
9. R.A. Rapp, "The Closed-Circuit Degassing of Liquid Aluminum Alloys by Argon," *JOM*, **49**[5] (1996) 16-19.
10. R.A. Rapp, "The Closed-Circuit Degassing/Fluxing of Liquid Aluminum Alloys by Nitrogen-Chlorine," *JOM*, **49**[5] (1996) 21-23.
11. R. Gallo, "Clean Up Your Aluminum Melt," *Modern Casting*, **98**[11] (2008) 32-37.
12. D.V. Neff, "Ensuring Quality Prior to Pouring," *Modern Casting*, **96**[6] (2006) 27-29.
13. S. Makarov, D. Apelian and R. Ludwig, "Inclusion Removal and Detection in Molten Aluminum: Mechanical, Electromagnetic and Acoustic Techniques," *AFS Trans.*, **107** (1999) 727-735.
14. R.A. Olson, III and L.C.B. Martins, "Cellular Ceramics in Metal Filtration," *Adv. Eng. Mater.*, 7[4] (2005) 187-192.
15. E. Nazari, S.H. Razavi and S.M.A. Boutorabi, "Effect of Filtration on the Morphology and Mechanical Properties of Mg Molten Alloy Entering the Mould Cavity," *J. Mater. Proc. Tech.*, **210** (2010) 461-465.
16. F. Degrève, J.-C. Carle and N. Gonzalez, "New Methods for the Determination of Hydrogen Content of Aluminum and Its Alloys: Part I. Improvements in the Vacuum Extraction Method," *Metall. Trans. B*, **6B** (1975) 539-544.
17. F. Degrève and C. Jardin and N. Gonzalez, "New Methods for the Determination of Hydrogen Content of Aluminum and Its Alloys: Part II. Rapid Determination by the Nitrogen Carrier Fusion Method," *Metall. Trans. B*, **6B** (1975) 545-550.
18. W. Rasmussen and C.E. Eckert, "RPT Gauges Aluminum Porosity," *Modern Casting*, **82**[3] (1992) 29-31.
19. R. Gee and D.J. Fray, "Instantaneous Determination of Hydrogen Content in Molten Aluminum and Its Alloys," *Metall. Trans. B*, **9B** (1978) 427-430.
20. M. Zheng and X. Zhen, "$SrCeO_3$-Based Solid Electrolyte Probe Sensing Hydrogen Content in Molten Aluminum," *Solid State Ionics*, **59** (1993) 167-169.
21. T. Yajima, K. Koide, H. Takai, N. Fukatsu, T. Ohashi and H. Iwahara, "A New Hydrogen Sensor for Molten Aluminum," *Sensors and Actuators B*, **13-14** (1993) 697-699.

22. T. Yajima, K. Koide, H. Takai, N. Fukatsu and H. Iwahara, "Application of Hydrogen Sensor Using Proton Conductive Ceramics as a Solid Electrolyte to Aluminum Casting Industries," *Solid State Ionics*, **79** (1995) 333-357.
23. N. Fukatsu, N. Kurita, T. Yajima, K. Koide and T. Ohashi, "Proton Conductors of Oxide and Their Application to Research into Metal-Hydrogen Systems," *J. Alloys Comp.*, **231** (1995) 706-712.
24. N. Fukatsu and N. Kurita, "Hydrogen Sensor Based on Oxide Proton Conductors and Its Application to Metallurgical Engineering," *Ionics*, **11** (2005) 54-65.
25. N. Fukatsu and N. Kurita, "Proton Conduction in α-Alumina and Its Application to Hydrogen Sensor for Molten Metals," *Ionics*, **13** (2007) 183–194.
26. D.P. Lapham, C. Schwandt, M.P. Hills, R.V. Kumar and D.J. Fray, "The Detection of Hydrogen in Molten Aluminium," *Ionics*, **8** (2002) 391-401.
27. M. Zheng and X. Zhen, "Hydrogen Probe Equipped with $SrCeO_3$-Based Proton Conductor and Ca/CaH_2 Reference Electrode," *Metall. Mater. Trans. B*, **24B** (1993) 789-794.
28. C. Schwandt and D.J. Fray, "The Titanium/Hydrogen System as the Solid-State Reference in High-Temperature Proton Conductor-Based Hydrogen Sensors," *J. Appl. Electrochem.*, **36** (2006) 557-565.
29. C. Schwandt and D.J. Fray, "Hydrogen Sensing in Molten Aluminium Using a Commercial Electrochemical Sensor," *Ionics*, **6** (2000) 222-229.
30. N. Kurita, N. Fukatsu, K. Ito and T. Ohashi, "Protonic Conduction Domain of Indium-Doped Calcium Zirconate," *J. Electrochem. Soc.*, **142**[5] (1995) 1552-1559.
31. M.W. Chase, Jr., *J. Phys. Chem. Ref. Data, NIST-JANAF Thermochemical Tables*, Monograph No. 9, 4th Ed. (1998).
32. G. Róg, M. Dudek, A. Kozłowska-Róg and M. Bućko, "Calcium Zirconate, Properties and Application to the Solid Oxide Galvanic Cells," *Electrochim. Acta*, **47** (2002) 4523-4529.
33. R. Gallo, "Cleaner Melts in Foundaries: A Critical Review and Update," *AFS Trans.*, **116** (2008) 195-220.
34. A. McLean, "Sensor Aided Process Control in Iron and Steelmaking," *Solid State Ionics*, **40/41**(1990) 737-742.
35. D. Janke, "Recent Development of Solid Ionic Sensors to Control Iron and Steel Bath Composition," *Solid State Ionics*, **40/41**(1990) 764-769.
36. W.L. Worrell and Q. Liu, "New Zirconia-Electrolyte Sensors for Measuring Oxygen in Iron and Steel Melts," in D.P. Turner (Ed.), *Proc. Symp. Chemical Sensors*, **PV 87-9** (The Electrochemical Society, Pennington, NJ, 1987) 113-121.
37. S. Seetharaman and D. Sichen, "Development and Application of Electrochemical Sensors for Molten Metals Processing," in R.G. Bautista (Ed.), *Emerging Separation Technologies for Metals II* (The Minerals, Metals and Materials Society, 1996) 317-340.
38. C.B. Alcock and S. Zador, "Experimental Considerations in the Use of Solid Oxide Electrolytes," *Can. Metall. Quart.*, **13**[2] (1974) 321-323.
39. T.A. Ramanarayanan and W.L. Worrell, "Limitations in the Use of Solid State Electrochemical Cells for High-Temperature Equilibrium Measurements," *Can. Metall. Quart.*, **13**[2] (1974) 325-329.
40. K.S. Goto, M. Sasabe, Y. Iguchi, M. Iwase and M. Moritani, "Collaborate Research Activities of Sensor Sub-Committee and J.S.P.S.," *Solid State Ionics*, **40/41**(1990) 758-760.
41. M. Iwase, "Zirconia Electrochemical Sensors for Monitoring Oxygen, Silicon, Sulfur, Aluminum, and Phosphorous in Iron and Steel," *Adv. Ceram.*, **24B** [Sci. Technol. Zirconia 3] (1988) 871-878.
42. J.W. Patterson, "Conduction Domains for Solid Electrolytes," *J. Electrochem. Soc.*, **118**[7] (1971) 1033-1039.

43. T.H. Etsell and S.N. Flengas, "The Electrical Properties of Solid Oxide Electrolytes," *Chem. Rev.*, **70**[3] (1970) 339-376.
44. D. Janke, "Oxygen Sensing in Iron- and Steelmaking," *Adv. Ceram.*, **12** [Sci. Technol. Zirconia 2] (1984) 636-645.
45. D. Janke, "Oxygen Probes Based on Calcia-Doped Hafnia or Calcium Zirconate for Use in Metallics Melts," *Metall. Trans. B*, **13B** (1982) 227-235.
46. C.B. Alcock, B. Li, J.W. Fergus and L. Wang, "New Electrochemical Sensors for Oxygen Determination" *Solid State Ionics*, **53-56** (1992) 39-43.
47. R.V. Kumar and D.J. Fray, "Application of Novel Sensors in the Measurement of Very Low Oxygen Potentials," *Solid State Ionics*, **70/71** (1994) 588-594.
48. A. Davies, D.J. Fray and S.R. Witek, "Measurement of Oxygen in Steel Using β Alumina Electrolytes," *Ironmaking and Steelmaking*, **22**[4] (1995) 310-315.
49. J. Sun, C. Jin, L. Li and Y. Hong, "A Novel Electrochemical Oxygen Sensor for Determination of Ultra-Low Oxygen Contents in Molten Metal," *J. Univ. Sci. Tech. Beijing*, **8**[2] (2001) 137-140.
50. G.M. Kale and R. Kurchania, "On-Line Electrochemical Sensors in Molten Metal Processing Technology: A Review," *Ceramic Trans.*, **92**[Electrochemistry of Glass and Ceramics] (1999) 195-220.
51. Q. Liu, S. An and W. Qiu, "Study on Thermal Expansion and Thermal Shock Resistance of MgO-PSZ," *Solid State Ionics*, **121** (1999) 61-65.
52. K. Huang, Y. Xia, W. Wu, Q. Li, W. Liu and H. Clauss, "Investigations on Commercially Available MgO-PSZ Electrolytes with Y_2O_3-FSZ Coating for Low Oxygen Determination in Liquid Steel," *Solid State Ionics*, **70/71** (1994) 563-568.
53. Q. Liu, K. Huang, Y. Xia, W. Liu, W.L. Worrell and H. Clauss, "Oxygen Sensor with Double Layer Electrolyte for Low Oxygen Measurement of Steel Melts," in M.A. Butler, A.J. Ricco and H. Yamazoe (Eds.), *Proc. Symp. Chemical Sensors II*, **PV 93-7** (The Electrochemical Society, Pennington, NJ, 1993) 281-286.
54. Q. Liu, "The Development of High Temperature Electrochemical Sensors for Metallurgical Processes," *Solid State Ionics*, **86-88** (1996) 1037-1043.
55. Q. Liu and W.L. Worrell, "Development of Solid-State Electrochemical Sensors for High-Temperature Applications," *Solid State Ionics*, **28-30** (1988) 1668-1672.
56. W.L. Worrell and Q. Liu, "Development of an Extended-Life Oxygen Sensor for Iron and Steel Melts," *Solid State Ionics*, **40-41** (1990) 761-763.
57. K.T. Jacob and S.K. Ramasesha, "Design of Temperature-Compensated Reference Electrodes for Non-Isothermal Galvanic Sensors," *Solid State Ionics*, **34** (1989) 161-166.
58. S.K. Ramasesha and K.T. Jacob, "Studies on Nonisothermal Solid State Galvanic Cells – Effect of Gradients on EMF," *J. Appl. Electrochem.*, **19** (1989) 394-400.
59. T.H. Etsell and C.B. Alcock, "Non-Isothermal Probe for Continuous Measurement of Oxygen in Steel," *Solid State Ionics*, **3/4** (1981) 621-626.
60. H. Tominaga, K. Yajima and S. Nishiyama, "Application of Oxygen Probes for Controlling Oxygen Content in Molten Copper," *Solid State Ionics*, **3/4**(1981) 571-574.
61. J.W. Matousek, "Thermodynamic Potentials of Oxygen Dissolved in Copper," *JOM*, **62**[3] (2010) 75-77.
62. N. Kurita, N. Fukatsu, S. Miyamoto, F. Sato, H. Nakai, K. Irie and T. Ohashi, "The Measurement of Hydrogen Activities in Molten Copper Using Oxide Protonic Conductor," *Metall. Mater. Trans. B*, **27B** (1996) 929-935.
63. N. Fukatsu, N. Kurita, K. Koide and T. Ohashi, "Hydrogen Sensor for Molten Metals Usable up to 1500 K," *Solid State Ionics*, **113-115** (1998) 219-227.

64. K. Katahira, K. Koide and T. Iwamoto, "Structure and Performance Evaluation of Hydrogen Sensor for Molten Copper under Industrial Conditions," in B. Mishra and C. Yamauchi (Eds.), *Second Int. Conf. on Processing Materials for Properties* (The Minerals, Metals & Materials Soc., Warrendale, PA, 2000) 347-352.
65. Y. Okuyama, N. Kurita, A. Yamada, H. Takami, T. Ohshima, K. Katahira and N. Fukatsu, "A New Type of Hydrogen Sensor for Molten Metals Usable up to 1600K," *Electrochim. Acta,* **55** (2009) 470–474.
66. L-F. Zhang, "Indirect Methods of Detecting and Evaluating Inclusion in Steel - A Review," *J. Iron Steel Res. Int.,* **13**[4] (2006) 1-8.
67. L. Zhang, B.G. Thomas, X. Wang and K. Cai, "Evaluation and Control of Steel Cleanliness - A Review," in *85th Steelmaking Conf. Proc.* (ISS-AIME, Warrendale, PA, 2002) 431-452.
68. L-F. Zhang, "Inclusion and Bubble in Steel - A Review," *J. Iron Steel Res. Int.,* **13**[3] (2006) 1-8.
69. ABB (http://www.abb.com/product/seitp330/c1256dde004b6b1d85256e2300764e3b.aspx).
70. J. Wannasin, D. Schwam and J.F. Wallace, "Evaluation of Methods for Metal Cleanliness Assessment in Die Casting," *J. Mater. Proc. Tech.,* **191** (2007) 242-246.
71. D.P.K. Singh and D.J. Mitchell, "Analysis of Metal Quality in a Low Pressure Permanent Mold Foundry," *AFS Trans.,* **109** (2001) 333-345.
72. D.V. Neff, "Methodologies for Evaluating Filtering Efficiency in Aluminum Casting Processes," in *6th International AFS Conference on Molten Aluminum Processing 2001* (American Foundry Society, Des Plaines, IL, 2001) 104-116.
73. R.I.L. Guthrie and M. Li, "In Situ Detection of Inclusions in Liquid Metals: Part II, Metallurgical Applications of LiMCA Systems," *Metall. Mater. Trans. B,* **32B**[6] (2001) 1081-1093.
74. R.I.L. Guthrie and M. Li, "In Situ Detection of Inclusions in Liquid Metals: Part I. Mathematical Modeling of the Behavior of Particles Traversing the Electric Sensing Zone," *Metall. Mater. Trans. B,* **32B**[6] (2001) 1067-1079.
75. M. Li, C. Carozza, R.I.L. Guthrie, "Particle Discrimination in Water Based LiMCA (Liquid Metal Cleanliness Analyzer) System," *Can. Metall. Quart.,* **39**[3] (2000) 325-338.
76. C. Dupuis, F. Dallaire and B. Maltas, "The Measurement of Controlled Size Particles in Molten Aluminum Using the LiMCA II Technique," in C.E. Eckert (Ed.), *Light Metals 1999* (The Minerals, Metals & Materials Society, Warrendale, PA, 1999) 1069-1077.
77. A.C. Currie, S.M. Millman and S. Johnstone, "Development of an Ultrasonic Liquid Steel Inclusion Monitor," in D.O. Thomson and D.E. Chimenti (Eds.), *Review of Quantitative Nondestructive Evaluation,* **Vol. 29** (Am. Inst. Phys, 2010) 1051-1058.
78. Y. Ono, J.-F. Moisan, Y. Zhang, C.-K. Jen and C.-Y. Su, "An On-Line Ultrasonic Cleanliness Analyzer for Molten Light Metals," *JOM,* **56**[2] (2004) 59.
79. H.N.G. Wadley, "Sensors for Intelligent Processing of Materials," *J. Metals,* **38**[10] (1986) 49-53.
80. N.D.G. Mountford, I.D. Sommerville, A. Simionescu and C. Bai, "Sound Pulses Enable the On Line Visualization of Liquid Metal Quality," in C.M. Cickert and R.I.L. Guthrie (Eds.), *Proc. Int. Symp. Light Metals 1997* (Can. Inst. Mining, Metall. and Petr., Montreal, Canada, 1997) 197-211.
81. N.D.G. Mountford, A. Simionescu and I.D. Sommerville, "Visualization of the Particle Content of Liquid Aluminum Alloys," in R. Huglen (Ed.), *Light Metals 1997* (The Minerals, Metals & Materials Society, Warrendale, PA, 1997) 937-943.

Sensors, Sampling, and Simulation for Process Control
Edited by: Brian G. Thomas, James A. Yurko, and Lifeng Zhang
TMS (The Minerals, Metals & Materials Society), 2011

DEVELOPMENT OF AN AQUEOUS PARTICLE SENSOR (APS III) SYSTEM AS A RESEARCH TOOL FOR STUDYING THE BEHAVIOUR OF INCLUSIONS IN WATER MODELS OF TUNDISH OPERATIONS

Mihaiela Isac, Abhishek Chakraborty, Luis Calzado, Roderick Guthrie
McGill Metals Processing Centre, 3610 University Street, Montreal, Quebec, H3A 2B2, Canada

Keywords: LiMCA, Aqueous Particle Sensor (APS), water modeling, Electric Sensing Zone (ESZ)

Abstract

The control of liquid metal cleanliness during refining operations is an effective procedure used to improve the material properties of the final product. Over the years, low temperature simulation studies on inclusion behavior in steelmaking tundish operations have been modeled in order to help develop techniques to float out as many inclusions as possible, in liquid steel systems, prior to casting. The inclusions in liquid steel are simulated by glass microspheres submerged in water, and their behavior was studied with a new Aqueous Particle Sensor (APS), recently re-constructed at McGill, this time using digital based micro-computing technology. The working principle of the APS is similar to the well known Liquid Metal Cleanliness Analyzer (LiMCA), used worldwide for the detection of inclusions in molten aluminum and steel. Both are based on the Resistive Pulse, or Electric Sensing Zone (ESZ) approach. The latest "water LiMCA", or APS III system, relies on the processing speed of current microprocessors. This allows us to simplify the acquisition and interpretation of data input. The APS III has a wide particle size measurement capability, ranging between 25 and 170 microns, gathering data, on-line, or off-line, with high accuracy.

Introduction

Research at McGill University has concentrated on the direct measurement of inclusion behavior in both real steelmaking systems, and in their appropriate water models. We have studied the removal of inclusions from steel, as it is flowing through a tundish, before being fed into two, or more, nozzles, down into the continuous casting machines, set below. Since large tundishes can have liquid steel residence times in excess of half an hour, it is an excellent location to carry out inclusion separation from the melt. All inclusion particles occurring in molten steel are oxides, all of which have significantly lower densities compared to liquid steel. This fact, plus the relatively low levels of bath agitation generally found within a large part of a tundish, facilitates their floating out, up to the surface, where they can be entrapped in an upper slag layer.
The last APS II system was based on a DSP (Digital Signal Processing) approach, and was built in 1992. Since that time, microprocessors have become much faster, so the need for a DSP system is no longer mandatory for routine tests. Following the retirement of the original APS II system due to the need for upgraded software, we took advantage of the ESZpas system developed by Heraeus Electro-Nite for liquid steel. This was adapted to work in water, and used for about six years, in our water model tundish experiments. Unfortunately, its design and mode of operation severely limited its versatility as an APS system. For instance, researchers had to collect samples for off-line analysis, had to add salt for increasing conductivity (like Coulter Counters), and were unable to make changes in software for its application to differing experimental setups.

The current study consisted of developing a new APS III version, having more versatility, accuracy and reliability, than any instrument available commercially, and then testing its use as an inclusion sensor in our water model tundish experiments. The new APS III proved easy to operate and is user-friendly for researchers.

Aqueous Particle Detection System

The basic design of APS detectors includes the tried and tested, side-aspirated, glass tubes. Figure 1 shows the working principle of a LiMCA II machine for liquid aluminum. A differential pressure system operates within the tube, so as to draw (suck) liquid into the tube for sampling, and to then exhaust the sampled liquid back out, as depicted in Figure1a. Thus the fluid containing a suspension of the inclusion particles is allowed to pass through a narrow orifice in the presence of a simultaneous electrical current. Two electrodes are used so as to apply the necessary constant electrical current supply (I) through it (Figure 1c). As a particle passes through the orifice, it registers as a jump in a voltage pulse across the electrodes (Figure1d). This is digitally recorded, and its magnitude is an indication of the size of the particle, or diameter [1, 2]. It should be noted that the transit time of the particle through the orifice is small (~1 ms), so that if the recorded times for the detection of signals is of any modest time length (20 seconds or more), then the width of the peak relative to the entire train of signals becomes extremely small. The result is a set of signals shown in Figure1b, i.e. each particle being detected shows up as a narrow transient voltage spike.

The APS Equation Adopted

Obviously, during actual measurements for discrete particles within an Electric Sensing Zone (ESZ), the number of peaks detected should equal the number of particles sampled. The height of each peak is related to the particle size according to the equation [1, 2];

$$\Delta V = \frac{4\rho_e I d^3}{\pi D^4} \quad \text{or} \quad \Delta V = kd^3 \qquad [1]$$

ΔV is the change in voltage when the particle passes through the orifice into the tube, ρ_e is the electrical resistivity of the fluid, I is the constant current flowing through the orifice, d is the diameter of the particle, D is the diameter of the orifice, and k is the constant, representing $\frac{4\rho_e I}{\pi D^4}$

This equation was derived from Maxwell's approximation for dispersed particles that have no effect on the electric field within the orifice, except in a region close to the particle surface. The individual voltage peaks in the raw signals are, however, far too small to be accurately measured by a data acquisition system. As such, these raw signals from the detector must first be amplified by a factor α.

$$\Delta V_{amplified} = \alpha k d^3 \qquad [2]$$

The exact value of α was chosen, based on an order of magnitude analysis using equation [1]. Considering a CMOS (Complementary Metal Oxide Semiconductor) data acquisition system that was identified for this new instrument, with a total signal swing of 0 to 5 volts, an amplifier gain of 100 was chosen. This is sufficient to produce a voltage peak of around 5 volts, when the largest particle in the range of interest (~170 microns) goes through the orifice.

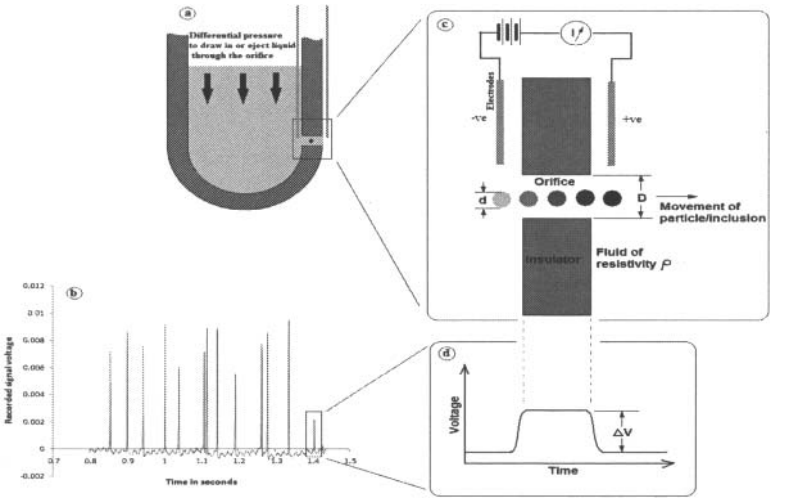

Figure 1 - Electric Sensing Zone (ESZ) principle for inclusion detection systems for water, liquid aluminum, and molten steel.

Design of the New APS III Sensor Probe

In designing a new APS III system, our first concern was to be able to operate it under water. The previous APS II probe, was not, nor was the later Heraeus Electro-Nite "single-shot" sensor probe, as adapted to water. Both these previous systems would have short-circuited, if submerged. Figure 2 shows an image of the Heraeus Electro-Nite Sensor, adapted to water, and Figure 3 presents its schematic diagram. As seen, an important part of the device is the electrode assembly, which applies the excitation current across the orifice.

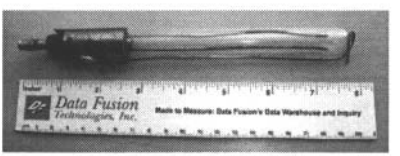

Figure 2 – Image of the detector probe designed by Heraeus Electro-Nite for H_2O.

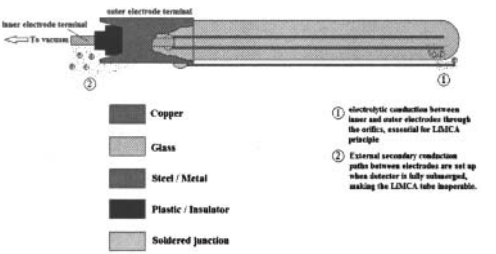

Figure 3– Schematic diagram of the Heraeus Electo-Nite Probe.

Clearly, the ESZ technique only functions when the conduction path between the two electrodes occurs exclusively through a small filament of electrolyte passing through the orifice. We refer

this as the "Electric Sensing Zone", or ESZ. In the Heraeus design for liquid steel, a small metallic tube acts both as the vacuum feed to draw in the liquid steel (or water), as well acting as an electrical conductor between the inner electrode and the external lead wire. As can be seen in Figure 2, if the modified steel probe were to be completely immersed in water, the external surface of the vacuum lead protruding out of the tube would be exposed to the electrolyte and act as an extension of the internal electrode. This would set up conduction paths between the inner and outer electrodes externally through the fluid, and not through the orifice, thereby rendering the ESZ principle inoperable. As such, the necessary modifications for the new APS III involved electrically isolating the entire inner electrode lead wires and contacts with epoxy and insulating the tube, such that only the lower portion of the inner electrode was exposed to establish electrical contact with the fluid inside the tube. The metallic vacuum lead was also replaced by one made of insulating material. The new probe used generous copper electrodes vs the Heraeus adaption. Figure 4a shows the rendered model using AutoCAD 2004. Figure 4b presents the final prototype.

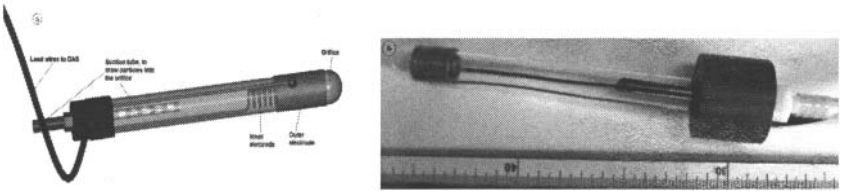

Figure 4 a) Computer Aided Design (CAD) Model of the final APS III sensor developed. **4b)** Working prototype for the APS III sensor.

Size and Shape of the Orifice

As mentioned in the introduction, the exact size and shape of the orifice is of marked importance in the final operation of the transducer. The tubes used in developing the present version of the aqueous particle sensor were manufactured from close-ended silicate glass tubes with the orifice laser-drilled through the sidewall, close to the bottom. The tubes were provided by Heraeus Electro-Nite, and were identical to those used for their ESZ-pas (LiMCA) sensor for steel. As mentioned, for commercial production, the orifices were bored using a laser pulse. This resulted in a more or less cylindrical orifice with its exterior end slightly fluted. A number of tube orifices were sectioned and examined microscopically. The average diameter of the cylindrical portion of the orifice was determined to be very close to 500 microns (Figure 5).

Figure 5 Microscopic view of the APS orifice.

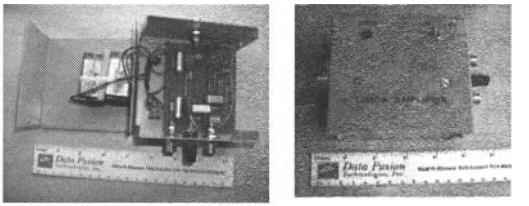

Figure 6 a,b. – Final Set-up of the APS Amplifier [3].

Choice of Amplifier

A high quality 75 Ohm coaxial connector cable was used for all external wiring, in order to keep extraneous noise pickup to an absolute minimum. Oscilloscope traces revealed that an appreciable amount of the 50 Hz main component had filtered into the excitation voltage of the Heraeus Electro-Nite system. Though both the computers and amplifiers were housed in shielded metal boxes, the fact that these devices are meant to operate in laboratories which are inherently electrically noisy, meant it was difficult to eliminate the mains hum. By isolating the APS III detector and associated electronics from any mains driven power supply and employing dry cells for electrical power, as with the previous APS II system, the quality of the excitation voltage was substantially improved. Since the maximum voltage amplitude generated by the probe is only about 50 mV, adequate signal amplification (α~100) was essential, so as to bring the maximum pulses up the maximum amplitude of 5 Volts, before feeding the signal into the data acquisition system. The small amplitudes of the original signals, the transient nature of the peaks generated, and the high gain, placed stringent performance demands on the amplifier used.

The amplifier chosen was an AD 624 single substrate operational amplifier. This particular Integrated Circuit was chosen for its superior performance [3], ready availability, and the need for a smaller number of external supporting components. The final signal from the amplifier is fed to an external CMOS based data acquisition system, filtered through a 1 micro Farad capacitor to remove all DC components from the signal. The circuit constructed, Fig 6a, was made as small as physically possible, so as to reduce chances of extraneous noise pickup. It was housed in a shielded metal box, together with 9V DC batteries for the power supply.

The amplified signal was fed to an analogue input channel of an InstruNET i-NET100 data acquisition board and DASYLab software. The DASYLab worksheet was configured to 2 kHz in analyzing voltage readings from the analogue input channel which was set at a sampling frequency of 20 kHz. This was kept sufficiently high, as the individual peaks comprising of the APS signal are of short duration (~1ms), and only a high sampling rate would provide the necessary resolution to capture all the transient artifacts of the signal. Figure 6 a&b shows the final, assembled APS amplifier.

Algorithm Used for Study of Particle Sizes

The signal processing algorithms developed, classified all the particles that were detected into a number of appropriately chosen bins. Counters were used to store the number of particles falling into each size range, or bin, and the resulting values of each counter were displayed as a histogram. This sort of data was much more convenient for easy analysis by the user. The final version of the DASYLab worksheet classifies particles into 11 different size ranges or bins. Figure 7 shows a screenshot of the final worksheet. The size fractions of particles in each bin (obtained by dividing the value of its corresponding counter with the total particle count) are displayed as a histogram, and the total particle count is also displayed. The choice of using the DASYLab data acquisition software was an advantage in itself due to its superior user interface, and its menu driven structure. Once an algorithm was developed, it was entered into the DASYLab workplane [2,3]. The use of this particular software was also useful in incorporating software based filters to remove some extraneous noise from the signal, considering the fact that the device was meant to operate in electrically noisy environments. A narrow band stop filter across 60 Hz would remove any mains components, while a low pass filter was used to block any high frequency noise that may be picked up. The new algorithm adopted here worked flawlessly with a 2.10 GHz Core II Duo Intel processor running on 4 GB of RAM. It should be noted that while the algorithm itself should classify a particle on the basis of its diameter, it's the signal voltages that it is measuring.

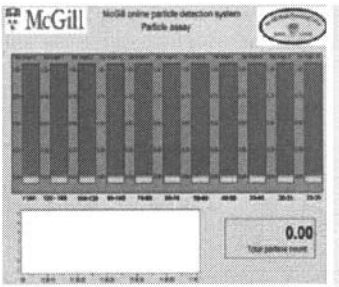

Figure 7 – Screenshot of the user input interface for APS III.

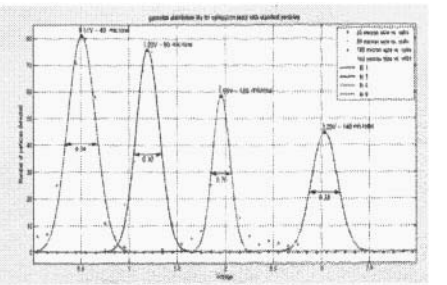

Figure 8 – Gaussian distribution peaks obtained with standard particle sizes.

Calibration of APS III Sensor

Calibration of the device was performed using 4 different particle "size" ranges. Separate experiments were performed using suspensions of standard silica particles of nominal sizes 20, 40, 90, 120 and 140 microns in normal tap water. Figure 8 shows the plots of voltage vs. number of peaks detected. Gaussian fits were calculated for the four experiments using the CFTOOL option in MATLAB. The voltage corresponding to the point of maxima on the Gaussian curves were taken as corresponding voltages for the chosen particle sizes. The uncertainty in voltage measurement was taken as the error measured at half heights of the Gaussian curves. Figure 9 shows the final calibration curve obtained by plotting the 4 data points relating a particle size to its signal peak voltage.

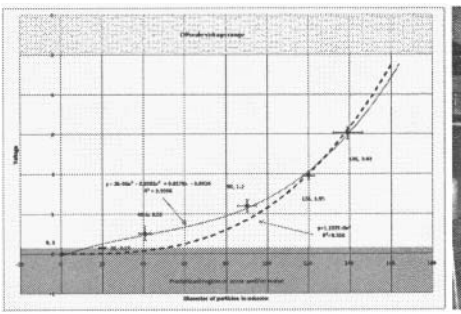

Figure 9 – Final calibration curve for APS III

Figure 10 – A water model of a full scale 12 tonne delta shaped model tundish at MMPC

The error bars in the x axis shows the deviation in particle size as reported by the manufacturer of the standard particles. A similar error analysis with the 20 micron particles could not be done as the small voltage peaks produced have an error range partially coincident with the threshold noise region of 0 to 0.15 volts. However the data point generated with the 20 micron particles was used in generating the final calibration curve. Using similar curve fitting techniques, an equation of the type described in Equation 1 was obtained in MATLAB, which is as follows, (bold dotted line in Figure 9):

$$\Delta V = 1.57 * 10^{-6} d^3 \quad [3]$$

However, a best fit polynomial of type $f(x)=ax^3+bx^2+cx+d$ through the data points cooresponding to the standard sized spheres, including the twenty micron spheres and zero, shows a much better adherence to the data points:

$$\Delta V = 2 * 10^{-6} d^3 - 0.002 d^2 + 0.017 d - 0.042 \quad [4]$$

While a detailed analysis of this behaviour was not undertaken, the calibration curve obtained was markedly stable, easily reproducible, and propitiously fortunate for small inclusions.

Experimental Procedures

A full scale water model (Fig.10) of a generic, 12 tonne, delta shaped, tundish was fitted with APS III detectors at several locations to measure the amount of inclusions per volume of water.

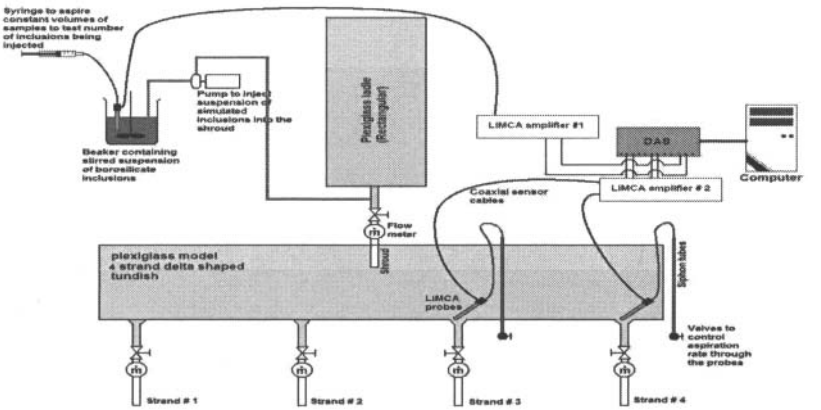

Figure 11 – Schematic diagram of the experimental setup

Small, hollow, glass microspheres, of a fixed size range were used to simulate the inclusions. The tundish was set to operate at steady state, such that the height of water remained constant. The APS III probes were activated and hollow glass particles of a known size distribution and number density were then introduced into the ladle shroud. The numbers and size distributions of inclusions reaching the inner and outer strands were continuously measured as a function of time. The tests were conducted with, and without a standard impact pad, so as to assess any improvements in the water quality entering the moulds.

Figure 12 provides a typical plot for the bare tundish, of the total number of inclusions detected as a function of time, exiting the tundish into strands 3 and 4. As seen, both slopes begin to increase with time, until steady state values are reached. The outer strand 4 records a lower steady state slope, since the water exiting strand 4 has had a longer time to allow its larger inclusions to float to the surface. With the new online APS system operational, it was decided to use the experimental setup with a standard impact pad, in order to judge its performance versus a "bare" tundish. Since the slopes of the individual APS curves indicate the total inclusion count entering a given strand.

The **RRI**'s (**R**esidual **R**atio of **I**nclusions) is a more precise measure of the actual inclusions entering a given strand, in which the size distribution is also given. For steady state conditions,

shown in Figure 13, one sees that the higher Stokes rising velocities of the larger inclusions facilitates their easy float-out. Very few of them enter the strands, whether or not any impact pad is used. Meantime, the very small particles rise much more slowly, so their residence time is completely inadequate for their removal, with, or without, "furniture".

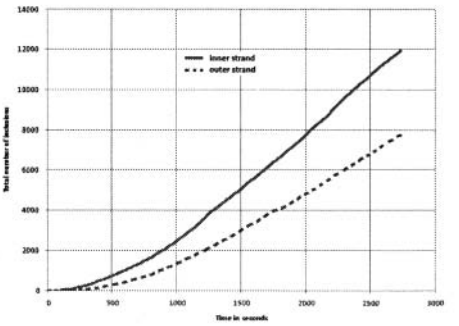

Figure 12 – Total particle count at inner and outer exit strands in a bare tundish, during initial transient, and then steady state, operations.

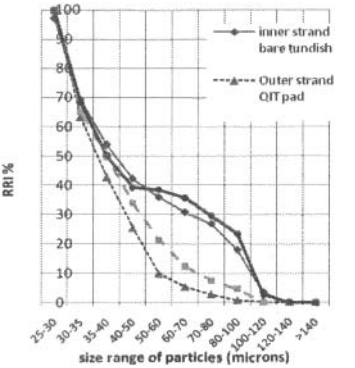

Figure 13– Comparison of RRI values at differing size ranges between bare tundish and standard impact pad.

These two facts are well known, and are corroborated by the RRI curves shown in Figure 13. Tellingly, there is little difference between a standard impact pad and a bare tundish on the amounts of inclusions entering either the inner or outer strands. A careful study of Figure 13 reveals a minor improvement in inclusion removal with the standard impact pad for the outer strands, but almost no improvement for the inner strands.

Conclusions

As a result of the present study, a very convenient Aqueous Particle Detector (APS III) has been built, based on first principles [5]. The capability of the new device to perform online tests under totally submerged conditions makes it a useful (critical) research tool for carrying out inclusion behavior studies in full scale water modeling experiments. The versatility of the present device lies in the fact that 1) there is no need to collect samples during the actual tests for later off-line analysis, 2) the probes may be placed at any convenient location within the experimental vessel, and 3) the data is collected in real-time, immediately.

References

1) D.A. Doutre and R.I.L. Guthrie: "Method and Apparatus for the detection and Measurement of Particulates in Molten Metal" US patent, 4555662
2) R.I.L.Guthrie, H.Nakajima: "Continuous-Use Molten Metal Inclusion Sensor" US Patent, 5241262
3) S. Hajj, Recommendations for the "Water LiMCA" MMPC sensor project, 2009,Aug12th.
4) DASYTEC ® Daten System Technik GmbH, Germany: DASYLab Book 2: Guide 93
5) Abhishek Chakraborty, M.Eng.Thesis, McGill University, 2010.

Sensors, Sampling, and Simulation for Process Control
Edited by: Brian G. Thomas, James A. Yurko, and Lifeng Zhang
TMS (The Minerals, Metals & Materials Society), 2011

THE DEVELOPMENT OF A SENSOR TO DETERMINE THE DIRECTION OF VELOCITY IN LIQUID ALUMINUM

Mitren Sukhram, Stavros A. Argyropoulos

Department of Materials Science & Engineering, University of Toronto;
184 College St, Toronto, Ontario, M5S 3E4, Canada

Keywords: Liquid Aluminum, Velocity, Temperature Profile, Cylinder

Abstract

This paper shows that the temperature distribution within a cylindrical rod, while inserted into flowing liquid aluminum (Al), produces different heating profiles regarding the direction of flow. One can deduce the direction of velocity in the metal by understanding the heating pattern of the cylinder. Specifically, by being able to track the temperature as a function of spatial and temporal coordinates within the cylindrical rod, one can infer the direction of velocity.

Experimental research work involving liquid Al has been conducted using this sensor in the Revolving Liquid Metal Tank (RLMT) at the University of Toronto. The RLMT is capable of melting approximately 50 kg of Al and imposing specified tangential velocities up to 0.35 m/s.

It will be shown that our cylindrical rod sensor records different heating patterns under different fluid flow conditions. This temperature information is then used to infer the direction of velocity in the bath.

Introduction

To date, there is no widely accepted means to measure the velocity of a high temperature liquid metal. Pure aluminum melts at 660°C; metals with processing temperatures equal to and greater than that of liquid aluminum are referred to as high temperature liquid metals. Research into the measurement of velocity of liquid metals has involved a wide range of techniques, where the liquid metal may not necessarily be deemed from the above definition as high temperature. Several of these methods are listed below:

- Photographic Methods [1]
- Reaction Probes [2]
- Tracer Studies [3]
- Electromagnetic Methods [4]
- Hot Wire Anemometry [5]
- Dissolution Probes [6]
- Karman Vortex Probes [7]
- Ultrasonic Doppler Velocimetery [8]
- Melting Methods [9]

Although many techniques have been explored, a method which has wide scale acceptance is yet to be achieved. With respect to high temperature liquid metal processing operations, the need for in situ process measurement is of paramount importance for process efficiency. It has been reported that the efficiency of the electrolytic aluminum cell depends on the velocity within the

reactor. Fluid flow phenomena occur in liquid metal processing operations. The efficiency of these processes depends on the fluid flow conditions inside these liquid metal production systems. Having a means to measure these unknown process variables is beneficial to industry.

Experimental Apparatus

This section will describe the probe construction and experimental apparatus. Figure 1a through Figure 1b are schematic diagrams depicting the cylindrical rod, with thermocouple holes which are used to create the sensor. The sensor is fabricated from AISI 12L14 steel. The rod is 152.4mm (6.00") in length and 41.1mm (1.62") in diameter. Four holes located at 90 degrees from one another are gun drilled at 3.6mm (0.14") in diameter to a depth of 76.2mm (3.00") from the upper circular surface of the probe. All four holes are located 0.7mm (0.03") from the curved surface of the probe. Four type K thermocouples measuring an outer diameter of 3.3mm (0.13") are inserted into the gun drilled hole. The thermocouple junction is exposed. These four thermocouples are connected to a National Instruments Data Acquisition (DAQ) System. This system comprises of an SCXI 1000 chassis, SCXI 1125 amplifier and a SCXI 1320 input data module. The DAQ is connected via a National Instruments PCI 6033E card to a 32bit Windows XP operating system computer. Six channels from the DAQ are recorded:

- Four correspond to the four thermocouples inserted into the steel probe
- One measures the bath temperature
- The remaining channel records the voltage of an immersion circuit

The immersion circuit is used to signify the exact immersion time of the sensor into the aluminum bath. A 5V bias is applied across the probe and a ground rod that is inserted into the bath. When the probe is immersed into the bath, a short circuit of 0V is recorded by the DAQ. The voltage drop from 5V to 0V signifies the immersion of the probe. An increase in the voltage reading to 5V signifies the removal of the probe from the bath. Figure 2 is an example of typical data recorded by the DAQ. In Figure 2, segment AB denotes the start of recording of data. Segment BC marks the immersion of the probe into the bath. The portion CD demarcates the period of time the probe remains in the flow. Segment DE signifies the removal of the probe from the liquid aluminum. Segment EF represents the cooling of the probe in air.

The Revolving Liquid Metal Tank (RLMT) is an electric resistance furnace which is capable of melting 50kg of aluminum and rotating it at specified tangential velocities. The cylindrical steel crucible has an interior diameter of 380.0mm (14.96") and a depth of 200.0mm (7.87"). This crucible is coupled via pulleys to a DC motor. This motor is capable of controlling the revolution speed per minute (RPM) of the furnace within a resolution of 1 RPM. The crucible rotates about its centre in clockwise direction, about the z axis. As mentioned previously, the furnace is equipped with one bath thermocouple located at the centre of the crucible and one grounding rod for the immersion circuit. The placement of these items along with the probe in the crucible is shown in Figure 1c through Figure 1e.

As mentioned previously, the temperature response of four points in the probe is recorded. In order to generate data which gives insight into the temperature distribution about the circumference of the cylinder, the device is rotated counter clockwise at 12 degree increments about its z axis. Thus temperature data as a distribution of the polar coordinate of the probe is logged with respect to the imposed flow field. To clarify, this rotation is not performed while the probe is immersed in the bath. A different experimental run is performed at another

rotation angle for the same flow field. Figure 4 is a schematic overview of the rotation of the thermocouple locations with respect to the flow.

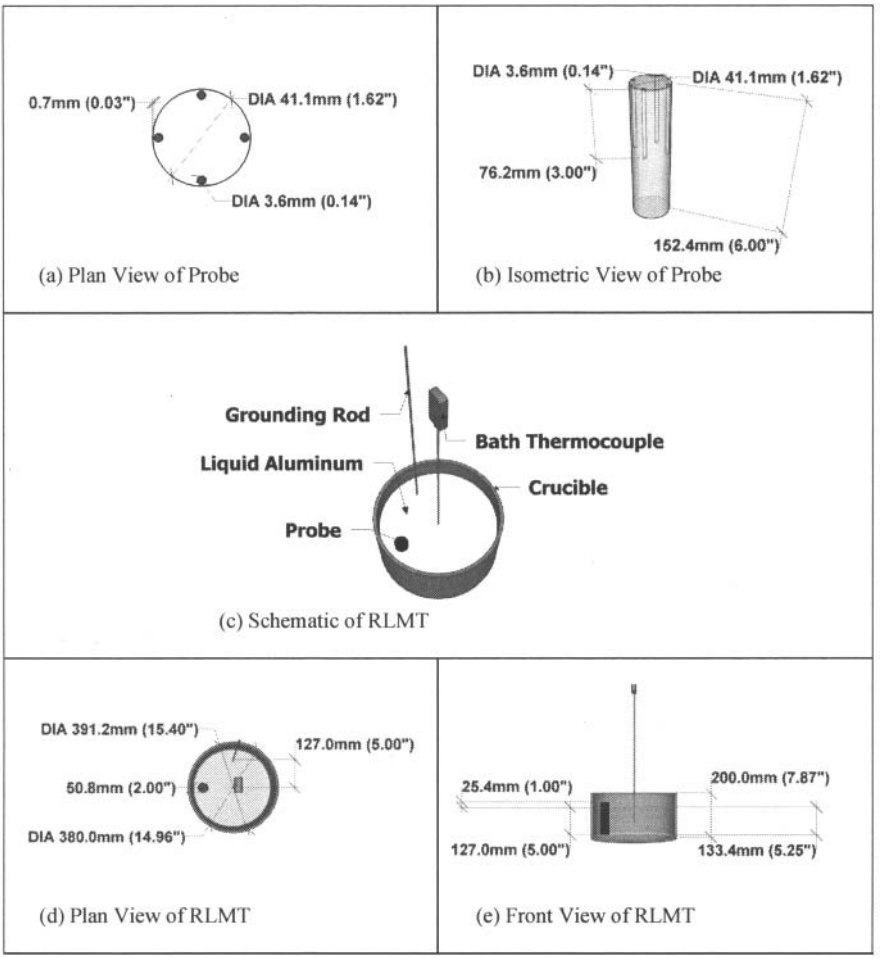

Figure 1: Schematic Overview of AISI 12L14 Probe & Revolving Liquid Metal Tank (RLMT)

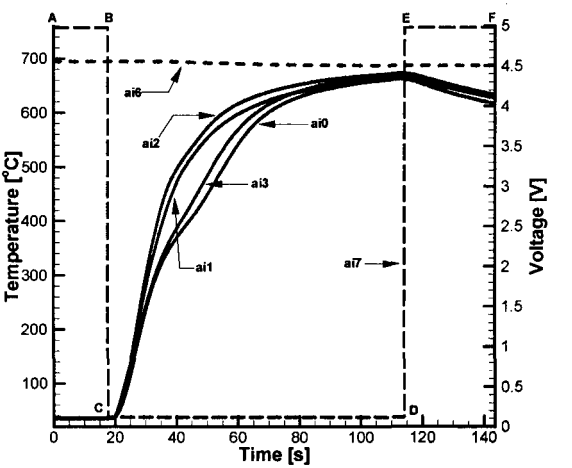

Figure 2: Typical Experimental Data
Channels ai0 to ai3 Probe Thermocouples
Channel ai6 Bath Temperature
Channel ai7 Immersion Circuit
Data for 48 Degree Angle of Rotation 8RPM 30SPH

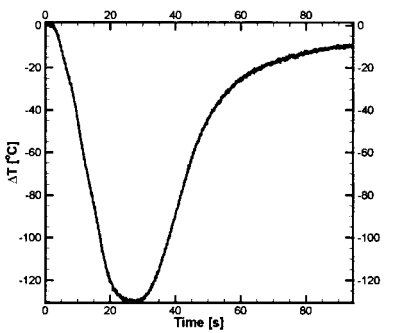

(a) Temperature Difference
Difference Between Locations (ai0-ai2)

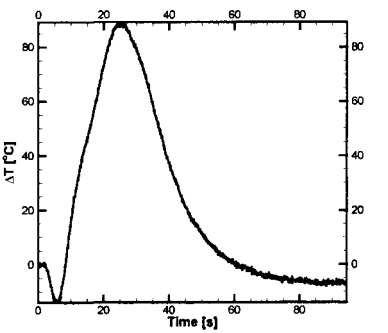

(b) Temperature Difference
Difference Between Locations (ai1-ai3)

Figure 3: 48 Degree Angle of Rotation Temperature Difference Data 8RPM 30SPH

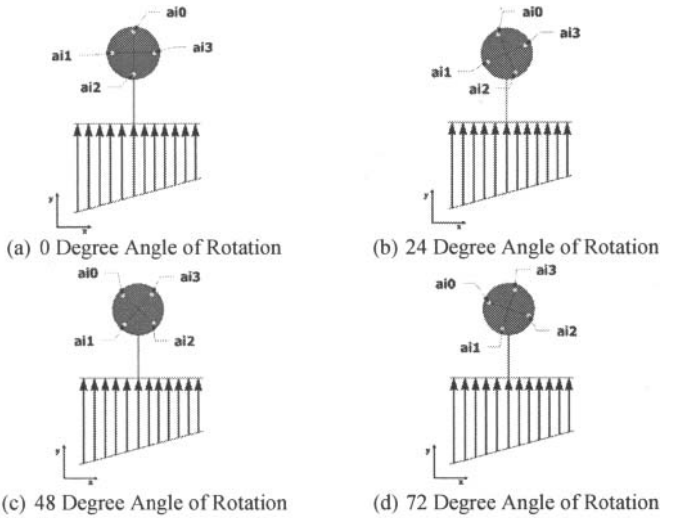

Figure 4: Probe Rotation Diagram

Results and Discussion

From Figure 2 one may note that the rate of change of temperature of each thermocouple location is different. This data is generated for a speed of 8RPM and a bath superheat (SPH) of 30 degrees. In general, location ai2 heats the fastest as it has the steepest slope. Location ai0 heats the slowest, with locations ai1 and ai3 heating in a range bounded by the curves of ai0 and ai2. This signifies that the heat flux at location ai2 is greater that the heat flux at location ai0. Figure 2 is the experimental result for 48 Degree angle of rotation. Notice from Figure 4c that locations ai1 and ai2 are roughly symmetrical with respect to the stagnation point of the flow. From Figure 2 it can be seen that locations ai1 and ai2 heat similarly. Thermocouples ai0 and ai3 which are located downstream with respect to locations ai1 and ai2 heat slower than those that are upstream. Using this methodology, it is beneficial to define the temperature difference between the thermocouple positions. Figure 3 plots the difference in temperature data between thermocouple location (ai0-ai2) and the difference between location (ai1-ai3). Examining Figure 3a which is the temperature difference of the data between position (ai0-ai2) it can be seen that there is a global minimum which occurs. This global minimum signifies the largest difference in temperature between the values at position ai0 and ai2. A minimum occurs since location ai2 heats faster than location ai0. Figure 3b depicts the difference in temperature between thermocouple positions (ai1-ai3). A global maximum can be seen occurring in this plot, signifying location ai1 heats faster than ai3.

Figure 5 plots the difference between the temperature values of (ai0-ai2) as a function of time. Several curves are depicted in the graph; each curve signifies a different angle of rotation of the probe with respect to the flow. In Figure 5 it can be seen that the global minimum which

occurs in each curve is different for each angle of rotation. The trend from the experimental results is that as the rotation angle of the probe increases, the global minimum increases, approaching a value of zero for the dataset of (ai0-ai2). In the proceeding section, a simple means to determine the direction of velocity will be proposed by using these global minima and maxima data.

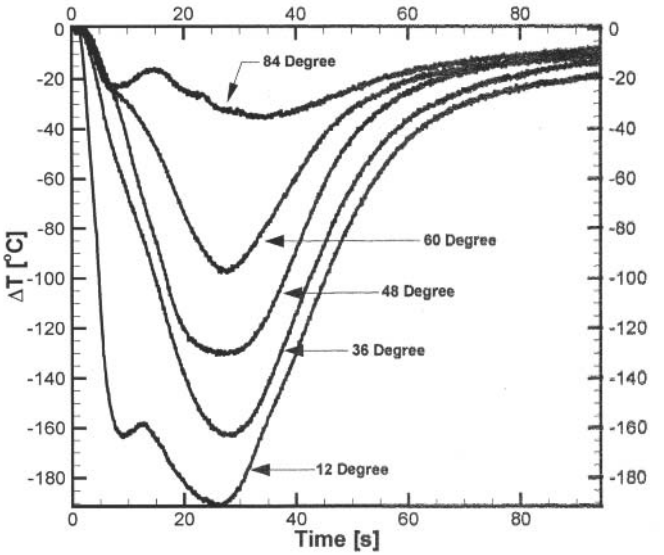

Figure 5: Temperature Difference Data as a Function of Time
[12, 36, 48, 60, 84] Degree Angle of Rotation
Difference Between Location (ai0-ai2)
8RPM 30SPH

A Methodology to Determine the Direction

This section describes a simple way by which the direction of the flow can be deduced from the temperature readings of the steel rod. If one assumes that for a single phase steady 1D flow of liquid aluminum, the temperature distribuion around the periphery of the rod inserted to this flow is characteristic based on the magnitude of velocity and the bath superheat, the direction of the flow field can be deduced by knowing the temperature response of the rod. Figure 6 plots the global maximum of the difference in temperature between thermocouple locations (ai1-ai3) for 8 angles of rotation ranging from 0-84 degrees in 12 degree increments. Data for more than one experimental run at the specified anlge of rotation is presented in Figure

6. The following trend is seen in this plot. The global maximum values of the difference between thermocouple locations (ai1-ai3) increase as the anlge of rotation increases. Keep in mind this is for the imposed flow field of Figure 4. How can we use this information to determine the flow direction of the 1D flow field? If we assume that the difference in temperature between the stagnation point of the flow and the location 180 degrees from the stagnation point of the rod gives the largest difference in temperature, finding this largest difference value with respect to the thermocouples embedded in the rod will tell us the flow direction. Thus if we know how the probe heats with respect to different flow conditions we can deduce the direction of the flow from comparing the temperature differences of the thermocouple positions.

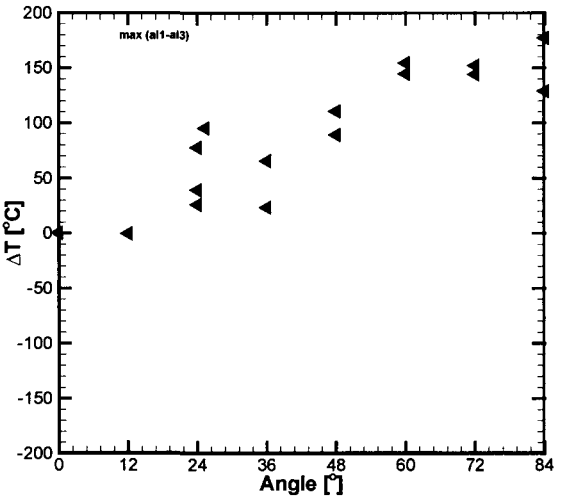

Figure 6: Global Maximum Temperature Difference Values as a Function of Angle of Rotation for 8RPM 30SPH, Difference (ai1-ai3)

Conclusion and Future Work

In conclusion, this paper presents a simple cost effective means to determine the direction of velocity in liquid aluminum by monitoring the temperature distribution at select points in a circular cylinder immersed in flow. Our work in the future aims at reducing the maximum temperature difference scatter shown in Figure 6 for coinciding angles of rotation. This reduction may be realized in different thermocouple installations into the cylinder.

References

[1] Tarapore, E.D and Evans J.W. "Fluid Velocities in Induction Melting Furnaces: Part 1: Theory and Laboratory Experiments," Metallurgical and Materials Transactions B, Vol 7B, 343-351 (1976).

[2] Szekely, J., Chang, C.W., and Ryan, R.E. "The Measurement and Prediction of the Melt Velocities in a Turbulent, Electromagnetically Driven Recirculating Low Melting Alloy System," Metallurgical and Materials Transactions B, Vol 8B, 333-338 (1977).

[3] Berge, B., Grjotheim, K., Krohn, C., Naeumann, R. and Torkelp, K. "Recent Studies of Convection in Commerical Aluminum Reduction Cells" Metallurgical Transactions, Vol 4, 1945-1952 (1973).

[4] Ricou, R. and Vives, C. "Local Velocity and Mass Transfer Measurements in Molten Metals Using an Incorperated Magnet Probe," International Journal of Heat and Mass Transfer, Vol 25, 1579-1588 (1982).

[5] Murthy, A. and Szekely, J. "Hot Film Anemometry in Molten Woods Metal," Metallurgical and Materials Transactions B, Vol 14B, 499-502 (1983).

[6] Johnson, A.R. "Metal Pad Velocity Measurements in Aluminum Reduction Cells," Light Metals, Vol 1, 45-58 (1978).

[7] Scoones, D.J. and Nijman, S. "Measurement of Steel Velocities in the Mould," La Revue de Metallurgie, Cahiers d'Informations Techniques, Vol 100 No 6, 633-635 (2003).

[8] Eckert, S., Cramer, A. and Gerbeth, G. "Velocity Measurement Techniques for Liquid Metal Flows," Magnetohydrodynamics – Historical Evolution and Trends, Springer, 2006.

[9] Melissari, B. and Argyropoulos, S.A. "Measurement of Magnitude and Direction of Velocity in High Temperature Liquid Metals. Part 2 Experimental Measurements," Metallurgical and Materials Transactions B, Vol 36B, 639-649 (2005).

Sensors, Sampling, and Simulation for Process Control
Edited by: Brian G. Thomas, James A. Yurko, and Lifeng Zhang
TMS (The Minerals, Metals & Materials Society), 2011

NEW SENSORS FOR THE VELOCITY MEASUREMENT IN LIQUID METAL PROCESSES

Klaus Timmel, Sven Eckert, Thomas Wondrak, Frank Stefani, Gunter Gerbeth

Forschungszentrum Dresden-Rossendorf e. V., P.O. Box 510119, 01314 Dresden

Keywords: Flow measurements, Ultrasonic Doppler Velocimetry, Contactless Inductive Flow Tomography; Liquid metal model, Continuous casting

Abstract

The shortage of commercially available measuring techniques for opaque liquids obstructs the determination of flow velocities in many technological processes involving liquid metals or semiconductor melts. We present two measuring techniques which have been proven to deliver reliable quantitative velocity data in liquid metals, at least in a temperature range up to about 700°C: the Ultrasound Doppler Velocimetry (UDV) and the Contactless Inductive Flow Tomography (CIFT). Within this paper the efficiency of both measuring techniques is demonstrated by presenting exemplary measurements of the mould flow within a mockup of the continuous casting process which was designed for modeling the related fluid flow and transport processes. Both measuring methods give consistent results for the jets evolving from the nozzle outlets.

Introduction

Significant research effort is permanently focused on the optimization of technologies and facilities for materials processing such as smelting, refining and casting of metals and alloys. The main objectives are an improvement of the final product quality, an enhancement of the process efficiency and an economical consumption of resources and energy. Further developments of processes involving metallic melts require a better, detailed knowledge about the flow structure and the transport properties of the flow. Numerical simulations could provide a better understanding of the complex flow behavior, but, experimental data are indispensable with respect to a validation of the respective CFD codes. The determination of flow quantities in liquid metals is considerably impeded by the special material properties. Powerful optical methods as used for measurements in transparent liquids are obviously not applicable in molten metals. Further serious restrictions arise from the high temperature or the chemical reactivity of the melt. As a consequence there is a very constrained choice of commercially available techniques to measure the velocity structure of fluid flows at elevated temperatures.

Substantial research activities have been carried out at FZD during the last 15 years on the development and qualification of various methods to measure the velocity field in liquid metal flows. In this connection, we follow a twofold strategy. On one hand, we try to develop measuring techniques for applications under real industrial applications. On the other hand, we use liquid metal models as an important tool to investigate the flow structure and related transport processes in melt flows being relevant for metallurgical applications. Besides the classical, invasive probes new ultrasonic or electromagnetic techniques come up and allow a satisfying characterisation of flow quantities in the considered temperature range until 300°C already today. A discussion concerning the perspectives and limitations of such measuring techniques for liquid metal flows can be found in [1]. Within this paper we focus on two complementary techniques: the Ultrasound Doppler Velocimetry (UDV) and the Contactless Inductive Flow Tomography (CIFT). The capabilities of both measuring techniques are

demonstrated at a small mockup of the slab continuous casting process at room temperature in which liquid steel is substituted by the eutectic alloy GaInSn.

Ultrasound Doppler Velocimetry

The measuring principle

Owing to the pioneering work of Takeda [2, 3], ultrasound Doppler methods have been established for fluid flow measurements in physics and engineering during the last twenty years. The Ultrasound Doppler Velocimetry (UDV) is based on the pulse-echo technique and delivers instantaneous profiles of the local velocity along the ultrasonic beam. Ultrasound pulses of a few cycles are emitted from the transducer which might be in direct contact with the liquid flow or attached to the wall of the fluid container. The measuring principle relies on the reflection of the ultrasonic wave by moving particles suspended in the fluid. The echo signals reflected from microparticles are received by the same transducer. The complete information being necessary for reconstructing the velocity profiles is contained in the echo. The knowledge of the sound velocity of the liquid allows for calculating the particle position from a time-of-flight measurement which provides the time delay between the emitted pulse and the corresponding echo of the scattering particles in the path of the beam. The movement of an ensemble of scattering particles inside the measuring volume will result in a small time shift of the signal structure between two consecutive bursts. The velocity is obtained from a correlation analysis incorporating several bursts. For a more detailed description of the measuring principle we refer to Takeda [3]. An important advantage of the method consists in the capability to attain quantitative measuring data from the bulk flow in opaque liquids. Thus, the UDV technique became an accepted method for flow investigations in various liquid metals (see [1] and references therein). The feasibility of velocity profile measurements by UDV has already been demonstrated for low temperature liquid metals such as mercury [4], gallium [5] or liquid sodium at 150°C [6]. A more detailed description of the specific problems arising in the context of UDV measurements in liquid metal experiments such as the acoustic coupling, resonance effects connected with the transmission through material interfaces or the allocation of suitable tracer particles can be found in [7].

Progress in sensor technology

The use of the UDV-technique in hot melt flows is limited by the maximum operating temperature of ultrasonic sensors. The use of the conventional transducer made of PZT based materials confines the range of application of ultrasonic techniques to maximum temperatures of about 150°C (long term load) and 200°C (short term load), respectively. If the measurements have to be performed with direct contact between the ultrasonic probe and the metallic melt, one has to take care for a sufficient wetting between the probe and the liquid metal in order to guarantee a good acoustic contact, but on the other hand, the sensor has to be saved against a chemical attack of the melt.

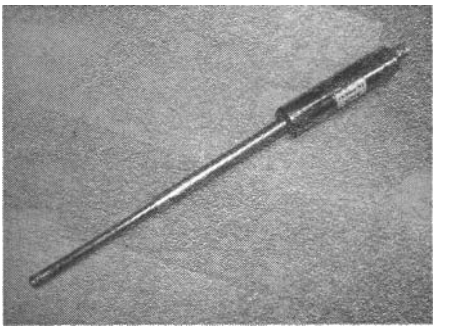

Figure 1: Ultrasonic sensor with stainless steel wave-guide

For this reason a new concept of an ultrasonic transducer with integrated acoustic wave guide has been proposed [8] in order to achieve a thermal as well as a chemical decoupling between the active transducer and the fluid. Stainless steel was selected as wave-guide material. From the acoustic point of view there are also some ceramic materials as suitable candidates, however, it is difficult to achieve a sufficient wetting between a liquid metal and a solid ceramic surface at moderate temperatures. The integrated ultrasonic probe consisting of the piezoelectric element and the acoustic wave-guide is shown in Fig. 1. The working frequency of the transducer is 4 MHz. The wave-guide is fabricated from a stainless steel foil with a thickness of 0.1 mm which is wrapped axially around a capillary tube. The wave-guide is closed at the front end by means of laser beam welding leading to a flat stainless steel surface. This surface is in direct contact with the melt and has to be prepared before the measurements to obtain a sufficient wetting with the liquid metal. Typically, the wave-guide has an outer diameter of about 8 mm and a length between 200 and 400 mm. Such an integrated ultrasonic probe was successfully tested in several melts like PbBi, CuSn or liquid aluminium up to 750°C [8, 9].

The enhancement of the capabilities towards a multidimensional flow mapping with high frame acquisition rates and spatial resolutions would be exceedingly desirable for examinations of highly turbulent, three-dimensional flows such as occurring during electromagnetic stirring of metals. Detailed investigations of such kind of complex flows and a validation of respective numerical simulations require a multidimensional acquisition of the flow field with a reasonable temporal and spatial resolution. Imaging techniques becomes more and more important for detailed explorations of three-dimensional turbulent flows, in particular with respect to the generation of a suitable experimental data base for an efficient validation of respective numerical simulations. New measuring systems are under development using specific combinations of linear sensor arrays and have recently been demonstrated in liquid metal flows driven by a rotating magnetic field [10].

Contactless Inductive Flow Tomography

The measuring principle

Exposing the flow of liquid metals like steel or silicon to an externally applied magnetic field, electrical currents are induced which give rise to a perturbation of the applied field. This flow induced field perturbation, which is detectable outside the fluid volume, contains information about the flow structure and can be exploited to reconstruct the velocity field. By applying consecutively the external magnetic field in different directions, different induced currents and magnetic fields can be produced from the same velocity. This enables a sort of tomographic reconstruction of the flow field. Such a contactless inductive flow tomography (CIFT) was proposed in [11], and later verified experimentally in [12]. In this experiment the full three-dimensional velocity structure in a cylindrical vessel was reconstructed. If an electrically conductive fluid with stationary velocity $\mathbf{u}$ is exposed to a magnetic field $\mathbf{B}$, according to Ohm's law in moving conductors, the current $\mathbf{j} = \sigma(\mathbf{u} \times \mathbf{B} - \nabla\phi)$ is induced, with σ denoting the conductivity of the fluid and ϕ denoting the electric potential. This current $\mathbf{j}$, in turn, induces the magnetic field $\mathbf{b}$ which can be calculated by applying Biot-Savart's law, yielding the following integral equation [13]:

$$\mathbf{b}(\mathbf{r}) = \frac{\sigma\mu_0}{4\pi}\int_D \frac{(\mathbf{u}(\mathbf{r}') \times \mathbf{B}(\mathbf{r}')) \times (\mathbf{r} - \mathbf{r}')}{|\mathbf{r} - \mathbf{r}'|^3} dV' + \frac{\sigma\mu_0}{4\pi}\iint_S \phi(\mathbf{s}') \frac{\mathbf{r} - \mathbf{s}'}{|\mathbf{r} - \mathbf{s}'|^3} \times d\mathbf{S}' \qquad (1)$$

Thereby μ_0 denotes the magnetic permeability of free space, D the volume and S the boundary of the fluid. In order to calculate the potential on the boundary of the fluid, we apply the second Green's identity to the solution of the Poisson equation, which results from taking

the divergence of equation (1). This way we arrive at the following boundary integral equation for ϕ:

$$\phi(\mathbf{s}) = \frac{1}{2\pi}\int_D \frac{(\mathbf{u}(\mathbf{r}')\times\mathbf{B}(\mathbf{r}'))\cdot(\mathbf{s}-\mathbf{r}')}{|\mathbf{s}-\mathbf{r}'|^3}\,dV' - \frac{1}{2\pi}\oint_S \phi(\mathbf{s}')\,\frac{\mathbf{s}-\mathbf{s}'}{|\mathbf{s}-\mathbf{s}'|^3}\cdot d\mathbf{S}' \qquad (2)$$

For most technological applications, it is well justified to replace the total magnetic field $\mathbf{B}$ under the integrals of equations (1) and (2) by the applied magnetic field $\mathbf{B}_0$, thus skipping the induced magnetic field $\mathbf{b}$ there. The reason for this is that in most technical flows with typical length scale L and typical velocity U the magnetic Reynolds number $Rm = \mu_0 \sigma LU$ which is a measure of the ratio of induced to applied magnetic field, is far smaller than 1. With $\mathbf{B}$ being replaced by $\mathbf{B}_0$ in the equations (1) and (2) we can formulate a linear relation between $\mathbf{u}$ and $\mathbf{b}$.

In contrast to the CIFT demo experiment, described in [12], with two consecutively applied magnetic fields pointing in orthogonal directions, for the present continuous casting application we use only a single external magnetic field $\mathbf{B}_0$ which points mainly in vertical direction. This approach is justified by the geometry of the thin slab caster for which the velocity components parallel to the wide face of the mould are the most relevant ones. In view of later applications at real casting machines, this vertical magnetic field shows the positive side effect that the induction due to the oscillating copper walls of the mould is minimized.

For the inversion, we minimize the following functional [13]:

$$F[\mathbf{u}] = F_{B_0}[\mathbf{u}] + F_{2D}[\mathbf{u}] + F_{u_{inlet}}[\mathbf{u}] + F_{div}[\mathbf{u}] + F_{reg}[\mathbf{u}] \qquad (3)$$

The first functional $F_{B_0}[\mathbf{u}]$ represents the mean squared residual deviation of the measured field from the field modeled according to the integral equation system (1) and (2) for the applied magnetic field. The functional $F_{2D}[\mathbf{u}]$ enforces the velocity to be two-dimensional by setting to zero the u_y component (which is parallel to the narrow faces of the mould). Optionally, the mean velocity at the inlet of the SEN can be prescribed by the functional $F_{u_{inlet}}[\mathbf{u}]$. The functional $F_{div}[\mathbf{u}]$ enforces the velocity to be solenoidal, and the last functional $F_{reg}[\mathbf{u}]$ is the regularization functional for the Tikhonov regularization which tries to minimize the kinetic energy of the flow. The optimal solution is found at the point of strongest curvature of Tikhonov's L-curve which is done by an automatic search [13].

Experimental model of the continuous casting process

Background

About 92% of the worldwide annual output of crude steel is produced using the continuous casting process [14]. The liquid steel flow in the mould has a great influence on the obtained quality of steel. In particular, an inappropriate flow regime can lead to the entrapment of oxides, slag or gas bubbles and their transport into the solidification zone. The application of electromagnetic fields provides a considerable potential to control the fluid flow in the mould cavity and to influence the solidification in the strand. Many numerical investigations have been reported until now to improve the understanding of the magnetic field influence on the mould flow (see for instance [15-18]). However, the problem has to be considered as challenging because of the complexity of the geometry, the highly turbulent flow or specific peculiarities occurring in case of MHD turbulence. Obviously, a validation of the numerical predictions by liquid metal experiments is indispensible. However, related experimental studies are rather scarce until now. Several plant trials were carried out [19, 20] to test the efficiencies of electromagnetic brakes in the real casting process. Because of the lack of suitable measuring techniques for liquid steel at 1500°C such trials cannot provide any

reliable knowledge to validate numerical calculations. A Japanese group reported some experimental studies employing simple mercury models [20, 21]. With our work we want to continue the strategy of cold metal models. The main value of such cold metal laboratory experiments consists in the capabilities to obtain quantitative flow measurements with a reasonable spatial and temporal resolution.

Experimental set-up: The Mini-LIMMCAST facility

Fig. 2 shows the small-scale mockup, which is operated with the eutectic alloy GaInSn as model fluid at room temperature. A stainless steel cylinder serves as the tundish which contains about 3.5 l of the GaInSn alloy. The melt is discharged through a Plexiglas tube as SEN with an inner diameter of 10 mm into the mould with a rectangular cross section of 140 $\times$ 35 mm^2 also made of Plexiglas. Two nozzle ports are situated about 80 mm below the free surface in the mould. From the mould the liquid metal flows through a U-bend channel into a storage vessel. The vertical position of the vessel inlet controls the free surface level in the mould. An electromagnetic pump conveys the melt from the vessel back into the tundish. The experiments presented here were performed in a discontinuous mode, i.e. after filling the tundish with the melt the stopper rod was lifted to drain the fluid into the mould. During this process the liquid level of both the tundish and the mould were monitored using a laser distance sensor. The liquid flow rate has been derived from the descent of the surface level in the tundish. For some experiments, a DC magnet is utilized to supply a transverse magnetic field with a strength of B = 310 mT. Measurements of the field strength have shown a good homogeneity of the field between the pole faces within a tolerance of about 5%. The pole faces of the magnet cover the wide side of the mould completely. The vertical extension of the pole shoes is 40 mm.

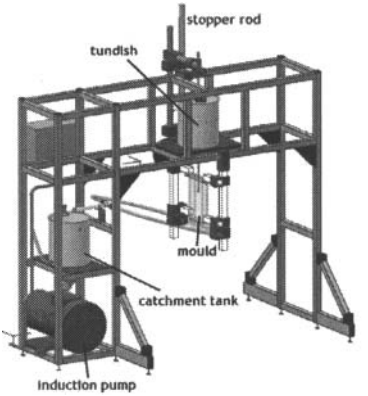

Figure 2: 3D-scheme of the small-scale GaInSn model.

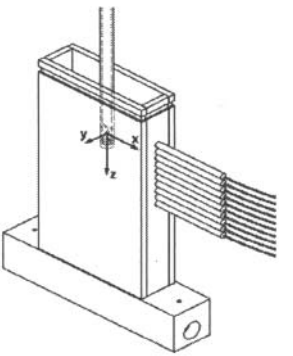

Figure 3: Mould with submerged entry nozzle (SEN) and the linear arrangement of 10 ultrasonic transducers.

In the experiments we have applied the DOP2000 velocimeter (model 2125, Signal Processing SA, Lausanne) equipped with up to ten 4MHz transducers (TR0405LS, acoustic active diameter 5 mm). The transducers were arranged within a vertical line array which was attached at the outer wall and located at the midsection of the narrow mould side. Profiles of the horizontal velocity were recorded along the wide faces of the mould between the narrow side wall and the submerged entry nozzle. Figure 3 sketches the arrangement of the transducers at the model mould.

Experimental results

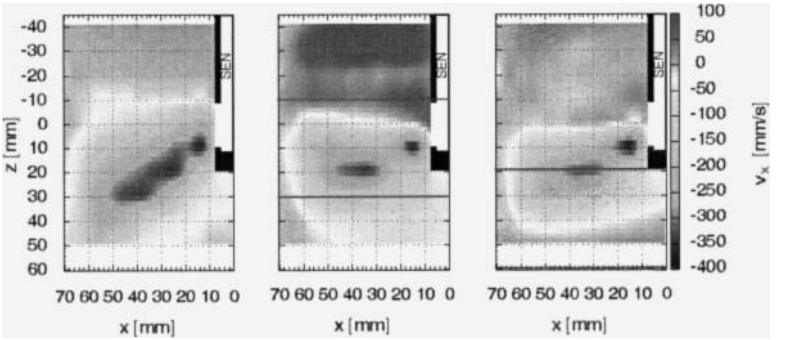

Figure 4: Mould flow without magnetic field (left), with B=310 mT covering the SEN-port (middle) and with B=310 mT below the SEN.

Figure 4 shows the time-averaged horizontal velocity in the mould near the submerged entry nozzle (SEN) measured by UDV. The left figure depicts the uninfluenced flow. The transverse magnetic field was applied between the green horizontal lines at two different positions. The largest impact on the flow occurs if the magnetic field is installed just at the region of the nozzle ports where the jet flow shows the highest intensity. The presence of the magnetic field reduces the jet angle remarkably and creates a recirculation zone above the liquid metal jet. The intensity of the velocity within the jet is only slightly reduced. The application of the magnetic field at a lower vertical position causes a slow-down of the turbulent flow below the jet. Further results and detailed discussions can be found in [23].

The CIFT measuring assembly of a rectangular coil around the mould cavity is displayed in figure 5(a). In a first series of experiments one single flux-gate sensor was used for measuring the induced magnetic field at 36 vertical positions by just changing the vertical sensor position. Before starting the measurements the induced magnetic field was calculated outside the mould using a simulated velocity profile. It turned out that the strongest induced magnetic field is located at the narrow faces of the mould. Using a realistic number of 8 sensors in the middle of the narrow face with a distance from the fluid of 20 mm, we reconstructed the velocity by minimizing the functional (3) and achieved a correlation around 78 per cent and a mean squared error of about 0.4 comparing the simulated and the reconstructed flow field. The comparison between the vertical dependence of the resulting data with the simulated magnetic field shows a quite convincing agreement, as seen in figure 5(b). With these experimental data at hand, the velocity reconstruction was carried out once again. By assuming a symmetric flow configuration, we have mirrored the data measured at one narrow face to the opposite one. The resulting reconstructed velocity is depicted in figure 5(c). The jet and the double roll are clearly visible. The reconstructed velocity of this experiment was also compared with independent UDV measurements, which shows a good qualitative agreement [13].

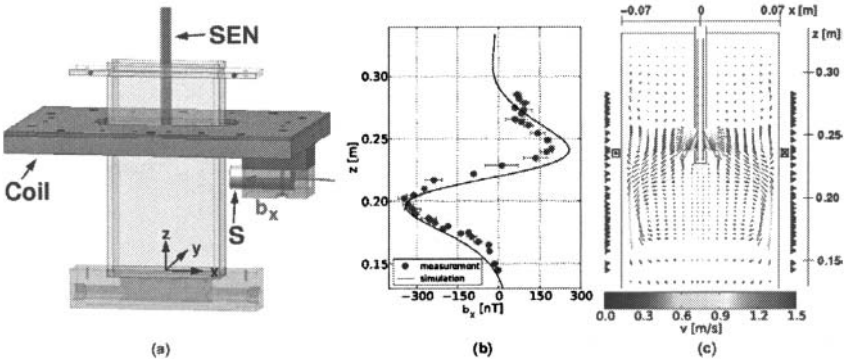

Figure 5: Schematic sketch of the measurement setup for CIFT (a), comparison of the simulated induced magnetic field component b_x and the measured field at 36 positions along z (b), and the reconstructed velocity (c)

A further series of measurements was carried out in which the induced magnetic field was recorded using flux-gate sensors at 7 positions on each narrow side of the mould with a time resolution of 1-2 Hz. Within these experiments argon gas was injected through the stopper rod into the SEN. Figure 6 shows snapshots of the flow structure obtained at a gas flow rate of 500 sccm and a lift of the stopper of about 15 mm. The sequence of pictures reveals several changes of the flow pattern from a double to a single vortex flow regime and vice versa.

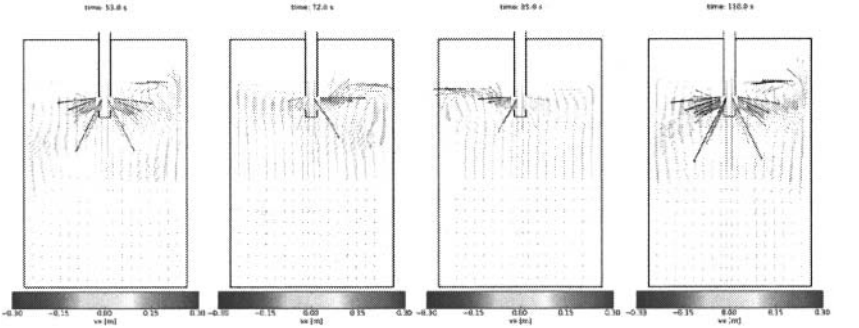

Figure 6: The reconstructed velocity field in the mould for the two flow measurement for 4 selected points in time.

Summary

The paper presented two measurement techniques applied for the investigation of liquid metal flows inside a small-scale mockup of the continuous casting process. Such cold liquid metal models appear as an important tool for the experimental investigation of many open questions in steel casting which can be related to the melt flow. Efficient measuring techniques are available in a temperature range until 300°C which provide valuable experimental data for the validation of numerical flow simulations. Within this paper we demonstrated the capabilities of the UDV and the CIFT technique to determine the flow structures in a GaInSn flow at room temperature. Both methods have been successfully applied for gathering the velocity field in the mould. In general, the CIFT-technique enables the acquisition of a full three-dimensional velocity structure by measuring the induced magnetic field outside the fluid. A modest number of 7 magnetic field sensors placed along each narrow face was sufficient to

reconstruct the two-dimensional velocity field in the mould with a good agreement with associated UDV measurements. Transient flows can be detected with a temporal resolution of about 1 Hz. The use of the ultrasound Doppler method allowed for an instructive insight into the flow pattern in the mould under the imposition of the horizontal magnetic field. Informative measurements of the velocity field in the regions of the magnet pole faces have been obtained. New developments of ultrasonic sensors provide new perspectives regarding future measurements of multi-dimensional and multi-component velocity fields at higher temperatures.

Acknowledgment

The research is supported by Deutsche Forschungsgemeinschaft (DFG) in form of the SFB 609 "Electromagnetic Flow Control in Metallurgy, Crystal Growth and Electrochemistry".

References

[1] S. Eckert, A. Cramer, G. Gerbeth, "Velocity measurement techniques for liquid metal flows", *Magnetohydrodynamics - Historical Evolution and Trends*, ed. S. Molokov, R. Moreau, H.K. Moffatt, (Springer, 2007), 275-294
[2] Y. Takeda, Int. J. Heat Fluid Flow, 7 (1986), 313-318
[3] Y. Takeda, Nucl. Eng. Design, 126 (1991), 277-284
[4] Y. Takeda, Nucl. Techn, 79 (1987), 120-124
[5] D. Brito, H.C. Nataf, P. Cardin, J. Aubert. J.P. Masson, Exp. Fluids, 31 (2001), 653-663
[6] S. Eckert, G. Gerbeth, Exp. Fluids, 32 (2002), 542-546
[7] A. Cramer, C. Zhang, S. Eckert, Flow Meas. Instrum., 15 (2004), 145-153
[8] S. Eckert, G. Gerbeth, V.I. Melnikov, Exp. Fluids, 35 (2003), 381-388
[9] S. Eckert, G. Gerbeth, T. Gundrum, F. Stefani, W. Witke, Proc. of the 4th Int. Conf. on Electromagnetic Processing of Materials, EPM2003, Lyon (France), (2003), 601-608
[10] S. Franke, L. Büttner, J. Czarske, D. Räbiger, S. Eckert, Flow Meas. Instrum., 21 (2010), 402-409
[11] F. Stefani, G. Gerbeth, Meas. Sci. Techn., 11 (2000), 758-765
[12] F. Stefani, T. Gundrum, G. Gerbeth, Phys. Rev., E 80 (2004), 066303
[13] T. Wondrak, V. Galindo, G. Gerbeth, T. Gundrum, F. Stefani, K. Timmel, Meas. Sci. Techn., 21 (2010), 045402
[14] World Steel Association, „Steel Statistical Yearbook 2008", (2008)
[15] B.G. Thomas, L. Zhang: ISIJ Int., 41 (2001), 1181-1193
[16] K. Takatani, K. Nakai, N. Kasai, T. Watanabe, H. Nakajima: ISIJ Int., 29 (1989), 1063-1068
[17] B. Li, F. Tsukahashi: ISIJ Int., 46 (2006), 1833-1838
[18] K. Cukierski, B.G. Thomas, Metall. Mater. Trans., 39B (2008), 94-107
[19] P. Gardin, J.-M. Galpin, M.-C. Regnier, J.-P. Radot, Magnetohydrodynamics, 32 (1996), 189-195
[20] K.H. Moon, H.K. Shin, B.J. Kim, J.Y. Chung, Y.S. Hwang, J.K. Yoon: ISIJ Int., 35 (1996), S201-S203
[21] K. Okazawa, T. Toh, J. Fukuda, T. Kawase, M. Toki, ISIJ Int., 4 (2001)1, 851-858
[22] H. Harada, T. Toh, T. Ishii, K. Kaneko, E. Takeuchi, ISIJ Int., 41 (2001), 1236-1244
[23] K. Timmel, S. Eckert, G. Gerbeth, F. Stefani, T. Wondrak, ISIJ Int., 50 (2010), 1134-1141

Sensors, Sampling, and Simulation for Process Control
Edited by: Brian G. Thomas, James A. Yurko, and Lifeng Zhang
TMS (The Minerals, Metals & Materials Society), 2011

MEASUREMENT OF MOLTEN STEEL SURFACE VELOCITY WITH SVC AND NAIL DIPPING DURING CONTINUOUS CASTING PROCESS

R. Liu[1], J. Sengupta[2], D. Crosbie[2], S. Chung[3], M. Trinh[3] and B.G. Thomas[1]

[1]Department of Mechanical Science and Engineering,
University of Illinois at Urbana-Champaign; 1206 West Green Street, Urbana, IL 61801
[2]Global R&D – Hamilton, ArcelorMittal Dofasco Inc.;
1390 Burlington Street East, Hamilton, Ontario L8N 3J5 CANADA
[3]Steelmaking Technology, ArcelorMittal Dofasco Inc.;
1330 Burlington Street East, Hamilton, Ontario L8N 3J5 CANADA

Keywords: continuous casting, SVC, nail boards, meniscus instantaneous velocity

Abstract

Surface velocity of the molten steel is critical to final product quality during the continuous casting of steel. Plant experiments using two different new sensors, Sub-meniscus Velocity Control (SVC) devices and nail dipping, are performed to evaluate their performance, and to quantify liquid steel velocities at locations 50 mm apart on the surface of ArcelorMittal Dofasco's No. 1 continuous caster under different casting conditions, including different throughputs and mold widths. Correlation between the height difference of the solidified lump on the nail and surface velocity is confirmed and extended. Reasonable agreement between the two sensing methods of surface velocity is obtained, both in trends and magnitudes for both time-averaged velocity and transient flows. The effects of casting speed, mold width, and gas volume fraction on meniscus velocity are also discussed.

Introduction

In continuous casting (CC) process, molten steel flow in molds cannot be directly observed or measured using conventional flowmeters due to the opaque slag layer on top (Fig. 1) and high temperature of liquid steel inside. Information of liquid steel flow patterns in mold could be achieved from meniscus steel velocities which can be measured. The liquid steel surface velocity is also a key factor that affects the final product's quality: too high a surface velocity induces excessive turbulence and shear instability at slag-steel interface and increases the possibility of slag entrainment[2,3]; too low a surface velocity results in lack of heat transfer near narrow face and meniscus regions, which further leads to hook formation and entrapment of slag or inclusion particles[4,5,6]. Thus it is of great significance to measure and control meniscus steel velocities in the mold during CC process.

Various methods to measure liquid steel velocities have been developed and reported[7~16]. Mass Flow Control (MFC) sensors were imbedded behind mold walls, and liquid steel velocities were measured by computing the time delay of signals recorded by the two probes, which was caused by a change of induced electromagnetic current by flow variation as liquid metal traveled through the magnetic field[7]. This expensive technique was implemented to only measure velocities near the shell and around meniscus where the molten steel flow is more uniform[8].

Argyropoulos[9, 10] *et al.* developed a method to measure the liquid metal velocity by measuring the time needed to melt a metal sphere immersed in liquid bath of the same metal with three sensing wires imbedded at the sphere center. The sphere melting time is related to the local liquid velocities as well as the superheat contained. Mathematical models were also developed to predict the time required for the sphere to melt under different flow conditions. This sphere melting method needs a new sphere with all sensing wires imbedded for every trial, thus is very expensive for industrial use.

The methods mentioned above adopt complicated multi-physics procedures such as magnetohydrodynamics and heat transfer coupled flow to quantify the molten steel velocity. These methods are much more expensive to use and complicated to analyze the data obtained. *On the other hand, simpler methods using basic fluid mechanics principles were also developed.*

The Karman vortex probe was developed by Iguchi *et al.*[11,12,13] to measure the liquid steel velocities near meniscus based on the linear relationship between molten steel velocity and the shedding frequency of Karman's vortex streets formed behind the cylindrical probe immersed in the mold. This method only works well for one-dimensional flows. Other shapes of the probe were also tested in plant trials, and the triangular shape was confirmed most accurate in measuring low steel velocities (down to ~0.05 m/s) provided the direction of the flow is known[13]. The probe used in this method requires a rigid support to filter the noises in the signal. However, other sources generating the noise might not be prevented with this method.

Kubota[14] *et al.* utilized a simpler technique with a rod dipped into the molten steel, and the deflection angle of the rod and the torque acting on it were measured. These quantities were then transformed into surface steel velocities. The SVC technique[15] used in the current work operates via a similar principle.

A much simpler method to measure meniscus steel velocities using nail boards was pioneered by Dauby[1] *et al.* at LTV steel, then further developed and utilized by Thomas[16-18] *et al.* In addition to measuring instantaneous surface steel velocities in the mold and the direction of flow, the nail board method also provides extra information such as thickness of the slag layer, and the meniscus liquid level profile across the top surface.

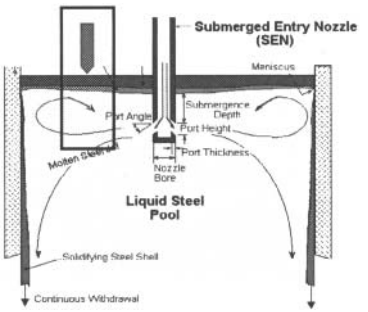

Fig. 1 Surface Slag Layers and CC Process[1]

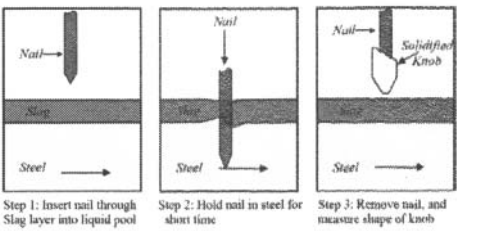

Fig. 2 Procedures for Nail Board Test[17]

For both nail board and single nail dipping tests, nails are inserted into molten steel for 3~5 seconds, then removed, and lumps form due to the solidification of the liquid steel and slag around the nails, as shown in Fig. 2. As molten steel flows past the nail, liquid steel builds up at the impinging point on the nail lump as it solidifies, and all kinematic energy is converted into

potential energy at the stagnation point. Liquid steel level drops at the opposite side of the nail lump due to the lower pressure at the wake region. This deformation of the meniscus is recorded by the shape of the solidified lump, as shown in Fig. 3. By investigating the lump shape and lump height difference between the facing-flow side and its opposite side, the magnitude and direction of the surface steel velocity can be determined. CFD models for nail dipping tests were developed by Rietow and Thomas[18] to study the liquid steel flow past a nail with a liquid slag layer on top using FIDAP. The standard k-ε model was employed to describe turbulence, and the SPINE method was used to track the slag/steel interface. The surface tension and gravity effects were also taken into account by the model. Further details of this computational model are provided elsewhere[19]. Correlation between the lump height difference and the surface steel velocity magnitude was established by performing parametric studies, as shown in Fig. 4.

Fig. 3 Nail and Lump

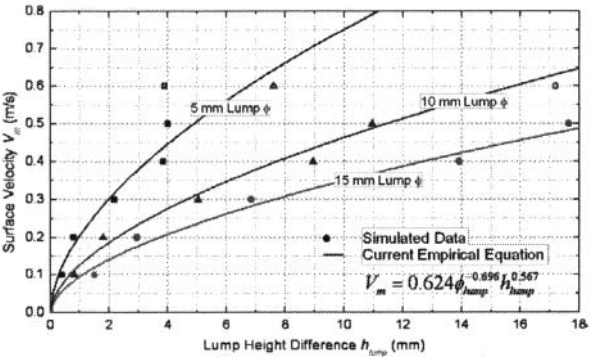

Fig. 4 Curves to convert nail lump height difference into velocity magnitude

The simulation results marked as hollow symbols in Fig. 4 suggest a drop of lump height difference at a free stream velocity of 0.6 m/s for all three lump diameters investigated, indicating that lump height difference does not always increase with liquid steel surface velocity. The maximum lump height difference from the simulation results occurs around a surface steel velocity of 0.5 m/s for all three lump diameters. However, the maximum lump height difference measured in practice was found to exceed the simulated maximum lump height difference significantly. Assuming possible convergence issues with the computational model at high free stream velocities, the simulated data above 0.6 m/s surface velocities are neglected, and a curve fit of rest data points is performed using a simple power law relation. The fitted curves are further extended to take into account cases with large lump height differences, as shown in Fig. 4 with the dashed lines.

In the present work, two sensor techniques, Sub-meniscus Velocity Control (SVC) device and nail dipping, are used together to measure the surface velocity in No. 1 continuous caster mold at ArcelorMittal Dofasco. The extended curve fit of Rietow's simulation results is utilized to quantify the liquid steel surface velocity from measured lump height difference. Use of nail dipping as a simple sensor is shown to be a reliable method to measure the liquid steel surface transient velocities from the comparisons.

Results and Discussion

In current work, meniscus velocities were measured from two plant trials at ArcelorMittal Dofasco's No. 1 continuous caster. Both SVC and nail dipping measurements were performed in the first trial on strand 1, in order to compare and evaluate the two sensing methods. The SVC probe has a diameter of 25 mm, and was inserted at a depth of 100 mm below meniscus at quarter point of the mold. The instantaneous velocities were measured and recorded with a sampling frequency of 1 Hz. Instead of using a row of nails fixed in a board to measure liquid steel meniscus velocities at multiple locations, a single nail with a diameter of 6 mm was inserted about 50 mm closer to the narrow face than the SVC probe for each measurement time. The location for dipping the nail was chosen so that the two sensing methods were measuring velocities at almost the same location at meniscus, and also that the steel flow at meniscus was not disturbed much by the SVC probe or the nail. For the sign convention of meniscus velocity, positive meniscus velocities indicate flow towards the SEN, and negative velocities indicate flow away from the SEN towards the narrow face. The process conditions and sensing methods used in measurements for these trials are listed in Table I for the standard SEN. The complete history of the changing casting speed for the first trial is shown in Fig. 5(a).

Table I. Processing Parameters for Two Trials

Trial #	Mold Width (mm)	Mold Thickness (mm)	Sensing Methods	SEN Depth (mm)	Gas Injection Rate (SLPM)
1	1248	225	SVC + Nail	177	6
2	983		Nail	185	

Comparison of SVC and nail dipping measurements

The change of casting speed with time for trial #1 is shown in Fig. 5(a), and steel meniscus surface velocity histories monitored by SVC and nail dipping are shown in Fig. 5(b). In addition to the instantaneous SVC data for surface velocity, Fig. 5(a) also shows a 30-second moving average velocity during the trial. The locations in the top of the mold where the nail and SVC probe were inserted are also given in the figure. The error bars for the nail dipping test results are obtained by performing an error analysis, assuming an uncertainty of 0.5 mm during the lump height difference measurements.

It is observed from Fig. 5(b) that the SVC data and nail dipping results match closely with each other. Furthermore, most nail dipping measurements match the moving average of the SVC data. At a few points, the nail dipping results fall outside the moving average, but still always fall within the range of the instantaneous SVC data. Perhaps the velocities from the nail dipping measurements are slightly less than the SVC data. This might be expected, considering that the SVC probe extends to 100mm below the surface and measures an average over that range. The nail dipping test measures velocity closer to the surface, which should be lower, owing to the drag effect from the slag layer.

Effects of Casting Speed and Mold Width on Meniscus Velocity

The steel meniscus surface velocities measured by both the SVC and nail dipping methods illustrate the same trends with casting speed change. At the high casting speed of 1.9 m/min, Fig. 5 shows the average meniscus velocity with the standard SEN design reaches around +0.6 m/s, which suggests a strong double-roll flow pattern in the mold. At the medium casting speed of 1.4 m/min, meniscus velocity is always positive (0.3 to 0.5 m/s), which indicates a consistent

double-roll flow pattern in the mold. At the low casting speed of 1.0 m/min, meniscus velocities appear both positive and negative, indicating a complex flow pattern, with variable reversing flows where neither method is expected to be particularly accurate.

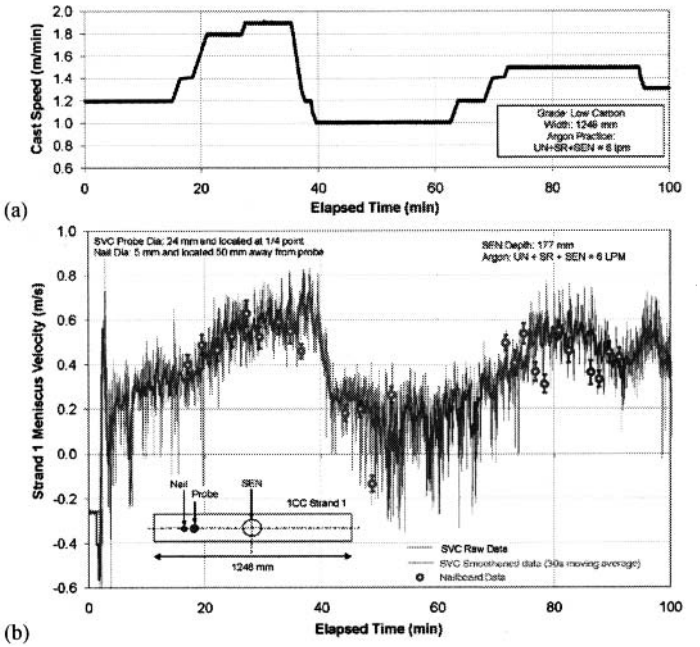

Fig. 5 Casting Speed Change in Trial #1 and Measured Meniscus Velocity
(a) Casting speed change; (b) Meniscus Velocity History from SVC and Nail Dipping.

For trial #2 with the narrower mold width (983 mm), the SVC device could not fit into the mold due to lack of supporting system within the limited space at meniscus region, so only nail dipping tests were performed in this trial. Three casting speeds (1.9 m/min, 1.7 m/min and 1.5 m/min) were tested during this trial. Ten nail samples were taken for each casting speed. The SEN submergence depth is 185 mm. Results from nail dipping measurements are shown in Fig. 6, together with the SVC and nail dipping test data from trial #1.

For a constant mold width, higher casting speed has two effects: increasing SEN mean velocity at port exit and lowering gas volume fraction. Both effects encourage higher surface velocities. From Fig. 6, these effects are clearly shown that average meniscus steel velocity increases almost linearly with casting speed for both trials.

For a constant casting speed, Fig. 6 suggests that surface velocities in the 983 mm mold width (nail dipping) are lower than in the 1248 mm mold width (both tests). Larger mold widths lead to higher throughputs, which increases SEN velocities. However, this increase in SEN velocity does not necessarily cause higher surface velocities because the distance for the jet to travel from SEN port exit to meniscus also increases, so the momentum of the jet diffuses more. The result is complicated because mold width also affects gas volume fraction, as discussed in the section

below. Note that the range for variation of instantaneous velocities in trial #1 from SVC decreases as casting speed increases, which suggests a more stable flow in the mold for higher casting speeds with double-roll flow patterns.

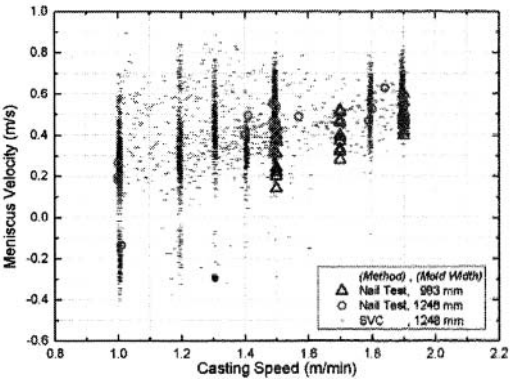

Fig. 6 Casting Speed Effects on Measured Meniscus Velocity

Effects of Gas Volume Fraction on Meniscus Velocity

Besides factors such as casting speed and mold width, gas injection is another critical factor that affects the flow patterns in the mold and meniscus velocities. Though the argon gas flow rate remains the same for both trials at different casting speeds, the gas volume fraction is actually varying according to throughput. Because gas expands at higher temperatures, the gas injection rate will be ~5X higher in the mold than at room temperature (STP). Gas volume fractions were calculated via the ideal gas law using the ferrostatic pressure and temperature values at port exit.

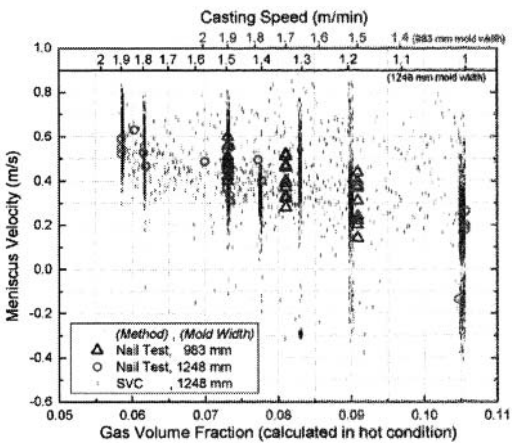

Fig. 7 Gas Volume Fraction (calculated in hot condition) Effect on Meniscus Velocity

The effect of calculated gas volume fraction on surface velocity measured for both trials is shown in Fig. 7. The meniscus velocities decrease almost linearly with increasing gas volume fraction, and show no influence of mold width. This observation suggests that injected argon gas has a more important effect on steel flow patterns in the mold than width. Gas rising from SEN port exit drags steel upward, which generates surface velocities away from SEN, and tends to make a single-roll flow pattern. For higher casting speeds, steel throughput is higher, and the gas volume fraction is lowered. Then a double-roll flow pattern is more likely to occur.
Thus, the trend for increasing gas volume fraction to cause a transition of flow pattern from double-roll to complex flow is clearly shown in Fig. 7. Finally, all three sets of measurements from both trials match consistently with the same trends.

Conclusions

Two different velocity probes for measuring surface velocity in molten steel were tested and compared in a commercial steel slab casting mold, leading to the following conclusions:

1. A reasonable match between SVC measurements and nail dipping tests has been achieved using a new correlation between lump height difference and meniscus steel velocity, based on a curve fit of previous simulation data.
2. The SVC system can provide reliable continuous surface velocity measurements in molten steel and successfully validated the nail dipping tests in the current work. Though only discrete data points can be obtained by nail dipping tests, nail dipping is a simple, reliable, and capable method of measuring slag layer thickness and capturing instantaneous meniscus steel velocities as well as flow directions at multiple locations. Thus, nail dipping is a powerful tool to quantify meniscus velocities and to study flow in the mold for industrial applications.
3. Based on velocity measurements at the mold quarter point using both methods, surface velocity increases with increasing casting speed and/or decreasing gas volume fraction, as the flow pattern tends towards double-roll. The effect of increasing mold width is complicated because it increases port velocity, increases travel distance, and decreases gas fraction, with a net effect of increasing surface velocity.

Acknowledgements

We would like to thank the members of the Continuous Casting Consortium in University of Illinois at Urbana-Champaign for their support of our research work, and also to M. Yavuz at ArcelorMittal Global R&D in East Chicago and D. Currey at ArcelorMittal Dofasco Global R&D in Canada for their help with the project. ArcelorMittal Global R&D in Maizières, France is acknowledged for providing the SVC devices for trials.

References

1. P.H. Dauby, W.H. Emling, and R. Sobolewski, *Lubrication in the Mold: A Multiple Variable System. Ironmaker and Steelmaker*, 1986. 13(Feb): p. 28-36.
2. M. Iguchi, J. Yoshida, T. Shimizu, and Y. Mizuno, *Model Study on the Entrapment of Mold Powder into Molten Steel.* ISIJ International 40:7 (2000), pg. 685-691.
3. L. Hibbeler and B.G. Thomas, *Investigation of Mold Flux Entrainment in CC Molds Due to Shear Layer Instability.* AISTech 2010 Steelmaking Conference Proc., (Pittsburgh, PA, May 5-8, 2010).

4. J. Sengupta, B.G. Thomas, H.J. Shin, G.G. Lee, and S.H. Kim, *Mechanism of Hook Formation during Continuous Casting of Ultra-low Carbon Steel Slabs*. Metallurgical and Materials Transactions A, Vol. 37A, No. 5, (May), 2006, pp. 1597-1611.
5. J. Sengupta, H.J. Shin, B.G. Thomas, and S.H. Kim, *Micrograph Evidence of Meniscus Solidification and Sub-Surface Microstructure Evolution in Continuous-Cast Ultra-Low Carbon Steels*. Acta Materialia, Vol. 54, No. 4, Feb. 2006, pp. 1165-1173.
6. B.G. Thomas. *Chapter 14. Fluid Flow in the Mold, in Making, Shaping and Treating of Steel: Continuous Casting*, A. Cramb, Editor. 2003, AISE Steel Foundation, Pittsburgh, PA. p. 14.1-14.41.
7. K.U. Kohler, et al., *Steel Flow Velocity Measurement and Flow Pattern Monitoring in the Mould*, in Steelmaking Conf. Proc. 1995, ISS, Warrendale, PA: Nashville, TN. p. 445-49.
8. B.G. Thomas, et al., *Comparison of four methods to evaluate fluid velocities in a continuous slab casting mold*. ISIJ International (Japan), 2001. 41(10): p. 1262-1271.
9. B. Melissari and S.A. Argyropoulos. *Measurement of Magnitude and Direction of Velocity in High-Temperature Liquid Metals. Part I: Mathematical Modeling*. Metallurgical and Materials Transactions B, Vol 36(B), 2005, p. 691-700.
10. B. Melissari and S.A. Argyropoulos. *Measurement of Magnitude and Direction of Velocity in High-Temperature Liquid Metals. Part II: Experimental Measurements*. Metallurgical and Materials Transactions B, Vol 36(B), 2005, p. 639-649.
11. M. Iguchi, et al. *Development of a Karman Vortex Probe for Measuring the Velocity of Molten Metal Flow. Materials Transactions*, JIM, Vol. 35, No. 10(1994), p. 716-721.
12. M. Iguchi, et al. *Development and Calibration of a Karman Vortex Probe for Measurement of Molten-Steel Velocities*. Metallurgical and Materials Transactions B, Vol 30(B), Feb. 1999, p. 53-59.
13. M. Iguchi and Y. Terauchi. *Karman Vortex Probe for the Detection of Molten Metal Surface Flow in Low Velocity Range*. ISIJ International, Vol. 42 (2002), No. 9, p. 939-943.
14. J. Kubota, et al., *Steel Flow Control in Continuous Caster Mold by Traveling Magnetic Field*, NKK Tech. Rev.. 2001. p. 1-9.
15. J. F. Domgin, et al., *Effect of process parameters variation on CC mold hydrodynamics and inclusion behaviour*, Revue de Metallurgie-CIT, No. 10, Oct. 2005, p. 703-710.
16. R. McDavid and B.G. Thomas, *Flow and Thermal Behavior of the Top-Surface Flux/ Powder Layers in Continuous Casting Molds*. Metall. Trans. B, 1996. 27B(4): p. 672-685.
17. K. Cukierski and B.G. Thomas, *Flow Control with Local Electromagnetic Braking in Continuous Casting of Steel Slabs*. Metals and Materials Transactions B, 2007.
18. B. Rietow and B.G. Thomas, *Using Nail Board Experiments to Quantify Surface Velocity in the CC Mold*. AISTech 2008 Steelmaking Conference Proc., (Pittsburgh, PA, May 5-8, 2008).
19. B. Rietow, *Investigations to Improve Product Cleanliness during the Casting of Steel Ingots*. 2007, University of Illinois at Urbana-Champaign: Urbana, IL.

Sensors, Sampling, and Simulation for Process Control
Edited by: Brian G. Thomas, James A. Yurko, and Lifeng Zhang
TMS (The Minerals, Metals & Materials Society), 2011

Measurement of Transient Meniscus Flow in Steel Continuous Casters and Effect of Electromagnetic Braking

Seong-Mook Cho[1], Hyoung-Jun Lee[1], Seon-Hyo Kim[1],
Rajneesh Chaudhary[2], Brian G Thomas[2],
Duck-Hee Lee[3], Yong-Jin Kim[3], Woong-Ryul Choi[3],
Sung-Kwang Kim[3], Hui-Soo Kim[3]

1. Department of Materials Science and Engineering, Pohang University of Science and Technology, Pohang, Kyungbuk, South Korea
2. Department of Mechanical Science and Engineering, University of Illinois at Urbana-Champaign, IL, USA
3. Steelmaking Department, POSCO Gwangyang Works, South Korea

Keywords: steel, continuous casting, level sensor, EMBr, transient flow, flow control

Abstract:

Unstable meniscus flow leads to slab surface defects during continuous casting of steel, due to level fluctuations and vortex formation, which causes entrapment of argon bubbles and mold flux. Applying electromagnetic fields across the liquid steel pool, such as the "double-ruler" or "FC-mold" braking system, has been commercialized to stabilize meniscus flow. Plant measurements were performed using nail boards to quantify meniscus flow in a typical steel slab-casting mold with a slide gate system. The shape of the meniscus level, the surface velocity, and the direction of meniscus flow, are all quantified with time and location by analyzing the shape of the skull of solidified steel that encases each dipped nail. The results reveal interesting insights into time-variations of the flow pattern, which cannot and should not be detected with a standard mold-level sensor used for flow control. Further, the effect of applying the electromagnetic braking field on the flow pattern is revealed.

Introduction

Continuous casting is used to manufacture over 90% of steel in the world [1] so it is essential to understand and optimize this process to minimize defects. Most of the defects affecting slab quality are associated with surface flow in the mold [2]. Surface level variations caused by excessive surface velocity can entrain slag inclusions resulting in both surface and internal defects in the product [3-5]. Thus, it is important to optimize the surface flow velocity to reduce the defects of steel slabs. Many efforts have been made to optimize nozzle geometry [6] and caster operation to achieve an optimal and stable mold flow pattern. Adding electromagnetic force to the steel fluid flow may improve the ability to control fluid

flow in the mold. Commercial systems include static local-, single-ruler-, double ruler-, and moving electromagnetic fields. The FC (Flow Control)-mold braking system consists of two rectangular magnets across each wide face that create a double-humped magnetic field that is roughly constant through the mold thickness. This type of EMBR (Electromagnetic Brake) system aims to stabilize the jet flowing from the SEN ports. Plant measurements of meniscus flow are important to investigate the electromagnetic effects on flow in the mold.

Many researchers have suggested different methods to measure surface velocity. Iguchi et al. developed an electromagnetic non-contact sensor to measure surface velocity of the molten metal flow [7]. Kubota suggested a method that uses an immersed bar to quantify surface velocity by measuring the angle of inclination of the bar by the flow [8]. Nail board measurements suggested by Dauby et al [9] have been commonly used to measure slag thickness and flow direction due to their convenience and efficiency. Rietow and Thomas extended this method to acquire velocity information. They suggested a relation between steel surface velocity and solidified skull height difference measured on a dipped nail [10].

The measurements using nail board are efficient to measure the level and surface velocity at the many positions across the meniscus both with and without electromagnetic braking. Electromagnetic sensor methods may be adversely affected by induced magnetic fields, and the immersed refractory bar is expensive and sometimes difficult to employ due to space restrictions. The nail-board method was successfully used by Cukierski and Thomas to validate their computational fluid flow model with electromagnetic braking effects [11].

This work applies nail board measurements to investigate time variations in surface velocity and level in a commercial steel continuous caster to gain new insight into transient turbulent flow in the mold. Measurements are made at different times and locations, both with and without the effect of a double-ruler electromagnetic braking force.

Measurement and Procedure

Measurements were performed using nail board sets, as shown in Fig. 1. Each wood nail board has two rows of ten 5mm-diameter stainless steel nails, spaced 50mm apart, centered between the SEN (Submerged Entry Nozzle) and the NF (Narrow Face). Thus, each line of nails parallel to the wide face was 55mm from the mold midplane. Figure 2 shows more details about the nail board, and its stable positioning above the oscillating mold using stainless-steel rods for support. Six trials each were performed with (FC-on) and without (FC-off) electromagnetic braking. For each trial, the nail board was dipped into the molten steel pool for 3 seconds, with 1 minute between each trial. A time gap of 30 minutes was given between the FC-on and FC-off trials, to allow plenty of time for the new flow pattern to stabilize.

Table I provides details of the casting conditions, flow control system, nozzle and mold dimensions of the continuous caster, and the FC-current applied during the measurements.

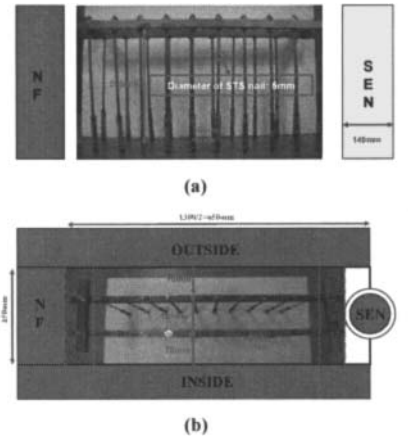

Figure 1. Schematic of nail board set : (a) front view, (b) top view

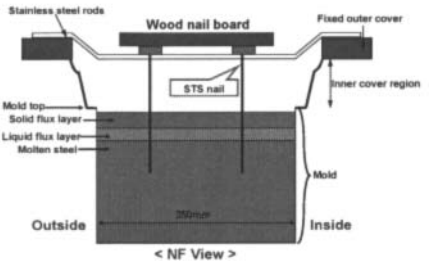

Figure 2. Position of nail board in mold (side view)

Table I. Measurement conditions

Steel flow rate		552.5 LPM
Casting speed		1.70 m/min
Argon gas injection rate		9.2 SLPM (1atm and 273K)
Flow control system		Slide-gate
Nozzle	Bottom type	Well bottom
	Port angle	52 to 35degree step angle at the top, 45 degree angle at the bottom
	Port area	80mm (width) x 85mm (height)
	Bore diameter(inner/outer)	90 (at UTN top) to 80 (at bottom well) mm / 140 mm
Mold	Width	1300 mm
	Thickness	250 mm
EMBr Current	FC off	Upper: 0A, Lower: 0A
	FC on	Upper: 300A, Lower: 300A

After dipping the nail board into the steel liquid pool and removing it, the steel skulls that solidified on the end of each nail were measured and converted to meniscus surface level, flow direction, and surface velocity. Surface level was measured by recording the average distance of each skull from the wood plate. The flow direction is recognized by the orientation of the wave, which is pushed up highest where the steel flow impinges on the nail, as shown in Fig. 3. The difference between the maximum and minimum skull heights

around the perimeter of each nail was converted to meniscus velocity using the relation between flow velocity and skull height given in Fig. 4 from Rietow and Thomas [10]. Both inner and outer skull height differences were measured to give two meniscus velocities for each nail and averaged. This required accounting for the different diameters of the outer skull (always ~10mm) and the inner skull at the nail surface (constant 6mm).

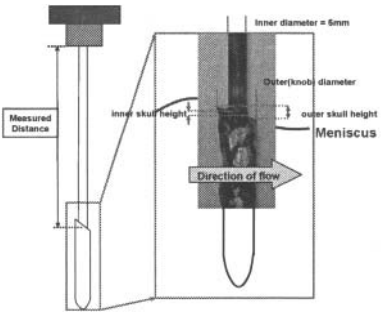

Figure 3. Sample nail with solidified skull

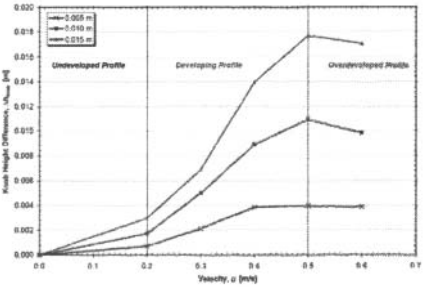

Figure 4. The relation between surface velocity and skull height difference [10]

Results and Discussion

Six meniscus level profiles collected over 5-minute time intervals were averaged for both EMBr (FC-on) and non-EMBr (FC-off) conditions. The asymmetric level profiles between the inside and outer-radius sides of the mold indicate asymmetric flow caused by the asymmetric opening area of the slide-gate flow control, and time variations due to turbulence. Time-averaged meniscus level profiles are shown in Fig. 5. Generally, the surface level is raised higher near the NF, and falls lower near the SEN, which indicates a classic double-roll flow pattern in the mold. The average surface level is flatter with electromagnetic braking on.

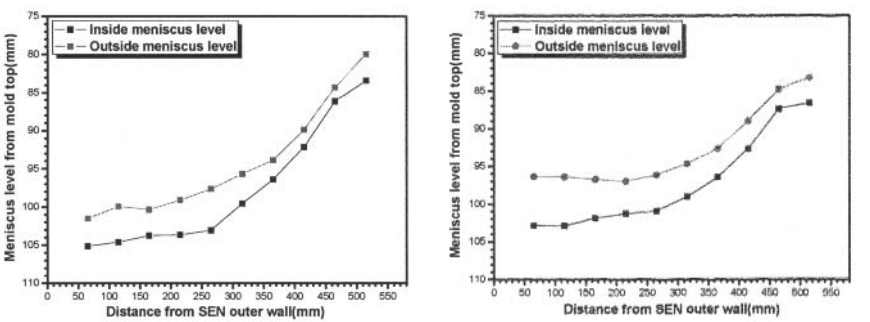

Figure 5. Time-averaged meniscus level : (a) FC off , (b) FC on

The surface level fluctuates with time showing a sloshing pattern. The instantaneous surface level profiles used to create Fig. 5 are shown in Figs. 6 and 7, for conditions of FC-off and FC-on respectively. The changing level profiles show evidence of a least 2 periodic oscillations over the 5-min time interval for FC off and at least 3 with FC on. The target level point for the standard mold-level sensor is shown as a blue cross symbol and is roughly satisfied in all cases. These results reveal that a standard mold-level sensor can be used to control a stable meniscus level when properly positioned at the central "node". Naturally, this sensor cannot detect the level variations which exist in other regions of the mold surface.

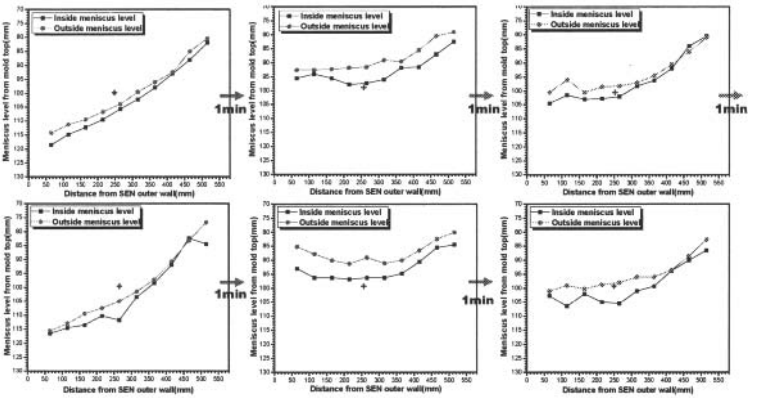

Figure 6. Time progression of level variations measured with FC-off

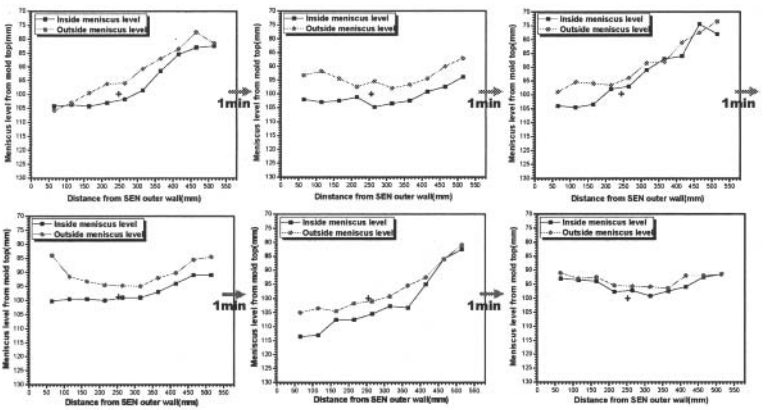

Figure 7. Time progression of level variations measured with FC-on

The standard deviation of the levels measured at each nail over the 5-min. time interval was calculated and plotted in Fig. 8. The smallest time fluctuations (indicating stable nodes) are observed closer to the NF with FC off and at the region midway between SEN and NF with FC on. These characteristic level variations are consistent with the wave behavior in Fig. 9.

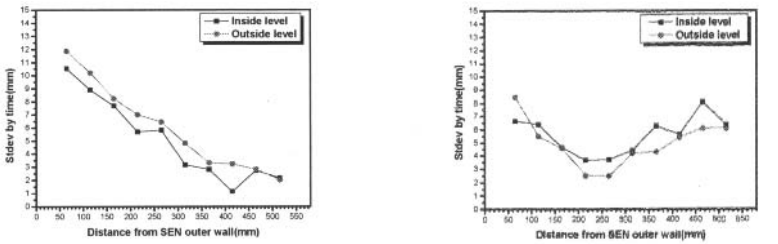

(a) **(b)**

Figure 8. Comparison of time-average variations of measured level: (a) FC off, (b) FC on

(a) (b)

Figure 9. Schematic of level variation mechanism: (a) FC off, (b) FC on

To visualize the transient evolution of the surface flow pattern with time, flow direction and velocity magnitudes are represented by vector arrows at each time in Figs. 10 and 11 for FC-off and FC-on respectively. Both conditions indicate a classic double roll flow pattern, with surface flow towards the SEN. With FC off, surface flow is slightly biased towards the inside radius. Surface flow with FC-on shows more random variations for the chaotic turbulent flow.

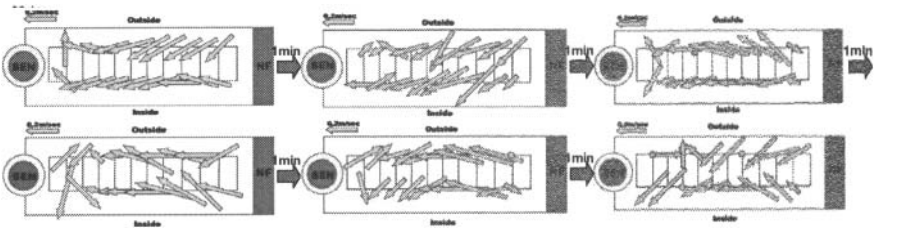

Figure 10. Time-evolution of flow pattern with FC off

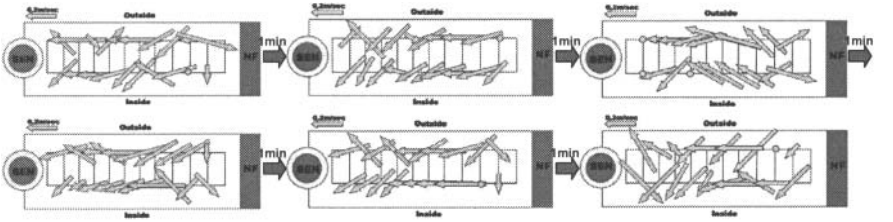

Figure 10. Time-evolution of flow pattern with FC on

Time-averaged surface velocity vectors were calculated by splitting the measured velocity magnitudes into x and y components as shown in Fig. 12 and averaging each velocity component at each nail. Flow vectors were plotted from calculating the flow direction and velocity magnitude from the averaged components.

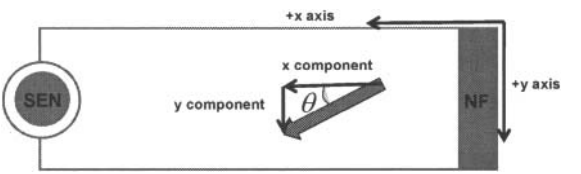

Figure 12. Quantifying average surface velocity vectors

The resulting time-averaged flow patterns are shown in Fig. 13. Meniscus flow shows a slightly biased pattern with FC off and a more symmetric pattern with FC on. With EMBr (FC-on), flow near narrow face goes towards the narrow face. This flow suggests that the electromagnetic field causes a change in flow circulation in the upper corner of mold. Electromagnetic forces also appear to slightly suppress the asymmetric flow towards the inside radius, giving a more symmetrical surface flow pattern. Chaotic flow variations caused by turbulence is more dominant than these effects, however, so more research is needed.

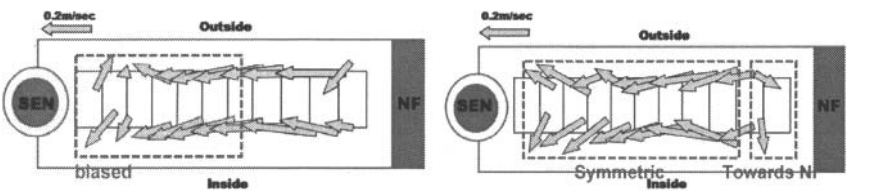

(a) **(b)**

Figure 13. Time-averaged flow pattern : (a) FC off , (b) FC on

Conclusions

- Nail board experiments offer an efficient method to measure meniscus level and velocity.
- Surface meniscus level, velocity and flow pattern appear to be transient with strong periodic sloshing, which is changed by electromagnetic forces.
- A standard mold level sensor can best be used to control meniscus level when positioned near a relatively stable "node" position in the surface level.
- In reality, the surface level in the mold fluctuates greatly with time variations that cannot be detected with standard mold level sensors.
- Electromagnetic forces of a double-ruler (FC-mold) braking system makes the meniscus level profile slightly flatter, with slightly slower and more symmetrical surface velocities.

Acknowledgements

The authors thank POSCO Gwangyang works and POSCO Technical Research Laboratories for supporting measurements. Support from the Continuous Casting Consortium, University of Illinois at Urbana-Champaign, POSCO, South Korea (Grant No. 4.0004977.01) and the National Science Foundation (Grant No. DMI 07-27620) is gratefully acknowledged.

References

1. Wolf, M.M., History of Continuous Casting, in Steelmaking Conf. Proc. 1992, Iron & Steel Society, Warrendale, PA: Toronto, Canada. p. 83-137.
2. Thomas, B.G. and S.P. Vanka: Study of Transient Flow Structures in the Continuous Casting of Steel. in NSF Design & Manufacturing Grantees Conference. 2000. Vancouver, Canada: NSF, Washington, D.C.
3. Li, Baokuan and TSUKIHASHI: ISIJ Int., 2005. 45(1): p. 30-36
4. Seong-Mook Cho, Go-Gi Lee, Seon-Hyo Kim, Rajneesh Chaudhary, Oh-Duck Kwon, Brian G. Thomas: TMS proceeding paper, 2010, 71-77
5. Lance C. Hibbeler and Brian G. Thomas: AISTech Proceedings, 2010
6. Chaudhary. R., G.G. Lee, B.G. Thomas and S.H. Kim, Metall. Mater. Trans. B, Vol.39 (6), 2008, 870-884.
7. M. Iguchi, K. Hanazaki and D. Iguchi: ISIJ Int., 43(6), 2003, p. 982-987
8. J. Kubota, N. Kubo, M. Suzuki, T. Ishii, R. Nishimachi and N. Aramaki: Tetsu-to-Hagane, Vol.86, 2000, 271
9. P.H. Dauby, W.H. Emling, and R. Sobolewski: Ironmaker and Steelmaker, Vol.13, 1986, 28-36
10. Bret Rietow and Brian G. Thomas: AISTech Proceedings, 2008
11. Kevein Cukierski, Brian G. Thomas: Metallurgical and Materials Transaction B, 2008, Vol. 39B, 94-107

Sensors, Sampling, and Simulation for Process Control
Edited by: Brian G. Thomas, James A. Yurko, and Lifeng Zhang
TMS (The Minerals, Metals & Materials Society), 2011

Sensors, Sampling, and Simulation for Process Control

Temperature-Related Process Monitoring Systems

Sensors, Sampling, and Simulation for Process Control
Edited by: Brian G. Thomas, James A. Yurko, and Lifeng Zhang
TMS (The Minerals, Metals & Materials Society), 2011

DYNAMIC RUN-OUT TABLE COOLING SIMULATOR AND TEMPERATURE CONTROLLERS

Nicolas PETHE[1], Kai ZHENG[2], Didier HUIN[3], Christian MORETTO[1], Evgueni POLIAK[2]

[1]ArcelorMittal Global R&D Maizières Process – Maizières-lès-Metz, France
[2]ArcelorMittal Global R&D East Chicago – East Chicago, USA
[3]ArcelorMittal Global R&D Maizières Automotive – Maizières-lès-Metz, France

Keywords: run out table cooling, coiling temperature control, model predictive controller, high carbon steel, CSP mill

Abstract

Intense competition in steel market has led to the development of a number of high strength steel grades which pose new serious challenges in their manufacturing. One of the major challenges lies in the control of strip cooling after hot rolling, which has become a key step in delivering the desired microstructure and mechanical properties of hot rolled products. To meet this need, SimROT, the dynamic run out table cooling simulator has been developed. Based on coupling between physically grounded thermal and metallurgical models, SimROT is able to predict temperature and mechanical property accurately for a wide range of steel chemical compositions and strip dimensions.
Implementation of SimROT also required studies and development of new temperature controllers. The first one is based on model predictions and allows controlling strip temperature on several positions on the table. The second controller based on classic feed-forward / feedback principle has also been developed. In addition, adaptation to compensate for un-modeled dynamics has been designed.
Due to the specificity of the process, the feed-forward / feedback controller has been implemented in the ArcelorMittal USA Riverdale CSP (Continuous Strip Production) with the objective to replace the old commercial system. Production data have shown significant improvement in run-out table cooling performance for the entire product mix.

Introduction

The control of strip temperature on the run-out table after hot rolling is one of the key operations to deliver the required microstructure and mechanical properties of hot rolled steel products. The market driven demand for steels with enhanced mechanical properties has called for designing the new steel grades with higher alloying, as well as to development and implementation of new process technologies that require more sophisticated methods for cooling after hot rolling. The respective run-out table control system has to be highly responsive, flexible and robust to ensure stable production.

Conventional hot strip mills of integrated plants produce hot bands in batches with large number of bars of the same chemical compositions and strip dimensions. One of the main advantages of such process is relatively straightforward coiling temperature control learning, even for complicated run-out table cooling strategies. However, disadvantageous is a significant variability of process parameters that complicates the process control.

By contrast, in the case of CSP and other mini-mill technologies the disturbances in parameters occurring in conventional hot strip mill, including those on run-out table are much

less important. On the other hand, the number of processed bars of the same chemistry is limited to a single heat and even within the heat the variation in strip dimensions is substantial due to specifics of the combined casting-rolling technology. These limitations also present challenges for process control.

To meet market demands the hot rolling process control in general and particularly the run-out table cooling control requires precise modeling and good learning capabilities. At the same time, differences in the nature of processes between conventional hot strip mills and CSP technologies call for different solutions in process control.

Modeling of Strip Cooling on Run-Out Table

The main tool to obtain the desired coiling temperature of a hot rolled strip is the proper utilization of the available cooling system and first of all – the correct initialization of the cooling devices in terms of timing order and water flow. The initial configuration and sequence (setup) should be assigned prior to the beginning of cooling. To properly set up the run-out table cooling a rigorous modeling of all phenomena occurring during strip cooling and especially that of microstructural changes is necessary; the model based calculation have to be performed with the highest possible accuracy.

Metallurgical Modeling

Metallurgical model employed in this work aims at describing decomposition of austenite phase into polygonal ferrite and then further into pearlite with account for steel chemical composition, austenite grain size out of the finishing rolling mill, as well as for the run-out table cooling path. This metallurgical model is grounded on the assumption of local equilibrium without partitioning of substitutional atoms. The nucleation of ferrite is assumed to occur at austenite grain edges and faces; the driving force for nucleation and the carbon concentration at the austenite/ferrite interface are computed with account for concentrations of alloying additions (Si, Mo, Cr, Ni, Cu, Al). Mixed mode of growth of nuclei is adopted where the instantaneous interphase boundary velocity during the austenite/ferrite transformation is calculated as the result of diffusion in austenite of carbon rejected by the transformation and mobility of iron atoms at the austenite/ferrite interface. With the increase of ferrite fraction, the carbon concentration in the remaining portions of austenite increases until the critical concentration is reached at which pearlite transformation begins. In the model, the onset of pearlite transformation is described using Hultgren formalism (Figure 1).

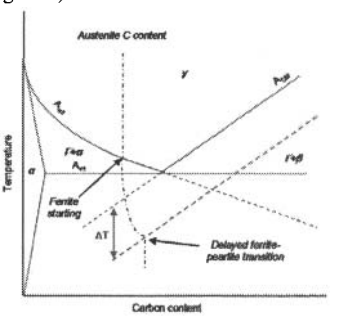

Fig 1 - Successive phase transformations during C-Mn steel cooling.

The model has been validated by numerous dilatometers tests covering wide range of C-Mn steel compositions.

Thermal Modeling

In order to properly compute the strip thermal path, heat transfer equation has to be solved with account for various phenomena occurring at the strip surfaces. While traveling on the run-out table a strip can be cooled by:

i. air;
ii. water coming from the headers;
iii. water remaining on the strip after it passes the header.

Air cooling. Equations describing cooling of a plate by radiation and convection have been applied. The variation of air convective cooling regime is also taken into account.

Water cooling under header. For strip sample under a water header, the following type of equation is applied to calculate the heat flux φextracted by water:

$$\varphi = f(T_w, v, d, l, T_s)$$

i.e., the heat flux is given as a function of the cooling water temperature T_w, strip speed v, water flow rate d, water flow coverage length l and the strip surface temperature T_s.

Remaining Water. Observations of cooling process on run out table show that after the strip has passed an activated header, some water is carried over and still stays on strip top surface until it is blown off by cross sprays downstream. The heat flux extracted after an activated header has been passed is modeled by the maximum value between the heat flux under air cooling and the heat flux extracted by last header multiplied by a factor describing exponential decrease with distance from this last header.

The boundary conditions described above are then used to solve heat transfer equation. The solution provides a single strip sample model for steady-state process conditions.

Extension to Dynamic Conditions

During strip cooling on the run-out table various parameters are changing as the strip is being hot rolled. In particular, the speed of strip exiting the finishing mill can vary which causes variation in strip speed on the run-out table; the cooling system has to be adjusted accordingly to allow attainment of the aim coiling temperature and the aim microstructure. These and other in-bar variations require a dynamic model to accurately predict the strip temperature.

In this work, the dynamic control is realized through fine discretization of the cooling time: at each sampling time, all strip elements that are on the table are assumed to be in the steady state. Since the sampling time is very short the error linked to the steady state assumption is very small. This way the state (e.g. temperature and volume fractions of phases) of each strip element is constantly updated. The principle summarized in the flowchart in Figure 2 is repeated until the end of strip cooling.

Results

The model has been validated by calculations utilizing massive industrial database. Figure 3 illustrates the SimROT performance by comparing predicted and measured coiling temperatures for various steel grades produced at a conventional HSM. The dashed lines in Figure 3 represent ±25°C prediction error which is typical for HSM run-out table cooling operation targets. It can

be seen that the majority of SimROT temperature predictions is within 25°C of the measured values. An average of 7.5°C and a standard deviation of 10°C in prediction error are achieved by the model even without adaptation.

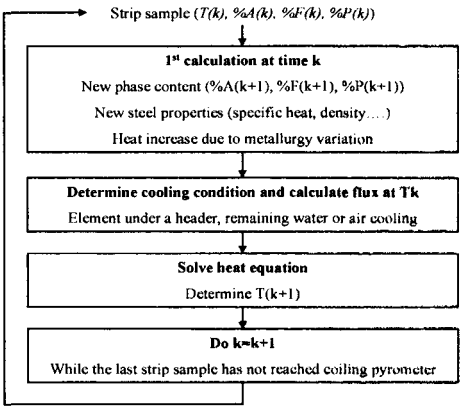

Figure 2. Calculation flowchart applied at each time step for each strip sample; $\%A(k)$, $\%F(k)$ and $\%P(k)$ are the fractions of austenite, ferrite and pearlite, respectively, at time k for the single given strip sample.

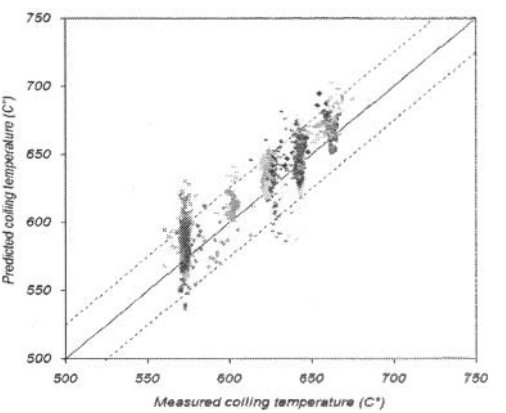

Figure 3. Predicted *versus* measured coiling temperatures without adaptation.

Figure 4 gives an example of good coiling temperature prediction along the entire coil length.

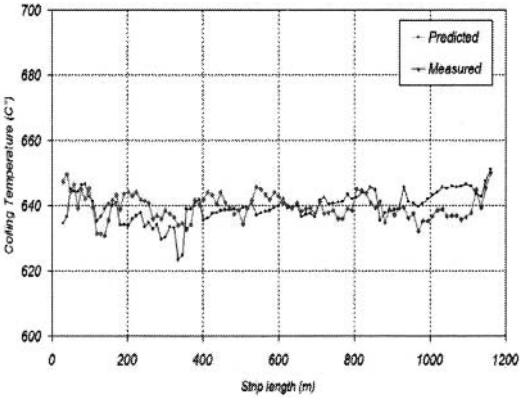

Figure 4. Predicted *versus* measured coiling temperature profile

Automatic Model Learning Function

A number of factors not taken into account by SimROT model still impact the accuracy of coiling temperature predictions, e.g., temperatures of run-out table rollers, variation of laminar water flow rate, etc. Because of that, in order to provide the most accurate prediction, the "long term/short term" based adaptation function has been designed.

As the unaccounted disturbances directly impact the extracted heat flux, it has been decided to multiply the heat flux by gain:

$$\varphi = k_a f(T_w, v, d, l, T_s),$$

where k_a is computed by the adaptation function:

$$k_a = f(G, S, Z, T_a)$$

where G is the strip grade, S the cooling strategy, Z the thickness and T_a is the aim coiling temperature. Once the strip is cooled, the process data are extracted and the computations using SimROT are performed. The adaptation function then calculates the new gain to minimize the difference between the predicted and measured values.

On site observations have indicated that, due to different process conditions, different amounts of water are required for the head end and for the body portions of the strip. Therefore, the adaptation factor computed for the strip body is not accurate for the head end and can induce error in setup calculation. To address this issue, the separate head-end adaptation coefficient is created that permits compensation for disturbances occurring at head end. At ArcelorMittal USA Riverdale this adaptation principle has been successfully applied to pearlitic grades for which erroneous adaptation can lead to substantial coiling temperature drops that can further result in coil reject.

Temperature Controller Design

ArcelorMittal USA produces hot rolled strips on hot strip mills of two types: conventional mills and CSP.

Model Predictive Controller

One of the major sources of disturbances occurring on the run-out table of conventional hot strip mill is the strip acceleration. The associated in-bar variation in strip speed, required to attain the aim rolling finishing temperature, generates significant variation in the number of headers and water flows and introduces delays in all of commands. To overcome this complication, the predictive controller referred to below as MPC determines the projected (would be future) strip temperature by considering:

- instantaneous coiling temperature;
- current run-out table configuration (opened/closed headers);
- current disturbances (e.g. run-out table entry speed variation);
- command delays.

Since it becomes possible to estimate the projected temperatures, the projected optimal cooling configuration that needs to be applied on run-out table to attain the aimed value can now readily be derived as well.

The determination of this optimal variation of cooling configuration for temperature control in multiple positions is done by minimizing the quadratic criterion:

$$\Delta\hat{U}_{opt} = \min_{\Delta U}\left(\alpha\sum_{j=1}^{P}\left(T_A(j)-\hat{T}(j)\right)^2 + \beta\sum_{i=1}^{N}\Delta U(i)^2\right),$$

where P is the number of control positions, N is the number of controlled cooling sections and T_A is the matrix of aim temperatures in the controlled positions; α and β are weighting coefficients allowing to fit the controller behavior: if $\alpha >> \beta$ then high command variation can be obtained leading to disturbed control. However, if $\alpha << \beta$, controller will determine a smoother command even if the error between target and prediction is not optimal.

Figure 5 illustrates the offline performances of programmed MPC to reach aim coiling temperature using disturbance profiles obtained from the mill data.

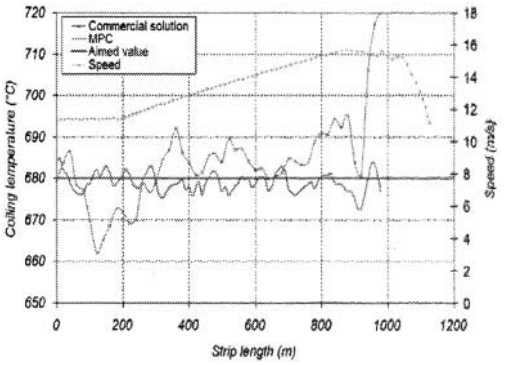

Figure 5. Comparison between programmed MPC and commercial controller installed at conventional hot strip mill.

It is noticeable that that the predicted controller allows for obtaining much more stable coiling temperature (within a tolerance of ± 5°C around aim value) than the commercial solution.

Feed-forward / Feedback Controller

Contrary to a classical hot strip mill where speed disturbance is typically a continuous ramp, the speed disturbances in a CSP is a downward step change. This is because the CSP tunnel furnace (or coil box) effectively prevents heat losses prior to the finishing rolling mill entry as opposed to delay table of a conventional mill. Advanced controller such as MPC structure is thus not required in case of CSP and a model-based feed forward / feedback control structure can be adopted.

The feed forward part compensates for strip speed variation and the feed back part aims at rejecting the remaining disturbances and regulating the coiling temperature. The gain value used in each part is obtained from model sensitivity calculation. This model-based structure is far more advantageous than the classical fixed parameter PID controller, which usually can only be tuned for a small range of products. Although its gain-scheduled counterpart may cover a wider product range, it would require exhaustive tuning.

The schematic diagram of the controller is shown in Figure 6 where T_{SP} is the coiling temperature setpoint, which, in general, is a function of the length $L(t)$ of the strip after the coiling pyrometer. K_{TV} is the sensitivity of strip temperature to speed change and K_{WT} is the sensitivity of cooling water to strip temperature change. K_{HW} is the coefficient converting the amount of water to the number of headers to be activated.

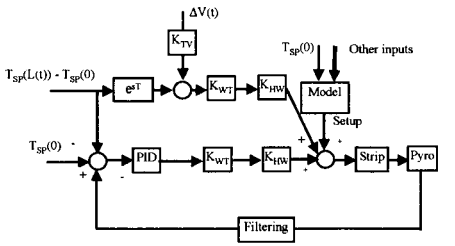

Figure 6. Schematic diagram of the feed-forward / feedback control system.

As seen from Figure 6, the control system consists of three parts: the setup model based on strip head end temperature setpoint $T_{SP}(0)$ and other model inputs; the feed forward branch reacting to strip speed changes; and the feedback branch compensating for coiling temperature tracking error.

Riverdale CSP Coiling Temperature Controller Revamp

First industrial implementation of SimROT with controller has been carried out at ArcelorMittal USA Riverdale CSP plant to replace its old commercial control system. The latter was not able to satisfactory control the cooling of most of the high carbon and high alloy steel grades. The implemented controller structure is the feed-forward / feedback controller.

During commissioning, extensive trials were run to test the setup and dynamic control for entire product mix. The results show that SimROT provides equally good performance as the existing commercial control system for all low carbon grades and significantly outperforms the commercial system for all high carbon high alloy grades.

Figure 7 exemplifies the comparison of coiling temperature performance between the old commercial system and SimROT for steel with 0.6% C and high Mn, Si and Cr contents. Clearly, SimROT provides significantly better and more stable temperature control.

Performance has also been compared for a number of high carbon grades (C > 0.5%) to demonstrate that the new control system allows for obtaining significantly higher percentage of strip length within the coiling temperature tolerance, as illustrated in Figure 8.

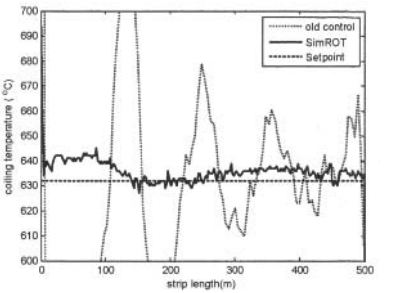

Figure 7. Improvement of coiling temperature control

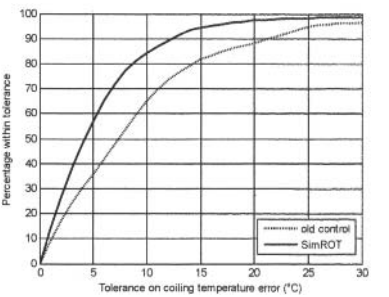

Figure 8. Percentage of coil length within coiling temperature tolerances for high carbon steel grades

Conclusions

Advanced dynamic run out table simulator (SimROT) has been developed. Based on advanced metallurgical and thermal models, SimROT is able to correctly predict the temperature of a strip under dynamic conditions. The model employed has been used as a reference to study and develop two types of controllers, each of the controllers being dedicated to a specific rolling process (either CSP mill or conventional mill). The predictive controller allows obtaining promising offline results. Future online utilization at conventional mills is under consideration.

The feed-forward / feedback controller has been successfully implemented at ArcelorMittal Riverdale. Whereas the existing commercial solution fails to provide the required cooling control and attainment of the aim coiling temperature for a number of steel grades, SimROT solution allows for obtaining much more stable coiling temperature performance for these grades.

Sensors, Sampling, and Simulation for Process Control
Edited by: Brian G. Thomas, James A. Yurko, and Lifeng Zhang
TMS (The Minerals, Metals & Materials Society), 2011

IMPLEMENTATION OF A REAL-TIME MODEL-BASED SPRAY-COOLING CONTROL SYSTEM FOR STEEL CONTINUOUS CASTING

Bryan Petrus[1], Kai Zheng[1], Xiaoxu Zhou[1],
Brian G. Thomas[1], Joseph Bentsman[1], Ron O'Malley[2]

[1]University of Illinois, Mechanical Science and Engineering;
1206 West Green Street; Urbana, IL 61801, USA
[2]Nucor Steel Decatur
4301 Iversion Boulevard; Trinity, AL, 35673, USA

Keywords: Heat Transfer, Solidification Model, Thin Slabs, Secondary Cooling, Real-Time Simulation, Proportional-Integral Control

Abstract

In continuous casting of steel, maintaining the shell surface temperature profile under transient conditions is important to minimize surface cracks. For this purpose a spray-cooling control system, CONONLINE, has been implemented on a commercial caster. The system includes a software sensor of shell surface temperature, control algorithm, and a monitor allowing operator input and displaying the predicted shell surface temperature profiles and other important operating data. Simulation results demonstrate that the new control system achieves better temperature control performance than conventional systems during a change in casting speed. Plant trials have shown that the performance can be improved by modifying the classical anti-windup method, and modifying the control algorithm during unusual casting conditions.

Introduction

Since its development in the mid 1980's, an increasing amount of the steel produced in the world has been made through thin-slab continuous casting. Thin-slab casting, defined here as slabs less than 100 mm thick, has faster casting speeds and is usually based on scrap. In this process, molten steel is poured into a water-cooled mold at the top of the caster, where a solid shell is formed around the liquid core. This partially solidified "strand" is then driven through the "secondary cooling" region, which has a series of rolls alternating with water or water-mist sprays that contain and cool the strand until it is fully solidified into slabs. If the steel is not fully solidified when it leaves this containment region, the ferrostatic pressure causes the strand to bulge. This costly and possibly dangerous event is called a "whale."

Robust and accurate control of secondary cooling is vital to the production of high quality slabs[1]. Defects such as transverse surface cracks form unless the temperature profile down the caster is optimized to avoid excessive stress and strain, such as caused by unbending, during temperature regions of low ductility[2]. This is especially important in thin-slab casters, because high casting speed and a tight machine radius exacerbate cracking problems. Thus, there is great incentive to implement control systems to optimize spray cooling to maintain desired temperature profiles.

However, conventional feedback control systems based on hardware sensors have not been successful because emissivity variations from intermittent surface scale and the harsh, steam-

filled environment make optical pyrometers unreliable. Most casters control spray-water flow rates using a simple look-up table based on casting speed, but this produces undesirable temperature transients during process changes. Recent dynamic control systems have been developed based on real-time computational models.

Early systems[3-6] updated slowly or had relatively crude models, due to limited computing speed. More recently, significant achievements have been made in open-loop model-based control systems for conventional thick-slab casters[7-9], although none of the models are robust enough for general use, and none has been applied to a thin-slab caster.

A new online control system was briefly introduced in [10, 11] and is described in more detail in [12]. This system, called CONONLINE, has been implemented at the Nucor Steel casters in Decatur, Alabama. The system features a real-time solidification and heat-transfer model, CONSENSOR, of a longitudinal slice through the strand as a "software sensor" of surface temperature. A control algorithm, CONCONTROLLER, featuring a bank of proportional-integral (PI) controllers, uses this prediction to maintain the shell surface temperature profile at desired setpoints in each of the spray cooling zones through changes in casting conditions. Finally, a monitor interface provides real-time visualization of the shell surface temperature and thickness predictions, along with other information important to the operator, as well as to allow operator input through the choice of temperature setpoints.

Simulation results, described here, demonstrate that significantly better shell surface temperature control is achieved. Also, the useful lessons learned during implementation of this system at Nucor Decatur are discussed.

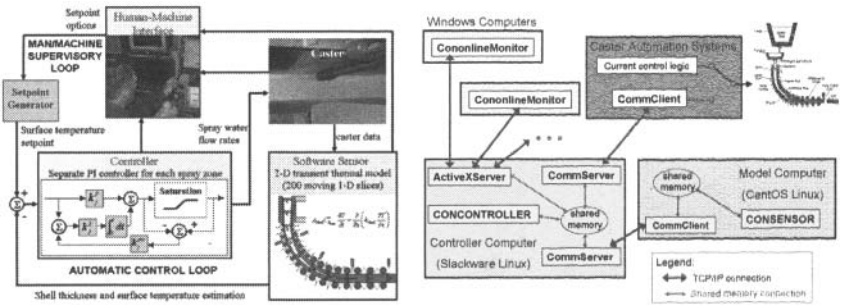

a) general overview b) system overview

Figure 1. Schematics of CONONLINE system

Model and Control System Design

An overview of the real-time control system is pictured in Fig. 1a. It features a "software sensor" CONSENSOR, which estimates strand temperature in real time from available casting conditions for CONTROLLER, which evaluates the error compared to operator-chosen setpoints and sends spray water flow rate "commands" to both the plant and CONSENSOR. Fig. 1b shows the computing setup, as implemented at Nucor Decatur. The software sensor and controller run on separate servers for stability and speed reasons. The monitor program runs on Windows PCs

to display the programs' outputs. The programs communicate using shared memory on each server and TCP/IP connections between the computers. Further details are given in [10] and [12].

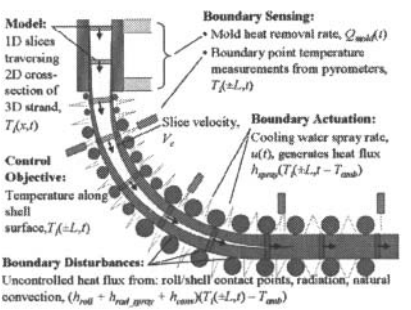

Figure 2. CONSENSOR slice diagram

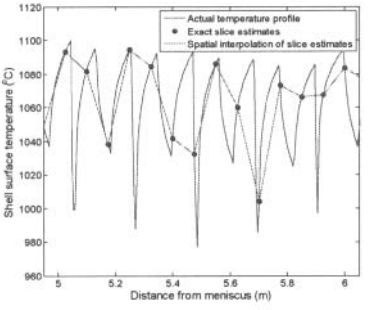

Figure 3. Slice interpolation

Software Sensor – CONSENSOR

At typical casting speeds, the continuously-cast strand has a high Peclet number, rendering axial heat conduction negligible. Hence, the temperature and solidification of the steel at any point in the strand can be predicted by modeling a "slice" of the material as it moves down through the caster at the casting speed. The temperature in each slice is described by the 1-D transient heat conduction equation[13]:

$$\rho_{steel} Cp^{*}_{steel} \frac{\partial T(x,t)}{\partial t} = k_{steel} \frac{\partial^2 T(x,t)}{\partial x^2} + \frac{dk_{steel}}{dT}\left(\frac{\partial T(x,t)}{\partial x}\right)^2 \qquad (1)$$

where k_{steel} is thermal conductivity, ρ_{steel} is density, and Cp^{*}_{steel} is the effective specific heat of the steel, which includes the latent heat based on liquid fraction via a modified Clyne-Kurz microsegregation model[13, 14]. The spatial dimension x extends through the entire thickness of the strand, perpendicular to the casting direction to allow nonsymmetrical heat extraction. The initial condition is the pour temperature, measured by a thermocouple in the tundish. Heat flux boundary conditions are applied based on plant measurements of cooling water flow rates and temperature rise for the mold, and heat transfer coefficients according to spray water flow rates for the secondary cooling region.

Focusing on the centerline of the strand, these model equations describing temperature in the one-dimensional slices can be computed quickly using an explicit finite-difference scheme[13]. By simulating and interpolating between multiple slices, as illustrated in Fig. 2, the temperature of the strand is estimated in real-time. More detail on this model is provided elsewhere [12, 13].

An offline computational model with these features was previously developed as the program CON1D. The accuracy of this model has been demonstrated through comparison with analytical solutions of plate solidification and plant measurements[13, 15]. Because of its accuracy, CON1D has been used in many previous studies to predict successfully the effects of casting conditions on solidification and to develop practices to prevent problems such as whale formation[16].

The software sensor, CONSENSOR, uses CON1D as a subroutine to simulate individual slices, starting each slice simulation at the meniscus at different times to achieve a fixed spacing between the slices. This is illustrated in Fig. 2 using $N = 10$ slices for simplicity. To assemble the complete temperature profile requires careful interpolation of the slice results. As illustrated in Fig. 3, the span between slices can pass over the temperature dips and peaks caused by the roll and spray spacing, resulting in errors of 100 °C or more. This problem is overcome by "delay interpolation," estimating the temperature at each point in the caster at time t from the latest temperature available from the CON1D slice histories. This process is described in detail in [12].

The model was calibrated to match the average surface temperatures measured under steady-state conditions using five pyrometers installed in the south caster at Nucor Steel Decatur in January, 2006. An example comparison of the measurements and temperature predictions is shown in Fig 4. The predicted temperatures generally exceed those measured by the pyrometers, except for the last pyrometer, which is outside the spray chamber and expected to be most reliable. The difference is believed to be due to the pyrometers reading lower than the real temperature, owing to steam-layer absorption and surface emissivity problems. Further work is needed to improve the accuracy of the pyrometer measurements, the spray heat-transfer coefficients, the spray-zone lengths, and the predicted variations in surface heat transfer and temperature, in order to improve the agreement.

The shell thickness prediction has also been calibrated to match recorded whale events at the Nucor Decatur casters, as well as high casting speed conditions where containment was not lost.

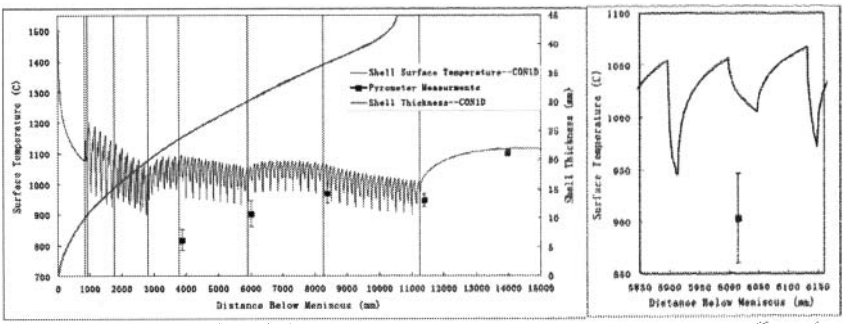

a) along entire domain b) close-up near one roll spacing

Figure 4. Comparison of CON1D surface temperature predictions and measurements

Control Algorithm – CONCONTROLLER

In a continuous caster, rows of individual spray nozzles are grouped into "spray zones" based on how they are connected via headers and pipes to control valves. All rows of nozzles in a zone have the same spray-water flow rate and spray density profile. The spray rate for zone j is denoted below as u_j. CONCONTROLLER controls each zone with an independent PI controller, tuned separately to meet the desired control performance. CONSENSOR, as described above, only predicts the temperature along the center of the strand. Hence, CONCONTROLLER only applies PI control to zones covering the center. The spray flow rates for other zones across the strand width are prescribed as a function of slab width using separate logic.

At each time step t, the shell surface temperature profile estimate, $\hat{T}(z,t)$ where z denotes the casting direction, is obtained by CONSENSOR and the desired temperature profile $T^s(z,t)$, or setpoint, is determined as discussed below. The difference between the two is averaged over each zone j, giving the zone errors $\Delta T_j(t)$. Then the spray-water flow rate command for the next time interval is calculated via the classic PI control law:

$$u_j(t+\Delta t) = u_j^P(t+\Delta t) + u_j^I(t+\Delta t), \quad j = 1,\ldots,n_{zone}, \tag{2}$$

where the proportional and integral components are calculated as:

$$u_j^P(t+\Delta t) = k_j^P \Delta T_j(t), \quad j = 1,\ldots,n_{zone}, \tag{3}$$

$$u_j^I(t+\Delta t) = u_j^I(t) + k_j^I \Delta T_j(t)\Delta t + \frac{1}{N_{aw}} \sum_{n=0}^{N_{aw}-1} \left[u_j^{measured}(t-n\Delta t) - u_j(t-n\Delta t) \right], j = 1,\ldots,n_{zone}. \tag{4}$$

The first part of (4) is a discrete-time integral over the time interval Δt. The summation term is an anti-windup[17] adjustment, adopted to avoid integrator windup when the control flow-rate commands are outside the limits on the possible flow rates through the valves. This tends to cause controller instability, known as "windup". This problem is prevented by subtracting the difference between the measured spray rates and the controller-suggested spray rates from the integral in Eq. (4). This difference is averaged over N_{aw} time steps to filter out oscillations caused by chattering in the valves, as discussed below.

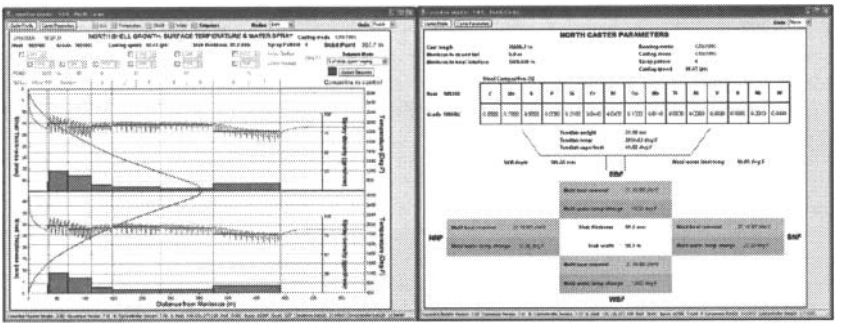

a) Profile screen b) Parameter screen

Figure 5. CONONLINE Monitor interface screens

Visualization – CONONLINE Monitor

The monitor, as illustrated in Fig. 1, is an important part of the system that provides real-time display of many variables, setpoints, and predictions, permitting operators and plant metallurgists to monitor the caster and the control system performance, and to make adjustments as needed. Fig. 5 shows typical screen shots of the two interface screens that the monitor can display.

Fig. 5a shows the "profile screen," which serves two purposes. The first purpose is to relay key simulation outputs to the operators and plant engineers. It is also an interface for operator input to the controller, via controls for changing the temperature setpoint in any zone manually. Fig. 5b shows the "parameter screen," which displays the most important caster measurements input to the model. This allows for easy checking of the casting conditions, and program statuses.

Setpoint Generation

Choosing a good setpoint profile $T^*(z,t)$ is as challenging and important as the control task itself. Traditional spray practice is based on "spray-table control." Spray flow rates for each zone that produce good quality steel in a specific caster are determined from plant trial and error and previous experience. Higher casting speeds require higher water flow rates to maintain the same cooling conditions, so a different spray profile is tabulated for several casting speeds in a database spanning the range of normal operation. This array of spray rates, or "spray pattern," is organized by zone and casting speed and may be different for differing grades of steel. During casting, spray setpoints are interpolated from the database, called a "spray table," for the chosen pattern and casting speed. This method does not accommodate transient behavior very well.

To take advantage of this available knowledge base, the spray table was converted to a table of surface temperature profile setpoints. For each pattern, CON1D was run at a typical casting speed (3.5 m/min for Nucor Decatur) using the water spray rates in the spray table. Therefore, each pattern has a corresponding temperature profile as the setpoint for the PI controller, $T^*(z,t)$.

The automatic setpoints can also be over-ridden in any zone(s) using the monitor interface.

Simulation Results

The model and controller programs can be also used to simulate the caster response to changing casting conditions, and the monitor can be used to view the results graphically in real-time. For example, Fig. 6a compares the zone-average surface-temperature histories extracted from the software sensor predictions in the fifth (next to last) spray zones below the meniscus during a sudden drop in casting speed from 3.0 m/min to 2.5 m/min at $t \approx 30$s. Fig. 6b shows the respective spray rates assigned to each zone using 3 different control methods. Additional results from these simulations are available in [12].

If no change is made to the spray-water flow rates, the surface temperature eventually drops. With a controller that changes spray water flow rates in proportion to casting speed, during the sudden speed drop, all of the spray rates drop immediately. However, with the recently higher casting speed, the upstream steel is hotter than expected, so the temperature overshoots the steady-state value. The steady-state temperatures are higher at the lower speed because the spray rates assigned in the spray table are predicted by the model to drop even more than the drop in speed requires. Finally, with PI control, the surface temperature is kept remarkably constant through the speed change. The spray flow rates decrease more gradually after the casting speed change. Furthermore, the flow rates lower in the caster drop more gradually than those nearer to mold exit (not shown). Steady state is not reached until steel starting at the meniscus at the transition time finally reaches the given point in the caster, after being cast entirely under the new conditions.

This case study demonstrates that all of the controllers perform as expected. The PI controller produces the best response for steel quality, as detrimental surface temperature fluctuations are lessened. The quality of the control system now depends on the accuracy of the software sensor

calibration to match the real caster. Work is proceeding to measure heat transfer, both with fundamental laboratory experiments, and with optical pyrometers and other experiments in the commercial steel thin-slab caster.

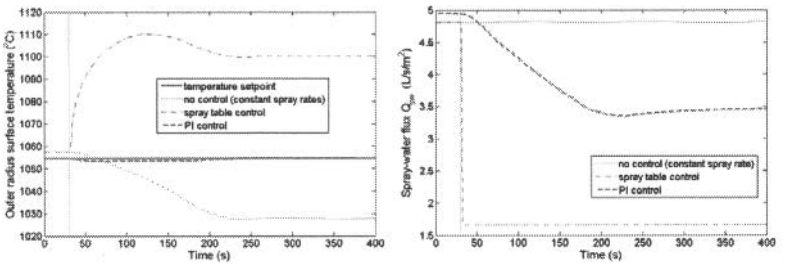

a) Zone-average outer radius surface temperature b) Spray water flow rates

Figure 6. Results of offline simulation of slowdown, comparing control methodologies

Implementation at Nucor Steel Decatur

The real-time CONSENSOR model has been running on servers at the Nucor Decatur sheet steel mill since 2006. Since 2008, dedicated workstations have been set up in the caster pulpit to run monitors for each of the two casters, which are called North and South caster at the mill. The system was run in "shadow mode," in which temperature and shell predictions are supplied to operators through the monitor, but the system does not control the water sprays. At first, the system was only installed on the North Caster. During this time, a whale event occurred on the South caster, while on the North caster operators used the visual prediction of the liquid core to reduce casting speed as needed to prevent loss of containment. The operators immediately requested the system also be installed on the South caster.

Several successful tests with CONONLINE in control of the water sprays have been performed, up to several hours in length. In addition to model calibration, changes have been made to the control algorithm to resolve issues noticed during the tests. In particular, the controller gains were made less aggressive when it was found that the spray valve system had a longer time constant than was anticipated. Also, the valves had some chattering that lead to sinusoidal noise in the spray rates. The classical anti-windup method, equivalent to Eq. (4) with $N_{aw} = 1$, transmitted these oscillations to the control signal. To prevent this, the oscillations were filtered out by averaging the anti-windup signal over time. The controller also sometimes called for sharp changes in spray rate in the first few spray zones, due to significant variations in strand surface temperature at mold exit caused by changes in mold heat flux, casting speed, and steel grade. To avoid this problem, the temperature setpoint for the first spray zone is now half-way between the surface temperature at mold exit and the setpoint for the second zone.

Finally, it has been found that additional logic is needed to deal with unusual casting conditions. In particular, Nucor Decatur has a breakout prevention system that sometimes slows down the casting speed to 0.25 m/min when thermocouple readings in the mold indicate a thin spot. However, since CONSENSOR uses average mold heat removal, it does not predict the highly localized thin spot. As discussed in the previous section, PI control would lower the spray rates during sudden slowdowns, which could cause the thin spot to break out. Instead, during these so-called "sticker slowdowns," CONCONTROLLER has been adjusted to override PI

control in the first three spray zones with default minimum sprays based on the spray table. Similar efforts are continuing to help with casting startups and tailouts. Once resolved, the plan is for CONONLINE to take over permanent control of the casters.

Acknowledgments

Matthew Smith, Rob Oldroyd, Terri Morris, Kris Sledge and the caster operation crews at Nucor Steel Decatur are gratefully acknowledged for their unwavering support and help with this work. We are grateful for work on CON1D calibration by former UIUC students Sami Vahpalahti and Huan Li. This work is supported by National Science Foundation Grants DMI 05-00453 and CMMI-0900138, and the Continuous Casting Consortium at UIUC.

References

1. J.K. Brimacombe, P.K. Agarwal, S. Hibbins, B. Prabhaker and L.A. Baptista: "Spray Cooling in Continuous Casting," in *Continuous Casting*, vol. 2, J. K. Brimacombe, ed., 1984, pp. 105-123.
2. M. M. Wolf: *Continuous Casting: Initial Solidification and Strand Surface Quality of Peritectic Steels*, vol. 9, Iron and Steel Society, Warrendale, PA, 1997, pp. 1-111.
3. K. Okuno, H. Naruwa, T. Kuribayashi and T. Takamoto: *Iron Steel Eng.*, 1987, vol. 12 (4), pp. 34-38.
4. K.-H. Spitzer, K. Harste, B. Weber, P. Monheim and K. Schwerdtfeger: *Iron Steel Inst. Jpn*, 1992, vol. 32 (7), pp. 848-856.
5. S. Barozzi, P. Fontana and P. Pragliola: *Iron Steel Eng*, 1986, vol. 11, pp. 21-26.
6. B. Lally, L. Biegler and H. Henein: *Met. Trans. B*, 1990, vol. 21B, pp. 761-770.
7. K. Dittenberger, K. Morwald, G. Hohenbichler and U. Feischl: "DYNACS Cooling Model - Features and Operational Results," *Proc. VAI 7th International Continuous Casting Conference*, (Linz, Austria), 1996, pp. 44.1-44.6.
8. R.A. Hardin, K. Liu, A. Kapoor and C. Beckermann: "A Transient Simulation and Dynamic Spray Cooling Control Model for Continuous Steel Casting," *Metal. & Material Trans.*, 2003, vol. 34B (June), pp. 297-306.
9. Seppo Louhenkilpi, Jukka Laine, Tuomo Raisanen and Tenho Hatonen: "On-Line Simulation of Heat Transfer in Continuous Casting of Steel," in *2nd Int. Conference on New Developments in Metallurgical Process Technology*, (Riva del Garda, Italy, 19-21 Sept, 2004), 2004.
10. K. Zheng, B. Petrus, B.G. Thomas and J. Bentsman: "Design and Implementation of a Real-time Spray Cooling Control System for Continuous Casting of Thin Steel Slabs,," in *AISTech 2007, Steelmaking Conference Proceedings*, , (Indianapolis, IN), 2007.
11. B.G. Thomas, J. Bentsman, B. Petrus, H. Li, A.H. Castillejos and F.A. Acosta: "GOALI: Online Dynamic Control of Cooling in Continuous Casting of Thin Steel Slabs," in *Proceedings of 2009 NSF CMMI Engineering Research and Innovation Conference*,Honolulu, Hawaii, June 22-25, 2009., 2009, p. 16p.
12. Bryan Petrus, Kai Zheng, Xiaoxu Zhou, Brian G. Thomas and Joseph Bentsman: "Real-Time Model-Based Spray-Cooling Control System for Steel Continuous Casting," *Metals and Materials Transactions B*, to appear.
13. Y. Meng and B.G. Thomas: "Heat Transfer and Solidification Model of Continuous Slab Casting: CON1D," *Metal. & Material Trans.*, 2003, vol. 34B (5), pp. 685-705.
14. Y.M. Won and B.G. Thomas: "Simple Model of Microsegregation during Solidification of Steels," *Metallurgical and Materials Transactions A (USA)*, 2001, vol. 32A (7), pp. 1755-1767, 179.
15. B. Santillana, L.C. Hibbeler, B.G. Thomas, A. Hamoen, A. Kamperman, W. van der Knoop: "Investigating Heat Transfer In Funnel-Mould Casting With CON1D: Effect of Plate Thickness," *ISIJ Internat.*, 2008, vol. 48 (10), pp. 1380-1388.
16. Joydeep Sengupta, Manh-Kha Trinh, David Currey and Brian G. Thomas: "Utilization of CON1D at ArcelorMittal Dofasco's No. 2 Continuous Caster for Crater End Determination," *Proc. AISTech 2009 Steelmaking Conference Proc.*, (St. Louis, MO, May 4-7, 2009), 2009, vol. 1.
17. C. Edwards and I. Postlethwaitex: "Anti-windup and Bumpless Transfer Schemes," *Proc. UKACC International Conference on CONTROL*, 1996, pp. 394-399.

Sensors, Sampling, and Simulation for Process Control
Edited by: Brian G. Thomas, James A. Yurko, and Lifeng Zhang
TMS (The Minerals, Metals & Materials Society), 2011

MEASUREMENT OF THE SOLIDIFICATION FRONT INSIDE A METALLURGICAL REACTOR

Clément Bertrand[1], Marc-André Marois[1], Martin Désilets[1], Gervais Soucy[1]

[1]Université de Sherbrooke; 2500 Boul. de l'Université; Sherbrooke, Québec, J1K 2R1, Canada

Keywords: Phase change, Solidification front, Measurements, Metallurgical reactor.

Abstract

Recent industrial developments related to metallurgical processes generally aim at boosting the metal production using a slightly modified reactor design while keeping its thermal equilibrium unchanged. The evaluation of the dynamic thermal behaviour of such reactors with regards to changes in design and operating point can sometimes become a challenge due to the aggressiveness of the molten reacting media and high temperatures. New sensors are thus needed to diagnose and control the thermal state of metallurgical reactors. Moreover, when phase change is involved, the location of the solidification front on the sidewalls may become critical with respect to energy efficiency and equipment life. However, the measurement of the solidification front location is tedious, imprecise and time consuming. A new measurement technique intended at the evaluation of the solidification front inside an experimental phase change reactor similar to a typical aluminium reduction cell is under development. The study of its thermal behaviour is used here to show the possibilities and challenges brought by this new technique. Direct measurements and numerical simulations support the development of such a sensor.

Introduction

Processes involving phase change transformations take place in a large variety of applications such as in latent-heat storage systems, in casting of alloys and in aluminium electrolysis cells. The control of these processes has been a real challenge for many researchers and engineers. Indeed, the dynamic formation of a solid-liquid interface is a complex problem because of the non-linearity of the governing heat transfer equation due to the unknown position of the interface. In addition, the measurement of the position of the solidification front is also a technological issue, especially when the phase change occurs in a harsh environment or in a production line. Many papers are devoted to the design of measurement techniques dedicated to explain the mechanisms of phase change phenomena and to validate numerical models.

Among the direct techniques used to track the location of the solidification front inside phase change reactors, one can find:
- Mechanical measurements usually achieved by measuring the position of a probe swept on the liquid-solid interface relative to a known reference location,
- Thermal measurements directly recorded by thermocouples.

As an example of mechanical measurement, Rye et al. [1] determined the profile of the frozen layer within two electrolysis cells of 155 and 125 kA respectively, thanks to an automated mechanical probe. The probe accuracy reached approximately ± 0.5 cm.

Table I: Nomenclature

L	latent heat of fusion, J. g^{-1}	λ	thermal conductivity, $W.m^{-1}.K^{-1}$
C_p	specific heat, $J.kg^{-1}.K^{-1}$	ρ	density, $kg.m^{-3}$
T	temperature, K	τ	diffusion time, min
T_f	temperature of fusion, K	Ω	boundary condition
T_i	initial temperature, K		
T_w	wall temperature, K	Subscripts	
T_∞	fluid temperature, K		
h	convection coefficient, $W.m^{-2}.K^{-1}$	c	crucible
f	liquid fraction	pcm	phase change material
H	height, m	l	liquid PCM phase
W	width, m	s	solid PCM phase
r, z	cylindrical coordinates	r	radius

In most of the works related to direct measurements, much of the emphasis has been on the employment of thermocouples directly plunged into the phase change material (PCM) at given positions. The cooling curve of each thermocouple was studied and analyzed in order to determine when and where the phase change took place [2, 3]. Although those measurements seem simple to implement, they have certain limitations. Thermocouples affect the material properties and disturb the temperature fields.

Along the years, many alternatives to direct techniques have been developed. Boily et al. [4] proposed to use an arrangement of thermocouples located inside the walls of an electrochemical reactor. As a result, this technique made it possible to measure the heat flux and its direction, a thermal parameter indirectly related to the thickness of solidified material formed on the internal walls. Bruncko et al. [5] based their development on the measurement of electrical resistance and temperature in a Pb-61.9Sn alloy melted within a Bridgman furnace. A better determination of the inflection point during the phase change was noted on the electrical resistance curves. Other experiments were carried out to validate the applicability of ultrasounds to detect the position of the solidification front. In this particular case, two approaches have to be distinguished. The first approach consists in emitting the ultrasound signal within the liquid phase by coupling a piezoelectric transducer with a transmission rod used as thermal plugs [6]. In the second configuration, the ultrasound system is directly in contact with the solid PCM undergoing a cooling process [7]. In both cases, the accuracy of the measurements depends on the signal-to-noise ratio.

It clearly appears that the development of techniques to measure the solid-liquid interface becomes critical for specific applications. Nevertheless, these techniques don't necessarily take into account the needs of metallurgical industries to obtain an easy-to-use and robust device making it possible for its implementation inside an industrial process control strategy. A new experimental bench, representative of typical metallurgical processes, has been designed to study phase change phenomena in a rigorously controlled environment. The objective of this experimental setup is twofold: First, it serves in the development of a new solidification front measurement technique. Second, it is employed in the validation of a numerical model used as a basis for a new indirect measurement method actually in development [8].

The two main objectives of the present work is 1) to shed light on the possibilities of a new indirect measurement technique in a bench simulating typical metallurgical processes and 2) to validate the direct numerical model against experimental data.

Experimental

The experimental setup was designed to support high temperatures and harsh environmental conditions such as those existing in aluminium reduction cells. It was built to allow repetitive experiments using large amount of PCM. This metallurgical reactor, illustrated in Figure 1, consists of a 20 kW oven designed by Pyradia and a carbon cylindrical crucible having an external diameter of 0.34 m. The carbon crucible bottom surface is directly accessible through an overture under the furnace where the cooling process occurs. This configuration permits to get an efficient control of the solidification speed and a preferential heat flow in the upward direction. The heat flow and gravity directions being aligned, the convective phenomena within the liquid phase were minimized. The furnace temperature is controlled with an E5CK Omron controller and a thermocouple (type K) *T/C 1*. Argon is used to provide a protective atmosphere for the carbon crucible when temperature exceeds 500°C. The temperatures inside the carbon crucible were measured by two type K thermocouples (accuracy ± 0.75%): *T/C 2* and *T/C 3*. Those thermocouples were placed respectively at 0.05 and 0.075 m from the crucible bottom and were used to get the evolution of the solidification front during the experiments. The location of the thermocouples was ensured to be within ± 2 mm. The cooling system is composed of a mass flow controller (Omega model FMA 2612A) and a brass nozzle with a 0.006 m internal diameter. A volumetric flow that ranges up to 250 $L.min^{-1}$ can be used. Nitrogen was employed as the cooling fluid. This inert gas helps to protect the crucible against air oxidation. Thermocouples were acquired by a five-slot PXI data acquisition instrument from National Instruments (model NI PXI-1033), including a multiplexer coupled to a digital multimeter.

Direct measurements

The experimental apparatus used for the direct measurement of the solidification front is mainly constituted of a linear variable displacement transformer (LVDT) coupled with a 0.76 m alumina rod. Previous tests showed that the temperature field inside the oven is mainly axisymmetric. Hence, the solidification profiles measurements were only taken along the crucible diameter by mean of a displacement system specially designed. The system was tested in normal operation conditions without any PCM in order to take into account the thermal dilation of the rod and of the crucible during the heating process. The rod is continuously inside the furnace in order to reduce its impact on the temperature distribution inside the PCM and to avoid any material solidification on the rod. An accuracy of ± 1.5 mm was obtained.

Indirect measurements

An infrared camera (Flir Systems model SC-620) was placed under the reactor to set a continuous reading of the temperature profile. Considering the accuracy specifications provided by the manufacturer, a temperature profile accuracy of ± 4% was achieved.

Experimental procedure

Since the experimental data are sought to serve as a benchmark for validating future works, the solidification front and temperature distribution of the crucible bottom were used here as basic data for evaluating the numerical model detailed in the next section. Commercial 99.9% zinc was used as the phase change material because of its low melting point (421°C). The controlled temperature inside the furnace was set to 525°C. During the heating process, an insulation block was installed under the oven to reduce the heat losses and to raise the temperature inside the crucible over the melting point. Once the thermal system reached the steady-state, the bottom

surface of the crucible was suddenly cooled. The brass nozzle was installed at 0.09 m from the bottom surface of the crucible.

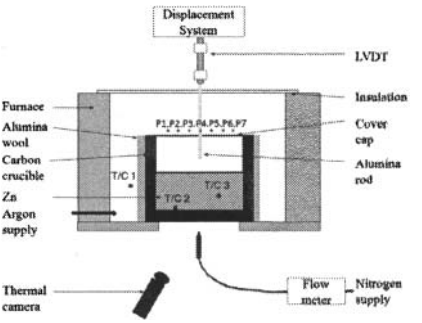

Figure 1: Experimental setup

Throughout the experiment, temperatures at locations *T/C 2* and *T/C 3*, as well as the shape of the solidification front, were acquired every 15 minutes during 4 hours. The points positions were prescribed at $P_i = \{-12.7, -10.2, -5.1, 0, 5.1, 10.2, 12.7 \text{ cm}\}$ from the center of the crucible.

Numerical procedure

As explained in the previous sections, the experimental setup also aims at validating a numerical model describing the phase change phenomena inside the reactor. The above phase-change problem is handled with the general source-based enthalpy method [9]. In this method, the entire domain is described by a single energy balance equation which accounts for the change of enthalpy within the system. The characteristics and the application of such a model compared to more simplified models were explained by Marois et al. [10].

A schematic of the phase-change problem under investigation is presented in Figure 2. At time $t < 0$, the crucible is filled with pure zinc at an uniform initial temperature above the melting point of the material. At time $t = 0$, the thermal system is supposed to be in steady-state. At time $t > 0$, a uniform temperature $T_w(t)$ is imposed on the Ω_1 and Ω_3 boundary to mimic the reactor heat load. On the Ω_2 boundary, the reactor is cooled down by a forced nitrogen convection system.

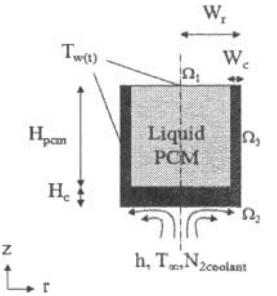

Figure 2: Schematic of the metallurgical reactor

The dimensions of the system are presented in Table II. The thermal properties of the carbon crucible and of the PCM, considered for the simulation, were measured (Table III).

Table II. Physical dimensions of the reactor

H_{pcm}	0.08 m
H_c	0.05 m
W_r	0.17 m
W_c	0.025 m

Table III. Thermophysical properties

ρ_{pcm}	7140 $kg.m^{-3}$
ρ_c	1750 $kg.m^{-3}$
$\lambda_{pcm}(T)$	$-0.079T + 151.4$ $W.m^{-1}.K^{-1}$
λ_c	20 $W\ m^{-1}.K^{-1}$
L	109.88 $J.g^{-1}$
$C_{p\_pcm}(T)$	$0.131T + 366.7$ $J.kg^{-1}.K^{-1}$
C_{p_c}	850 $J.kg^{-1}.K^{-1}$
T_f	421°C
T_∞	23°C
T_i	477°C

The mathematical model described below rests on the following assumptions:

1. Convection effects due to density variations within the liquid phase are neglected.
2. Temperature distribution in the system is assumed to be axisymmetric. This assumption reduces the problem to a 2-D cylindrical geometry (r, z).
3. Thermal conductivity and heat capacity of the PCM are temperature dependent.
4. Heat transfer coefficient h varies with the surface temperature, the physical properties of the cooling fluid and the geometrical parameters of the forced convection system [11].

Considering the foregoing assumptions, the governing heat diffusion equation for the metallurgical reactor may be stated as:

$$\rho C_p(T)\frac{\partial T}{\partial t} = \lambda(T)\frac{\partial}{\partial r}\frac{\partial T}{\partial r} + \lambda(T)\frac{\partial}{\partial z}\frac{\partial T}{\partial z} - \delta H\frac{\partial f}{\partial t} \tag{1}$$

Where $\delta H = \rho(C_{p,l} - C_{p,s})T + \rho L$

The boundary conditions imposed can be written as:

$$\lambda(T)\left.\frac{\partial T}{\partial z}\right|_{z=0} = h(T|_{z=0} - T_\infty)\ ;\ \lambda(T)\left.\frac{\partial T}{\partial r}\right|_{r=0} = 0 \tag{2}$$

$$T(z = H_{pcm} + H_c) = T(r = W_r) = T_w(t) \tag{3}$$

The direct problem represented by these equations (1-3) is concerned with the determination of the temperature field when the boundary uniform temperature $T|_{\Omega_1,\Omega_3} = T_w(t)$ is known. The governing equations are discretized using a control volume finite difference procedure.

The Dirichlet boundary condition

The Dirichlet boundary conditions on Ω_1 and Ω_3 (equations 3) are based on the temperature measurements recorded by thermocouples *T/C 2* and *T/C 3*. Figure 3 is showing a typical temperature evolution of the experimental setup, the beginning of the cooling phase occurring at time $t = 0\ s$. In the first hour of the experiment, before the phase change occurs, the characteristic diffusion time in the liquid PCM is small compared to the total duration of the

experiment$\left(\tau \approx \frac{H_{pcm}^{\ 2}}{\alpha} \approx \frac{\rho C_p H_{pcm}^{\ 2}}{k_{pcm,l}} \approx \frac{7140*458*0.085^2}{60} = 6.5\min\right)$. Therefore, the temperature gradient, as provided by the readings of the thermocouples *T/C 2* and *T/C 3*, is approximately constant all over the PCM. The surface temperature $T_w(t)$ on the Ω_1 boundary is calculated by extrapolating these values up to the surface of PCM and assumed to be $T_w(t)\big|_{t=0}^{t=1hre} = T_{T/C_1}(t)\big|_{t=0}^{t=1hre} + 17K$. In the second part of the experiment, identified as the phase change regime on figure 3, the temperature $T_w(t)$ is supposed to decrease linearly with time, using a value of $T_w \simeq T_f + 1K$ at the end of the experiment since the PCM is almost completely frozen at this point (see Figure 5). For simplicity, the same temperature profile is used on the Ω_3 boundary.

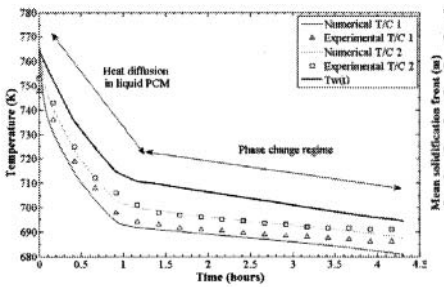

Figure 3: Temperature history

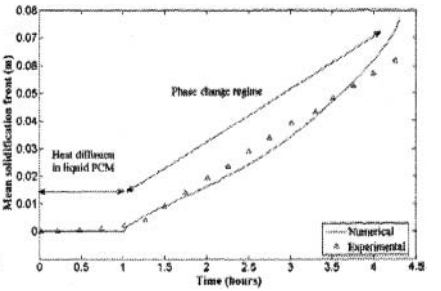

Figure 4: Predicted mean solidification front

Results

The numerical model described above was employed to predict the time-varying shape of the solidification front for the experimental setup described in section 2. Figure 3 compares the transient temperatures of the two thermocouples within the PCM to the numerical values obtained from the predictive model. A closer inspection of figure 3 reveals a slight difference, between the numerical and experimental results, after 3 hours. Nevertheless, one can assume that the boundary conditions considered are good approximations. Figure 4 compares the numerical mean solidification front to the corresponding experimental measurement. As mentioned earlier, a uniform temperature $T_w(t)$ is imposed on the top boundary Ω_1 and the side boundary Ω_2. Examination of Figure 4 shows that the mean solidification front calculated with the direct model is in good agreement with the experimental data providing by the LVDT instrument. Indeed, the time duration of the early regime is about 1 hour for both the numerical and the experiment curves. Moreover, the mean solidification rate, determined by the slope of the two curves in the late regime, is similar for both cases ($dS/dt = 0.022\ m.hr^{-1}$).

2D profiles

The variation of the numerical and experimental solidification fronts with time is given in Figure 5a. The model shows a good agreement for the first four hours of the experiment, despite the fact that the phase change phenomenon is rapid and influenced by a high thermal conductivity of the PCM. In each case however, the model underestimates the solidification front, especially close to the crucible sides. This was taken to be caused by the mean convection coefficient used at the boundary Ω_2 and by the uniform temperature imposed at the north face Ω_1. Considering that the nozzle was located at the center of the crucible, the convection coefficient should be decreasing

along the crucible radius. On the other side, $T_w(t)$ should increase from the sides to the center. At the end of the simulation, the last predicted solidification profile, close to the crucible side, is overestimated since this area is largely sensitive to the boundary conditions imposed at Ω_1 et Ω_3. The convection coefficient at the boundary Ω_2 can be improved considering a linear variation along the crucible radius. The previous simulations performed indicated that the mean convection coefficient stabilized around 80 $W.m^{-2}.K^{-1}$. In Figure 5b, a linear convection coefficient varying from 90 $W.m^{-2}.K^{-1}$ at the center to 20 $W.m^{-2}.K^{-1}$ at the side was tested. The numerical solidification front predictions gets very close to measured values even if a lack of precision can still be observed on the side of the system.

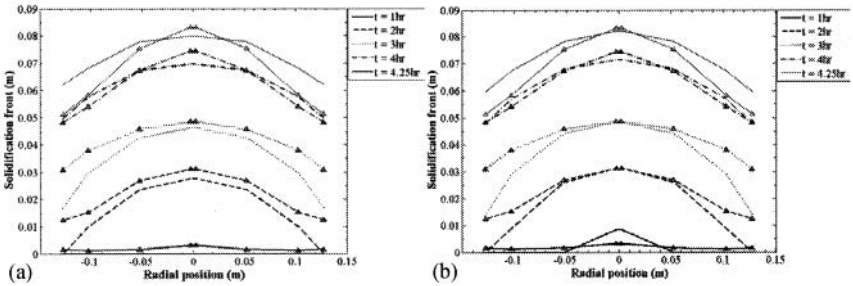

Figure 5: Solidification profiles history with (a) a mean convection coefficient and (b) with a linear convection coefficient (Experimental data: lines with markers; Numerical results: lines without markers)

Surface temperature predicted on the Ω_2 boundary

The previous analysis showed that the numerical model is efficient to predict the time-varying shape of the solidification front. We would like now to use the model predictions for the bottom surface temperature of the crucible and compare it to the infrared camera measurements on the same surface. Such a comparison would show the potential of using the external temperature measurements to estimate the solidification profile inside the reactor. Figure 6 is an example of the infrared analysis done to determine the experimental surface temperature distribution. Figure 7 shows that the difference between the numerical and the experimental surface temperature distribution is strongly dependent on the h ramp chosen. It is worth to mention that the experimental noisy data have been previously treated, resulting in a linear variation of the surface temperature with the radius of the crucible. Results indicate that this linear profile is also predicted by the direct model. Consequently, the direct model developed, coupled with external temperature measurements, may be used as a basis for an indirect 2D method that could eventually predicts the time-varying shape of the solidification front.

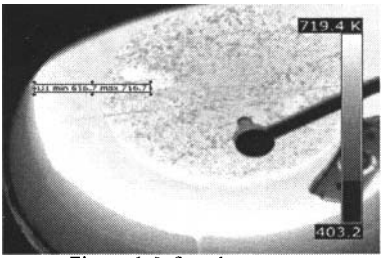

Figure 6: Infrared treatment

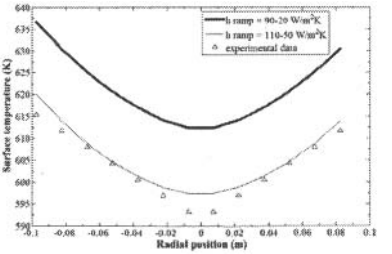

Figure 7: Experimental and numerical data for the crucible surface temperature

Conclusion

An experimental investigation of the solidification process of zinc was done, followed by a numerical study of the phase change phenomena occurring inside an experimental metallurgical reactor. The temperature inside the PCM, the surface temperature measured via a thermal camera and the direct measurements of the solidification front were considered. Results indicate that the numerical direct problem provides accurate predictions of the moving boundary compared to the experimental data despite the fact that a sensitive PCM was used. The small discrepancy between these numerical and experimental results however arises from the high heat conductivity of the PCM. Numerical simulations also show the importance of the convection coefficient considered on the accuracy of the direct model. Finally, the results confirmed that an infrared camera can be used as an indirect measurement technique. Further tests will be needed to see the applicability of the direct model and of the experimental techniques with a PCM having a mushy zone and higher melting point.

Acknowledgements

The authors are grateful to Rio Tinto Alcan (RTA), the Natural Sciences & Engineering Research Council of Canada and the Fonds Québécois de la Recherche sur la Nature et les Technologies for their financial support. Our thanks go to Mrs. Ayesha Khatun for her thermal properties measurements and to Mr Alexandre Blais from RTA for his help with the project.

References

1. K.A. Rye, T. Eidet, K. Torklep, "Dynamic ledge response in Hall-Heroult cells", *Light Metals*, 1999, p. 347-352.
2. Y. Wang, A. Amiri, K. Vafai, "An experimental investigation of the melting process in a rectangular enclosure", *International Journal of Heat and Mass Transfer*, 42 (1999), p. 3659-3672.
3. B.J. Jones et al, "Experimental and numerical study of melting in a cylinder", *International Journal of Heat and Mass Transfer*, 49 (2006), p. 2724-2738.
4. P. Boily et al., "Sensitivity analysis of the thermal detection of the freeze profile in an aluminum reduction cell", *Light Metals*, (2001), p. 1-7.
5. M. Bruncko, I. Anzel, A. Krizman, "Monitoring of directional solidification with simultaneous measurements of electrical resistance and temperature", *Materials Characterization*, 51 (2003), p. 185-199.

6. A. Eyer et al., "A pulse-echo ultrasonic technique for the localization of the solid/liquid interface during directional solidification of silicon ingots", *Conference Record of the Twenty Second IEEE Photovoltaic Specialists Conference*, 2 (6B) 1991, p. 982-985.
7. A. Drevermann et al., "Online process control for directional solidification by ultrasonic pulse echo technique", *Ultrasonics*, 42 (2004), p. 105-108.
8. M-A. Marois, M. Désilets, M. Lacroix, "Prediction of a 2D Solidification Front in High Temperature Furnaces by an Inverse Analysis", *Numerical Heat Transfer, Part A: Applications*, accepted for publication September 25th 2010.
9. V.R. Voller, C.R. Swaminathan, "Fixed grid techniques for phase change problems: a review", *International journal for numerical methods in engineering*, 44 (1990), p. 875-898.
10. M-A. Marois et al., "Comparison of two different numerical methods for predicting the formation of the side ledge in an aluminium electrolysis cell", *Light Metals, 2009*, p. 563-568.
11. Incropera, F. P., *Fundamentals of heat and mass transfer* (Hoboken , NJ: John Wiley & Sons, 2007), 6th edition, 995 p.

Sensors, Sampling, and Simulation for Process Control
Edited by: Brian G. Thomas, James A. Yurko, and Lifeng Zhang
TMS (The Minerals, Metals & Materials Society), 2011

INVERSE PREDICTION AND CONTROL OF THE BANK THICKNESS IN HIGH TEMPERATURE METALLURGICAL REACTORS

Marc LeBreux, Martin Désilets, Marcel Lacroix

Université de Sherbrooke, Département de génie mécanique
2500 Blvd. de l'Université, Sherbrooke, Qc, J1K 2R1, Canada

Keywords: Metallurgical reactors, Protective banks, Ledge, Virtual sensor, Control, PI, Kalman filter, Recursive least-square estimator.

Abstract

An inverse heat transfer procedure for predicting the time-varying bank thickness in high temperature metallurgical reactors is presented. A Kalman filter coupled with a recursive least-square estimator (inverse method) is employed to estimate the time-varying solidification front position from the data collected by a temperature and/or heat flux sensor located in the reactor wall. The inverse method, known also as a virtual sensor, is then combined to a proportional-integral (PI) controller in order to control the bank thickness by regulating the air forced convection cooling of the reactor external wall. The inverse prediction and the control strategy are thoroughly tested for typical phase change conditions that prevail inside industrial facilities. It is seen that the discrepancy between the exact and the estimated bank thickness remains smaller than 5% at all times, and that the controller performance is much better when the virtual sensor uses a heat flux sensor at the wall/bank interface.

Introduction

An interesting melting/solidification process that arises in many high temperature metallurgical reactors such as electric arc furnaces [1], blast furnaces [2] and electrolysis cells [3] is the formation of solid layers, sometimes called banks or ledges, on the inside surface of the reactor walls (Fig. 1). These banks are created as the molten material comes into contact with the cooled surface of the wall and undergoes a solidification process. In many cases, the presence of these banks is highly desirable. They serve as a protective barrier against the corrosive molten material, thereby maintaining the integrity of the metallurgical reactor and prolonging its active life [4,5]. On the other hand, too thick a bank is detrimental to the reactor as the active furnace volume is reduced, and as horizontal currents are created disturbing the reactor magneto-hydrodynamics stability, decreasing by the same way the current efficiency [4,6]. Keeping banks of optimal size at all times is therefore crucial for the safe and profitable operation of the metallurgical reactors.

Unfortunately, due to the hostile conditions that prevail inside the reactors, probing the time-varying thickness and shape of the banks with sensors submerged into the molten material is a very difficult task, not to say impractical. The standard method for measuring the bank thickness is to insert manually mechanical probes inside the reactor [7]. This method is time consuming and requires qualified personnel to perform the measurements. Also, the measurements are conducted at a low frequency (sometimes days apart), and the opening of the reactor's cover to make the measurements releases to the surrounding environment a large quantity of heat and chemicals [8]. Thus, the standard method for measuring the bank thickness is neither ideal nor efficient.

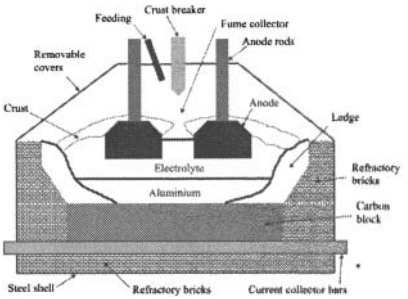

Figure 1 : Cross view of a typical high temperature metallurgical reactor with molten material (electrolyte) and protective banks (ledge).

The alternative is to attempt to predict the reactor's bank thickness with inverse heat transfer methods that rely on temperatures and/or heat fluxes recorded by non-intrusive sensors embedded into the reactor walls. The inverse method thus acts as a virtual sensor [9]. A virtual sensor may be pictured as a collection of sensors (temperature and/or heat flux sensors), that allow on-line measurements of process variables (temperature and/or heat flux). The virtual sensor employs an estimation algorithm (inverse method) in order to provide on-line estimates of immeasurable variables (bank thickness).

Shape design predictions of banks or ledges on reactor walls with inverse heat transfer methods have been the subject of few investigations in the past [1, 10-13]. Fig. 2 shows a schematic of such an inverse problem. The bank is represented by the solid phase of the phase change material (PCM). In the direct problem (Fig. 2 a), the time-varying heat flux $q''_{in}(t)$ at the right boundary is known. This heat flux may represent the heat load inside the metallurgical reactor. The solution for the temperature distribution $T(x,t)$ and for the thickness of the bank (the phase front position) $s(t)$ may then be determined from the solution of the energy conservation equation. In the inverse problem (Fig. 2 b), the time-varying heat flux $q''_{in}(t)$ at the right boundary is not known. It can be estimated however with an inverse method that uses temperatures and/or heat fluxes recorded by sensors located inside the brick wall. With the estimated heat flux $\hat{q}''_{in}(t)$, the bank thickness $\hat{s}(t)$ can therefore be estimated.

Inverse heat transfer methods for this one-dimensional heat conduction phase change problem have been developed with the sole purpose of predicting the location of the phase front $s(t)$. From an industrial point of view however, the interest and the real challenge is to control in real-time the thickness of the bank. As a result, most of the inverse heat transfer methods such as the Levenberg-Marquardt method or the conjugate gradient methods that have been developed for prediction purposes are unsuitable for real-time control systems. They are time-consuming and computationally inefficient [11,14,15].

The objective of the present study is to remedy this situation. An inverse heat transfer method (virtual sensor) based on a Kalman-filter and recursive least-square estimator reported in Ref. [16] is combined to a PI controller in order to control the bank thickness inside high temperature metallurgical reactor.

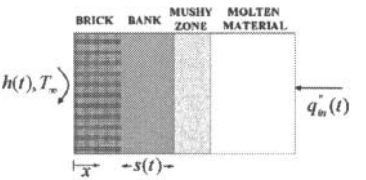

a) Direct problem: $q''_{in}(t)$ and $h(t)$ are known; $T(x,t)$, $q''(x,t)$, and $s(t)$ are predicted with the difference numerical model.

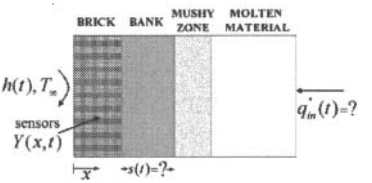

b) Inverse problem: $q''_{in}(t)$ is unknown. It is determined from temperatures and/or heat fluxes $Y(x,t)$ measured inside the brick wall.

Figure 2 : Schematic of a 1-D phase change problem inside a high temperature metallurgical reactor.

The overall calculation strategy to be developed in the present paper is the following. First, a mathematical model for the melting/solidification process of the banks inside the metallurgical reactor is presented. Second, an inverse method combining a Kalman filter with a recursive least-square estimator (RLSE) is discussed. Third, a proportional-integral (PI) controller is coupled with the virtual sensor in order to control in real-time the bank thickness inside high temperature metallurgical reactors. Finally, the inverse control strategy is thoroughly tested for typical phase change conditions that prevail inside industrial facilities.

Finite difference model of the metallurgical reactor

The one-dimensional phase change problem under investigation is depicted in Figure 2 a). A bank of thickness $s(t)$, which corresponds to the phase front location, is pressed against the inner surface of a brick wall of thickness L. The outer surface of the brick wall is cooled with an air stream at constant temperature T_∞ and with a known time-varying heat transfer coefficient $h(t)$. A time-varying heat flux $q''_{in}(t)$, which represents the metallurgical reactor heat load, is imposed on the right boundary condition at $x = L + D$.

The mathematical model for the phase change problem rests on the following assumptions:

- The temperature gradients across the wall are much larger than the temperature gradients in the vertical direction so that a one-dimensional analysis can be applied.
- The phase change problem is non isothermal, i.e. contains a mushy zone.
- The thermal contact resistance between the brick wall and the bank is neglected.
- The thermal properties of the phase change material (PCM) are temperature independent.
- The heat transfer across the liquid layer of the PCM is conduction dominated; an effective thermal conductivity enables to account the effect of the flow circulation inside the liquid [1].

With the foregoing assumptions, the governing heat diffusion equation for the wall and the PCM may be stated as:

$$\rho C_p \frac{\partial T}{\partial t} = \frac{\partial}{\partial x}\left[k \frac{\partial T}{\partial x}\right] - \delta H \frac{\partial f}{\partial t} \tag{1}$$

The boundary conditions are:

$$-k \left.\frac{\partial T}{\partial x}\right|_{x=0} = h(t)[T(0,t) - T_\infty] \tag{2}$$

$$-k \left.\frac{\partial T}{\partial x}\right|_{x=L+D} = q_{in}^{"}(t) \tag{3}$$

and the initial condition is

$$T(x,0) = T_0(x) \tag{4}$$

The second term on the right-hand side of Eq. (1) accounts for the solid/liquid phase change. The enthalpy δH is defined as $\delta H = \rho(C_{p,liquid} - C_{p,solid})T + \rho\lambda$. The liquid fraction f varies linearly between the solidus T_{sol} and the liquidus T_{liq} in the following manner:

$$f = f(T) = \begin{cases} 0 & T \le T_{sol} \\ \left(\dfrac{T - T_{sol}}{T_{liq} - T_{sol}}\right) & T_{sol} < T < T_{liq} \\ 1 & T \ge T_{liq} \end{cases} \tag{5}$$

Eqs. (1-5) were discretized using finite differences. The resulting set of difference equations is then solved using a tri-diagonal matrix algorithm (TDMA). For each time step, the liquid fraction f in Eq. (1) is determined according to the iterative procedure reported in Ref. [17]. The above finite difference model (FDM) was thoroughly tested and validated using analytical solutions and results available in the open literature [16].

Due to the fact that no experimental measurements are possible at the moment, the present paper assumes that the FDM simulates perfectly the thermal behaviour of a real high temperature metallurgical reactor. Moreover, the thickness of the brick wall was fixed at L = 0.1 m and the width of the PCM layer (solid, mushy, and liquid) was set equal to D = 0.1 m (Fig. 2 a). The outside temperature was kept constant at T_∞ = 300 K. The time step dt and mesh size dx were respectively set equal to 100 s and 0.5 x 10^{-3} m. The physical properties of the refractory bricks and of the PCM are reported in Ref. [16].

Inverse method for estimating the bank thickness: the virtual sensor

In the inverse problem, the heat flux $q_{in}^{"}(t)$ on the right boundary is unknown (Fig. 2 b). It is estimated however with an inverse method which uses temperature and/or heat flux measurements $Y(x,t)$ from sensors embedded in the brick wall. With the estimated heat flux $\hat{q}_{in}^{"}(t)$, the bank thickness $\hat{s}(t)$ can therefore be estimated. The overall inverse methodology based on the Kalman filter/recursive least-square estimator is shown in Figure 3. The method may be divided into four steps.

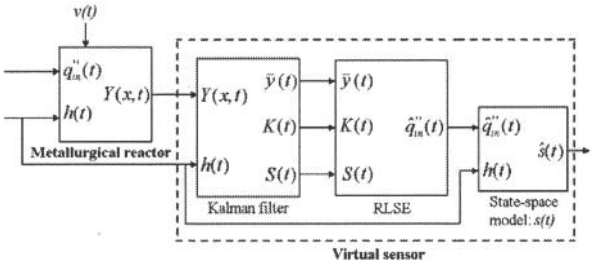

Figure 3 : The inverse method; a Kalman filter coupled with a recursive least-square estimator. It acts as a virtual sensor enabling the bank thickness estimation.

While the smelting process is running, the metallurgical reactor will undergo several melting/solidification scenario due to heating $q''_{in}(t)$ and cooling $h(t)$ conditions varying inside the reactor. The temperature and/or heat flux sensor installed in the refractory wall will then produce the corresponding thermal readings $Y(x,t)$ that contain noise $v(t)$, that is assumed to be white, with a null mean, and with a Gaussian variance. From these measurements and the known heat transfer coefficient $h(t)$, the Kalman filter estimates the thermal state of the phase change process, and therefore produce the measurement residual residual $\bar{y}(t)$, the optimal Kalman gain $K(t)$ and the residual covariance $S(t)$. Theses information are then fed to the recursive least-square estimator (RLSE) that estimates the unknown heat flux $\hat{q}''_{in}(t)$ using the information generated from the Kalman filter. The fourth and last step of the inverse method consists of calculating the bank thickness $\hat{s}(t)$ with the estimated heat flux $\hat{q}''_{in}(t)$ given by the RLSE, and a direct state-space model of the bank behaviour inside the reactor. Further details on the inverse method procedure and the calculation algorithm are reported in Refs. [15,16].

The virtual sensor testing is exemplified in Figure 4. The bank initially rests at the working point steady-state conditions ($q''_{in,0}$=15000 W/m^2, h_0= 60 W/m^2.K). This working point represents typical values for the heat load inside the metallurgical reactor [18] and the heat transfer coefficient for air forced convection [19]. At time $t = 0.8 \times 10^4$ s, the bank is suddenly exposed to a series of step functions for the input heat flux $q''_{in}(t) = q''_{in,0} \pm \delta q''_{in}(t)$, where the maximum amplitude of $\delta q''_{in}(t)$ is equal to 2000 W/m^2. The heat transfer coefficient $h(t)$ remains at its steady-state value h_0, while the sensor noise standard deviations take values of 25 W/m^2 for heat flux and 0.5 K for temperature.

Figure 4 compares the exact results obtained from the reactor with the results from the inverse method. Two cases are studied: 1) using an heat flux sensor at the wall/bank interface, i.e. $Y(x,t) = q''(x = L,t)$, and 2) using a temperature sensor at the reactor external wall, i.e. $Y(x,t) = T(x = 0,t)$. Figure 4 shows that the discrepancy between the exact and the estimated bank thickness results remains smaller than 5 x 10^{-3} m for the two cases. However, the estimation obtained by the heat flux sensor has a smaller time lag, which is reflected by calculating the relative root-mean-square errors (RRMSE) [16]. The calculated RRMSE values are 3.2% and 5.4% for the heat flux and temperature sensors respectively.

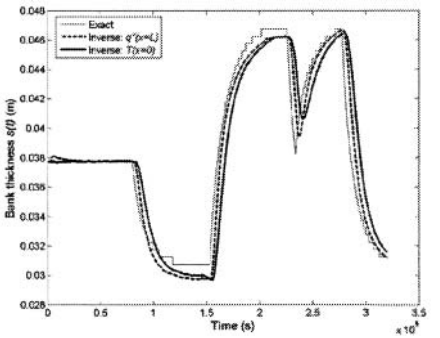

Figure 4 : Predicted (inverse method) and exact (reactor) bank thickness using a temperature or heat flux sensor embedded in the reactor wall.

Thus, even if the RRMSE values are not equal to zero, the use of the virtual sensor still overcomes the problem of measuring manually the bank thickness with mechanical probes, and thus eliminates all the disadvantages associated with these measurements.

Inverse control of the bank thickness using a virtual sensor

The inverse control of the bank thickness using a virtual sensor is schematized in Figure 5. From the thermal readings $Y(x,t)$ containing noise $v(t)$, and the known heat transfer coefficient $h(t)$, the virtual sensor estimates the unknown bank thickness $\hat{s}(t)$. From the tracking error $e(t)$, which is the difference between the bank thickness setpoint $r(t)$ and the virtual sensor bank thickness estimation $\hat{s}(t)$, the control strategy regulates the cooling $h(t)$ on the external wall of the reactor in order to ensure that the bank thickness setpoint $r(t)$ is maintained continuously even when the metallurgical reactor is subjected to an unknown input heat flux $q''_{in}(t)$.

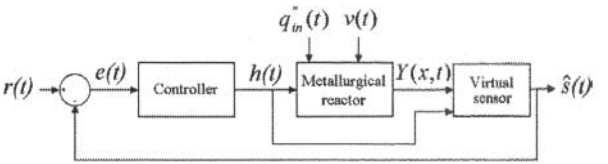

Figure 5 : Inverse control of the bank thickness using a virtual sensor.

The control strategy rests on a classic proportional-integral (PI) controller [20]. In this case, the heat transfer coefficient $h(t)$ is different from its steady-state value h_0, and is calculated from the PI discrete velocity form (Eq. 6).

$$h(t) = h(t-1) + K_p\left[e(t) - e(t-1)\right] + \frac{K_p\,dt}{T_i}e(t) \qquad (6)$$

where the controller proportional gain K_p = 80000 and the integral time constant T_i = 15000 s were obtained from classic tuning method [20].

The inverse control of the bank thickness is exemplified in Figure 6. Once again, the bank initially rests at the working point steady-state conditions ($q''_{in,0}$=15000 W/m^2, h_0= 60 W/m^2.K). At time t =1.25 x 10^4 s, it is suddenly exposed to an input heat flux of 17000 W/m^2, while the bank thickness setpoint remains at the steady-state value s_0 = 3.78 x 10^{-3} m.

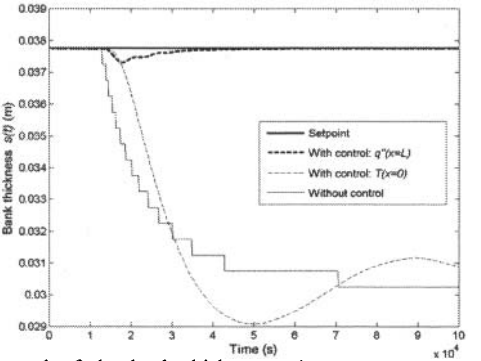

Figure 6 : Inverse control of the bank thickness using a temperature or heat flux sensor embedded in the reactor wall.

Results show that the PI controller using the heat flux sensor ensures a null steady-state tracking error and provides an overshoot of only 3.5 x 10^{-4} m, compared to 8 x 10^{-3} m, which is the bank thickness variation without control. Figure 6 shows also that the inverse control of the bank thickness using the temperature sensor located at the reactor's external wall give poor results. This is easily explained by considering that the cooling system of the reactor wall "cools" down the temperature sensor as it cools down the wall, disturbing by the same way the thermal readings from the sensor. The virtual sensor cannot afterwards distinguish correctly the effect due to heating $q''_{in}(t)$ or cooling $h(t)$, and thus give poor results in the inverse estimation of the bank thickness $\hat{s}(t)$.

Concluding remarks

An inverse heat transfer procedure for predicting the time-varying bank thickness in high temperature metallurgical reactors was presented. A Kalman filter coupled with a recursive least-square estimator (inverse method) was employed to estimate the time-varying phase front position from the data collected by a temperature and/or heat flux sensor located in the reactor. The inverse method, known also as a virtual sensor, was then combined to a proportional-integral (PI) controller in order to control the bank thickness by regulating the air forced convection cooling of the reactor wall. The inverse prediction and the control strategy were thoroughly tested for typical phase change conditions that prevail inside industrial facilities. It was seen that the discrepancy between the exact and the estimated bank thickness remained smaller than 5% at all times, and that the controller performance was much better when the virtual sensor used a heat flux sensor at the wall/bank interface.

Acknowledgments

The authors are very grateful to the *Fonds québécois de la recherche sur la nature et les technologies* (FQRNT), to the *Centre québécois de recherche et de développement de l'aluminium* (CQRDA), to the Natural Sciences and Engineering Council of Canada (NSERC), and to the Aluminium Research Centre (REGAL) for their financial support.

References

[1] O. Tadrari, M. Lacroix, Prediction of Protective Banks in High Temperature Smelting Furnaces by Inverse Heat Transfer, Int. J. of Heat & Mass Trans. 49 (13-14) (2006) 2180-2189.
[2] R.J. Groth, Y. Zhao, US Patent No. 5961214, 1995.
[3] C.C. Wei, J.J.J. Chen, B.J. Welch, V.R. Voller, Modelling of dynamic ledge heat transfer, Proc. of the TMS, Orlando, FL, 1997, pp. 309-316.
[4] J.G. Peacey, G.W. Medlin, Cell sidewall studies at Noranda Aluminium, Proc. of the TMS, Warrendale, PA, 1979, pp. 475-491.
[5] M.P. Taylor, B.J. Welch, M.J. O'Sullivan, Sidewall ledge dynamics in cells used for electrowinning aluminium, Proc. of the 11th Australian Conf. on Chem. Eng., 1983, pp. 493–500.
[6] K. Grjotheim, H. Kvande, Introduction to Aluminium electrolysis, 2e ed., Aluminium-Verlag, 1993, pp. 147-160.
[7] K. Torklep, T. Nordbo, Some applications of the Elkem position probe, Proc. of the TMS, San Francisco, CA, 1994, pp. 449–456.
[8] O. Bonnardel, P. Homsi, Pechiney semi-continuous & automatic measurement device, a new tool for automatic measurements, Proc. of the TMS, Warrendale, PA, 1999, pp. 303-309.
[9] J.C.B. Gonzaga, L.A.C Meleiro, C. Kiang, R. Maciel Filho, ANN-based soft-sensor for real-time process monitoring and control of an industrial polymerization process, Comp. & Chem. Eng. 33 (1) (2009) 43-49.
[10] C.K. Chen, C.R. Su, Inverse Estimation for Temperatures of Outer Surface and Geometry of Inner Surface of Furnace with Two Layer walls, Ener. Conv. & Manag. v49 (2) (2008) 301-310.
[11] C.H. Huang, B.H. Chao, An Inverse Geometry Problem in Identifying Irregular Boundary Configurations, Int. J. of Heat & Mass Trans. 40 (9) (1997) 2045-2053.
[12] C.R. Su, C.K. Chen, Geometry Estimation of the Furnace Inner Wall by an Inverse Approach, Int. J. of Heat & Mass Trans. 50 (19-20) (2007) 3767-3773.
[13] P. Boily, L.I. Kiss, R.T. Bui, P. Desclaux, Sensitivity analysis of the thermal detection of the freeze profile in an aluminium reduction cell, Proc. of the TMS, Warrendale, PA, 2001, pp. 1209-1215.
[14] J.V. Beck, B. Blackwell, A. Haji-Sheikh, Comparison of some inverse heat conduction methods using experimental data, Int. J. of Heat & Mass Trans. 39 (17) (1996) 3649-3657.
[15] P.C. Tuan, C.C. Ji, L.W. Fong, W. Huang, An Input Estimation Approach to On-Line Two-Dimensional Inverse Heat Conduction Problems, Num. Heat Trans. B 29 (3) (1996) 345-363.
[16] M. LeBreux, M. Désilets, M. Lacroix, Fast Inverse Prediction of Phase Change Banks in High Temperature Furnaces with a Kalman Filter coupled with a Recursive Least-Square Estimator, Int. J. of Heat & Mass Trans. 53 (23-24) (2010) 5250-5260.
[17] V.R. Voller, C.R. Swaminathan, General Source-Based Method for Solidification Phase Change, Num. Heat Trans. 19 (1991) 175-189.
[18] J.N. Bruggemann, Pot Heat Balance Fundamentals, Proc. of the 6th Australasian Al. Smelter Tech. Conf. & Workshops, 1998, pp. 167-189.
[19] Y. A. Çengel, Heat and Mass Transfer: A Practical Approach, 3e ed., McGraw-Hill, 2007, pp. 1-34.
[20] K.J. Aström, T. Hägglund, PID Controllers: Theory, Design and Tuning, 2e ed., Instrument Society of America, 1995, pp. 59-197.

Sensors, Sampling, and Simulation for Process Control
Edited by: Brian G. Thomas, James A. Yurko, and Lifeng Zhang
TMS (The Minerals, Metals & Materials Society), 2011

ON-LINE IMAGING PYROMETER FOR LASER DEPOSITION PROCESSING

James E Craig[1], Thomas Wakeman[1], Richard Grylls[2], James Bullen[2]

[1]Stratonics, Inc.; 25002 Castlewood Street; Lake Forest, CA 92630-3205, USA
[2]Optomec, Inc.; 3911 Singer Blvd. NE; Albuquerque, NM 87109, USA

Keywords: Imaging Pyrometer, Melt Pool Temperature, LENS, Laser Additive Manufacturing

Abstract

An online imaging pyrometer has been developed to monitor the temperature distribution of the melt pool in laser additive manufacturing processes. The imaging pyrometer uses two CCD cameras with "long" and "short" wavelength filters in the near infra-red (NIR) waveband. The intensity ratio is formed and the two-wavelength temperature is determined from a calibration, relating the intensity ratio to the temperature. In the experiment, deposits of tool steel (H13) are formed over a variety of laser power levels, ranging from standard power to about half the initial power level. As the power is lowered, the deposit efficiency is reduced, as are the melt-pool dimensions. Melt pool temperature distributions were measured in the final five of the 10 passes, and their properties are presented and described. Peak temperatures of about 2000°C are noted for standard power levels and in general lower temperatures are observed at lower power levels.

Introduction

Thermal monitoring is considered crucial to the control of laser additive manufacturing (LAM) processes to achieve proper deposit metallurgy in a reliable manner. Peak temperature and cooling rate are thermal parameters which are a necessary component of LAM control. As an initial step towards developing fully controlled processes, an online, two-wavelength imaging pyrometer has been developed to monitor the temperature distribution of the melt pool in LAM processes. The imaging pyrometer uses a sophisticated computer algorithm to calculate temperatures in and around the melt pool created by the LAM process. A two-wavelength approach to temperature measurement was selected to reduce sensitivity to melt pool emissivity. An imaging approach was selected to provide spatial information required to measure the material cooling rate near the solidification temperature.

The Stratonics two-wavelength pyrometer (ThermaViz®) was integrated into a Laser Engineered Net Shaping (LENS®) system, marketed by Optomec, Inc. The LENS system uses a high powered fiber laser, coupled with powder feed and motion control, to build up a three-dimensional structures of metal, composite, or ceramic with excellent mechanical properties.

An experiment was designed to evaluate the ability of the pyrometer to measure temperature distributions in the melt pools developed in LAM processes and the associated thermal parameters of peak temperatures and cooling rate. A series of tool steel (H13) deposits were formed over a variation of laser power levels, ranging from standard levels to about half the initial level. Pyrometer movies were recorded for each deposit and analyzed for peak temperature and cooling rate.

The LENS Process

Unlike many of existing rapid prototyping methods, the LENS technology uses metal powders to create functional parts that can be used in very demanding applications. A schematic representation of the LENS process is depicted in Figure 1 and the actual process in operation is shown in Figure 2. The process uses up to 3kW of Fiber Laser power focused onto a metal substrate to create a molten puddle on the substrate surface. Metal powder is then injected into the molten puddle to increase the material volume. The substrate is then scanned relative to the deposition apparatus to write lines of the metal with a finite width and thickness. Rastering of the deposition head back and forth to create a pattern and fill where material is required allows a layer of material to be deposited. Finally, this procedure is repeated many times until the entire object represented in the three-dimensional CAD model is produced on the machine. In this fashion, a part is built up from powders to form a solid object. This approach to producing a mechanical component in a layer-by-layer fashion allows the user to fabricate the part with features that cannot be readily produced by other methods. These features include hollow passages that can conform to a surface, deposition and encapsulation of other materials within a normally homogeneous structure, and transitioning between different materials in both abrupt and graded fashions. Using an appropriate combination of processing parameters, solidification rates of ~10^3 to 10^5 K/sec can be achieved in LENS processing. Such rapid solidification conditions allow for the formation of chemically homogeneous microstructures with good mechanical properties. Table I shows some typical tensile mechanical properties. It can be seen that strength is often similar to standard wrought material, with no loss in ductility.

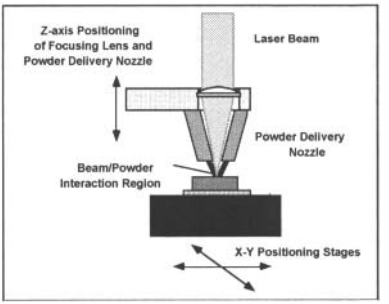

Figure 1. Schematic representation of the LENS process.

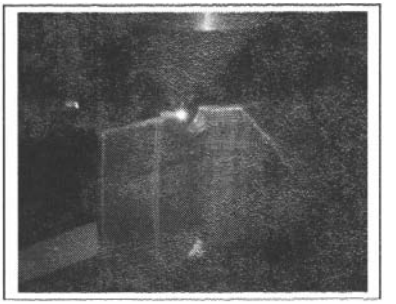

Figure 2. LENS deposition of a section of an IN718 diffuser case. The section is approximately 6" tall.

Table I. Measured Tensile Values for LENS Fabricated Specimens as Compared to Conventionally Processed Materials

Material Type	Ultimate Strength (MPa)	Yield Strength (MPa)	Elongation (% in one inch)
LENS Processed 316 Stainless Steel	799	500	50
316 SS Anneal Bar	591	243	50
LENS Processed Inconel 625	938	584	38
IN 625 Annealed Bar	841	403	30
LENS Processed Ti-6Al-4V	1077	973	11
Ti-6Al-4V Annealed Bar	973	834	10

Description of Experiment

LENS System

The experiment utilized the new Optomec LENS MR-7 System, Figure 3 integrated with Stratonics on-line imaging pyrometer, ThermaViz®. The LENS System includes dual powder feeders, closed-loop melt-pool control, inert processing chamber, specifically designed deposition heads, and a single-mode fiber laser. These features make it an ideal system for materials research, rapid alloy discovery, process development, solidification and materials processing research.

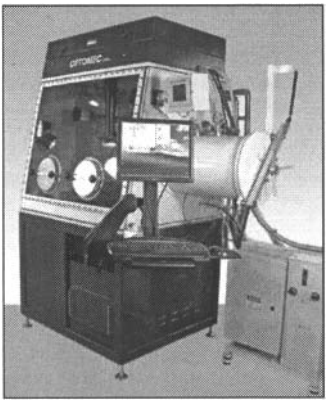

Figure 3. LENS System MR-7.

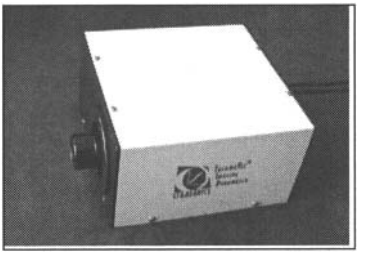

Figure 4. Stratonics ThermaViz Two-Wavelength Imaging Pyrometer.

Thermal Control in the LENS Process

Thermal control of the LENS process is critical to producing specified metallurgy in a repeatable fashion. Previous efforts to investigate melt pool temperature characteristics of the LENS process used a single wavelength CCD camera with modest spatial resolution (64 x 64 pixels) and a high frame rate (near 1000 frames per second) [1]. The pyrometer used in this current effort incorporates two CCD cameras, utilizing two wavelengths, similar to the pyrometer used in previous experiments [2]; however, the new technique views the melt pool along the laser line of sight as opposed to the previous method of side-on viewing. The current pyrometer is based on the former steel industry efforts with spot radiation thermometers [3], but now provides the temperature distribution of the LENS melt pool with image based temperature measurements. Also, previous efforts at thermal monitoring of LENS processes have used Nd:YAG lasers [4] and [5], whereas the current LENS system used in these experiments utilizes a fiber laser.

Pyrometer Architecture & Operation A two-wavelength imaging pyrometer has been developed for the purpose of measuring the temperature distribution of the melt pool during materials processing. The pyrometer field of view is integrated to be co-axial with the processing laser, providing a top view of the melt pool. The effective field of view for the pyrometer is approximately 4 mm in diameter. The pyrometer uses two cameras and their fields of view are coupled through a beam splitter, each viewing exactly the same field of view. The camera images are aligned to about ½ a pixel, or 8 microns in the image scene. Each camera sees

through a band pass filter, with one camera seeing through the short band at 750 nm and the other camera seeing through the long band at 875 nm. The melt pool scene is magnified to achieve an effective pixel sampling of 14.4 μm/pixel. Therefore, for a typical melt pool of 1-2 mm in diameter, the image resolution provides 100's of pixels in both directions for a total number of pixels of about 10,000 per melt pool. Thus, the peak temperature is easily resolved, as are the heating and cooling rates. The camera outputs are digital, 12 bit, and acquire a synchronous image that is output to the computer over a USB interface. The dual frame acquisition is one frame per two seconds with live temperature display, or four frames per second without display, in which case the images are saved directly to RAM. The camera exposures are set to provide bright or high signal levels, typically 3000 counts out of the 4096 count signal, e.g. 12 bits. Typical camera exposures are in the 10-20 millisecond range.

Calibration The pyrometer measures the temperature in the classical two-wavelength method, i.e. by measuring the intensity ratio directly and determining the temperature through a calibration. A two-wavelength pyrometer can measure temperature because the Planck radiation intensity changes faster at shorter wavelength than at longer wavelength. The calibration is performed with a Tungsten lamp over a range of temperatures, typically 1000°C to 2000°C. The calibration data are plotted in a transformed space, inverse temperature against natural log of the intensity ratio (long over short wavelength). In this space, the data form a straight line and a linear fit is obtained, providing fit parameters as shown, Figure 5.

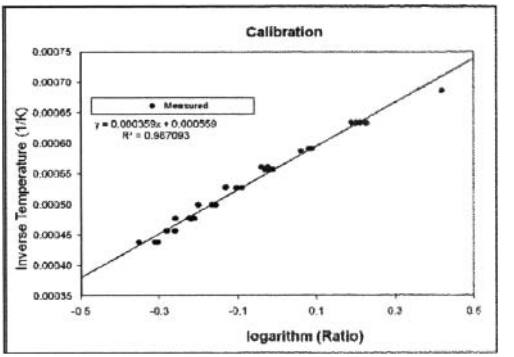

Figure 5. Calibration data plotted in pyrometer coordinates, inverse temperature against natural log of the intensity ratio, note fit parameters of 0.000359, linear term and 0.000559, off-set term.

Theoretical Basis for Temperature Measurement The theoretical development of the pyrometer response begins with the Planck radiation relationship:

$$I(\nu, T) = (2h / c^2) \cdot \nu^3 / [\, e^{(h\nu)/(kT)} - 1 \,] \qquad (1)$$

h (Planck's constant)=6.6260693 $\times 10^{-34}$ J·s
c (vacuum speed of light)=2.99792458 $\times 10^{8}$ m/s
k (Boltzmann's constant)=1.3806505 $\times 10^{-23}$ J / Kelvin

At a single wavelength, the Planck radiation relationship provides an implicit relationship between the temperature and the intensity.

$$T = C / \ln(1 + q / I_{theory}) \quad (2)$$

$$q = 2\,h\,\nu^3 / c^2 \quad (3)$$

$$C = h\,f / k \quad (4)$$

For a two-wavelength development, the Planck radiation relationship leads to a result where the absolute emissivity is canceled

$$R = I(\nu_1, T) / I(\nu_2, T) = (\nu_1/\nu_2)^3 \cdot [\, e^{(h\nu 2)/(k\,T)} - 1\,] / [\, e^{(h\nu 1)/(k\,T)} - 1\,] \quad (5)$$

Which can be approximated with high accuracy as,

$$\ln(R) = 3\ln(\nu_1/\nu_2) + (h/k)(\nu_2 - \nu_1)(1/T) \quad (6)$$

and leads to the relationship used in calibration to obtain the linear, M, and off-set parameters, B.

$$1 / T = M \ln(R) + B \quad (7)$$

The linear and off-set parameters are used in fitting the calibration data, previously shown in Figure 5. The parameters are then used in the software analysis to convert measured (long over short) intensity ratios to temperature.

Description of the Test An experiment was performed in which the LENS system was programmed to deposit a tool steel, H13. The deposits were built from front to back, e.g. always in one direction, at a velocity of 8.47 mm/s. Each deposit consisted of 10 passes. The standard laser power for this process was 300 watts and deposits were built over a range of powers from 350 watts to 175 watts, Figure 6. The deposit dimensions were measured and increased with laser power, Figure 7.

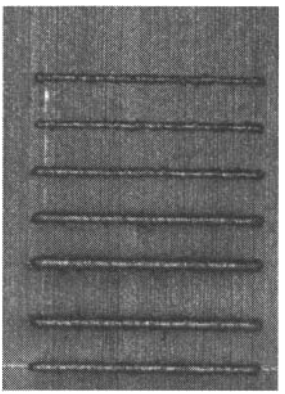

height (mm)	width (mm)	laser power (W)
1.17	0.86	175
1.14	0.91	200
1.35	1.14	250
1.55	1.27	300
1.60	1.40	350
1.63	1.40	350
1.55	1.27	300

Figure 6. Photograph of deposits with corresponding deposit dimensions.

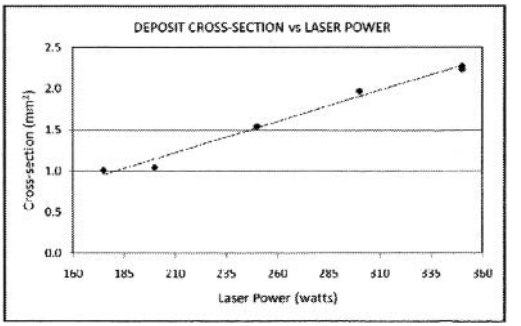

Figure 7. Measurements of deposit dimensions for a range of laser powers.

Analysis of Data

A movie of the melt pool was recorded using the ThermaViz sensor for each laser power, beginning with the 6th pass and ending with the final 10th pass. The movies have about 3 or 4 images for each pass and about 15 or 20 for the entire build. For each laser power the images in the movies were analyzed to measure the peak temperature and the cooling rates.

The temperature distribution in the build direction is measured by sampling the temperature image, Figure 8, where the melt pool temperature image is from Frame 18 of 24 with a laser power of 300 watts. The temperature is shown in a color scale from green to red, which corresponds to temperatures of 1300°C to 2100°C, respectively.

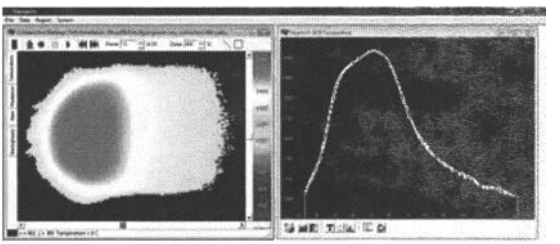

Figure 8. Temperature image, color scaled temperature, with temperature plot, screen capture.

Measurement of Peak Temperature

The peak temperature is measured from the ThermaViz temperature image. A rectangular region having the short dimension (7 pixels) centered about the optical axis of the LENS system and the long axis (200 pixels) parallel to the direction of motion, is analyzed. The average temperature is taken across the vertical dimension of the region, yielding a temperature profile through the point of peak heating, Figure 9, where the scale factor of 14.4 μm/ pixel is used.

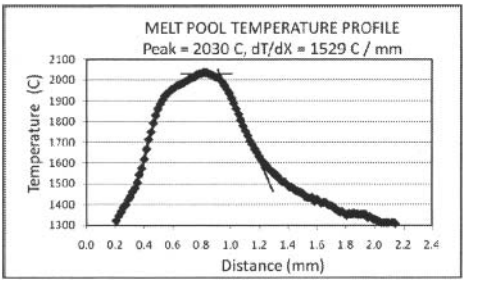

Figure 9. A temperature distribution through the melt pool in the build direction, note peak temperature of 2030°C, and a cooling rate of 1529°C / mm.

Multiple images of the melt pool were taken at each laser power and each temperature profile was analyzed. The average and standard deviation of the peak temperatures were determined for each movie, Figure 10.

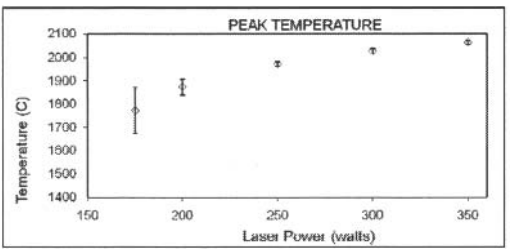

Figure 10. The peak temperatures and standard deviations are plotted against laser power.

Measurement of Cooling Rates

The first derivative of the temperature profile was taken, and the peak negative value was found (corresponding to the inflection point on the cooling side of the temperature curve). This value, in degrees per pixel, was then scaled by the optical calibration (14.4 μm/pixel) and the deposit velocity (8470 μm/s) to yield the time-dependant peak cooling rate in degrees centigrade per second, Figure 11.

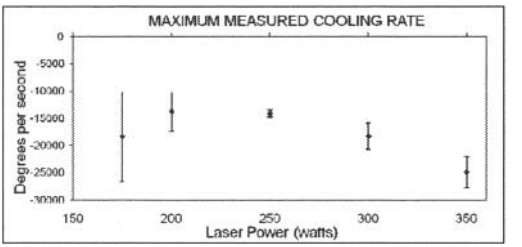

Figure 11. Peak cooling rate plotted against laser power.

Conclusions

An online imaging pyrometer has been developed to monitor the temperature distribution of the melt pool in laser additive manufacturing processes. The imaging pyrometer uses two CCD cameras with "long" and "short" wavelength filters in the NIR waveband, e.g. 750 nm for the short band and 875 nm for the long band.

In the experiment, deposit strips are formed over a variation of laser power levels, ranging from standard levels for a tool steel to about half the initial level. As the power is lowered, the deposit cross-section is reduced by approximately 50%, as are its dimensions. A movie of the melt pool temperature distribution was recorded with the imaging pyrometer for each laser power, beginning with the 6^{th} pass and ending with the final pass, e.g. the 10^{th} pass. The movies have about 3 or 4 images for each pass, and about 15 or 20 for each build.

For standard laser power levels, 300 watts, the peak temperature was observed at 2026°C which dropped to 1773°C for the lowest power of 175 watts. The variation of the temperature from frame to frame is quite small (STD = +/- 10°C) at standard power levels and increases considerably (STD = +/-99°C) at the lowest laser power level. At standard laser power levels the peak cooling levels are observed to be 18,300°C/second. Again, much larger variations in peak cooling rates are observed at the lowest laser power level when compared to the standard power level. A two-wavelength imaging pyrometer has been successfully integrated into a LENS MR-7 system. The pyrometer has been used to measure the critical deposit parameters of peak temperature and cooling rate necessary for controlling metallurgy.

References

1. W. Hofmeister, et al., "Investigation of Solidification in the Laser Engineered Net Shaping (LENS™) Process," *JOM*, 51, (7).

2. l. Wang, S.D. Felicelli, J.E. Craig, "Experimental and Numerical Study of the LENS Rapid Fabrication Process," *Metallurgical and Materials Transactions*, Sept 2007.

3. R.G. Peacock, "A Review of Non-contact Process Temperature Measurements In Steel Manufacturing," *SPIE*, 3700, (March 1999), 171-180.

4. M.L. Griffith et al., "Thermal Behavior in the LENS Process," *Proceedings of the Solid Freeform Fabrication Symposium*, Austin, TX (August 1998), 89.

5.M. L. Griffith et al., *Journal of Materials Design*, volume 20 (2/3), June 1999, 107-114.

Sensors, Sampling, and Simulation for Process Control
Edited by: Brian G. Thomas, James A. Yurko, and Lifeng Zhang
TMS (The Minerals, Metals & Materials Society), 2011

OPTIMIZATION OF CONTINUOUS HOT DIPPED GALVANIZATION LINES THROUGH THE ADDITION OF A HOT COATING WEIGHT SENSOR

Christopher Burnett[1] Dr. Andreas Quick[2]

Thermo Fisher Scientific
[1]607 Arrowwood Circle, Mount Airy, MD 21771 USA
[2]Frauenauracher Str. 96, D-91056 Erlangen Germany

Key words: Coating weight gauge, coating weight auto-control, X-ray fluorescence, hot dip galvanizing, hot gauge, metal coatings

Abstract

The ability to reliably measure the zinc coating directly above the pot allows for dramatic improvements in hot dipped galvanizing line performance. The feedback time for air knife control is nearly instantaneous. When coupled with intelligent control software in a complete coating weight auto-control system, a "hot" coating weight gauge can reduce overcoating to save raw materials, avoid undercoating and increase overall mill yield. While this location significantly improves coating weight auto-control performance due to short dead length between air knife and measurement, the environment presents electrical, mechanical, and thermal challenges that must be considered in the final sensor design.

Introduction

Sheet steel is used in every aspect of our lives, from the cars we drive, to the buildings we work and live in, to the containers that hold and transport our food. With its strength and flexibility, it is the ideal material for so many applications. It can be recycled over and over again, helping reduce landfill waste. One of the only negative properties of steel is it that it corrodes, or rusts. To prevent corrosion, sheet steel producers use specialized coatings that extend sheet steel applications into some harsh and challenging environments. Industry standards specify minimum coating weights that must be maintained. These coatings, when properly applied, improve the lifetime of the end product, and add to its aesthetic quality. The coating material and the application process can be expensive, so coating weight instruments are used to verify the thickness meets industry standards but does not exceed them to the point of wasting material.

Traditional Sensors

A variety of coating measurement methods are available to galvanization lines. ASTM Standard A 90/A 90M[1] details the laboratory method known as "weigh-strip-weigh". A sample coupon is cut from the coil, weighed, then dipped in an acid bath to remove the zinc coating and weighed again. The difference in the two masses can be converted to thickness through the density of zinc. Other coating sensors use capacitance, eddy currents or magnetic sensors that are touched to the sample coupon providing a faster, cleaner measurement. Often these measurements are made in quality control laboratories near the line. However, this is not the ideal location, as the measurements are made only in a few locations at the head or tail of the coil well after the product is made. Any required changes to the process variables are made minutes or hours later and only reflect the results of those few samples and not the coating in the body of the coil. When deficiencies are discovered, entire coils must be scrapped or downgraded, and new coils produced.

On-line Measurements

The ideal location for a coating weight instrument, when considering coating control feedback, is on-line, directly above the air knives. The on-line environment brings its own challenges, as the sensor must be non-contact, fast, and insensitive to environmental changes. The first practical consideration in selecting a sensor is that it must be non-contact. The coating applied has a primary job to inhibit corrosion, but in many cases, its secondary task, to look good, is equally important. If the sensor touches the strip at all, it would make marks, and lose much of its appeal to consumers. In the typical hot dip line (see Figure 1) a coating sensor located directly above the air knife provides the shortest feedback time possible. But the heat from the pot and horizontal strip movement physically limit a measurement sensor at this location. The more traditional sensor placement is well downstream from the cooling tower, where the environment is a bit friendlier to sensors. A complete sensor solution is available that includes sensors in both locations for maximum process optimization.

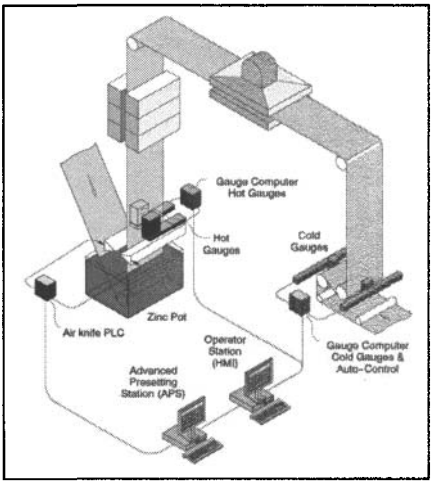

Figure 1: Hot Dip Galvanizing (HDG) Line with Cold Gauge and Hot Gauge Measurements

Measuring Principle

The coating weight of pure metal coatings on steel is generally measured by excitation of the characteristic X-ray fluorescence radiation caused by the photoelectric effect (see Figure 2). This well-known state-of-the-art method is also used as the basis for various other types of measurement, such as evaluating the intensity of several material-characteristic fluorescence radiation energies.

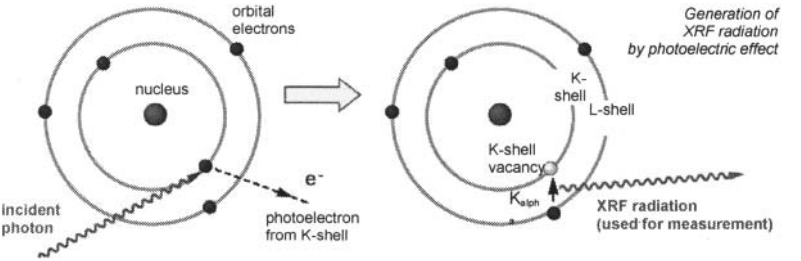

Figure 2: Generation of XRF radiation by photoelectric effect

Each element has characteristic fluorescence energies (K-alpha and L-alpha), and associated absorption-edges (K_{ab}, L_{ab}) at slightly higher energies. In practice, only the K series are normally used in coating weight gauges. The primary radiation beam must have some component energies which are higher than the K_{ab} absorption-edge energy of the element required to fluoresce at its corresponding K-alpha energy.

For measurement of thin metallic coatings applied to steel strips this X-Ray Fluorescence (XRF) principle is used. (see Figure 3) The coated steel strip is exposed to a primary beam of photon radiation. This photon radiation can be gamma rays or X-rays, having sufficiently high energy to stimulate excitation and emission (fluorescence) of X-rays. The excitation of iron atoms in a steel strip leads to emission of fluorescence radiation with an energy of 6.4 keV (1 kilo electronvolt = $1.6 \cdot 10^{-16}$ J).

If the steel strip is coated by another material, the 'iron fluorescence' radiation is attenuated while passing through the coating. If the coating weight increases, less 6.4keV radiation emitted by the steel will pass through the coating. It is also possible to use the fluorescence radiation of the coating material, zinc, to calculate a coating weight measurement. In this case, as the coating weight increases, the intensity of the zinc fluorescence will also increase.

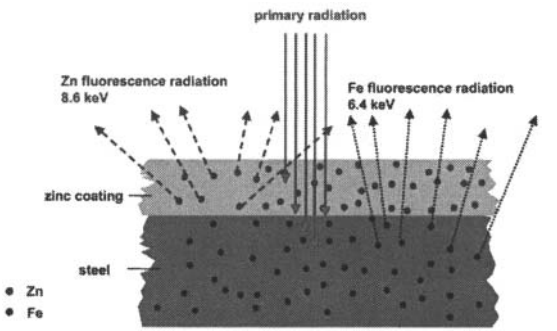

Figure 3: Measurement of zinc coating by x-ray fluorescence

Measurement at the Hot Position of the Galvanizing Line

Coating Weight Measurement

The 'hot' measuring heads for coating weight measurement of top and bottom side of the strip are using the X-ray fluorescence measuring principle described above. The coating material is exposed to the radiation from the gamma or X-ray source that causes excitation of characteristic X-ray fluorescence radiation. The intensity of this radiation depends on the coating weight being measured.

The 'Hot' measuring heads are installed in detector housings, which contain further sensors for measuring the distance from strip to measuring head and temperature. Detector housing and measuring head are water-cooled for use up to 100 °C (212 °F) ambient temperature. Additionally the detector windows are cooled by air jets. The distance between the measuring head and strip (standard distance approx. 25 mm) is continuously measured to follow the strip movement by a distance control loop with tracking mechanism. The influence of high frequency distance variations due to strip flutter is compensated by software. A temperature sensor measures the air gap temperature between measuring head and strip to compensate for changes in the temperature of the air gap. Another temperature sensor inside the measuring head checks the internal temperature to generate an alarm if over-temperature occurs and to automatically retract the measuring head from the strip.

Measuring Mechanism for 'Hot' Measuring heads

The measuring heads are mounted on detector arms that can be driven independently to the measuring or standardization position. In the standardization position, coated samples can be measured as well a capability check can be made. The detector arms can be installed on a moveable base carrier for driving to the measuring position and to the maintenance position beyond the strip zone. For the whole measuring mechanism, a maintenance and installation platform is available. The detector support and drive mechanism, junction boxes and cooling unit on this platform are completely assembled. This will drastically reduce the installation time, which is always important for galvanizing line modernization projects.

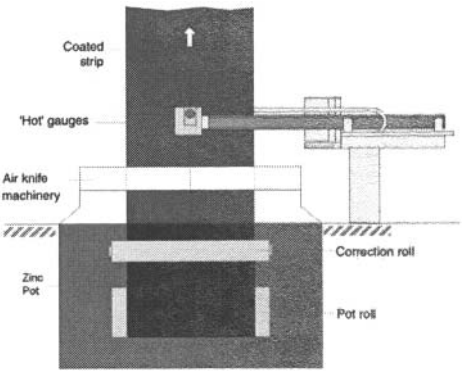

Figure 5: Typical arrangement of 'Hot' gauges

Electronics and operation

The processing electronics mainly consists of processor unit, analogue and digital I/O, high-resolution A/D converter and the Ethernet switch. The Ethernet is used for connecting to the coating weight auto-control system, the operator station and the electronics of the 'cold' measuring system for cascaded auto-control mode. Operators issue commands and monitor coating measurements through logical, easy-to-navigate screens on a PC-based operator station.

Improvement of Manual Operation of the Air Knives

At line start up, e.g. after coating device changes (air knife, bath rolls, etc.) the hot gauge provides an immediate check of the new set-up. The operator can directly see the effects of their adjustments as changes in the measured coating weight of the top and bottom side. In manual mode, each effect of fine-tuning of the coating device (air knife distance, height and angle, pot and correction roll) can be seen within a few seconds. The effects are shown on large digital displays nearby the 'hot' gauges (see Figure 6).

Figure 6: Immediate check of the adjustments of the air knives. The actual coating weight values of top and bottom side are displayed.

Improvement of Coating Weight Auto-control by 'Hot' Gauges

Typically, a coating weight auto-control system is based on the coating weight measurement with scanning cross profile gauges at the 'cold' end of the hot dip galvanizing line.

The position of the 'cold' end measuring system is about 120 m behind the air knife. (see Figure 1) At a line speed of e.g. 100 m/min (330 ft/min) the dead time is about 72 seconds. During this time, no feedback control actions can be carried out. Therefore, effects like off-center displacement of the strip between the air knives or change in roughness of the strip's surface will be recognized too late.

A closed loop auto-control using the 'hot' coating weight measurement system overcomes these disadvantages. For comparison: the position of the 'hot' end measuring system is only 2 m behind the actuator, with a dead time of only about 1 second. The auto-control performance increases significantly due to the very short response time of feedback control.

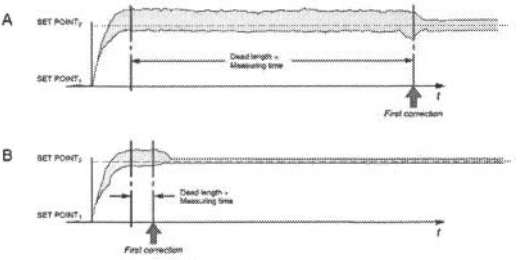

Figure 7: Reduction of dead time for auto-control by using 'Hot' gauges

The coating weight auto-control system mainly consists of a model-based Adaptive Auto-control (AAC) for continuous control during production and the Advanced Presetting System (APS). The APS serves as a presetting system for the pressure control to assure a short transition time during product change and to minimize over- or undercoated strip during and immediately after product change. The AAC provides data for the closed loop coating weight auto-control by air or nitrogen pressure control of the air knife. The following parameters can be configured in order to customize the Advanced Presetting System (APS):

Definition of "Good" Production. When storing data sets automatically, it is necessary to specify the production which should be considered as "good". For this, the coating weight variation in machine direction and along the length of the coil can be configured.

Searching the Best Matching Data Sets. The next coil data is automatically selected by comparing the setup up variables with the stored data sets. The comparison criteria for searching the best matching data sets can be configured. For example, if the variable must be equal to a specific number (e.g. air knife number), or fall within a set tolerance (e.g. air knife distance). The APS will use the criteria to search the existing preset data sets for most ideal set up for the next coil. To influence the search process, engineers can establish weights, for each variable to be used in the search. This search option provides a very flexible tool to operators when handling the technical demands of various coating processes such as Zinc, Galvalume, or Galvanneal. Operators can view the current search criteria on the main HMI page of the APS.
The ideal architecture of the coating weight auto-controller does not require a hot gauge and will still provide excellent results when working with a cold gauge only. But in order to emphasise the advantages of having a hot gauge, it is assumed in the following that both gauges are available.

Control Features and Control Loops

The coating weight control (CWC) is based on an adaptive non-linear process model, which uses the results of the measurement systems for feed-back control. Changes of the material speed and the air knife to strip distance lead to a feed-forward control step. The control steps are based on a process model which is obtained from the data automatically learned in the presetting system. To improve the base algorithm of the coating weight controller the following control features are available to control the air pressure of the air knives:

Cascade Control

Both gauge systems are used for coating weight control in a combined control algorithm (intermeshed control). New coating weight set points for the hot gauges are calculated by evaluating the average value of the cross profile considering the three spot values. Since the results of the cold gauges are used for the quality reports, the cold gauges are the "master" in the cascade control. In addition to getting the set points from the cold gauge, the controller continues to perform the primary control cycles based on the hot gauge measurement values in order to control fast product variations (either using feed-back or feed-forward steps).
If the hot gauge is not available or switched off for maintenance, the "Cascade Control" function is not available, but the coating weight controller is fully functional and coating weight control is executed based on the values from the cold gauge only.

Target Optimization Control (TOC)

The measurements taken by the scanning cold gauges are used for a dynamic optimization of the coating target to keep the zinc consumption as low as possible. Through evaluation of the statistical distribution (sigma value) of the coating in machine and cross direction, the control set point is adjusted, considering the given tolerance limits and the actual production variance. Production of the coated product will be as close as possible to the allowed minimum coating weight set point (see Figure 8).

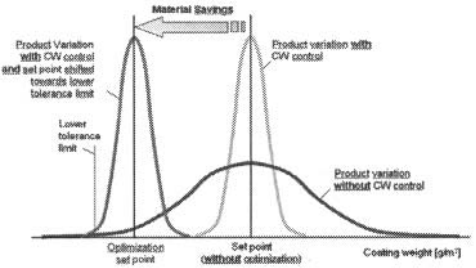

Figure 8: Production without CWC, with CWC, and with TOC

Sum Coating Control (SCC) With this control feature, the arithmetic average of the top and bottom target pressures is applied to the air knife system. With both sides of the air knife then operating with the same pressure, 'blowing away' of the strip is avoided. Using this control feature, the sum coating weight is on target, but the top and bottom coating weights may be different. In this case, the air knife distance can then be adjusted either by the operator or automatically by Automatic Balance Control (ABC) as a supplemental feature for the sum coating control. To work completely, the "same spot scanning" function of top and bottom cold gauge is required for systems with two single beam scanners in the cold location.
The following control-loops are available to manage the mechanical position of the air knives, but only if the air knives can be positioned and if the air knife PLC allows remote positioning control of the air knives.

Automatic Balance Control (ABC) If product requirements demand the same coating weight for top and bottom side (set point top = set point bottom), the function Automatic Balance Control can be activated together with the Sum Coating Control function. Automatic Balance Control adjusts the air knife to strip distance, so that the coating weight of both sides is the same.

Cross Profile Control (CPC) The cross profile control works independently from the air knife pressure control and corrects the coating weight cross profile through adjustment of the air knife distance at the edges. Appropriate implementation of this control function results in a smooth cross profile with minor variations in cross direction.

Air Knife Distance Adjustment (AKD) If the pressure set point calculated by the CWC exceeds the upper and lower pressure limits configured at the HMI of the CWC, the distance of the air knife to the strip is automatically changed such that the pressure set point is brought back to the allowed range.

SUMMARY

For HDG lines, the ideal coating weight measurement and control architecture described in this paper leads to homogenous and cost-effective production. Auto-control improves the product quality and minimizes the zinc consumption. When dealing with varying line conditions and changing product targets, an adaptive coating weight controller is necessary. By using a coating weight gauge designed for the challenging environment directly above the air knives, the zinc consumption can be significantly reduced. The savings are dependent on the line condition and on the number of product changes per day, but have exceeded a half a million dollars annually for some installations. When coupled with the coating weight controller presented in this paper, the product variation can be tightened shifting the target set point very close to the minimum set point. This leads to a uniform production with minimized zinc consumption and higher profits.

REFERENCES

1. ASTM Standard A90 / A90M (2009), " Standard Test Method for Weight [Mass] of Coating on Iron and Steel Articles with Zinc or Zinc-Alloy Coatings," ASTM International, West Conshohocken, PA, 2006, DOI: 10.1520/C0033-03R06, www.astm.org.

Dr. Andreas Quick, Rainer Mestermann and Christopher Burnett, "Ideal Coating Weight Controller Architecture for Hot Dip Galvanizing Lines" (Paper presented at the Asia Pacific Galvanizing Conference 2009, Jeju, Korea, November 8, 2009)

Dr. Joachim Olschewski, "Improvement of the Hot Dip Gavlanizing Process by a 'Hot' Coating Weight Measuring and Control System" (Paper presented at the AIST Mexico/CONAC, Moterrey, Mexico, November 15, 2005)

Sensors, Sampling, and Simulation for Process Control
Edited by: Brian G. Thomas, James A. Yurko, and Lifeng Zhang
TMS (The Minerals, Metals & Materials Society), 2011

MONITORING OF MENISCUS THERMAL PHENOMENA WITH THERMOCOUPLES IN CONTINUOUS CASTING OF STEEL

B.G. Thomas[1], M.A. Wells[2] and D. Li[3]

[1]Department of Mechanical Science and Engineering,
University of Illinois at Urbana-Champaign; 1206 West Green Street, Urbana, IL 61801

[2]Department of Mechanical and Mechatronics Engineering, Waterloo University

[3]Belvac Metal Forming Company 237 Graves Mill Road, Lynchburg, VA 24502-4203

Keywords: Thermocouples, Sensors, Measurement, Continuous casting, Modeling, Level control

Abstract

Many quality problems in continuous-cast steel are related to mold level fluctuations, stickers, deep oscillation marks, and other events at the meniscus. These phenomena may be detected by monitoring temperature signals in the wall of the copper mold. This work applies computational models of transient heat conduction to investigate the potential capabilities of mold thermocouples to detect such phenomena by computing the sensitivity of the detected signal to heat flux variations at the meniscus. The three-dimensional model is first validated with temperature data recorded in a commercial slab casting mold, and in a previous laboratory measurement. The method is capable of monitoring meniscus level, and to detect large surface level fluctuations. However, its ability to detect temperature fluctuations decreases with decreasing magnitude and duration of the level fluctuations and the distance of the thermocouple from the hot-face surface. Sensitivity calculations with the model are presented to quantify these detection limits. Finally, a new inverse heat-conduction model is applied to extract new insights into heat transfer at the meniscus from thermocouple measurements.

Introduction

During continuous slab casting, molten steel flows through a "Submerged Entry Nozzle" (SEN) into a water-cooled copper mold. The steel solidifies a thin shell, which contains the liquid and is withdrawn at a casting speed that matches the flow rate. Fluctuations of the position of the molten meniscus (metal level) disrupts solidification at the meniscus, entrains slag inclusions, and leads to many quality problems. These include deep oscillation marks, stickers, and even catastrophic "breakouts. Liquid level is usually measured with an expensive commercial system to maintain liquid level within +/- a few millimeters, using a suspended eddy-current level sensor (which measures a single spot somewhere between SEN and the narrow face), or a radiation detector (which averages over a volume that is blocked by metal) [1].

Another potential method to quantify the metal level during continuous casting is to utilize the temperatures measured continuously by thermocouples (TC's) embedded in the copper mold. This inexpensive method has been applied commercially by "LevelTherm" to control level within +/-20-30mm in billet/bloom casting [2]. If sufficiently accurate, this method would have the potential advantage of providing information around the entire perimeter of the meniscus,

allowing for more precise monitoring of surface quality in addition to controlling liquid level. This paper investigates the potential use of a two-dimensional Inverse Heat Conduction model to interpret the dynamic variations of measured TC temperature signals into the dynamic variation of the metal level in the mold during the process. The ability of a model-based system to achieve this goal is investigated by comparing the predictions of a transient heat-conduction model with actual mold temperature measurements. A parametric study is then performed to determine the theoretical sensitivity of this method to resolve level fluctuations of different amplitudes and frequencies. This work provides important new insights into the use of thermocouples to monitor meniscus heat transfer and liquid surface level in continuous casting of steel.

Model Description

A three-dimensional finite-element model of transient heat conduction has been developed to predict temperature histories in a representative segment of a commercial continuous casting mold. The 132.5mm-wide x 172.5mm-long model domain of a segment of the top portion of the copper mold wall is shown in Fig. 1. This segment domain includes the top portions of 7 water slots (2 deep and 5 shallow) with their curved ends, the molten steel meniscus, and two recessed bolt holes, each containing a thermocouple from the two thermocouple rows used for breakout detection. To match the plant measurements, the thermocouples are modeled as 2.2mm diameter cylinders centered in 2.4mm holes drilled through the bolts, with air in the annular gap and a 0.1mm layer of conductive paste between the TC tip and the copper mold. The vertical boundaries are symmetry planes, as the segment can be repeated to reproduce the entire wide face of the mold. The water slots are constant heat convection boundaries with a coefficient 45kW/m^{2}K to an ambient temperature of 30°C. The mesh contains 24,836 elements and 40,310 degrees of freedom. Further details are given in Tables I and II and elsewhere [3].

Table I. Model Geometry and Simulation Conditions

Copper plate thickness	43mm
Bolt diameter	16mm+2mm threads = 20mm total
Steel grade	441(01) ferritic stainless steel
Casting speed	1.04 m/min
Strand width	1290 mm
Segment width	132.5mm
Base meniscus level below mold top	95mm
Top thermocouple height above meniscus	42mm
Bottom thermocouple below meniscus	115mm
Water channel spacing / spacing across bolts	15mm / 45mm
Water channel thickness	5mm

Table II. Model Material Properties

Material	Thermal Conductivity (W/m °C)	Specific Heat (J/kg-K)	Density (kg/m^3)
Copper (Cu-Ag-0.1P)	364.	386.	8960.
Constantan (for K-thermocouples)	216.	416.	8900.
TC conducting Paste	0.9	2800.	2100.
Air (for air gap)	0.028	1040.	1.2

Model Validation

To test the accuracy of the model, it is first applied to simulate the transient temperature variations during a severe level fluctuation at the commercial steel continuous caster [3]. The hot-face is given a heat flux boundary condition which varies with distance down the mold (z-direction) as shown in Fig. 2. This profile is translated vertically up and down the mold according to the surface level history recorded by the eddy-current sensor at the plant. The severe level fluctuation during this time interval dropped ~30mm and lasted ~50s. Results are presented in Figs. 3 and 4.

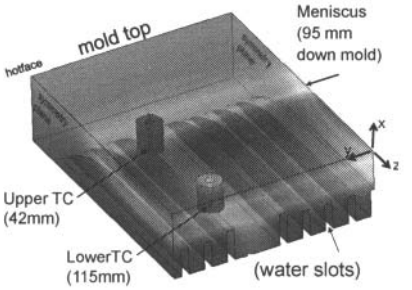

Fig. 1. Model domain and steady temperature distribution

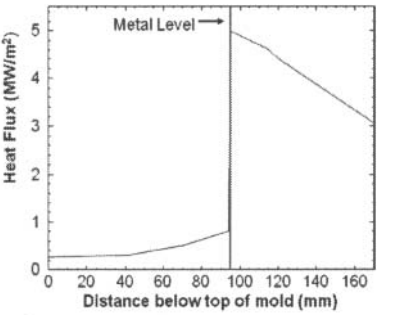

Fig. 2. Heat flux profile on mold hot-face versus distance below top of mold

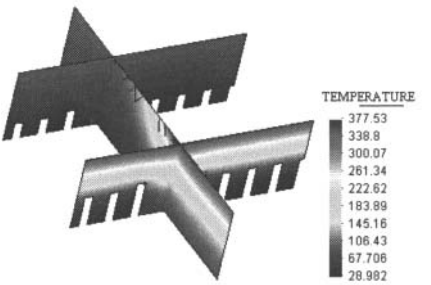

Fig. 3. Steady temperature contours (°C) in mold sections for base mold level (95mm down mold)

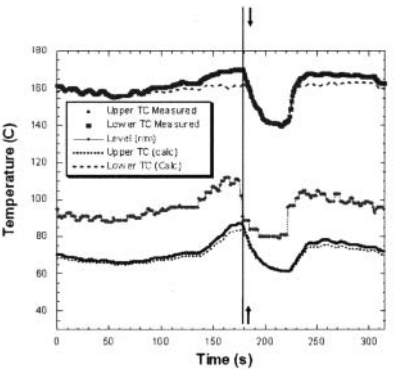

Fig. 4. Transient temperature histories predicted at thermocouple locations compared with measurements. Measured surface level position is also shown (in mm below mold top).

The initial steady-state temperature distribution is shown in Figs. 1 and 3, where the base liquid surface (meniscus) level is 95mm. The bolts require a larger spacing between water slots, which tends to increase the mold temperature in that region. To compensate for this, the two adjacent water slots are machined deeper into the mold beside this region, which tends to lower the

temperature in this region. The net result is a surface temperature distribution across the mold (y-direction) which is only slightly larger opposite the bolts. The sharp peak in heat flux at the meniscus diffuses both up and down the mold (z-direction), which causes the mold hot-face surface temperature to reach a peak of ~380°C at about 25mm below the heat flux peak at the meniscus, which is below the lower TC for these conditions. The maximum cold-face temperature at the root of the water slots exceeds the water boiling temperature, which is ~120°C for the pressurized conditions in this mold. The upper and lower TC tip temperatures are 68°C and 159°C.

The transient results in Fig. 4 show that the temperature responses predicted at the location of the thermocouple beads in the mold wall match very well with the actual measurements. This demonstrates that the model is reasonably formulated, including the boundary conditions, and that liquid level variations cause mold temperature variations which can be accurately predicted. Even the small wiggles in the temperature response caused by wiggles in the liquid level can be detected. A slight error is observed for the lower thermocouple location, where the model tends to smooth away the peaks. This may have been due to insufficient mesh refinement. Mesh resolution was improved in the copper hot-face above the TC tips for the later parametric study.

The liquid level drop causes a drop in temperature at both TC locations in this work, owing to the net decrease in heat flux reaching the interior at each location. At the upper TC, heat must always conduct upwards (z-direction) from the meniscus region, so its temperature always drops when the level drops. When the lower TC is positioned lower down the mold, however, a drop in level sometimes causes its temperature to increase, as the peak in the heat flux curve becomes closer. In addition, a level fluctuation may cause changes in mold flux infiltration, leading to changes in the heat flux profile. Thus, temperature response at the lower TC is more difficult to interpret for several reasons. Fig. 4 also shows that the temperature response of both TCs lags behind the level signal by several seconds, as expected, owing to the large thermal inertia of the thick copper mold wall.

Parametric study of TC sensitivity to level fluctuations

The validated model was then run to investigate the influence of level fluctuation severity on the mold thermocouple temperature response. The ability of thermocouples to detect liquid level was found by manufacturing a sinusoidal level fluctuation and varying its duration (1/frequency) from 1-6s, amplitude from 2-20mm, thermocouple detection limit (+/- 1-2 °C), and thermocouple position beneath the hot-face surface in the mold wall.

A typical manufactured surface level signal is shown in Fig. 5 for a liquid surface level

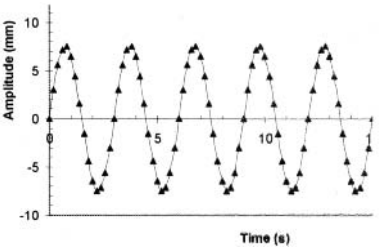

Fig. 5. Liquid level oscillation frequency and amplitude

oscillating with 7.5mm amplitude (15-mm variation from peak to peak), and 3s-duration (0.33 Hz frequency).

Fig. 6 shows the corresponding temperature responses predicted for the two thermocouples. After a brief initial transient, the model converges to a "pseudo-steady state" stably-oscillating temperature profile. The frequency matches the level fluctuation frequency, with a phase lag, as expected. The peak-to-peak magnitude of the fluctuating temperature signal is ~0.2°C (0.1 °C amplitude) at the upper TC and ~1°C at the lower TC. For a TC detection limit of 1°C, this variation at the upper TC is not detectable for this example, while it is at the critical detection limit at the lower TC. Peak-to-peak magnitudes were recorded from the steady converged results of 34 different simulations.

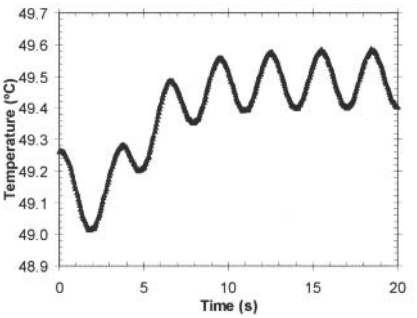

Fig. 6 a). Temperature predicted at upper TC

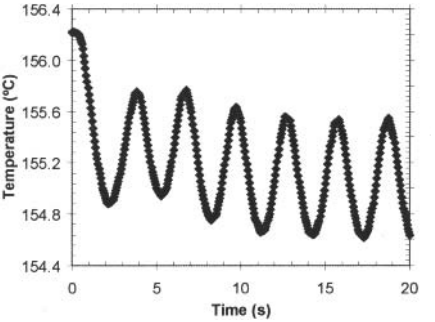

Fig. 6 b). Temperature predicted at lower TC

Fig. 7 shows the critical metal level fluctuation that produces a 1°C temperature fluctuation at the upper and lower thermocouples. Error bars indicate the uncertainty that arises from interpolating these critical detection limits from discreet simulation results. Larger fluctuations of longer duration (upper right of the lines) are detectable, while smaller fluctuations of shorter duration (lower left of the lines) are not. These results show that detecting a level fluctuation requires both a sufficiently-high amplitude and a long-enough duration. Short-duration (< 1s at the lower TC) level fluctuations cannot be detected, even if they are very large. Similarly, small height (<2mm) level changes cannot be detected, even if their duration is long.

The temperature changes at the lower TC are much larger, owing to the larger heat flux below the meniscus. Thus, the effects of a surface level change are predicted to be easier to detect at the lower TC, as indicated by its critical line being closer to the origin in Fig. 7. In reality, however, the lower TC is subject to other sources of temperature variation, such as variations in mold slag infiltration and conductance across the mold-shell gap. Thus, the upper TC might produce more reliable signals for the detection of mold level changes. The upper TC can just barely detect a level fluctuation of 12.5mm-amplitude and 4s duration. Such a level fluctuation is quite severe, and would likely produce a surface quality problem in the cast product. Thus, it would be desirable to find a sensor that is more responsive.

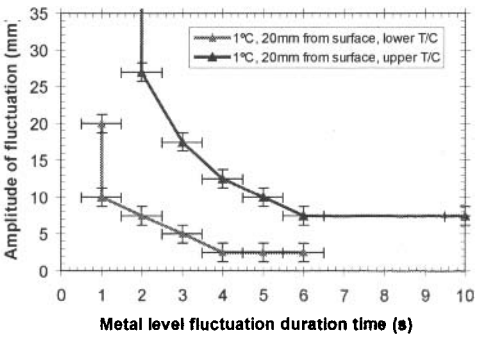

Fig. 7. Thermal response at standard upper and lower TC locations (1°C detection limit)

The opposing effects of decreasing the TC sensitivity and moving the TC closer to the hot-face surface of the mold are shown in Fig. 8 for the lower TC. Moving the TC closer to the hotface makes detection easier. The 10-mm deep TC can detect level fluctuations that are only 2/3 the duration of the detection limit at 20-mm. On the other hand, decreasing the TC sensitivity from 1°C to 2°C almost exactly cancels this improvement, as the 10-mm 2°C case in Fig. 8 almost exactly matches the 20-mm 1°C case in Fig. 7. Naturally, level fluctuations are more easily detected by more sensitive thermocouples located closer to the mold hotface surface. These findings are consistent with findings based on experimental thermocouple measurements with oscillating surface heat flux [4].

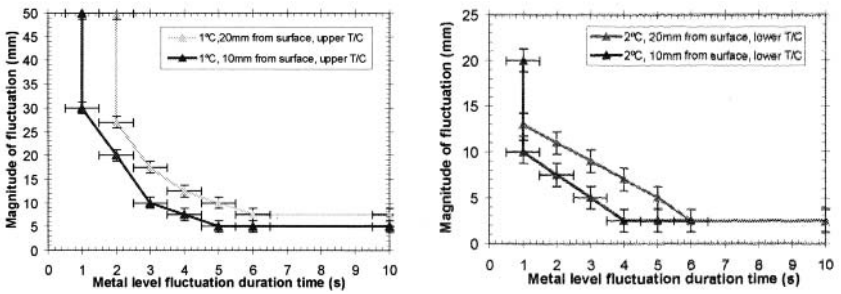

a) 1°C detection limit b) 2°C detection limit

Fig. 8. Effect of TC distance beneath hot-face on critical detectable level fluctuation at lower TC

Inverse Heat Conduction Model

To predict the liquid level change directly from the measured thermocouple history requires inverting the transient heat conduction model used to generate the preceding results. As a first step towards this goal, a two-dimensional inverse heat-conduction model was developed in this work to predict the time-varying heat flux profiles from an array of measured mold temperature histories. To test the model, it was applied to interpret the TC measurements of a mold simulator [5]. The water-cooled mold plate has two columns of embedded thermocouples located 1.5mm

and 5mm from the hot-face surface, as shown in Fig. 9. The TC labels represent the TC distance from the plate bottom. This plate is inserted into the molten steel bath at a "casting speed" of 12.7mm/s while being oscillated at a frequency of 1.3Hz (i.e. period of 0.77s) and a stroke of 6.3mm. Property data for the copper is given in Table 1. The nominal meniscus level was adjacent to TC 4. Further details on this experiment and the measured TC temperature histories are published elsewhere [5].

Results from the inverse model are presented in Figs. 10-12. First, a 1-D form of the inverse model was performed by neglecting axial heat conduction, and solving for horizontal heat conduction between each TC pair. As shown in Fig. 10, these predictions agree reasonably with the previous heat flux results, which used a similar 1-D inverse heat conduction model [5].

Predictions using the new 2-D inverse heat conduction model are shown in Fig. 11. The time averages of the 1-D and 2-D results are compared in Fig. 12. Much greater variations in surface heat flux are predicted, owing to the important averaging effect of axial conduction in the copper wall. These wide variations range from very high values, approaching those found in

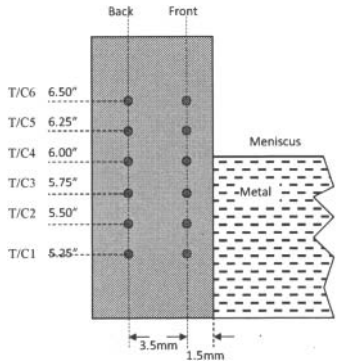

Fig. 9. TC locations in mold simulator [5]

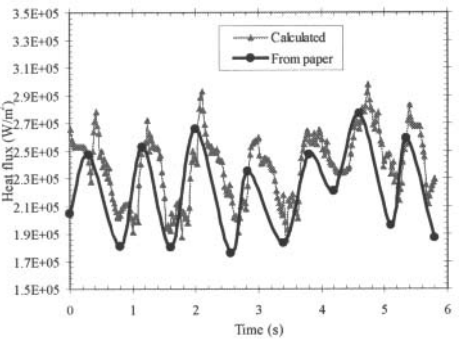

Fig. 10. Comparison of 1-D inverse model results [5]

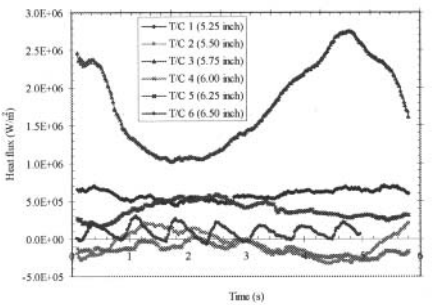

Fig. 11. Calculated heat flux histories on the mold surface (2-D inverse model)

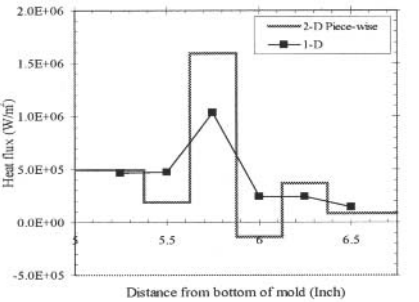

Fig. 12. Time-average heat flux profile down mold (z direction)

commercial casters, to very small – even negative! - values. The negative values are believed to be numerical errors associated with sudden drops to very small heat fluxes, which are expected when the liquid level drops below a given point on the mold wall. These results suggest that surface heat flux variations are much larger than expected from previous work, owing to liquid level variations and related transient behavior.

Conclusions

A new method to understand mold temperature variations near the meniscus has been developed using inverse transient heat-conduction models and has been applied to investigate the measurement of mold level fluctuations using thermocouples embedded in the mold walls. Compared with other techniques used to measure mold level variation, this new inexpensive method is shown to be capable of providing quantitative information on the temporal fluctuation of the metal level in the mold. The method is limited, however, in the amplitude and frequency of the level fluctuations it can detect by the large distance of the thermocouples from the mold surface. For conventional thermocouples used in commercial practice, located 20mm beneath the hot-face surface, temperature response can be accurately related to surface level fluctuations in the mold, at least when they are severe. The minimum level fluctuation that can produce a barely-detectable 1°C variation at a 20-mm-deep upper TC is about 8-mm amplitude (for a low-frequency level fluctuation) or 2s duration (for a high-amplitude level-fluctuation). Thermocouples located above the meniscus are more reliable for level detection, even though they are less sensitive, due to the smaller temperature changes. Locating the thermocouples closer to the hot-face surface of the mold greatly increases their sensitivity. Inverse heat conduction models can be used to transform mold thermocouple temperatures into liquid level and to reveal variations in meniscus heat flux.

Acknowledgements

Initial work on this project by former UIUC PhD student Tim Morthland is greatly appreciated. Thanks are also extended to Johan Ackermann and Columbus Stainless Steel, Middleberg, South Africa, for supplying the plant measurements and data. This work was funded by the Continuous Casting Consortium at the University of Illinois, and an NSERC grant at the University of British Columbia, which is gratefully acknowledged.

References

1. C. Singh, X. Rabec, and M. Dussud, "Mould Level System Upgrade at ArcelorMittal Dofasco's #1 Caster", AISTech 2008, Steelmaking Conference Proc., Pittsburgh, PA, May 5-8, 2008, Assoc. Iron Steel Tech., Warrendale, PA, Vol. 1, 2008.
2. R. Caskey, "Thermal Mold Level Control at Nucor Steel Seattle Inc.", AISTech 2008, Steelmaking Conference Proc., Pittsburgh, PA, May 5-8, 2008, Assoc. Iron Steel Tech., Warrendale, PA, Vol. 1, 2008.
3. Thomas, B. G., and T. Morthland, "3-D Transient Heat Transfer Analysis of Columbus Slab Casting Mold," Continuous Casting Consortium Report, UIUC, 42, Dec. 15, 2002.
4. Badri, A.B., and A. W. Cramb: "Heat Flux Calculation from Thermocouples-What can be measured?", 85th Steelmaking Conference, Nashville, TN, USA, Mar. 10-13, 2002, 2002, Iron and Steel Society, 65-76.
5. A. Badri, T. T. Natarajan, C. C. Snyder, K. D. Powers, F. J. Mannion, and A. Cramb: 'A Mold Simulator for the Continuous Casting of Steel: Part I. The Development of a Simulator', Metallurgical & Materials Transactions B, 2005, 36B, 355-371.

Sensors, Sampling, and Simulation for Process Control
Edited by: Brian G. Thomas, James A. Yurko, and Lifeng Zhang
TMS (The Minerals, Metals & Materials Society), 2011

IMPLEMENTATION OF TEMPERATURE AND STRAIN MICRO-SENSORS INTO A CASTING MOLD SURFACE

B.G. Thomas and M.K. Okelman

Department of Mechanical Science and Engineering,
University of Illinois at Urbana-Champaign; 1206 West Green Street, Urbana, IL 61801

Keywords: Fiber Bragg Grating, Thin-film thermocouples, Embedded sensors, Measurement, Continuous casting, Coatings, Electroplating

Abstract

Microfabricated thin-film thermocouples (TFTCs) and Fiber Bragg Grating (FBG) sensors can be embedded in the coating layers of the mold during electroplating to measure temperature, heat flux, and strain during continuous casting. Embedding sensors within 1mm near the surface has the advantages of sensitive real-time monitoring of thermal behavior without damping by the copper mold, and protection from the hostile environment. A method to embed TFTCs and FBG optical fibers in a coating layer was developed, implemented and tested. The signal output by FBG sensors embedded in a nickel coating layer on a copper mold has been investigated and can be predicted with simple equations. These sensors are able to monitor both temperature and strain in real time during casting operation with high resolution.

Introduction

Many problems in continuous casting of steel and other processes arise during initial solidification near the meniscus where molten metal first touches the mold. These include surface defects in the final product as well as cracks in the mold surface due to thermal stress. Understanding the underlying phenomena and controlling them requires both advanced modeling and measurements. Sensors are limited to indirect measurements, because the mold surface and beyond is an extremely hostile environment and sensors there would interfere with the process. In current industrial practice, several horizontal rows of thermocouples are embedded into each mold wall, keeping 7 to 20 mm away from the hot face, due to safety considerations [1]. Their temperature signals are interpreted by systems installed in most casters to control mold level control [1], to detect and prevent sticker breakouts [2], and to monitor steel quality [3]. While they are very useful, these systems are limited by the slow response time of the thermocouples, which are dampened by the thick copper mold layer between them and the solidifying steel, so they cannot fully capture the rapid thermal events that occur at the meniscus [4, 5]. Moreover, problems related to thermal distortion of the mold, and thermal cracks cannot be detected, owing to the lack of robust thermal strain sensors.

Microfabricated thin-film thermocouples (TFTCs) and / or Fiber Bragg Grating (FBG) sensors can be embedded in the nickel coating layer that is electroplated onto many continuous-casting molds and then used to measure temperature, heat flux, and thermal strain within 1 mm of the meniscus. This cost-effective method would enable sensitive real-time monitoring of critical thermal and mechanical behavior with fast response time, and protection from the hostile environment. With the ability to place many sensors within close proximity of one another, embedded sensors could enable more accurate prediction of liquid level and its transient

fluctuations. More sensitive online monitoring of mold temperature variations would extend their usefulness, providing additional insights into casting phenomena, thereby enabling detection of the formation of defects such as longitudinal cracks, by better distinguishing their distinctive temperature-history "signatures" [5].

Implementing these advantageous micro-sensors requires a robust attachment method that 1) provides a secure bond between the sensor and the copper with no gaps, 2) enables the sensor to survive the acid pretreatment and electroplating processes, and 3) allows it to provide accurate measurements during operation. This paper presents the design, installation, and interpretation of micro-sensors in commercial molds for continuous casting of steel. Equations are developed to interpret the signals from embedded FBG sensors as functions of temperature and strain. The final system proposed aims 1) to revolutionize online thermal monitoring of industrial continuous casting molds and 2) to create a new research tool to investigate meniscus behavior so that defect formation can be better understood.

The design is presented in Fig. 1, for the example of a TFTC sensor strip. In addition to their expense, these rectangular cross-section sensors were found to be susceptible to gap formation during plating, which could cause catastrophic temperature increases during operation [6]. Their implementation is still feasible using a robust conductive silver paste, as discussed elsewhere [6]. This paper focuses on FBG sensors.

The first step is to embed the fiber containing the sensor(s) into the coating layer during electroplating of the mold. The optical fiber consists of a 9 μm diameter core, protected with a 125 μm thick layer of thermoset polyimide, which can survive the entire temperature range of mold operation up to 500°C [7]. The total fiber diameter of 155μm easily fits inside a typical 300 - 400 μm thick nickel coating layer. Each FBG sensing region consists of several grating layers that are optically etched into the fiber in order to amplify and reflect back light of a particular frequency. After plating, the sensor fiber extends from to the top of the mold, allowing easy extraction of the sensor signals to a computer, such as by attachment to a miniature circuit box for wireless transmission to a computer located elsewhere.

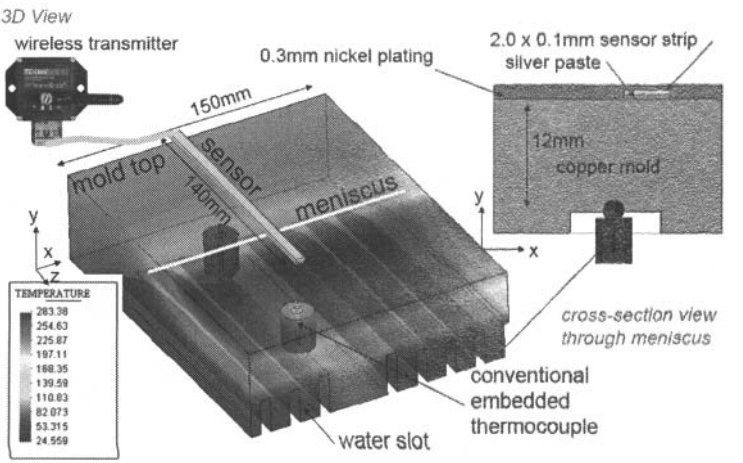

Figure 1. Sensor embedded in Ni coating layer of continuous casting mold (temperature in °C)

Testing was conducted to embed optical fibers into the nickel coating layer of continuous casting mold samples using the commercial electroplating process for continuous casting molds at a commercial mold plating facility in Benton Harbor, MI. Pretreatment involved immersion in dilute acid solution, followed by electroplating in nickel sulfamate for several hours. Cylindrical fibers always produced sound plating, for both conducting and insulating fiber materials. Sound plating was found even when several fibers were very close together, as seen in Fig. 2. Such close spacing can enable high spatial resolution.

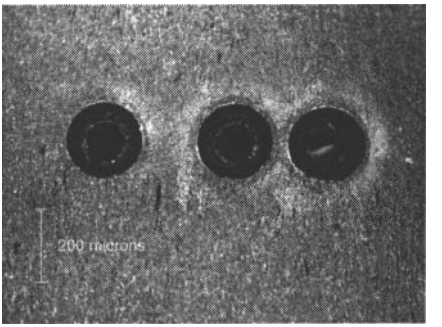

Figure 2. Several FBG sensors (200 μm diameter, plastic coated optical fibers) after electroplating with nickel

Close proximity to the substrate also produced sound plating. Further details on the electroplating trials are reported elsewhere [8].

Trials were conducted on both embedded FBG fibers and on 316-stainless steel tubes containing the fibers. The latter are pictured in Fig. 3. A closeup of the fiber exiting the tube near the top of the mold is shown in Fig. 4. Larger tubes (OD 330 μm, ID 178 μm) contained the 155 μm diameter plastic-coated fibers, while smaller tubes (OD 254 μm, ID 127 μm) housed bare optical glass fibers.

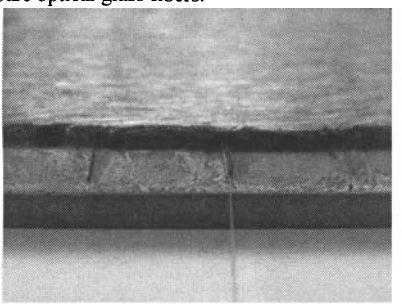

Figure 3. Stainless steel tubes embedded in coating layer

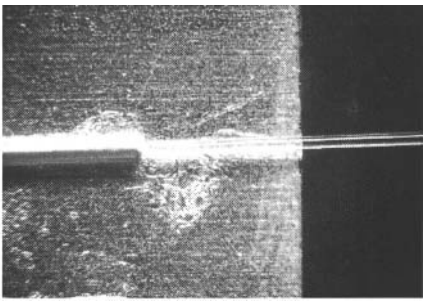

Figure 4. Closeup of polyimide-coated fiber with FBG sensors inserted into a steel tube

Having demonstrated that both cylindrical optical fibers and steel tubes containing free-moving fibers can be embedded soundly into the mold coating, heating and cooling tests were conducted on the final system to demonstrate the ability of the sensors to measure temperature and strain. The fiber was a transmission-type FBG sensor with center wavelength 1543.30 nm (provided by O/E Land Inc.). A second fiber of just the bare-glass core was damaged during handling, which is a difficulty to address for commercial operation. Specifically, the fibers extending from the mold need to be encased in temporary protective material during plating, and the fragile junction where they attach to the transmission box at the top of the mold needs to be protected during operation.

Interpretation of Fiber-Bragg-Grating Sensor Signals

The interactions between the sensor and substrate are complex, so interpretation of the signals from the FBG sensors into temperature or strain measurements is not simple. Each FBG sensor measures a Bragg wavelength shift according to the length fiber length, with changes with both temperature and mechanical strain. The signal output is potentially a combination of four quantities (three principle strains and temperature) [9]. It is possible to calibrate a FBG sensor (or FBG sensor system containing more than one sensor) for a given load, but the results would only be valid under conditions that produce a nearly identical temperature and strain as those used during calibration. Instead, for structurally embedded FBG sensor temperature measurement systems it is better to determine the optical properties of the FBG sensor as a function of temperature and wavelength [9] and use them together with the FBG sensor's strain-based properties to predict the temperature.

The signal output by the FBG sensor corresponds to the temperature and strain at the FBG sensor, not to the substrate, as a sensor embedded inside the substrate disturbs the strain and temperature field. The signal output by the FBG sensor (the "temperature" and "strain" at the sensor) must be related to the temperature and strain in the host material. This analysis has been conducted for both bare and coated fiber optic sensors [6,10]. The results show that some of the strain components inside the sensor may differ if the sensor is bare or coated. Furthermore, the difference depends on the thickness and properties of the coating.

As inferred from above, when a strain is applied to a FBG sensor its grating spectral response, or Bragg wavelength, is changed (i.e. the Bragg wavelength is dependent on both temperature and strain). Assuming that the bond between the fiber and the substrate is strong (i.e. the "temperature" and "strain" at the sensor is equal to the temperature and strain of the substrate), the total Bragg wavelength shift for an embedded FBG sensor has two components:

$$\Delta\lambda_{total} = \Delta\lambda_{temperature} + \Delta\lambda_{strain} \tag{5}$$

The thermal effect component ($\Delta\lambda_{temperature}$) is related to the change in index of refraction:

$$\Delta\lambda_{temperature} = \lambda_{CW}\left(\alpha_f + \frac{1}{n_0}\frac{dn_0}{dT}\right)(T - T_0) \tag{6}$$

where λ_{CW} is the Bragg center wavelength of the FBG sensor (1543.30 nm for the embedded FBG sensor, 1541.04 nm for the free-floating FBG sensor), α_f is the coefficient of thermal expansion (CTE) of the fiber (i.e. silica), n_0 is the index of refraction, dn_0/dT is the thermo-optic coefficient, T_0 is defined as the temperature at the first measurement of the Bragg wavelength, λ_0, during calibration and T is the temperature corresponding to any of the Bragg wavelength measurements.

The strain component ($\Delta\lambda_{strain}$) due to the physical elongation of the sensor, as well as the change in refractive index due to photoelastic effects, is given by:

$$\Delta\lambda_{strain} = \lambda_{CW}(1 - p_e)\left(\varepsilon - \alpha_f(T - T_0)\right) \tag{7}$$

where ε is the mechanical strain and p_e is the photoelastic coefficient given by:

$$p_e = \left(\frac{n_0^2}{2}\right)\left[p_{12} - \nu(p_{11} + p_{12})\right] \tag{8}$$

where ν is the Poisson's ratio of the fiber (i.e. silica) and p_{11} and p_{12} are Pockel's coefficients. Typical values selected for theoretical calculations are given in Table I [6].

Table I. Optical fiber constants used in calculations

α_s	Substrate coefficient of thermal expansion	13.1 x 10^{-6} /°C
α_f	Fiber coefficient of thermal expansion	0.55 x 10^{-6} /°C
n_0	Refraction index	1.46
dn_0/dT	Thermo-optic coefficient	11 x 10^{-6} /°C
v	Poisson ratio	0.2
p_{11}, p_{12}	Pockel's coefficients	0.113, 0.252

The mechanical strain can be calculated two different ways. The strain of the fiber surface is equivalent to the applied strain from the substrate in case of good contact and can be approximated by the following simple "CTE" equation:

$$\varepsilon = \alpha_s (T - T_0) \tag{9}$$

where α_s is the coefficient of thermal expansion of the substrate. Alternatively, the mechanical strain can be calculated via the analysis of a bimetallic beam. When a beam made up of two strips of materials of different elastic moduli and of different coefficients of thermal expansion is subject to a uniform temperature change it will bend [11]. Its curvature and deflection, as well as the mechanical strain in the axial direction of either of the two strips, can be calculated. The curvature of a bimetallic beam is not very sensitive to differences in elastic moduli but is rather sensitive to the differences in the coefficients of thermal expansion [11]. Using this assumption it can be shown that the mechanical strain in the axial direction in the top strip can be calculated using the following "beam" equation:

$$\varepsilon = \alpha_{top}(T - T_0) + \frac{1}{4}\frac{(\alpha_{bottom} - \alpha_{top})}{\left(1 + \frac{E_{top}}{E_{bottom}}\right)}(T - T_0) - \frac{3}{2h}(\alpha_{bottom} - \alpha_{top})\left(y - \frac{h}{4}\right)(T - T_0) \tag{10}$$

where y is measured from the bottom of the bottom strip, h is the total thickness of both strips, α_{top} is the coefficient of thermal expansion (CTE) of the top strip, α_{bottom} is the coefficient of thermal expansion (CTE) of the bottom strip, E_{top} is the elastic modulus of the top strip, and E_{bottom} is the elastic modulus of the bottom strip. In our case the top strip is nickel and the bottom strip is copper. This analysis can be applied to calculate the mechanical strain in the nickel coating layer of our nickel plated copper substrate near the embedded FBG sensor. The effects of mechanical strain not in the axial direction have been ignored.

The temperature measured by the FBG sensor can be predicted with the following equation:

$$T = \frac{1}{m}(\lambda - \lambda_0) + T_0 \tag{11}$$

where m is the sensitivity (either theoretical or experimental), λ is the Bragg wavelength, and λ_0 and T_0 are the Bragg wavelength and temperature measured at calibration, respectively.

Results

To test the accuracy of the thermal response, the nickel-coated copper substrate containing the embedded FBG sensor and the free-floating FBG sensor was heated with a heat gun, and allowed to cool. Further tests were conducted by cooling in ice water. Signals from the FBG sensors were recorded using an O/E Land interrogator and software. For validation, a Type K thermocouple was silver pasted to the surface of the nickel above the embedded FBG sensor to record the actual temperature. The temperature measured by the thermocouple is plotted against the wavelength signal of the FBG sensors in Fig. 5. The two FBG sensors exhibit different sensitivities, or slopes. Computing the slopes of the two sets of experimental points gives the following measured sensitivities: 0.0294 nm/°C for the sensitivity of the nickel embedded FBG sensor with a Bragg wavelength of 1543.30 nm and 0.0122 nm/°C for the free-floating FBG sensor with a Bragg wavelength of 1541.04 nm. The nickel coating increases the sensitivity of the FBG sensor by more than twice due to its high coefficient of thermal expansion that imposes significant strain, stretching the fiber more as temperature increases.

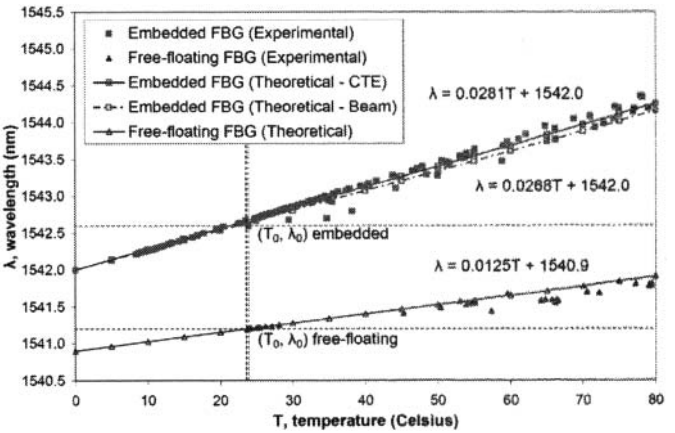

Figure 5. Thermal response of embedded and free-floating FBG sensors (intersection of dashed lines indicates start of experiment/calibration point).

Notice that several temperature measurements near the calibration point corresponding to the first heating of the embedded FBG sensor do not follow the theoretical prediction. This was not observed as the FBG sensor and assembly was allowed to cool back to room temperature, or during subsequent cycles. It is hypothesized that the polyimide coating allowed the cladding and core to "slip" within the coating during the first 10 or 20°C increase from room temperature during the first heating. For all subsequent heating and cooling cycles, it appears that a strong bond developed between the fiber and the substrate.

The theoretical sensitivity for the free-floating FBG sensor was calculated as 0.0125 nm/°C using Eqn. 5 with mechanical strain calculated using Eqn. 9 with α_f substituted for α_s. This means that no mechanical force acts upon the free-floating FBG sensor. This calculation shows that the experimental sensitivity is 2.1% off from the theoretical sensitivity for the free-floating FBG sensor. The theoretical sensitivity for the embedded FBG sensor was calculated as 0.0281 nm/°C using Eqn. 9 to compute the mechanical strain (CTE method), shown plotted on the above

figure. The alternative method of calculating mechanical strain using Eqn. 10 (beam method), produces a theoretical sensitivity for the embedded FBG sensor of 0.0268 nm/°C, shown plotted on the above figure. Both methods of predicting the mechanical strain yield theoretical sensitivities approximately 5% off the experimental sensitivity. When using Eqn. 10, this error is most likely due to the fact that the temperature change applied during testing is most likely not uniform.

To avoid calibration, the free-floating FBG sensor gives correct absolute temperature predictions for the reference temperature, $T_0^{'}$, of 10°C, (which is presumably the actual ambient temperature that corresponds with the center wavelength, λ_{CW}, from the manufacturer). For the embedded fiber, the reference temperature $T_0^{'}$ appears to be 48°C. This is presumably higher than the actual reference temperature from manufacturing. This is likely due to mechanical strain due to compressive residual stress arising during the electro-plating process. Assuming the same actual reference temperature of 10°C, and an elastic modulus of 207 GPa for the nickel coating layer, this corresponds to a residual stress, $\sigma = -E\alpha_s\left(T - T_0^{'}\right)$, of -103 MPa. This result makes sense, although it is not obvious. Often coating layers are manufactured in compression, as the mold at steady-state goes into tension. With the residual compression, adding the tension will produce a net stress that is hopefully still in compression, thus causing fatigue cycles that are entirely in compression, and thus not a problem. Fatigue cycles involving tension would surely cause plating cracks quickly, given the high level of tensile stress calculated in the next section. If the tension can overcome the initial compressive stress in the coating layer, then cracks in the coating layer might develop. This might happen over time, owing to high-temperature creep. The embedded sensor would provide a lifetime measurement of this stress

Conclusions

A new method to measure temperature and/or heat flux near the surface of the hot face of continuous casting molds has been designed. It consists of embedding a thin optical fiber with fiber Bragg gratings inside a thin stainless steel tube into the nickel coating layer during electrodeposition onto the surface of the copper molds used to continuous cast steel slabs and/or billets. During casting, this sensor will monitor the thermal condition of the mold. The sensors inside the fiber function using optical-based technology (resonating frequency of light captured in an embedded optical fiber system causes the wavelength of light emitted along the fiber to depend on thermal strain, which varies with the temperature).

Embedded sensors have the advantage of real-time monitoring at critical locations as well as immunity to electromagnetic interference and resistance to hostile environments, but cannot be commercial successful without a robust attachment method. Key advantages of the new sensor over conventional thermocouples include:

- The small size of the active sensor is much smaller than current thermocouple beads, allowing greater sensitivity to temperature variations both spatially and temporally;
- The active part of the sensor is embedded inside a fiber, and protected by a metal tube, allowing it to be manufactured in a controlled environment, and handled, prior to attaching to the dirty environment of the mold;
- The attachment method of embedding into the coating layer during the electroplating process allows the sensor to be close to (but not at) the mold surface without drilling a hole through the mold or otherwise damaging its structural integrity.

- The proximity of less than 1 mm from the mold surface is more than an order of magnitude closer to the hot face surface than conventional thermocouples, giving corresponding better resolution of thermal and strain events.

The new sensor can provide new insight into transient temperature and heat flux behavior of casting molds. It solves several problems inherent to conventional thermocouple systems (currently used to monitor mold wall temperature), and conventional mold level sensors (currently used to monitor mold level). If a second optical fiber is embedded, then the sensor can additionally monitor thermal stresses in the mold surface, enabling it to provide feedback to signal crack formation in the coating layer.

Acknowledgements

Funding for this work was provided by the National Science Foundation (Grant CMMI 05-28668) and the Continuous Casting Consortium at the University of Illinois. Optical microscopy was carried out in the Frederick Seitz Materials Research Laboratory Central Facilities, University of Illinois, which is partially supported by the U.S. Department of Energy under grants DE-FG02-07ER46453 and DE-FG02-07ER46471. Special thanks are extended to Mike Powers of Siemens VAI Services, LCC for assistance with trials.

References

1. R. Caskey, "Thermal Mold Level Control at Nucor Steel Seattle Inc.", AISTech 2008, Steelmaking Conference Proc., Pittsburgh, PA, May 5-8, 2008, Assoc. Iron Steel Tech., Warrendale, PA, Vol. 1, 2008.
2. W. H. Emling and S. Dawson: 'Mold Instrumentation for Breakout Detection and Control', 74th Steelmaking Conf., Washington, D.C., 14-17, Apr., 1991, ISS, Warrendale, PA, 197-217.
3. B. G. Thomas: 'On-line Detection of Quality Problems in Continuous Casting of Steel', in 'Modeling, Control and Optimization in Ferrous and Nonferrous Industry', (eds. F. Kongoli, et al.), 29-45; 2003, TMS, Warrendale, PA, 2003.
4. A. B. Badri and A. W. Cramb: 'Heat Flux Calculation from Thermocouples-What can be measured?', 85th Steelmaking Conf., Nashville, TN, Mar. 10-13, 2002, ISS Society, 65-76.
5. B.G. Thomas, M.A. Wells, and D. Li, "Monitoring of Meniscus Thermal Phenomena with Thermocouples in Continuous Casting of Steel", in "Sensors, Sampling, and Simulation for Process Control", TMS Annual Meeting, San Diego, CA, 2010.
6. M. Okelman, "Design and Installation of Novel Sensors into the Continuous Casting Mold", MS Thesis, University of Illinois, 2008.
7. Udd, E., Fiber Optic Smart Structures. 1995, New York: Wiley (Interscience).
8. M. K. Okelman, B. G. Thomas, and M. Powers: 'Effect of geometry on void formation in commercial electroplating of thin strips to copper', Surface & Coatings Technology, 2008, 202(17), 4153-4158.
9. Sirkis, J.S. and A. Dasgupta, What Do Embedded Optical Fibers Really Measure?, in 1st European Conference on Smart Structures and Materials. 1992, EOS/SPIE and IOP Publishing: Glasgow. p. 69-72.
10. Li, X. and F. Prinz, Metal Embedded Fiber Bragg Grating Sensors in Layered Manufacturing. Journal of Manufacturing Science and Engineering, 2003. 125: p. 1-9.
11. Timoshenko, S., Bending and Buckling of Bimetallic Strips. J. Optical Soc. of Am., 1925. 11: p. 233.

Sensors, Sampling, and Simulation for Process Control
Edited by: Brian G. Thomas, James A. Yurko, and Lifeng Zhang
TMS (The Minerals, Metals & Materials Society), 2011

SKELP TEMPERATURE PROFILE CONTROL DURING LAMINAR COOLING USING GENETIC ALGORITHMS

B. Binesh[1], A. Ben-Zvi[1], J.B. Wiskel[1] and H. Henein[1]
[1]Department of Chemical & Materials Engineering, University of Alberta, Edmonton, Canada

Coiling temperature, Temperature profile control, Genetic Algorithms, Model based optimization, Steel cooling, Run-out table, Laminar cooling

Abstract

A Genetic Algorithm optimization method, in conjunction with a finite element thermal model, was used to simulate control of the temperature profile (i.e. both cooling rate and coiling temperature) of a steel skelp during laminar cooling. Simulated optimization parameters include skelp velocity and laminar cooling configuration. As an example case, the Genetic Algorithm was used to obtain a simulated laminar cooling configuration for an imposed uniform (or constant) skelp cooling rate of 11.5°C/s and a coiling temperature of 600°C. The ability to achieve the desired skelp cooling profile was found to be sensitive to the control point location (e.g. location where temperature was measured, inside skelp) used in the Genetic Algorithm.

Introduction

A common technique for producing steel skelp with acceptable properties and relatively low cost is by Thermo Mechanical Controlled Processing (TMCP). Included in TMCP are a reheat furnace, a hot rolling system and the laminar cooling system for reducing the hot rolled steel temperature from the austenite temperature to a low temperature ferritic phase. The mechanical properties of steel are highly dependent on the phase(s) formed during the cooling process.
In this work a method for controlling the cooling profile of a steel strip is presented. The method relies on a Finite Element (FEM) thermal model to predict the cooling profile of the steel strip as it travels though the laminar cooling system. A Genetic Algorithm-based method is used to compute a configuration of the laminar cooling system necessary to achieve the desired cooling profile. The optimal cooling system configuration was validated in simulation.

Background

In this section, a review of laminar cooling system and control strategies necessary for the implementation of the proposed methodology will be undertaken. In addition, the finite element model used to provide temperature data to the control system will be discussed.

Laminar Cooling

A schematic of the laminar cooling system used in this work is shown in Figure 1 and includes the approximate location of the cooling banks and side sprays used. The system shown in Figure 1 has three cooling zones: 1) The radiation zone before the first bank; 2) The water-cooling section; and 3) The radiation zone at the end between the last bank and the coiler. The heat transfer in the water-cooling section is the main method by which the temperature of the skelp is controlled. The laminar flow cooling system used in this work includes six water banks and side

sprays located after each of the water banks. The side sprays remove water from the surface of the skelp and will reduce the amount of heat removed from the skelp. Manipulated values in model are speed of the skelp, water bank condition (either on or off), and the condition of the side sprays (either on or off).

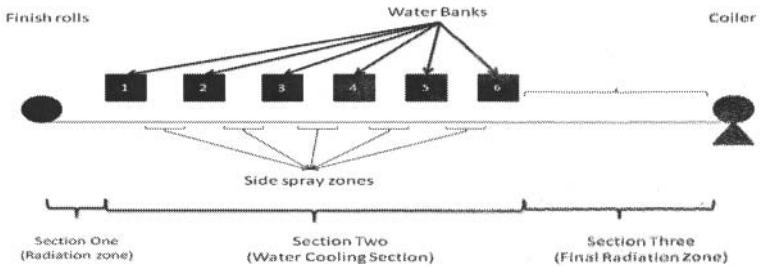

Figure 1. Schematic of the laminar cooling system

Online control is an effective option for industrial plants to regulate the temperature of steel during laminar cooling. Most of control systems implemented in the steel cooling process used feedback and feed-forward strategies to control the temperature on the run out table [3,7]. Research on control of steel skelp temperature started in the 1960's [3]. The main objective in a number of preceding works was to control the coiling temperature to a specific value [1, 5, 7]. However, there were a few studies where multiple objectives are considered (as opposed to controlling only the coiling temperature). While considerable attention has been paid to control of the skelp temperature at a particular point along the laminar cooling system (e.g., at the coiler), little attention has been paid to controlling the temperature profile along the entire length of the run-out table. Control of the entire cooling profile is advantageous because the cooling profile dictates the steel microstructure. The steel microstructure, in turn, determines the final mechanical properties of the steel. Controlling the steel cooling rate, however, requires an mathematical description of how different cooling system configurations will affect the steel temperature.

In previous work, a Finite Element (FEM) model of a laminar cooling system was developed and validated by Wiskel et al. [6]. The model includes radiation, direct single phase convection cooling and water boiling heat transfer. The transverse two dimensional finite element mesh used to model the steel skelp is shown in Figure 2. Included in the figure are the locations of the nodes used for temperature control in this work. For the optimization procedure proposed in this work, Node B was used to represent the temperature of the steel. Nodes A and C are used to determine the sensitivity of the results to the choice of measurement point. Node B is located at ¼ of the depth of the skelp.

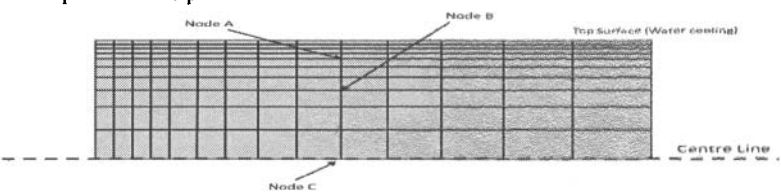

Figure 2. Schematic of FEM mesh and control Node location

Optimization Algorithms

In order to compute an optimal configuration for the system, an optimization procedure is required. In this paper a Generic Algorithm (GA) method [2] was used to determine the optimal laminar cooling configuration for controlling both temperature profile and coiling temperature. GA is a family of popular global optimization procedures which can be applied to systems where derivative information is not always available. For the laminar cooling system, the set of possible configurations includes the condition of the headers and side-sprays (on or off), as well as the speed of the skelp. An on is represented by a 1 and off by a 0.

Genetic Algorithms

Genetic Algorithms (GA) are a family of numerical optimization methods [2]. In this work GA is used to find an optimal strategy for control variables (laminar cooling system configuration) to obtain the specified temperature profile (e.g., a constant cooling rate) and coiling temperature. The optimization starts with a population of 20 individuals (or organisms), chosen from a uniform distribution, where each individual is a 15-bit string (for example. 1010...01) that represents a specific laminar cooling configuration. The first set of six digits represent the bank configuration (on or off), the next six digits represent the side-spray configuration (on or off) and the last three digits encode the speed of the skelp. Under the genetic algorithm formulation, individuals in the current generation are used to generate individuals in future generations (which correspond to a better, or more optimal, cooling system configuration). New individuals are generated using three methods: crossover, elite selection, and mutation. Individuals which are made from crossover (mating of individuals in previous generations), account for 12 of 20 individuals in the next generation. In addition, the four top ranked individuals are chosen as "elites" which are automatically included in the next generation. Finally, four individuals in the next generation are produced from "mutation" of individuals in previous generations. The GA algorithm is terminated when no improvement in the objective function is observed for ten generations [4].

The general fitness (objective) function, J, for the optimization in this work is given by:

$$J = A\left|T_f - T_f^d\right| - B(Speed) + C\sum_{i=1}^{i=n^*}\left|NT(i) - NT(i)^d\right| \qquad (1)$$

where the equation parameters are defined in Table 1. The first term in Equation (1) is used to penalize the deviation (or difference) between the coiling temperature that is obtained (T_f) and the desired coiling temperature (T^d_f). The second term in Equation (1) is used to penalize slow operation of the runout skelp because slow skelp velocity implies loss of production. The second term has negative sign which means the objective of this term is to maximize the velocity of the strip. The final term in Equation (1) is used to penalize deviation between the desired temperature at i^{th} node ($NT(i)^d$) and the temperature at the i^{th} node (NT(i)) that is obtained under a proposed cooling system configuration.

Table 1. Cost function parameters

Parameter	Definition/values
A	Coefficient used to penalize deviation from the desired coiling temperature.
B	Coefficient used to penalize slow speed values.
C	Coefficient used to penalize deviation from the temperature profile (e.g., cooling rate).
V	Velocity of the skelp between 3 and 5 m/s
T_f^d	Specified coiling temperature.
T_f	Coiling temperature.
NT(i)	Temperature at node i.
NT(i)^d	Specified temperature at node i.
n^*	The number of nodes in the water cooling section.

Optimization Results

The goal of this work is to control the temperature profile of a steel strip in a laminar cooling system. Three specific objective functions were examined. In the first case, the goal of the optimization procedure is to obtain a specific coiling temperature (regardless of the temperature profile) while maximizing the skelp velocity. This case corresponds to having the highest throughput while maintaining a specified coiling temperature. A coiling temperature of 600°C was arbitrarily chosen as the desired coiling temperature. In the second case, a constant cooling rate of 11.5°C/s was specified. In the third and last case, the system was optimized as to obtain, as nearly as possible, both a cooling rate of 11.5°C/s and a coiling temperature of 600°C.

The optimization results are summarized in Table 2. All optimization was done using Node B as the control node (see Figure 2 for Node B location) as the control point. The optimal cooling system configuration including the optimal number of banks, side sprays and skelp velocities are also listed in Table 2. For runs where the cooling rate was specified (i.e., Runs 2 and 3) both the standard deviation and mean difference between the desired and computed rate are reported.

Table 2. Optimization description and results

Run No.	*Target Coiling Temp (°C)*	*Target Constant Cooling Rate (°C/s)*	*Control Node*	*Optimal Banks Configuration*	*Optimal Side-sprays Configuration*	*Optimal Velocity m/s*	*Resulting Coiling Temp (°C)*	*Resulting Cooling Rate (°C/s)*
1	*600*	*n.a.*	*B*	*110001*	*000001*	*4.75*	*600.2*	*N/A*
2	*n.a.*	*11.5*	*B*	*111001*	*111001*	*4.75*	*633.4*	*4.2 +/- 4.9*
3	*600*	*11.5*	*B*	*110100*	*110000*	*4*	*599.6*	*10.3 +/- 15.0*

CR = constant cooling rate, CT = coiling temperature, 1= "ON", 0="OFF"

Coiling Temperature Control

In the first optimization case the coiling temperature was specified to be 600°C (for Run 1) with the objective being to maximize skelp velocity and minimize deviation from the desired coiling temperature. The coefficients of the general cost function (Equation 1) in this part are A=1, B=1, and C=0. The first term in the cost function penalizes the difference between the achieved coiling temperature and the specified coiling temperature. The second term in the cost function penalizes the choice of a low skelp velocity. While node B was used for optimization, the temperature profiles of Nodes A and C were also computed under the optimal configuration for achieving a coiling temperature of 600 °C and maximum skelp velocity.

The optimal configuration to achieve a 600°C coiling temperature was with Banks 1, 2, and 6 on, Side Spray 6 on, and velocity of 4.5 m/s (Run 1in Table 2). The deviation from the specified coiling temperature was 0.2°C.

The temperature profiles for nodes A, B and C are shown in Figure 3 superimposed on a sample CCT diagram. Nodes near the surface (e.g., Node A) exhibit large variations in temperature due to their proximity to the surface where the heat flux is rapidly altered by the impact and subsequent removal of water. Nodes that are more distant from the surface (e.g., Notes B and C) show a dampened thermal response due to the lower and the more constant heat flux inside the skelp. This effect is due to the geometry of the skelp and is therefore observed in all simulations regardless of the cooling system configuration.

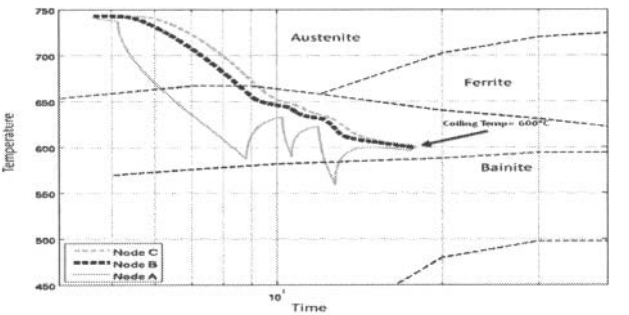

Figure 3. Temperature profile for Node A, B and C in CCT diagram (Objective: coiling Temperature= 600°C for Node B)

Constant Cooling Rate Control

While controlling the coiling temperature is important for mill operation, it is the *path* of the steel through the CCT diagram that ultimately governs the product microstructure and hence properties. In this section, the value of the coiling temperature was not used in the optimization (the case where the coiling temperature and cooling rate are simultaneously controlled is addressed in the next section).

In order to obtain the desired objective function for this section, the coefficients of general cost function (described in Equation 1) are A=B=0 and C=1. The third term (with the C coefficient) in cost function (i.e., Equation (1)) indicates the penalty for the difference between achieved and specified temperature profile during water-cooling section. In this part, 11.5 °C/s was specified as target cooling rate. The optimal configuration for cooling rate 11.5 °C/s is listed in Table 2

(Run 2). The optimized temperature profiles for cooling rates of 11.5 °C/s are shown in Figure 4. The solid line in Figure 4 is used to indicate the specified (i.e., target) cooling rate.

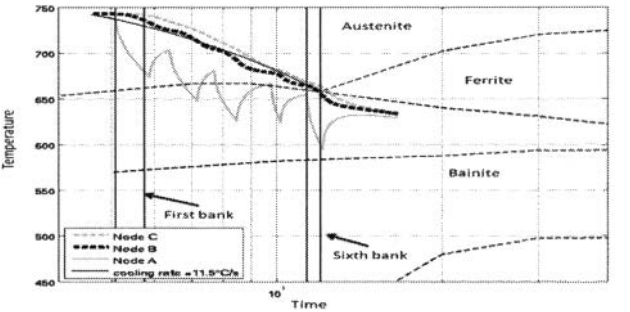

Figure 4. Temperature Profile for Node A, B and C in CCT diagram (Objective: Constant Cooling Rate=11.5°C/s for Node B)

Constant Cooling Rate & Coiling Temperature Control

In order to obtain the desired microstructure while meeting all of the mill's processing requirements, it may be necessary for both the constant cooling rate and final coiling temperature to be controlled. In this section the optimization objective is to control both the constant cooling rate (at 11.5°C) and the final temperature (at 600°C) for node B.

In this work an objective function which weights both the error in the coiling temperature and deviation from the desired cooling rate equally was chosen. As a result, the coefficients in the general cost function (shown in Equation 1) were as follows; A=100, B=0, C=1. The reason for the large value of A is that there are approximately a hundred points in the temperature profile of the water-cooling section in Figure 1, and, as a result, the coefficient used to penalize deviation from the desired coiling temperature (i.e., A) should be 100 times larger than the coefficient used to penalize deviations from the desired temperature profile (i.e., C). The optimal configuration to achieve the specified cooling rate and coiling temperature is listed in Table 2 (Run 3). The temperature profiles of nodes A, B and C versus specified cooling rate and final temperature for a coiling temperature of 600°C and cooling rates at 11.5°C/s is shown in Figure 5.

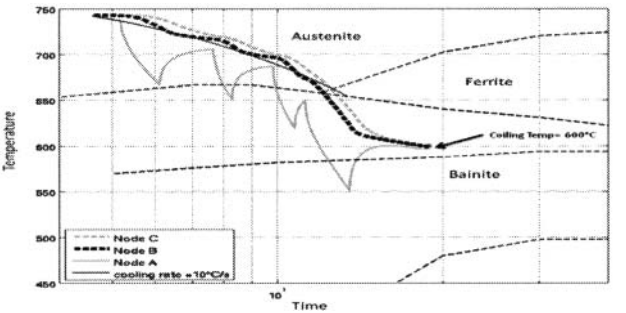

Figure 5. Temperature Profile for Node A, B and C in CCT diagram (Objective: Constant Cooling Rate=11.5°C/s and Coiling Temperature=600°C for Node B)

Sensitivity Analysis

The final temperature profile in the skelp is a function of the configuration of the cooling system. In this work, a configuration that is optimal for a specific node (Node B) was computed. However, this configuration may be suboptimal for other nodes. More generally, it is important to carefully examine the effect of node selection on the optimal cooling system configuration and temperature profiles within the skelp.

To assess the sensitivity of the system configuration temperature profiles to the choice of control node, two additional nodes were selected as a target for optimization. Due to the symmetry of the system, these two additional nodes were placed at the same horizontal position as Node B, but at different distances from the skelp surface. These nodes, labeled Node A, and Node C in Figure 2, correspond to a near-surface node and a centerline node, respectively. The optimization objective chosen for this analysis was constant cooling rate of 11.5°C, and a coiling temperature of 600°C. The objective function weights were A=100, B=0, and C=1.

The optimal configurations for the cooling-system using Nodes B, C, and A are listed in Table 3 as Runs 3, 4, and 5, respectively. Also listed in Table 3 is the optimal velocity, simulated coiling temperature, and the maximum deviation between the desired and simulated temperature profile for each run. As shown in Figures 6 and 7, the temperature profiles of Nodes B and C are offset with Node C being hotter than Node B. The choice of control node is important for obtaining the desired microstructure in the skelp. For example, nodes that are further from the cooling surface are more representative of the bulk temperature profile in the skelp. However, near-surface nodes provide a measure of the maximum temperature variation during the cooling process.

Table 3. Sensitivity analysis

Run No.	*CT (°C)*	*CR (°C/s)*	*Control Node*	*Optimal Banks Configuration*	*Optimal Side-sprays Configuration*	*Optimal Velocity m/s*	*Resulting Coiling Temp (°C)*	*Resulting Cooling Rate (°C/s)*
3	*600*	*11.5*	*B*	*110100*	*110000*	*4*	*599.6*	*10.3+/-15.0*
4	*600*	*11.5*	*C*	*111011*	*111001*	*4.5*	*600.3*	*6.1+/-7.5*
5	*600*	*11.5*	*A*	*011011*	*011011*	*3.5*	*631.6*	*16.1+/-19.9*

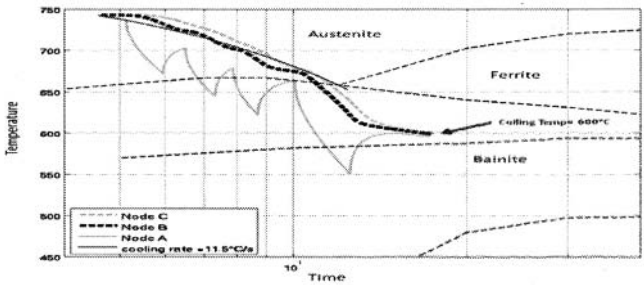

Figure 6. Temperature Profile for Node A, B and C in CCT diagram (Objective: Cooling Rate=11.5°C/s and Coiling Temperature=600°C for Node C)

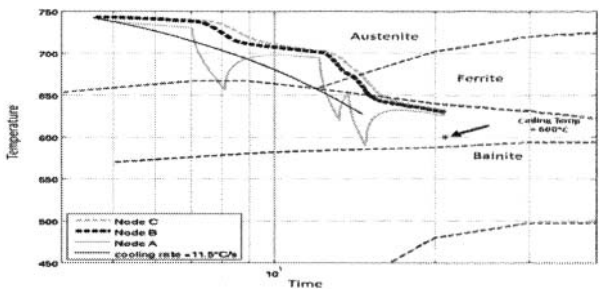

Figure 7. Temperature Profile for Node A, B and C in CCT diagram (Objective: Constant Cooling Rate=11.5°C/s and Coiling Temperature=600°C for Node A)

Summary and Conclusions

The mechanical properties of steel strip are defined by the steel microstructure. This microstructure is a function of the temperature profile in the strip during the cooling process. In this work, a genetic Algorithm based approach for obtaining a desired temperature profile in the strip is presented. It is shown that Genetic Algorithm is a computationally viable tool for obtaining optimal configurations for the laminar cooling system. Three general cases were considered: a fixed coiling temperature, a fixed cooling rate, and both a fixed coiling temperature and cooling rate. The optimization algorithm was used to, in simulation; provide configurations that could closely match the desired coiling temperature and cooling rates for the first two cases. Sensitivity analysis showed that the choice of control node greatly affects the optimal cooling system configuration. The temperature of near-surface nodes is much more difficult to control than near-centerline nodes because of the greater heat flux near the surface.

Acknowledgements

The authors would like to thank L. Collins of EVRAZ Inc. NA for discussions regarding this work. We would also like to thank NSERC and EVRAZ Inc. NA for financial support.

References

[1] S.K. Biswas, S.J. Chen, and A. Satyanaryana, "Optimal temperature tracking for accelerated cooling processes in hot rolling of steel," *Dynamics and Control*, 7(1997), 327-340.

[2] David E. Goldberg, *Genetic Algorithms in Search, Optimization and Machine Learning* (Boston, MA: Kluwer Academic Publishers,1989).

[3] R. Guo, "Modeling and simulations of run-out table cooling control using feed-forward-feedback and element tracking system", *IEEE Transactions on Industry Applications*, 33(1997).

[4] John. H. Holland, *Adaptation in Natural and Artificial Systems* (Ann Arbor,MI: University of Michigan Press,1975).

[5] L. Peng.,and Q. L. "Cooling hot rolling steel skelp using combined tactics", *Journal of University of Science and Technology Beijing*, 15(2008).

[6] J.B. Wiskel et al. "Infrared Thermography of a TMCP Microalloyed steel skelp at the upcoiler and its application in quantifying the laminar jet/skelp interaction", (Department of Chemical and Materials Engineering, University of Alberta, Edmonton, Alberta, Canada,2010).

[7] H.B. Xie et al., "Optimization and Model of Laminar Cooling Control System for Hot Strip Mills", *Journal of Iron and Steel Research*. 13(2006), 18-22.

Sensors, Sampling, and Simulation for Process Control
Edited by: Brian G. Thomas, James A. Yurko, and Lifeng Zhang
TMS (The Minerals, Metals & Materials Society), 2011

Sensors, Sampling, and Simulation for Process Control

Steel Processing; Online Sensors

Sensors, Sampling, and Simulation for Process Control
Edited by: Brian G. Thomas, James A. Yurko, and Lifeng Zhang
TMS (The Minerals, Metals & Materials Society), 2011

COMPREHENSIVE INTEGRATED LEVEL 2 MELT SHOP MANAGEMENT SYSTEMS

Dr John R Middleton

Multon Process Technology Ltd,
Normanby Gateway, Lysaghts Way,
Scunthorpe, North Lincolnshire,
United Kingdom, DN15 9YG

Keywords: Meltshop, Specialty Steels, Superalloys, Alloy, Blend, ERP, Inventory, Least Cost, Mixed Integer, Optimisation

Abstract

Based upon 30 years+ experience in the Development, Implementation and On-going Support of Computer based Melt Shop Systems in about 40 plants in the UK, Europe and the USA, consideration of:

- The facilities and functionality of a state of the art, comprehensive, Level 2 Integrated Melt Shop System covering Melting and Secondary Refining processes for all grades of steels, superalloys and aluminium.
- The application of Mathematical Models and Optimisation within those systems.
- Interfaces to Plant and Laboratory Instrumentation and Control.

Introduction

A current technology system should provide a wide range of functionality covering all aspects of the Melt Shop operations from the receipt of sales orders, through technical vetting, melt planning, raw materials and consumables procurement, level 2 manufacturing and technical control of melting, secondary refining processes and casting, through to shipping of the cast product. All Melt Shops are different and the system should be sufficiently configurable to provide 'Perfect Fit' for all environments. The extent to which the full range of functionality will be required will vary considerably from plant to plant. Access to the system needs to be available to all managers, supervisors and operators in the Melt Shop and also to the appropriate personnel in Sales, Planning, Purchasing, Technical and General Management.
The required functionality, the application of mathematical models, optimization and interfaces to laboratory instrumentation, plant instrumentation and level 1 control systems will be considered. The paper concludes with a description of the benefits arising from the application of such a system.

System Functionality

A diagram showing in broad outline Main Modules of a current technology Integrated Melt Shop management System and the data flow between modules is shown in Figure 1.

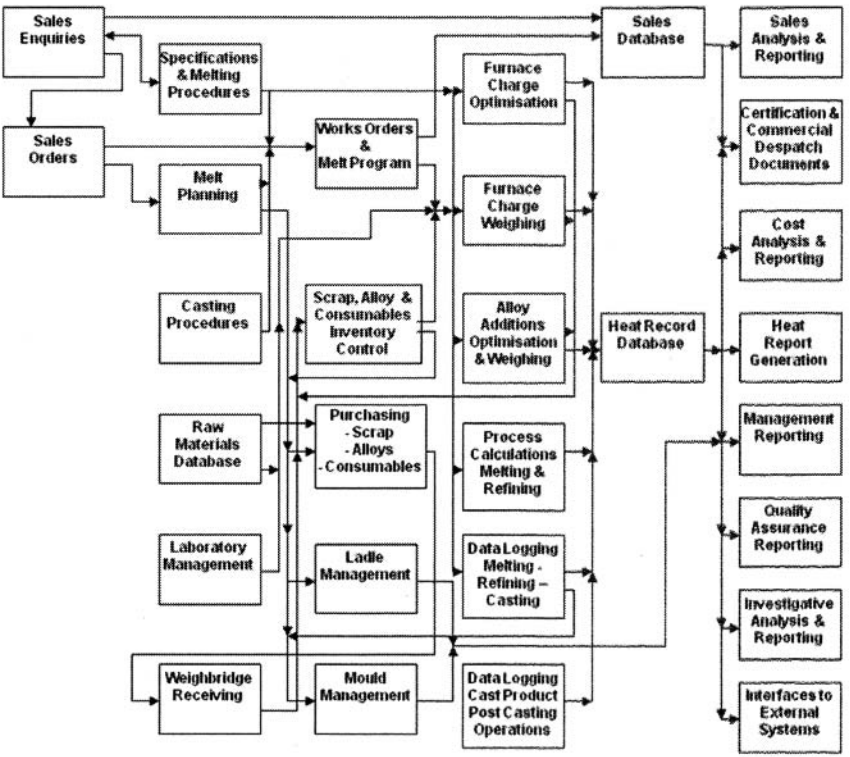

Figure 1. A Computer Integrated Level 2 Melt Shop Management System Main Modules and Data Flow

Access to the system needs to be available to all managers, supervisors and operators in the Melt Shop and also to the appropriate personnel in Sales, Planning, Purchasing, Technical and General Management.

The system will normally run on a dedicated network attached server, using a robust multi-user multi-tasking timesharing operating system. Reflecting the critical nature of the system which demands absolute reliability of service, it would be usual to provide a standby backup server and RAID data Storage..

Melt Planning

As Sales Enquiries are received they are provisionally allocated to heats via the Melt Planning facility in order to provide a delivery date as part of the Quotations process. Upon conversion to a firm order the heat allocation is reviewed and confirmed. For Enquiries which fail to become orders within the time validity of the Quotation the allocated heat in the Melting Plan is released for future planning. In the Melt Planning operation due account is made of:

- Delivery due dates
- Post casting processing
- Consolidation of orders to heat quantities
- Appropriate sequencing of melts by composition
- The need for wash out heats where necessary
- Availabilities of appropriate ladles and casting facilities
- Multiple melt requirements for large ingots or castings
- Partial tapping of a melt followed by a back charge to the remaining heel for the following Heat.

The Melt Planning function generates the Melting Program from which most system activities, such as charge optimisation, charge assembly and weighing control, process data recording are initiated. The heats in the program are displayed line by line with each line showing the scheduled time for each heat and its corresponding information such as grade, tap weight, the cast product type(s) and number(s), works order number, customer and the current heat status. Provision is made to switch heats to appropriate future orders in the event of the first melt sample being too far off composition to make the originally planned grade.

Specifications/Melting Operations Database

This database contains for each grade of steel produced :

- Finished product composition specifications
- Finished product physical/mechanical property requirements which can be related to chemistry, eg hardenability, ferrite control, pitting resistance, sigma phase control, weldability
- Working composition specifications, element recovery rates and raw material element constraints for each process stage, for example:
    - furnace charge of scrap and alloys
    - furnace alloy additions to melt
    - ladle alloy additions on tapping
    - secondary steelmaking alloy additions, pre vacuum
    - secondary steelmaking alloy additions post vacuum
- Standard materials restrictions at each process stage
- Restrictions on materials usage by physical type e.g. turnings, light scrap, heavy scrap, bales
- Standard operational instructions for charge calculation, melting and secondary processes

Raw Materials Database

For each type of scrap, ferro-alloy, pure metals and minerals consumed in the furnace charge or as deoxidation, desulphurisation or alloying additions throughout the process, the system stores for each material detailed data covering composition, quantities, costs and usage restrictions

The data in the Raw Materials Database is accessed by Raw Materials Receipts, Material Usages and updated by the Furnace Charge Optimisation, Alloy Additions Optimisation, AOD Process Calculations, Raw Materials Purchasing and Sales Enquiries modules of the system.

Raw Materials Inventory Control - Materials Receipts

In larger scale plants, raw materials deliveries are received as bulk quantities which are subsequently stored in large capacity bunkers or open storage designated open storage areas. These materials will be initially received over a Truck Weighscale where the following information is initially validated and recorded on the system:

- Purchase Order No.
- Supplier Shipping Document No.
- The Weigh Ticket Number – generated by the system
- Vehicle Registration Number
- Supplier – validated against Purchase Order No.
- Carrier
- Material Description – validated against Purchase Order No..
- Weighscale Gross Weight via automatic system interface to the weighscale equipment

After discharging its load the truck is tared on the weighscale and the inventory is updated.
The procedure for smaller items is the same as above but in this case the system will write the receipt record and update the inventory, A bar coded label will be generated and attached to the container before it is then stored in the appropriate storage location.

Furnace Charge Optimisation

The operator selects from his Melt Program display, the charge that he wishes to calculate. From the Melt Program, Works Order and Specifications data, the Charge Optimisation screen will display to the operator :

- The Steel Grade being produced
- The weight of liquid steel required at melt out
- Required melt out composition range
- Any standard restrictions on materials utilisation
- Any standard charge make up instructions

In the first phase of the calculation, the system displays a list of candidate materials for use in the charge. The operator may also view materials in stock but rejected for use in this charge together with the reasons for rejection e.g. unsuitable chemistry, physical form restrictions, not valid for use at this process stage.

In the second phase of the calculation, the optimum lowest cost charge is determined subject to current material stock and any standard materials usage constraints as held in the Specifications/Melt Operations database.
This calculation utilizes a mathematical model of the materials blending and melting process, which takes due account of:

- yield losses due to oxidation of the metallic materials charged,
- burning and transfer to the furnace slag of non-metallic contaminants
- some raw materials can be considered to be available in continuous quantities whilst others will be available only in specific weight pieces

The mathematical model is formulated as a set of equations:

- an objective function which is an equation defining the cost of the materials blend
- a set of constraint equations describing the grade specification element minima and maxima to be achieved in the resulting melt
- a set of constraint equations describing process limitations including, the required weight of the melt, limitations of charge materials by physical form.

These equations are solved by a mixed integer program to determine the least cost blend of raw materials to provide a melt which conforms to the Grade Chemistry melt out Specification limits and complies with the operations constraints selected.
To the user, the calculation of this optimum charge appears to be instantaneous.

Raw Materials Inventory Control - Charge Weighing Control
The system will cater for charge weighing control for both bulk and individual Stock Items. In the case of mobile or overhead cranes, charging buckets on a weighpad by grab or magnet, then these will be equipped with wireless mobile terminals for operator instruction and data entry. In the case of smaller floor weighscales where charge containers are manually loaded then a workstation will be placed adjacent to the weighscale. The system will be equipped with an interface to the weighscale enabling weights to be recorded throughout the weighing process.
In each case the operator will select from the Melting Program the Heat for which he needs to build a charge. He will then have a display of the appropriate previously calculated charge showing:

The operator will select on the screen, the material he is about to add to the charge container or, in the case of smaller Individual Stock Items he will scan the bar code label on the container. The Tare weight of the container will be recorded and the screen will show the balance weight of the selected material to be added to the charge container. The operator will then continue to add that material to the charge container until a colour display on his screen shows that he has successfully added the quantity within the specified weighing tolerance. This process is repeated for each component of the charge. In the unusual event the charge weighing operator encounters a problem in achieving the required charge the system will enable him to recalculate the charge having fixed the materials added thus far.

Laboratory Management
Wherever possible all laboratory instruments should be interfaced to the system. Functionality is provided to enable the Laboratory Technician to display, for a given heat, the analytical results from each relevant instrument. The results may adjusted against Type Standard results obtained previously, checked for completeness and conformity to specification and released. The complete analytical data are then written and stored in the Analytical Database.
Analytical Results are immediately available to the Alloys Additions module for the optimised calculation of additions to the furnace or ladle during tapping or secondary steelmaking.
Pit sample results are used by the system for the generation of Test Certificates.
In addition to mainstream laboratory analyses, provision is also made for the storage of data from the use of portable analytical instruments which are used for the analysis of scrap in the scrap storage areas.

Alloy Additions Optimisation
Immediately upon completion of the analysis of samples from the furnace bath or from the vessel or ladle during secondary steelmaking, the results are displayed in the appropriate control cabin. The results are read by the Alloy Additions module to provide an immediate display of the optimised alloy additions according to the working specifications held in the Specifications

Database, appropriate to the given process stage. These calculations utilize the same Mixed Integer Programming model as described in the Furnace Charge Optimisation Section.
Provision is made within this calculation for dilution in the event of an element(s) of the melt being above the maximum limit of the appropriate stage specification. Generally the dilution material will be specified from a restricted range of scrap or pure materials.
The display of required alloy additions will also show clearly as appropriate, the additions which will be needed at a later process stage to confirm to the user that due account has been made of this requirement. For example, based upon the result of a ladle sample from a VAD unit prior to degassing where a Cr or Mn addition is required but we will have to make our addition of nitrided FeCr or nitrided Mn to meet a nitrogen specification, then we need to take that into account when calculating the Cr and Mn additions prior to degassing. Thus in addition to showing the necessary Cr and Mn additions currently required, the provisional post degassing additions would also be displayed.

AOD Process Calculations
The AOD Control Model provides for calculation of the :

- The least cost optimized additions of ferroalloys, pure materials, oxides, and scrap required to achieve the required chemistry and liquid metal weight on tapping. The additions calculation will be performed first when the system receives, from the Laboratory Management Module, the results of the sample taken from the transfer ladle upon tapping of the melting furnace. The calculation will take due account of the contribution to melt chemistry which may arise from the selected reduction mix ferro-alloys eg the Cr from FeSiCr. The calculation will subsequently be used for calculating trimming additions based upon the bath sample taken following completion of the reduction phase. The types and quantities of the calculated additions are transferred to the PLC via the level 2 – PLC interface.
- Quantity of heat generation additions eg Aluminium, Ferrosilicon which react exothermically with the oxygen blown to raise the temperature of the liquid steel to the required tapping temperature.. The heat balance calculation has to take due account of heat losses from the vessel during the process cycle.
- Volume of oxygen to be blown during the decarburization phase taking account of the oxidation of fuel additions, carbon removal, and oxidation of oxidisable elements transferring to the slag as oxides. The blow rates for oxygen and ratios of argon and nitrogen and the tuyere shroud gases are taken from tables of values by ratio against process stage. These values vary by steel grade and are stored in the Grade Specification database. The required volumes and blowing patterns are transmitted to the PLC via the Level 2 – PLC interface.
- Reduction alloys additions to be made in the reduction phase to reduce the metallic oxides to the bath.
- Slag forming materials to achieve a slag composition which is 'engineered' to the best properties for decarburisation, fluidity, metallic yield, required condition for effective desulphurization and refractory protection.

Raw Materials Inventory Control - Alloy Additions to Furnace, Vessel or Ladle
Upon completion of each OPTIMAT Alloy Additions Calculation following receipt of a bath or ladle sample result, the operator is required to weigh the additions using the same procedure as in the case of charge weighing control. In the case where automated weighing and dispensing of alloy additions using hopper and conveyor systems then the system will be interfaced to the

Level 1 PLC control system to initiate the dispensing of the appropriate weights of alloys. The PLC will return the actual quantities weighed to the system.
The system utilises the actual alloys weigh data to update alloys inventory and to write data of the actual materials used to the appropriate Heat Record in the Heat Record Database

Process Data Recording
Process Data Recording screens are provided at the Melting and Secondary Process operator control consoles and input to these screens effectively replaces the traditional hand written Melting and Refining Record Sheets. Much of the data displayed on the screens is collected automatically from plant instrumentation, level 1 control systems or arises from other modules of the system. Operator input is kept to the minimum.
The Melting Furnace data recording screen typically would display :

Data Item	Source
Current Time and Date	System
Operator/Steelmaker/Shift Manager	Operator selection from dropdown list
Grade	System – from Melting Program
Heat No.	System – generates Heat Nos.
Charge – Scrap, Alloy and Slag Materials Types and Quantities	System – from Charge Weighing Control Load Cell output
Times/Verification of completion of Standard Operating Procedures	Furnace PLC, Operator single key press
Key process times – eg commence charge, power on, tap changes, slag off, samples taken, oxygen blown, tap	Furnace PLC, Operator single key press
Delays – Times and Reasons	Operator selection from dropdown list
Power Meter Readings	Furnace PLC
Sample Results	Laboratory Instrument Interface
Alloy Additions to the Bath or Ladle	System – from Charge Weighing Control Load Cell output
Bath Temperatures	Furnace PLC or from Temperature Recorder
Ladle Identifier	Operator selection from dropdown list
Weight Tapped	Ladle Crane Load Cell

The Secondary Steelmaking data recording screen displays:

Data Item	Source
Current Time and Date	System
Operator/Steelmaker/Shift Manager	Operator selection from dropdown list
Grade	System – from Melting Program
Heat No.	System – generates Heat Nos.
Charge – Scrap, Alloy and Slag Materials Types and Quantities	System – from Charge Weighing Control Load Cell output
Times/Verification of completion of Standard Operating Procedures	Unit/Vessel PLC, Operator single key press
Key Process Activities/Times – eg Ladle at Unit, Gases Blown/Volumes/Ratios, Vessel Position,	Unit/Vessel PLC, Operator single key press
Delays – Times and Reasons	Operator selection from dropdown list
Power/Gases/Pessure Readings	Unit/Vessel PLC
Sample Results	Laboratory Instrument Interface
Alloy Additions to the Vessel/ Ladle	System – from Charge Weighing Control Load Cell output
Bath Temperatures	Unit/Vesssel PLC or from Temperature Recorder
Ladle Identifier	Operator selection from dropdown list
Weight Out of Unit/ Tapped	Ladle Crane Load Cell

Full details of casting and stripping are recorded using handheld computers as appropriate and input to the appropriate Heat record including:

Data Item	Source
Current Time and Date	System
Operator/Supervisor/Shift Manager	Operator selection from dropdown list
Grade	System – from Melting Program
Heat No.	System – generates Heat Nos.
Pit setting, tiling and lifters conformance with Standard Operating Procedures	Operator – single key press for each item
Mould Flux, Anti Piping conformance with Standard Operating Procedures	Operator - single key press for each item
Key Process Activities/Times – eg Ladle at Pit, Start/Finish teeming each Plate, Stripping Start/Complete	Operator - single key press for each item
Pouring times and ladle discharge rates	Operator - single key press for each item, Ladle Car Load Cell,
Normal/Abnormal Teeming Events	Operator selection from dropdown list
Delays – Times and Reasons	Operator selection from dropdown list
Ladle Identifier	System – from Melting Program

Heat Record Database

The system provides a Cast Record Database in which for each cast produced a comprehensive detailed record is stored. This record includes all calculations, materials calculated and actual usages, all sample results, all operation and delay data, product data. A wide range of regular management reports covering production, costs and quality are generated from this database.

The Benefits of a Comprehensive Melt Shop Management System

The following benefits arise from the use of a plant wide integrated system to replace disjointed legacy systems, individual spreadsheet based systems and paperwork.

- Achievement of lowest cost production.
- Improved composition control throughout the process reflected in the finished product.
- Productivity improvement.
- A single database accessed by all the managers and operators maintained in real time and readily accessed by all personnel.
- No replication of data
- Data entered once only
- All functionality provided by a single integrated system
- A common look and feel across all facilities of the system
- Knowledge and experience of 'experts' built into the system rather than walking around in 'experts' heads
- Empowerment of operators enabling them to undertake tasks previously considered to be in the domain of 'specialists'
- Enhanced flexibility of personnel more readily cross-trained to undertake a wider variety of tasks

Sensors, Sampling, and Simulation for Process Control
Edited by: Brian G. Thomas, James A. Yurko, and Lifeng Zhang
TMS (The Minerals, Metals & Materials Society), 2011

ANALYSIS OF THE TRANSIENT PHENOMENA DURING STEEL CONTINUOUS CASTING THROUGH THE ON-LINE DETECTION DATA

Lifeng Zhang [1], Anping Dong [1], Shusen Li [2]

[1] Department of Material Sciences and Engineering
Missouri University of Science and Technology (Missouri S&T)
223 McNutt Hall, Rolla, MO, 65409-0330
Email: zhanglife@mst.edu

[2] Qian'an Steelmaking Co. Ltd., Shougang Group
Qian'an City, China
Email: shusen.li@163.com

Keywords: Transient Phenomena, Continuous Casting, On-line Detection Data

Abstract

The transient phenomena during steel continuous casting are analyzed through the on-line detection data of casting speed, top level fluctuation, and mold temperature. The macro-fluctuation and the micro-fluctuation are discussed. The macro-fluctuation is found to relate to the casting operation and the micro-fluctuation is related to the turbulent fluctuation in the continuous casting mold. The fluctuation itself induces the asymmetrical flow in the continuous casting vessels. The online detection data for a billet caster and a slab caster were analyzed. The level fluctuation, the casting speed and the liquid slag shape were discussed.

Transient Phenomena during Steel Continuous Casting

The transient phenomena during steel continuous casting include:

I. The casting during the period of cast start, ladle change, change of Submerged Entry Nozzle (SEN), and cast end. During this transient stage, the casting speed varies a lot, the level of the molten steel in the mold fluctuates seriously, and slag entrainment and air absorption are serious. This period is usually called transient (or unsteady) casting or transient (or unsteady) pouring period;
II. The casting during the period with big casting speed fluctuation and big level fluctuation in the mold due to operational reasons such as nozzle clogging. Slag entrainment and air absorption are serious in this period;
III. Due to the feature of the turbulent flow itself, for most of the time, the flow of the molten steel in the mold and even in the tundish has fluctuation, and at sometimes this fluctuation is serious;
IV. For some special period, such as the collapse of the flow control devices in the tundish, the fully blockage of the SEN, and breakout, the pouring and the casting have to be stopped.

During the transient stage I, due to the strong inlet impingement, in the tundish, near the shroud nozzle, the slag was pushed away and the molten steel is easy to be exposed to air, entrain slags and generates reoxidized inclusions. It was reported that at the cast start of the first heat, the sliver defects was five times than the half pouring of the first heat, and was 15 times of the later heats. [1] **Figure 1** shows the amount of >50 μm inclusions in a continuous casting slab at different heats, indicating that 1) the first heat had more inclusions than other heats: 2) Cast start and cast end had more inclusions than other period, approximately 5-16 times more than that at the steady casting period; and 3) Inclusions during ladle change was over 2 times than that during the steady state.

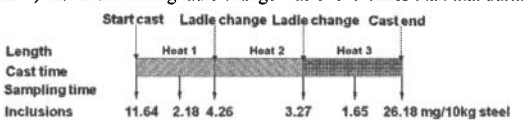

Fig.1 The amount of >50 μm inclusions extracted by Slime method in a continuous casting steel slab at different heats [2]

On-line Detection Data

As discussed above, the steel cleanliness during transient casting stage is much worse than that at steady stage, thus, controlling the transient phenomena during continuous casting is of importance. It is important if the transient casting phenomena can be analyzed by the online detection data which includes:

- The tundish weight, ladle weight, casting speed and casting temperature (or super heat), slide gate or SEN open percentage, the level position of the molten steel in the mold;
- The cooling water flow rate at the mold, and the temperature different between the inflow and outflow water, the temperature at different locations of the mold plate measured by thermal couples;
- The cooling water flow rate at the second cooling zone, and the drag force of the rollers.

The next sessions of the current paper will show the example of the online data and the use of these data to analyze the transient phenomena during continuous casting process.

Online Data Analysis for a Billet Caster

The billet caster, with a caster diameter of 10m, has four strands, each of which has a section dimension of 150mm×150mm. The mold length is 900mm, and the submergence depth of the bottom-open SEN is 100mm, and the average casting speed is around 2 m/min. The heat capacity is 60ton. The casting time for one heat is around 45 min, and the ladle change time is 2-3 min.

Level Fluctuation at the Mold

The severe mold level fluctuation causes slag entrapment, affects oscillation marks on the surface of billet, and even induces breakout thus is harmful to the cleanliness of molten steel. Industrial data of mold level positions and cast velocity was collected and analyzed in the current study. Actually, the reported online data of the level at the mold is the instantaneous level position changing with time rather than the level fluctuation, as shown in **Figure 2**. The definition of the level fluctuation should be:

$$\Delta l = l_t - \bar{l} \tag{1}$$

where Δl is the level fluctuation; l_t is the instantaneous level position; and $\bar{l}$ is the averaging level position in the neighboring 40 seconds. The average level position is shown in **Figure 2**. The abrupt increase of decrease of the level position – the macro-fluctuation – was induced by the casting operation such as the casting speed change or the sudden release of the clogged materials at the SEN. **Figure 3** shows the calculated level fluctuation – the micro-fluctuation – with time by Eq.(1). The micro-fluctuation should be related to the turbulent fluctuation in the continuous casting mold. The fluctuation itself induces the asymmetrical flow in the continuous casting vessels. **Figure 3** indicates that for the current billet casting process the level fluctuation at ladle change period was not larger than other times. The mold level fluctuation is inevitable because of the mold oscillation, however, too big level fluctuation causes slag entrainment. It is necessary to analyze the frequency distribution of the level fluctuation at the mold and the analyzed result is in **Figure 4**. For the current billet caster, 22% of the total time had >10mm level fluctuation. It should be noticed that 4% the level fluctuations were even larger than 20mm.This percentage has to be lowered down in order to obtain high quality steel and less slag entrainment because most of the defects in the steel products occur when there is big level fluctuation.

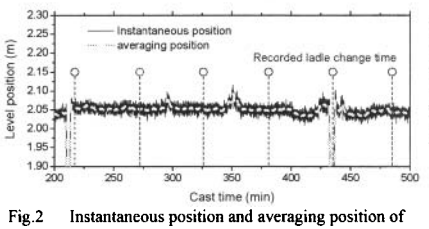

Fig.2 Instantaneous position and averaging position of

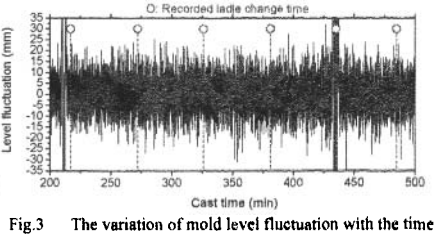

Fig.3 The variation of mold level fluctuation with the time

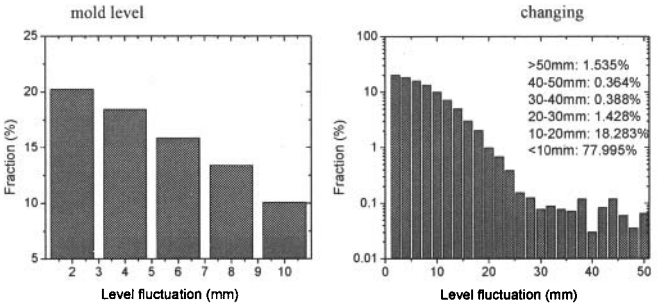

Fig.4 The range distribution of the level fluctuation

Differentiating the data with time in **Figures 2** or **3**, the vertical velocity of the mold level can be calculated and shown in **Figure 5** indicating that the level vertical fluctuation velocity is within ±7mm/s. The casting speed is approximately 1.8 m/min, corresponding to 30 mm/s. So, the vertical moving velocity of the level is approximately 25% of the casting speed.

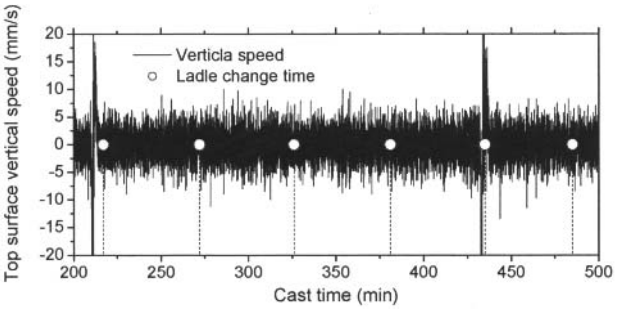

Fig.5 The vertical velocity of the mold top surface

The Liquid Slag Thickness and the Level Shape at the Mold

The liquid slag affects the lubrication and the heat transfer at the continuous casting mold. In the current study, a 1-mm thick steel plate was immerged into the molten steel of the mold for 2 seconds to measure the liquid slag thickness and the level shape at the half way from the mold plate to the SEN.

At the half way pouring of the first ladle (**Figure 6a**), the casting became steady stage. The thickness of the liquid slag was approximately 5mm, and the level shape was pretty flat although the flow near the mold plate was a little upwards. At the ¼ from the left, the slab thickness was very thin, approximately 2mm, which might be induced by the upward flow there and therefore the temperature there was higher than other places. The slag entrainment would be serious there.

At the end of the pouring of the third ladle (**Figure 6b**), the level was not flat but waved a lot. The thickness of the liquid slag was around 6-8mm. The flow around the mold plate, especially the right side, was very downwards, and the flow in the mold would be very asymmetrical. This kind of slag shape indicated a highly wavy flow pattern in the mold. The slag entrainment at the lowest point of the slag would be serious. This figure indicates that the flow in the mold during transient stage – the end of a heat – is very turbulent and asymmetrical.

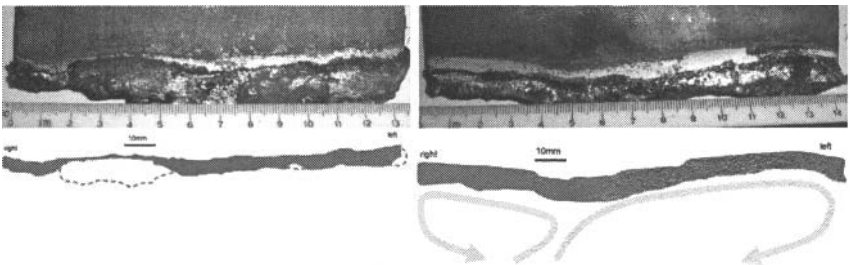

(a) The second strand, first heat and 50% poured (b) The first strand, the end of the third heat pouring

Fig.6 Liquid slag thickness, the level shape and the flow pattern in the mold

Casting Speed

During continuous casting, the casting speed is also not a constant value but mostly a transient value. As shown in **Figure 7**, for the current billet casing process, the casting speed was 1.75m/min~ 1.95m/min. At sometimes, the casting speed abruptly increased from 1.8m.min to 1.95 m/min. The study by the current author Zhang has revealed that the abrupt change of the casting speed induces big level fluctuation, slag entrainment, and affects inclusion removal. [8-9] The abrupt flow change will induce big friction force at the SEN surface and may induce the release of the clogged materials. [8-9] Another important finding from **Figure 7** is that for the current billet casting process, the casting speed always fluctuated rather than keeping a constant value. The same as the analysis for the level fluctuation, the casting speed fluctuation can be defined by

$$\Delta V_C = V_{C,t} - \overline{V}_C \tag{2}$$

where ΔV_C is the casting speed fluctuation; $V_{C,t}$ is the instantaneous casting speed; and $\overline{V}_C$ is the average casting speed in the neighboring 40 seconds. The obtained macro-fluctuation of the casting speed corresponded to the level macro-fluctuation shown in **Figure 2**. **Figures 8** and **9** show that for the current billet caster the casting speed fluctuated at ±35 mm/min (or 0.58 mm/s) and the casting speed fluctuation was independent of the ladle change except when the casting speed fluctuation was over ±30 mm/min (**Figure 9**). **Figure 10** shows the correlation between the level fluctuation and the casting speed fluctuation, indicating that the level fluctuation slightly depended on the casting speed fluctuation.

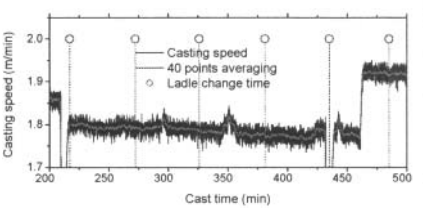

Fig.7 Casting speed *versus* time during casting of a billet

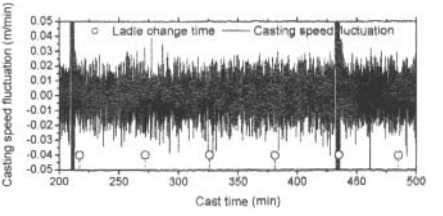

Fig.8 Casting speed fluctuation

Online Data Analysis for a Slab Caster

Casting Speed, Mold Level Position and Temperature of the Mold Plate

The caster had two strands and the slab size is 1300 mm × 230 mm. The casting speed was approximately 1.1 m/min. The heat was 300 ton, and the pouring time for a heat was approximately 50-65 min. Four cast sequences

were recorded – Cast 1 through Cast 4. **Figure 11** shows the casting speed, level position and the temperature of the mold copper plate for a slab continuous casting process. The temperature of the mold copper plate was measured at three different locations using three thermal couples. For Cast-1, the casting speed was dropped at the end pouring of each heat, and increased at the pouring start of each heat. For other cast sequences, the casting speed changed little. For the current slab casting process, the casting speed micro-fluctuation is invisible.

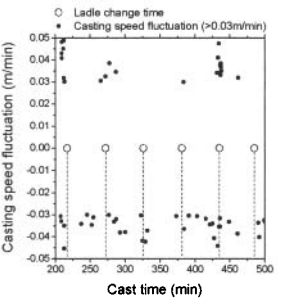

Fig.9 Casting speed *versus* time during casting of a billet

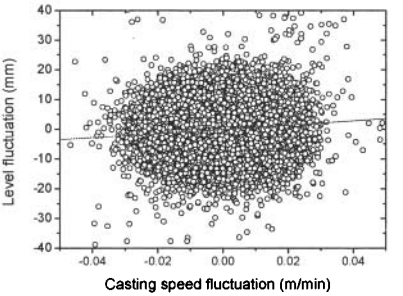

Fig.10 The level fluctuation *versus* casting speed fluctuation during continuous casting

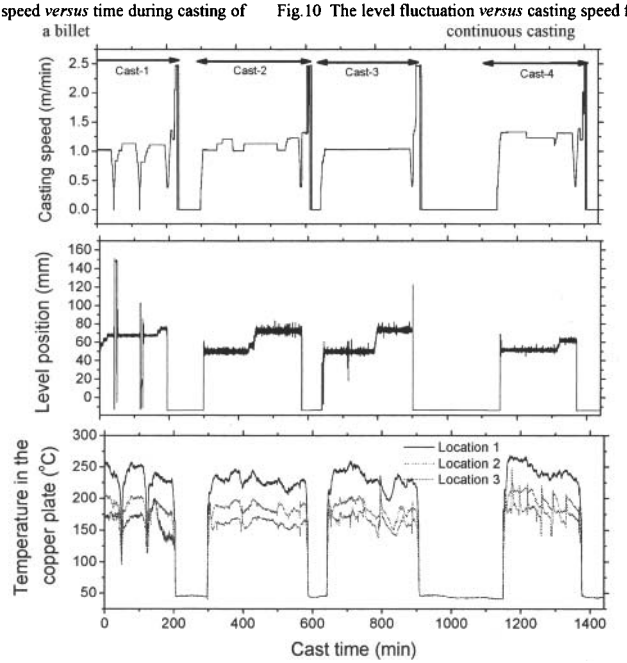

Fig.11 Online data of casting speed, level position and temperature in the copper plate

The level position can be converted to the level fluctuation using Eq. (1) and is shown in **Figure 12**, indicating the following features:

- The level fluctuation was big during ladle change, especially for the first cast sequence – Cast 1;
- The average level fluctuation for the four cast sequences was: Cast 2 > Cast 3 > Cast 4 > Cast 1;
- For any cast sequence, the level fluctuation increased with casting time, which is because the clogging of SEN became serious more and more and the flow in the mold became asymmetrical more and more, and thus induced bigger level fluctuation;
- For 3.8% of the cast time, the level fluctuation is over ±3mm (**Figure 13**). Most of the defects, such as surface defects and slag entrainment, occur during the casting period with big level fluctuation.

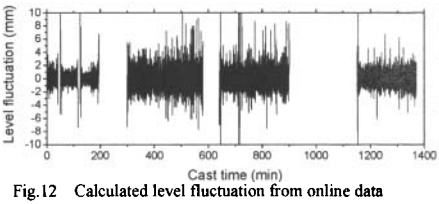

Fig.12 Calculated level fluctuation from online data

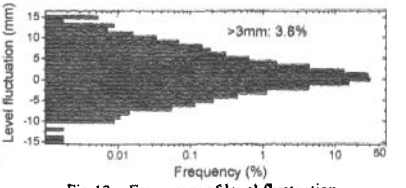

Fig.13 Frequency of level fluctuation

The temperature fluctuation at three locations of the inside of the mold copper plate can also be analyzed using the same method above, and is shown in **Figure 14**. From **Figures 11** and **14**, the following features can be concluded:

- The mold copper plate temperature was never a constant which corresponded to a transient heat transfer condition in the mold;
- The temperature of the mold plate for each heat did not always decrease but increased first and then decreased although the overall tendency of Cast-4 was decreasing. The temperature change depends on lots of conditions, such as the super heat of each heat, the flow pattern in the mold, the cooling water flow rate, and the heat transfer between the slab surface and the mold copper plate;
- The magnitude of temperature change at three different locations of the mold plate was not the same, indicating a different heat transfer conditions at different place of the mold;
- The temperature fluctuation was approximately ±1 °C for over 95% of the casting time. Cast-1 had larger temperature fluctuation than other cast sequences, and the temperature fluctuation increased with cast time.

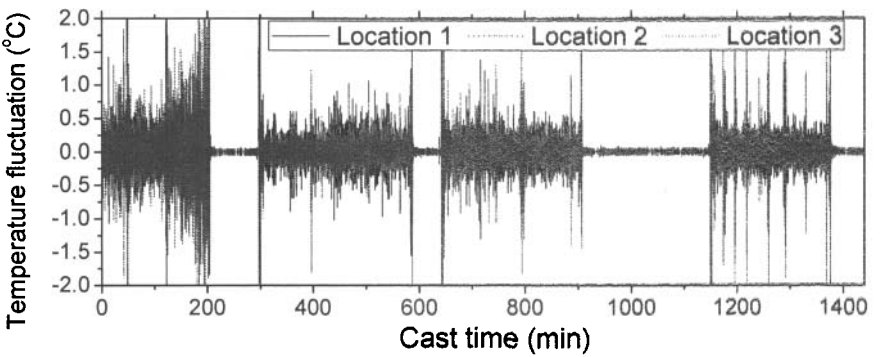

Fig.14 Calculated fluctuation of temperature in the mold plate from online data

Abnormal Cast Stop

Figure 15 is an example for an emergent stop of a continuous casting process (SS400 steel and 230×1800mm slab). When the casting length reached 1.63 m, the slab could not be further dragged, and the pouring had to be stopped. From the online reported data, it can be seen that the drag force on the rollers of the caster increased abruptly after 3 minute pouring. Later checking indicated that the tail of the dummy bar touched the roller and was blocked there. So, if the online data can be monitored in time, this kind of the emergency can be avoided. This kind of casting failure is very serious, since the molten steel will be kept in the mold and the caster, and has to be removed from the caster after being fully frozen. **Figure 16** shows the frozen slab in the mold region in the current abnormal cast stop.

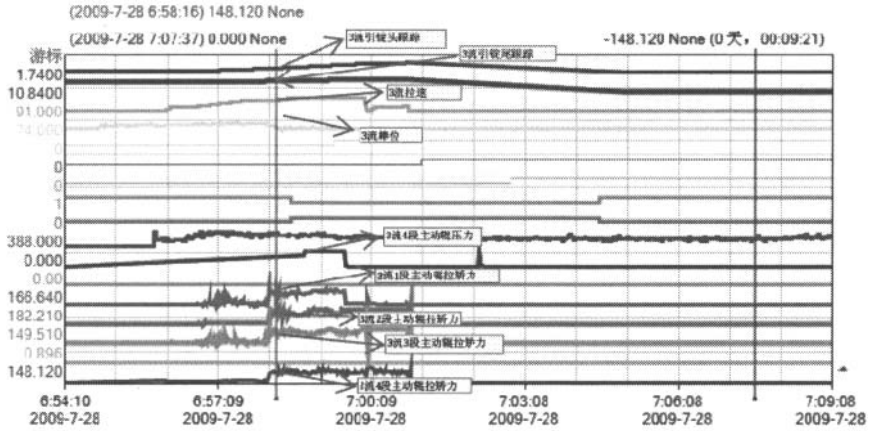

Fig.15 The online data for the stress at the roller

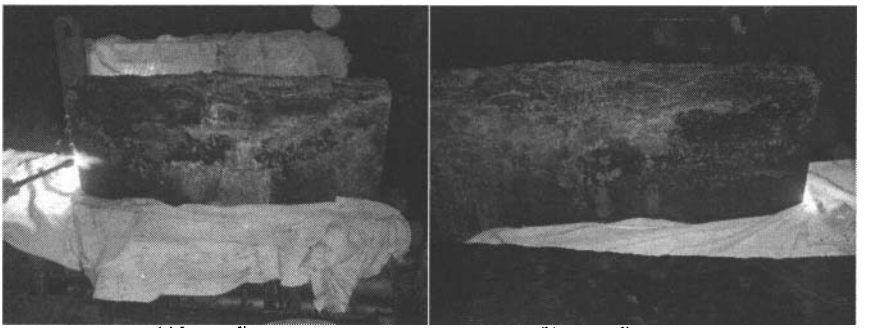

(a) Inner radius (b) outer radius

Fig.16 The frozen steel in the mold and the caster after failure of dragging dummy bar

Summary

The current paper firstly discussed the transient casting phenomena and the steel cleanliness during transient casting. The online detection data of the casting speed, level fluctuation, liquid slag shape, and the temperature in the mold were analyzed for a billet caster and a slab caster. The macro-fluctuation and the micro-fluctuation are discussed. The macro-fluctuation is found to relate to the casting operation and the micro-fluctuation is related to the turbulent fluctuation in the continuous casting mold. The online detection data of the stress at the roller for an abnormal cast stop was also analyzed and concluded that the dummy bar was blocked by the roller which induced the stop of the further motion of the slab. Industrial online detection data can be used to analyze lots of different quality issues of the continuous casting of steel.

Acknowledgements

This research is supported by the Research Board Grant, Laboratory of Green Process Metallurgy and Modeling (GPMM), Material Research Center (MRC), Intelligent Systems Center (ISC) at Missouri University of Science and Technology (Missouri S&T).

References

1. H. Uehara, H. Osanai, J. Hasunuma, K. Hara, T. Nakagawa, M. Yoshida, S. Yuhara, "Continuous Casting Technology of Hot Cycle Operations of Tundish for Clean Steel Slabs," La Revue de Metallurgie - CIT, Vol. 95 (10), 1998, 1273-1285.
2. L. Zhang, S. Yang, K. Cai, J. Li, X. Wan, B.G. Thomas, "Investigation on the Fluid Flow and Steel Cleanliness in the Continuous Casting Strand," Metallurgical and Materials Transactions B, Vol. 38B (1), 2007, 63-83.
3. R. Dekkers, B. Blanpain and P. Wollants, "Steel Cleanliness at Sidmar," in ISSTech2003 Conference Proceedings, ISS, Warrandale, PA, 2003, 197-209.
4. B. Hoh, H. Jacobi, H. Wiemer, K. Wunnenberg, "Improvement of Cleanliness in Continuous Casting," in 4th International Conference Continuous Casting, Vol. 1, Verlag Stahl Eisen mbH, Dusseldorf, Germany, (Brussels, May 17-19, 1988), 1988, 211-222.
5. P. Rasmussem, "Improvements to Steel Cleanliness at Dofasco's #2 Melt Shop," in 77th Steelmaking Conference Proceedings, ISS, Warrendale, PA, 1994, 219-224.
6. L. Zhang, B.G. Thomas, K. Cai, L. Zhu, J. Cui, "Inclusion Investigation during Clean Steel Production at Baosteel," in ISSTech2003, ISS, Warrandale, PA, 2003, 141-156.
7. L. Zhang and B.G. Thomas, "State of the Art in Evaluation and Control of Steel Cleanliness," ISIJ Inter., Vol. 43 (3), 2003, 271-291.
8. Y. Wang and L. Zhang, "Study on Transient Fluid Flow Phenomena during Continuous Casting: Part II - Cast Speed Change, Temperature Fluctuation and Steel grade Mixing " ISIJ Int., Vol. 50 (12), 2010, in press.
9. Y. Wang and L. Zhang, "Study on Transient Fluid Flow Phenomena during Continuous Casting: Part I: Cast Start," ISIJ Int., Vol. 50 (12), 2010, in press.

AUTHOR INDEX
Sensors, Sampling, and Simulation for Process Control

T

W

Z

SUBJECT INDEX
Sensors, Sampling, and Simulation for Process Control